Advances in wave-based acoustic emission sensor verification

Adelmo Fernandes de Oliveira Junior

Angaben zur Veröffentlichung / Publication details:

Fernandes de Oliveira Junior, Adelmo. 2026. “Advances in wave-based acoustic emission sensor verification.” Augsburg: Universität Augsburg.

Advances in Wave-Based Acoustic Emission Sensor Verification

Dissertation

for the attainment of the academic degree of

Dr.-Ing.

submitted to the

Faculty of Mathematics, Natural Sciences, and Technology

of the University of Augsburg

by

Adelmo Fernandes de Oliveira Junior

Augsburg, November 2025

First examiner:	Prof. Dr. Markus Sause
Second examiner:	Prof. Dr.-Ing. Kay Weidenmann
Date of the oral examination:	30 April 2026

Abstract

The acoustic emission technique is a non-destructive method used for condition monitoring of a wide variety of industrial assets and for material characterization. Although there are well-established procedures for acoustic emission sensor calibration, there is still a gap in sensor verification. The gap in sensor verification is the fact that current standard codes are not suitable for in-field sensor verification. This thesis addresses this gap by validating a wave-based mobile verification device for acoustic emission sensors. The methodology can be used for in-field, real-time verification of the sensor condition. The mobile verification device passed through several qualification tests to address each characteristic of a reliable and reproducible verification device, such as settling, environmental, and human-reproducible tests. The verification methodology is based on experimental tests in which the sensors were gradually degraded by impact, and the sensitivity of the mobile verification device was compared to a laboratory benchmark procedure, where the proposed mobile verification device showed similar performance to the benchmark procedure. It also takes into account the uncertainty in the measurements and the best features sensitive to gradual degradation. The verification methodology improves the field verification of the acoustic emission sensor, offering a mobile, reliable, and cost-effective solution compared to those restricted to laboratory applications.

Acknowledgements

This dissertation was written during my time as a research associate at the Institute for Materials Resource Management (MRM) at the University of Augsburg and was supported by the Federal Ministry for Economic Affairs and Climate Action through funding of the project calibrAEte within the WIPANO program, carried out between November 2022 and May 2025.

For supporting my PhD and for his mentorship, I express my sincere gratitude to Prof. Dr. Markus Sause. I am also grateful to Dr. Thomas Schlech for his mentorship and for the opportunity to work in the condition monitoring group. I further express my appreciation to Dr. Matthias Merzkirch for his mentorship and for providing valuable comments on this thesis. In this regard, the comments of Dr. Dhanalekshmi Prasad Yedurkar are also highly appreciated.

For technical support at the University of Augsburg, I acknowledge Dr. Robert Horny, Dr. Florian Linscheid, Dr. Marco Korkisch, Stefan Schmitt, Muhammet Bölükbas, and Frederik Siegmund.

I also acknowledge my colleagues Dr. Dhanalekshmi Prasad Yedurkar, Dr. Julia Reichmann, Kiran Kamath, Quy Raven Luong, Christina Baumeister, and Florian Becker for making my life at the University of Augsburg easier and lighter.

I also wish to acknowledge my new friends Javad Fattahi, Mohsen Omidi, Paras Ahuja, Neha Sahni, Luiz Lencioni Leite, and Leila Toledo that I made during my PhD journey. Thank you for the amazing time that we had together. They were fundamental as a relief valve during the most stressful moments of my PhD.

I thank my father, Adelmo Fernandes de Oliveira, for convincing me to become a Mechanical Engineer, and my brother, Marcelo Pampuch de Oliveira, for pursuing a PhD in his own particular way. I also thank my mother, Vani Pampuch, for her sacrifices in life that allowed me to be what I am today.

I am also thankful for the three angels, Caio Fernandes de Oliveira, Leticia Fernandes de Oliveira, and Luisa Flor de Oliveira, that God put in my life. I am also very thankful for my beloved wife, Fernanda Pereira Leite Flor. I do not have enough words to express how much I am thankful for you being by my side to share the weight of life.

This thesis received limited assistance from ChatGPT (OpenAI), used solely for editorial purposes such as correcting misspellings, typos, punctuation, and grammatical agreement errors in text written by the author. The AI system did not generate scientific content, results, or interpretations.

Contents

Chapter 1

Introduction

1.1 Motivation

Acoustic emission (AE) is a versatile nondestructive technique used in many fields of the industry, such as oil and gas [1, 2], wind [3, 4], and aerospace [5], just to name a few. Its relevance across industries reflects the interest in academia. Figure 1.1a presents the number of documents returned from a search performed on the Scopus platform using "acoustic emission" as the keyword. The search was performed at the beginning of September 2025.

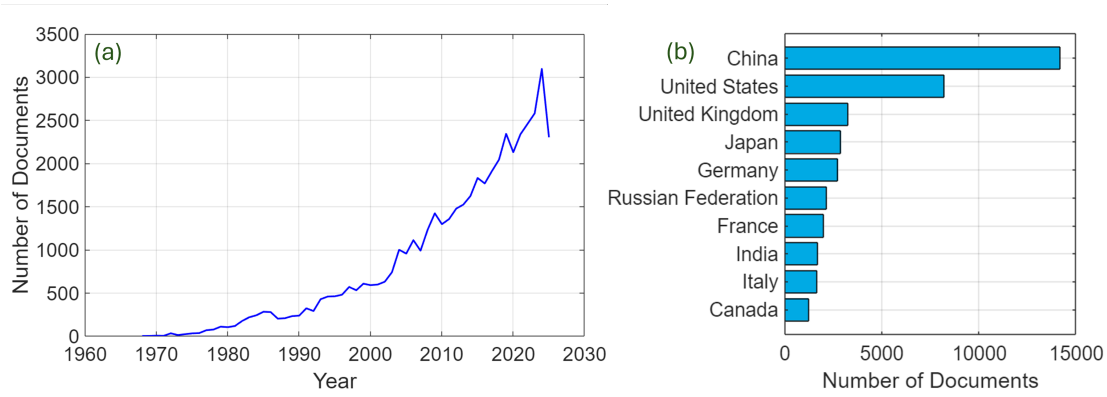

Figure 1.1: (a) Annual number of documents related to acoustic emission research published from 1986 to 2025. (b) Top 10 countries ranked by the number of published documents related to acoustic emission research. Based on Scopus data.

As can be observed in the same figure, there is a solidly growing number of scientific publications on AE over the past decades. Although a reliable estimate of the AE market size is not available, it is evident that AE research is primarily driven by the largest economies in the world, as shown in Figure 1.1b. China is the country with the majority

of publications, corresponding to 14,188 documents, followed by the United States with 8,221 documents. Germany is in the fifth position with 2,740 documents. In total, Scopus returned 48,167 documents from 1986 until 2025, where 68 % are journal articles and 28.7 % are conference papers. The three main subject areas are engineering, corresponding to 31.5 %, physics and astronomy, corresponding to 16.8 %, and materials science, corresponding to 15.3 %, as can be observed in Figure 1.2.

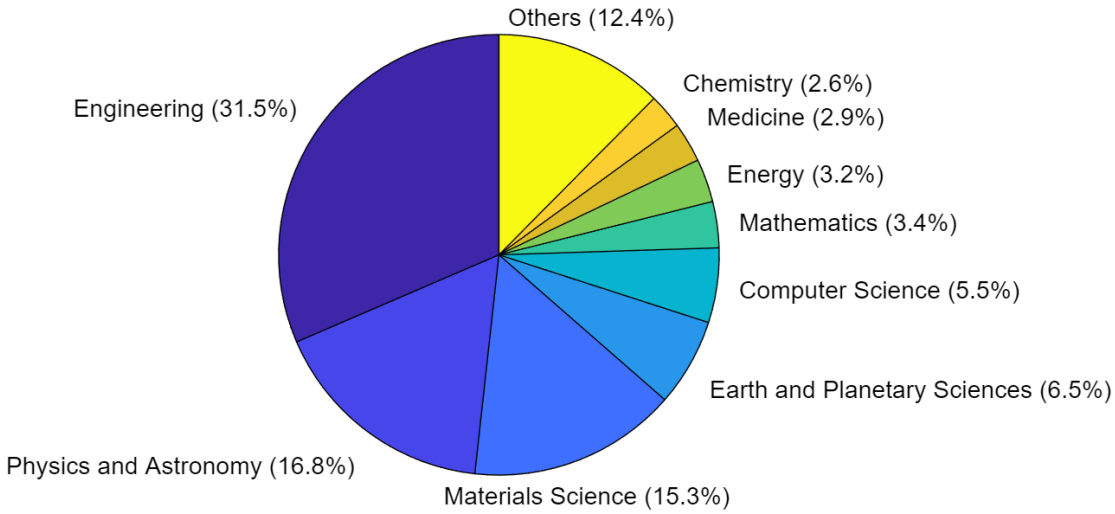

Figure 1.2: Distribution of published documents by subject area related to AE research, based on Scopus data.

One current issue in AE testing is the difficulty of finding institutions or companies that offer an absolute calibration service for AE sensors. This can be partially explained by the fact that current calibration standards require an approximately 2-ton steel block, in some cases, with a specularly finished surface [6, 7, 8, 9, 10]. A calibrated AE sensor is fundamental to fully exploit the potential of this technique. AE operators try to fill the gap in calibration services with verification procedures. AE sensor calibration is intended to characterize the sensitivity of the sensor over a certain frequency range. It allows researchers to better understand the AE phenomenon as well as to compare results. Although calibration allows one to determine whether a certain sensor is suitable for a specific AE application, it is not intended to assess the physical condition of the sensor, for example, to determine if the sensor is in good condition to play its role. This is the purpose of the verification standards [11, 12]. Although there are a few verification standards, these are not suitable for use in the field. Moreover, the influences that affect the reproducibility of the measurements of such a verification procedure have not been fully studied and resolved.

As there is a lack of devices to verify AE sensors in the field, the aim of this thesis is to fill the gap by presenting a mobile verification device dedicated to verifying the functionality of sensors in the field. An advantage of verifying an AE sensor in the field is that operators can promptly check the sensor condition after it has been exposed to harsh environmental conditions, such as chemicals, vibration, thermal cycles, or mechanical impact, without needing to go to a laboratory. In extreme cases where a laboratory is located far from the testing site, such as remote areas that are difficult to access, like offshore wind turbines, it could ruin a test campaign if there is suspicion regarding the condition of the AE sensor.

Another advantage of a mobile verification device is that it can easily fit within a climate chamber, allowing sensors to be characterized at different temperatures. It can be advantageous to check a sensor under the same temperature at which it will operate in the field. This can increase the level of reliability of the sensor, once the influence of temperature is well characterized and differentiated from possible degradation of the sensor itself.

1.2 Challenges

In order to build a robust and reliable mobile verification device, there are some challenges that must be overcome. The first is the size of the device, which are directly related to the size of the propagation medium. A large propagation medium is advantageous for guaranteeing sufficient signal length and, consequently, for better characterization of the sensor at low frequencies. However, there is a limit to the dimensions to avoid making the device difficult to transport. It is recommended that the propagation medium be as representative as possible of the real application. However, because AE testing covers a wide variety of applications, it is impossible to design a single propagation medium that represents all of them. Other challenging aspects are the cost and practicality of such a device. The goal is not to develop a device whose costs and complexity are prohibitive; therefore, the proposed solutions must be selected so that AE operators can easily replicate both the device and the procedure.

1.3 Research Objectives

The main objective of this work is to construct and validate a wave-based mobile AE sensor verification device for field and laboratory applications. To accomplish the main objective, several research questions must be addressed. The first question is to study the variables that cause uncertainty in the measurements and how they can be addressed. These include temperature, relative humidity, settling of the coupling agent, the operator, and others. For example, it is necessary to understand how the device behaves at different temperatures. Another question to be answered is whether the device remains stable after

exposure to a broad range of temperatures and relative humidity levels, as well as after reassembling it. The purpose of the research is also to assess the performance of the device in detecting damaged sensors by comparing it with a well-established benchmark device. A final objective is to establish the verification criteria based on the progressive degradation of AE sensors by impact testing.

1.4 Thesis Structure

The structure of this thesis is as follows. Chapter 2 presents the state of the art in the form of an overview of the theoretical foundations and relevant work on AE for sensor verification and calibration. Chapter 3 presents the mobile verification device, its characteristics, operation, and development. Chapter 4 presents the tests and investigations conducted to qualify the mobile verification device. Chapter 5 presents a case study to validate the mobile verification device, assessing its capability to detect sensor degradation, and to compare its performance with a benchmark device. Chapter 6 presents the verification criteria for AE sensors based on progressively degraded sensors. Finally, Chapter 7 presents the discussion, summary, and future work.

Chapter 2

State of the Art

This review of the literature is intended to cover only the highlights of the fundamental aspects so that the reader can at least gain an understanding of the context of this thesis. Although this high-level review is not intended to cover all the necessary aspects in detail, comprehensive references will be provided if further background is required.

2.1 AE Simulated Sources

An AE simulated source is an artificial source that generates AE signals which are recorded by the data acquisition (DAQ) system as a legitimate AE source. As there are several types of legitimate AE sources, there are correspondingly several AE simulated sources. In terms of sensor verification, ASTM E 976 [12] recognizes three types of AE simulated sources: pencil lead breaks (PLBs), piezoelectric transducers, and gas jets.

2.1.1 Pencil Lead Break (PLB)

Perhaps the most common AE simulated source is the PLB or the Hsu-Nielsen source [13] because it is inexpensive, practical, and fairly reproducible if performed by a skilled operator and under normal conditions. It simplifies the verification of the sensor and DAQ system performance in both field and laboratory environments. The mechanism for generating AE signals consists of breaking a brittle pencil lead with a 2H hardness, 0.3 mm or 0.5 mm in diameter and typically 3 mm in length. After pressing the pencil lead against the surface of the propagation medium with a force of approximately 3 N [14, 15], the pencil lead breaks, creating an elastic wave.

PLB produces signals that resemble crack opening and growth, making it ideal for checking the performance of the source location algorithm [16, 17]. The PLB is easy to simulate using the finite element method (FEM), generating good agreement with

experimental results [14, 15]. Although each PLB can be performed much faster than a glass capillary fracture, which is used in the AE calibration procedure, it is difficult to create a high number of events, limiting it to around 10 PLB per minute. Although this method was improved by reducing degrees of freedom and consequently eliminating any sideways components [18, 19], its variation is higher than that of piezoelectric transducers. Another negative aspect is that it generates debris of almost pure carbon, which can cause short circuits in electronic equipment.

2.1.2 Gas Jet Source

The gas jet is another common AE simulated source for sensor testing. The AE signal is generated by releasing compressed gas directly onto the surface of the sensor or propagation medium where the sensor is installed. It is capable of producing a continuous AE signal similar to actual liquid or gas leakage. One advantage of this simulated source is that it is easy to modify the parameters of the source, such as the nozzle size, type of gas, and pressure to achieve different frequencies and amplitudes of AE signals. Hsu and Breckenridge (1981) [13] suggested some control parameters for the helium gas jet as an AE source for sensor calibration. Other advantages of this source are that it is a non-contact and non-destructive source, able to produce a large number of signals, which is an advantage for averaging errors out. Its disadvantage is the difficulty of implementation outside controlled environments, such as laboratories or industrial facilities equipped with compressed air.

2.1.3 Piezoelectric Transducer Source

A piezoelectric transducer is also a common option for generating an AE simulated source that is able to be tailored to achieve different amplitudes and frequencies. It generates AE signals by the piezoelectric inverse effect, where an electric signal is applied to the piezoelectric element. This effect is explained in Section 2.4.3. The AE generated by this source can be easily modified by varying the parameters of the electric signal fed to the piezoelectric element [20, 21]. The piezoelectric element itself can be engineered to achieve specific amplitudes, frequency ranges, and waveforms. It is a non-destructive, consistent, and reproducible source, very common in sensor characterization. It can be permanently attached to the propagation medium and produce several hundred signals per minute. These two characteristics allow one to decrease measurement error even more [22, 23], because they eliminate the coupling uncertainty of the transducer, allowing for averaging random errors. Another advantage of this method is that many AE sensors can also operate as transmitters, enabling in-situ auto-check of an array of sensors installed on the test specimen. This feature is also known as auto-sensor test (AST) [24, 25, 26]. Figures 2.2 and 2.3 illustrate an AE transducer as a simulated source.

2.1.4 Laser Source

Another AE simulated source is a laser-based method. AE signals are mostly generated via a pulsed laser that creates thermal energy at a focused point on the propagation medium. The thermal energy generates rapid thermal expansion of the propagation medium, creating an elastic wave. Some parameters, such as the energy, duration, and spot size of the laser pulse, can be adjusted, producing a fine-tuned AE signal with a specific range of frequency contents and amplitudes, with excellent repeatability [27]. These characteristics make it ideal for sensor characterization [28, 29, 30]. Energy is a critical parameter, as it must be limited so as not to damage the propagation medium. One way to solve this problem and substantially increase the laser efficiency at once is to use a water-cooled jacket [31]. The disadvantages of the laser are the relatively high cost and the safety measures associated with it, which make its use limited to laboratories [32].

2.1.5 Comparison of the AE Simulated Sources

Breckenridge et al. (1990) [19] made a broad assessment of AE simulated sources, where various common sources such as PLB, glass capillary fracture, piezoelectric transducer, and ball impact, as well as some exotic ones such as spark and explosive-based methods, were tested. A total of seven types of AE simulated sources were studied by measuring their excitation via a high-fidelity sensor, including PLB, capillary fracture, capacitive transducer, conical transducer, ball impact, spark, and explosive. It was concluded that the explosive, capillary fracture, spark, and capacitive transducer were able to achieve a notable flat spectrum, with the explosive achieving the highest amplitudes, followed by the capillary fracture. However, high amplitudes are achieved at the cost of damaging the propagation medium. The ball impact was the one that produced the lowest amplitudes, with multiple zero amplitude readings. This source also created damage to the propagation medium in the form of small dents. This limitation was also observed in other studies [33, 34]. The spark damaged the propagation medium in the form of discoloration. All other sources did not cause damage or caused damage that was barely visible.

2.2 Acoustic Emission Waves

2.2.1 Longitudinal Waves (P-Waves)

Longitudinal waves are also known as primary or compressional waves. In this type of wave, the motion of the particle is parallel to the direction of wave propagation. This motion consists of alternations between compression and extension of the propagation medium. As the motion of the particles and the propagation direction of the wave are parallel, this type of wave is the fastest, and its velocity C_L is calculated using Equation (2.1) [35,

pp. 13–15]. Longitudinal waves can propagate in gases, liquids, and solids. In the context of AE testing, this type of wave is typically found in thick homogeneous materials.

$$C_L = \sqrt{\frac{E(1-\nu)}{\rho(1+\nu)(1-2\nu)}} \tag{2.1}$$

Where:

- E is the Young's modulus.
- ρ is the density.
- ν is the Poisson's ratio.

2.2.2 Transverse Waves (S-Waves)

Unlike longitudinal waves, the motion of the particle of the shear wave is perpendicular to the direction of propagation, similar to a shearing effect. Because of that, this type of wave is also known as shear waves. Its velocity C_T is typically 60 % of the longitudinal wave velocity and can be calculated using Equation (2.2) [35, pp. 13–15]. As shear motion is required to have this type of wave, it cannot propagate in liquids and gases.

$$C_T = \sqrt{\frac{G}{\rho}} = \sqrt{\frac{E}{2\rho(1+\nu)}} \tag{2.2}$$

Where:

- G is the shear modulus.

2.2.3 Rayleigh Waves (Surface Waves)

Rayleigh waves propagate through solid materials with an elliptical and retrograde particle motion. Their wave velocity C_R is 90 % of the velocity of shear waves [35, pp. 13–15]. This type of wave propagates on the surface of solid materials since its energy quickly attenuates with depth. Therefore, in the context of AE testing, this type of wave is used to detect defects on the surface or subsurface that have undergone wear or environmental degradation. The Rayleigh wave speed can be calculated by solving the transcendental Equation (2.2) [36, 37, 38]. However, for practical purposes, it can be approximated by Equation (2.4).

$$\left(1-\frac{C_R^2}{C_T^2}\right)^2-2\left(1-\frac{C_R^2}{C_T^2}\right)\sqrt{1-\frac{C_R^2}{C_L^2}}=0 \tag{2.3}$$

$$C_R \approx C_T \cdot (0.87+1.12\cdot\nu) \tag{2.4}$$

$$f_{\text{aper}}=\frac{C_R}{\phi} \tag{2.5}$$

Where:

- C_R is the Rayleigh wave speed in the medium (e.g., the material of the test specimen, such as aluminum).
- ϕ is the diameter (aperture) of the sensor.

2.2.4 Lamb Waves (Plate Waves)

Lamb waves, or plate waves, propagate in thin plate-like structures or shells and involve a combination of longitudinal and shear wave motions. This type of wave exhibits two primary modes: symmetric (S_0) and asymmetric (A_0). Depending on the propagation medium, it can exhibit higher-order symmetric and higher-order asymmetric modes as well. Their speeds strongly depend on the frequency and thickness of the plate [35]. Therefore, it is more convenient to represent the wave velocities in dispersion curves rather than with an equation. Figure 2.1 presents the phase velocity vs. frequency curves of a plate made of aluminum 5754 with a thickness of 3 mm. It can be observed that there are two asymmetric modes and three symmetric modes. Figure 4.2a and 4.2d from Section 4.1 present Lamb waves measured due to a pencil lead break (PLB) 125 mm from an AE sensor, where the S_0 mode starts at approximately 25 μs, and the A_0 mode at approximately 38 μs. Due to their multi-modes with low- and high-order components, combined with the low attenuation properties, Lamb waves are widely used in non-destructive testing (NDT) because a specific mode, and order, can be sensitive to a specific type of damage, and, due to low attenuation, a large surface can be covered.

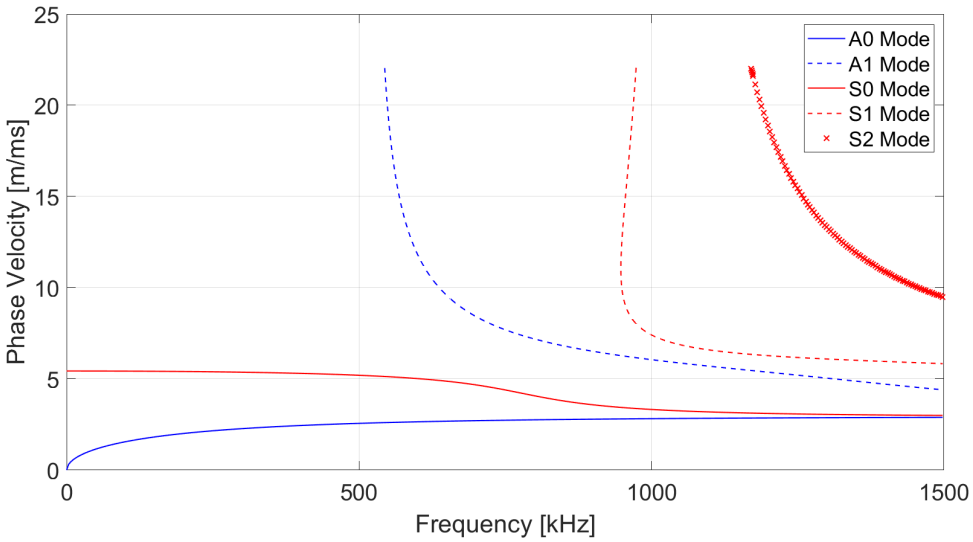

Figure 2.1: Lamb wave phase velocity vs. frequency curves of an aluminum 5754 plate with a thickness of 3 mm, obtained by a Lamb wave dispersion calculator [39].

2.3 Coupling the AE Sensor

For the elastic waves to be measured, they have to travel from the test specimen to the sensor. This is achieved by coupling the sensor to the surface of the specimen. Proper coupling is fundamental in AE testing to guarantee consistent and reproducible results. It is well known in the AE community that remounting the sensor is one of the greatest sources of uncertainty [40, 41]. Therefore, special attention must be paid to this subject. A well-known guide for coupling sensors is the ASTM E 650 standard [42], which deals with the main aspects of mounting piezoelectric AE sensors.

The first aspect of coupling a sensor to a test specimen is the coupling type, bracket, or bonding. Brackets have the shape of the sensor and can be attached to the surface of the specimen via magnets, in the case of ferromagnetic specimens, or they can be glued to them. Since they are practical, they are the most commonly used. In cases where multiple sensors are required, it is important to ensure that all brackets press the sensors against the surface of the test specimen consistently and securely to allow reproducible results [43]. Another method of coupling the sensor is to directly bond the sensor to the specimen. Although an applied force against the surface is no longer a concern, this type of coupling makes the sensor sensitive to shear waves. Moreover, it can damage the sensor wear plate during removal [44]. Another less common way of coupling the sensor to the test specimen is by screwing the sensor in place. In this case, the sensor must be a special type with threads in its body.

Another important aspect of mounting a sensor is the coupling agent (couplant). Nei-

ther the test specimen surface nor the sensor surface (wear plate) is perfectly smooth. Because there is some level of roughness on both surfaces, they will never achieve perfect contact, leaving air gaps between them. As the acoustic impedance of air differs significantly from that of both surfaces, these air gaps reduce the coupling efficiency [45]. Therefore, it is advantageous to apply a coupling agent to fill the air gaps. However, the coupling agent can also introduce variations in the measurement [41, 46, 43]. There are two main ways in which the coupling agent can introduce variation: (1) through variations in the thickness of the coupling agent layer [46, 47], and (2) through variations in the temperature of the coupling agent [48, pp. 247-248].

The coupling agent itself can influence the frequency response of the measurement system. An investigation comparing the performance of different agents–propylene glycol, glycerin, ultrasound gel, and silicone grease–showed that at low frequencies (below 200 kHz), their behavior is similar, with the observed differences attributable to variations in the coupling process [45]. In the range from 200 kHz to 350 kHz, silicone grease outperformed the other coupling agents. However, at higher frequencies (350 kHz to 900 kHz), silicone grease showed significantly poorer performance, while ultrasound gel outperformed all other coupling agents. It should be mentioned that the same study concluded that silicone grease demonstrated the least variation in coupling among all agents tested.

In a similar study of other coupling agents [49], acrylic adhesive pads, hot glue, honey, and Vaseline were investigated. Acrylic adhesive pads exhibited the least variation in sensor re-coupling in the range of 50 kHz to 100 kHz. Between 50 kHz and 65 kHz, hot glue and acrylic adhesive pads demonstrated similarly superior performance compared to honey and Vaseline. In the range from 65 kHz to 80 kHz, Vaseline and honey demonstrated superior performance.

The force that pushes the sensor against the surface of the specimen is another relevant variable, along with the coupling accommodation time. Although ASTM E 650 gives a rough guideline for the contact force, this parameter is obtained by experimental observations. In the literature, the force value used in most applications is around 10 N [21, 50, 51, 34, 52, 20]. However, some studies used values as low as 1 N [53] and as high as 35 N [54]. The coupling accommodation time is another variable for which there is no consensus in the literature, ranging from 15 to 30 minutes [53, 55, 54]. An extreme case is an investigation that reported that two days were used [40], which resulted in a coupling uncertainty of 1.6 %.

2.4 Acoustic Emission Sensing Technology

2.4.1 Acoustic Emission Phenomenon

The phenomenon of acoustic emission occurs when transient elastic waves propagate through a typical solid material in the range of 20 kHz to 1000 kHz due to the rapid release of localized energy [56]. The sources of elastic waves can be the formation and growth of cracks [57], the formation of corrosion [58], leaks [59], and so on. They can be used for a wide variety of applications, such as material characterization [60], condition monitoring [61], and structural health monitoring (SHM) [62], which is a subset of condition monitoring, just to name a few. These elastic waves can be detected by using strategically distributed sensors on the surface of the industrial asset or sample specimen, which convert the mechanical displacement caused by the elastic wave into an electrical signal, usually through the piezoelectric effect. This analog signal is usually amplified by electronic circuits inside or outside the sensor, and then converted into a digital signal using an analog-to-digital converter board [63, 56, 35].

2.4.2 Acoustic Emission Testing

In order to perform AE testing, appropriate sensors are placed at critical positions to ensure effective capture of transient signals. Sensors are selected by taking into account the frequency range of expected defect mechanisms or phenomena, as well as the material of the test specimen. The coupling agent, usually silicone grease, is applied between the surface of the test specimen and the sensor to increase the transmission of the elastic wave from the specimen to the sensor [35]. AE testing is passive, non-invasive, and non-destructive, allowing the collection of signals from the specimen during its normal operation or under controlled conditions. Data are collected, allowing real-time monitoring, or they can be further processed depending on the objective of the test. It is common practice to write a report after the AE testing with information about the test specimen, the settings, and the results of the test.

2.4.3 Acoustic Emission Sensor

There is a wide variety of acoustic emission sensor technologies available on the market, each with specific characteristics that make them suitable for specific applications, for example, at high temperatures or over long distances (a few kilometers). This section will briefly review the most common types of acoustic emission sensor technologies.

The first to be mentioned is based on the fiber Bragg grating (FBG) sensor technology [64]. A grating pattern is imprinted on a small segment of the optical fiber by ultraviolet (UV) light. This grating pattern reflects light at a specific wavelength. The elastic wave

distorts the grating pattern when the two interact, altering the peak of the reflected wavelength measured by a photodiode in the interrogator [65]. Some advantages of this sensor are its immunity to electromagnetic interference, the ability to achieve high density without a larger cost increase due to its multiplexing capability, and the capacity to transmit signals over long distances without signal attenuation, making this type of sensor ideal for SHM [66] of large civil structures.

The second type of AE sensor technology is the capacitive sensor. This type of sensor is capable of measuring very small changes in the distance between two conductive surfaces. One surface is the sample to be inspected, and the other is the resonant mass. An air gap of a few micrometers wide separates these two surfaces, where smaller gaps produce greater capacitance. The elastic wave is detected by the disturbance it causes in the air space, changing the capacitance of the sensor, and consequently, the sensor signal. The advantage of this type of sensor is its high sensitivity, making it ideal for primary (absolute) calibration of AE sensors [67, 68, 6].

The third type of AE sensor technology is the electromagnetic acoustic transducer (EMAT). There are two subgroups of this sensor type. The first is based on the Lorentz force principle and is intended for conductive materials [69]. The second is based on the magnetostriction principle and is intended for ferromagnetic materials [70]. This type of sensor is contactless and, consequently, is suitable for high-temperature environments [71] above 700 °C [72] and rough surfaces [73].

Laser interferometers can also be used to measure the AE phenomenon. However, because of the high cost of this equipment and its size, their use is restricted to laboratory measurements.

The most common type of AE sensor technology is based on the piezoelectric effect. In this type of sensor, a quartz crystal or piezoelectric ceramic can be used to convert the displacement on the surface of the specimen material caused by the elastic wave, into an electrical charge, which produces an electrical potential across the sensor. As this type of sensor is the most common, the following section explains in more detail the principle of the piezoelectric effect applied to acoustic emission. The biggest advantage of this type of sensor is that its technology is mature and well-established. These reasons may explain its relatively low cost compared to other technologies, and the ease with which new sensors can be built and prototyped.

Finally, the last type is the micro-electromechanical systems (MEMS) AE sensor. This type of sensor can have a micro-fabricated piezoelectric or capacitive element. Due to its extremely small size, it can fit in small spaces [74]. This advantage offers high spatial resolution for detecting damage, making it ideal for small test samples.

Piezoelectric Effects

Although it is possible to produce piezoelectric effects from natural and synthetic-formed crystals such as Quartz, the focus is on the piezoelectric ceramic sensors, more specifically, on lead zirconate titanate (PZT). Figure 2.2 shows an experiment that demonstrates the inverse piezoelectric effect.

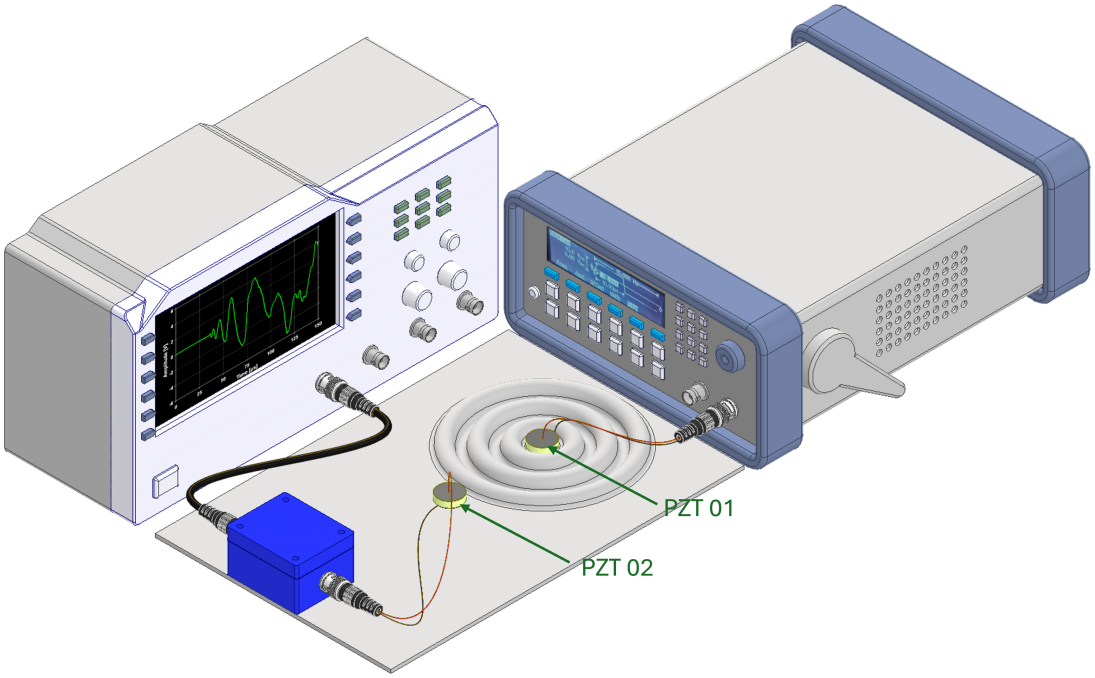

Figure 2.2: Illustration of the inverse piezoelectric effect applied to acoustic emission. The magnitude of the elastic waves is greatly exaggerated.

In the same figure, two piezoelectric ceramics are shown, named PZT 01 and PZT 02. PZT 01 has its electrodes connected to an arbitrary function generator via a Bayonet Neill–Concelman (BNC) connector, which applies an electric potential across the electrodes of the ceramic. This external potential generates an electric field that interacts with the internal electric field of the polarized PZT, which originates from the imbalance of charges aligned within its crystal lattice during poling. The interaction between the external and internal fields causes a deformation of the piezoelectric ceramic, an effect known as the inverse piezoelectric effect. Figure 2.3 presents this mechanism in detail.

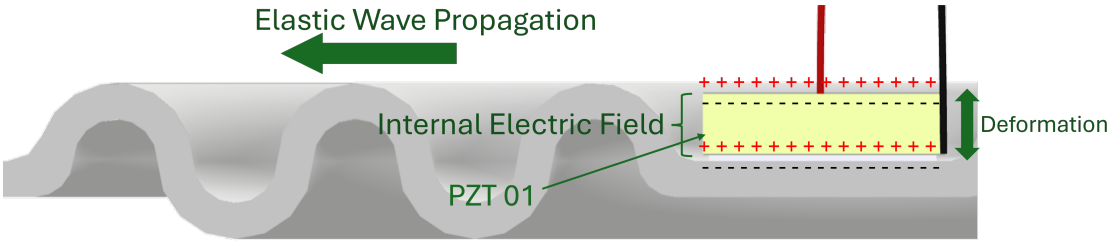

Figure 2.3: Detail of the PZT 01 element.

As PZT 01 is in contact (coupled) with the plate, it creates an elastic wave that propagates through the plate. When this elastic wave reaches the PZT 02 element, as shown in Figure 2.2, which is also coupled to the plate, it induces an electric charge on the electrodes of PZT 02. This is called the direct piezoelectric effect. This charge is amplified by a charge amplifier, indicated by the blue box in the same figure, allowing the transient signal generated by the elastic wave to be measured by the AE DAQ system. The direct piezoelectric effect was first discovered by Pierre and Jacques Curie in 1880 [75]. The inverse piezoelectric effect was verified within a year of the discovery of the piezoelectric direct effect.

Piezoelectric Acoustic Emission Sensors

Although there is a wide variety of AE sensor designs, the majority of sensors found on the market are of two types: those with and without a metal membrane, as shown in Figure 2.4a and Figure 2.4b, respectively. Sensors have a casing, usually made of stainless steel, to enclose the PZT element(s) and the amplifier circuit when the sensor has an integrated amplifier. This casing also has the function of ensuring watertightness and providing mechanical and electromagnetic shielding.

The wear plate is the element that connects the sensor to the surface of the test specimen. It has two functions. The first is to match the mechanical impedance of the test specimen material and the sensor. Another function assumed by the wear plate is to electrically isolate the sensor from the test specimen, in the case where the test specimen is made of electrically conductive material. Wear plates are usually made of alumina (Al_2O_3) or machinable glass. The wear plate is glued to the PZT element with electrically conductive adhesive in the case of sensors without a metallic membrane, or with epoxy adhesive in the case that the sensor has a metallic membrane.

There are many options for piezoelectric ceramic material, one very common being PZT ceramics [35]. It is glued to the wear plate or the metallic membrane. The bottom part of the PZT element is the negative electric terminal, or ground terminal. Therefore, the upper surface of the wear plate (for sensors without a metallic membrane), the bottom

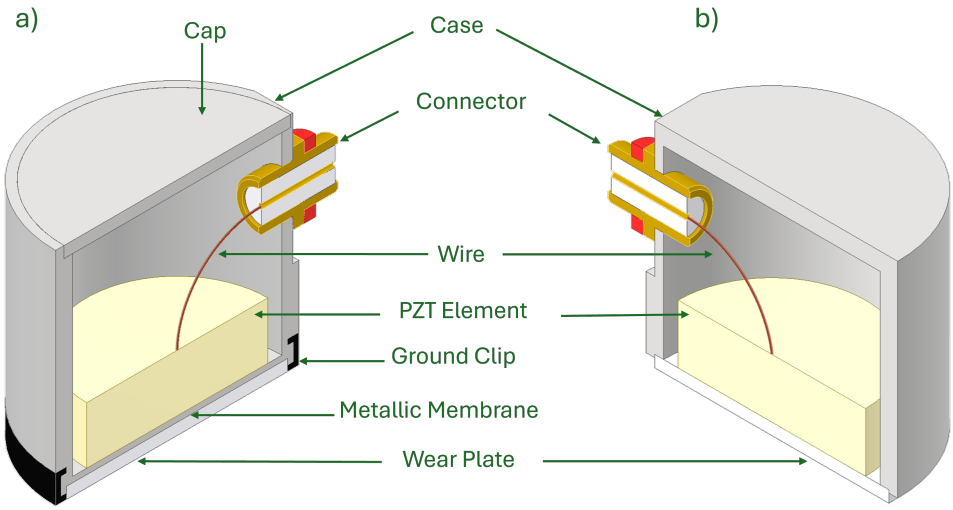

Figure 2.4: (a) AE sensor with a metallic membrane. (b) AE sensor without a metallic membrane.

surface of the PZT element, and the case must be electrically connected for the designs shown in Figure 2.4b.

One end of an electric wire is electrically welded to the top surface of the electrode of the PZT element, and the other end can be either connected to the positive electric terminal of the electrical connector or to the amplifier circuit, if the sensor has a built-in amplifier. The most common option for an electrical connector for an AE sensor is a BNC or a microdot when the sensor is of a small size.

AE sensors can have a built-in damping material, which consists of rubber or another type of viscoelastic material that surrounds the PZT element(s) inside the sensor. It serves to reduce mechanical vibrations and absorb unwanted noise. It can also suppress resonance at certain frequencies by reducing the amplitude of resonance peaks [35]. Therefore, the damping material can improve signal clarity. Figure 2.5a presents an illustration of an AE sensor with damping material.

Another element that can be present in an AE sensor is the backing mass. It consists of a mass bonded to the PZT element. The advantage of the backing mass is to delay the reflections of the elastic wave in the PZT element, avoiding its resonating, and thus improving the sensitivity over a broad band of frequencies [76, 77, 78]. Similarly to the damping material, it can also damp unwanted vibrations because it absorbs and dissipates unnecessary vibrations in the piezoelectric element. Figure 2.5b presents an illustration of an AE sensor with a backing mass.

AE sensors can also be divided into resonant and broadband sensors. Broadband sensors have a flat response in the frequency spectrum, hence they are suitable for material and damage characterization. Resonant sensors are specialized sensors engineered

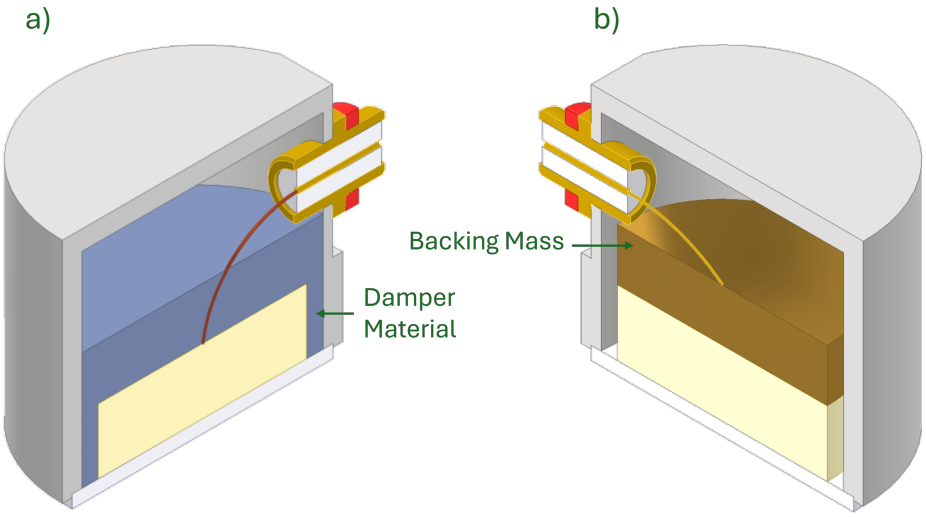

Figure 2.5: (a) AE sensor with a damper mass. (b) AE sensor with a backing mass.

for specific AE signal types. For example, low resonance frequency sensors are ideal for AE signals of low amplitude and for use with highly attenuated materials [79]. Another good example of this versatility is a sensor engineered for partial electrical discharge detection [80]. Figure 2.6 presents a sensitivity chart of three distinct sensors to exemplify different frequency ranges.

The VS75-V sensor presents a resonance frequency at 75 kHz, where it shows its highest sensitivity. One can notice that as it moves away from this frequency, the sensitivity of the sensor decreases rapidly. The VS150-R sensor has a resonant frequency at 150 kHz, where it is the most sensitive. Similarly to the VS75-V sensor, it rapidly loses sensitivity when moving far from this peak. The VS150-R sensor can be considered a multi-resonant sensor because it has other resonance peaks, such as at approximately 230 kHz and 310 kHz. The VS900-M sensor can be considered a broad-band sensor because it is sensitive to a wide range of frequencies.

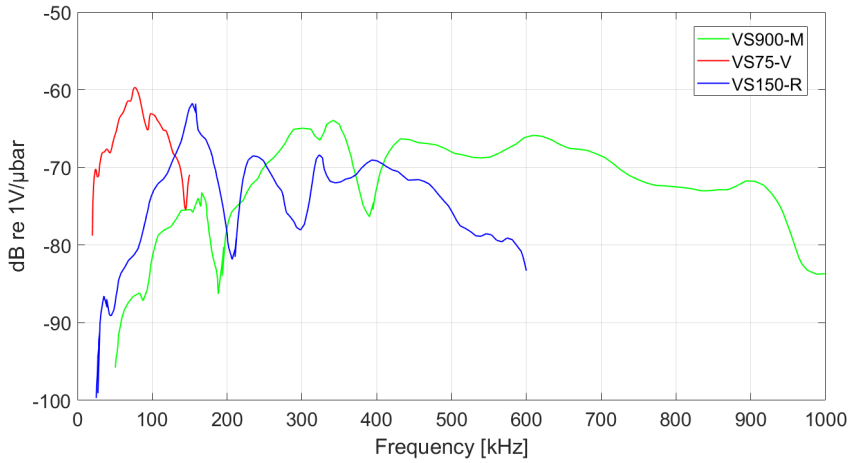

Figure 2.6: Sensitivity chart of three distinct sensors from Vallen Systeme GmbH [81, 79, 82].

AE Conical Transducer

Proctor (1982) [77] proposed a conical AE sensor that has a very high fidelity response, comparable to that of the capacitive sensor, but with much greater sensitivity. The aim of this sensor is to establish a reference sensor for the secondary calibration of AE sensors at the National Institute of Standards and Technology (NIST). This design is more robust, cost-effective, and easier to manufacture than the capacitive sensor developed for the primary calibration of AE sensors. It provides a flat amplitude response within ±3 dB in the 50 kHz to 1 MHz range. Its signal waveform is almost identical to that of the capacitive sensor, with only a slight deviation due to a small undershoot. This sensor consists of a truncated cone-shaped PZT element with a small diameter and a backing mass made of brass, which is attached to the larger diameter surface of the PZT element.

This design aligns two key features to obtain a high-fidelity response. The first one is the conical PZT element with its small tip area, which approximates a point contact area. This feature is fundamental in eliminating the fixture effect inside the frequency range of interest, which attenuates frequencies with wavelengths smaller than the diameter of the contact area. The conical shape itself also plays a role because it provides not just a small contact area, but also a relatively large volume compared to a cylindrical shaped element with the same diameter as the cone tip. This is an advantage because the larger the volume of the PZT element, the higher the sensitivity.

The second key feature of the conical sensor is its backing mass. One of the first to explore the backing mass was Oliver (1957) [76] when studying the dispersion of elastic waves. The backing mass serves as an extension of the PZT element, in a way that it delays the reflections of the high-frequency waves, with high velocities, giving time for the

low frequencies, with low velocities, to be measured without the interference of the high frequencies. Therefore, the larger the extension of the backing mass, the better the signal can be characterized because it reduces resonance effects. However, for the backing mass to work properly, its impedance has to match the impedance of the piezoelectric element, and the bonding layer between them must be sufficiently thin [83].

The major disadvantage of this design is the exposed tip of the PZT element. One consequence of that is that the tip, which plays the role of an electric terminal, can only couple to electrically conductive materials, limiting the range of materials usable as propagation media. Therefore, the propagation medium is the ground terminal, and the positive terminal is the wire connected to the brass mass or the other surface of the PZT element. Proctor (1982) [84] gave more details on the conical sensor in a further work: the flatness and and surface finish conditions of the backing mass are given, as well as recommendations to extend the usable life of the sensor. Chang and Sun (1988) [85] created a sensor version using a polyvinylidene fluoride (PVDF) film instead of PZT ceramic. It is flexible, durable, inexpensive, versatile, and suitable for metallic and non-metallic specimens. However, its sensitivity is about 100 times lower than that of the original Proctor design.

Greenspan (1982) [86] conducted a detailed analysis of the original design of the conical sensor proposed by Proctor, including the introduction of equivalent circuits to model the mechanical and electrical behavior of the sensor due to varying load and frequency conditions. Theoretical predictions were compared with the experimental results of calibration using steel plates as the propagation medium. The work underscores the conical sensor as a reliable and flat-response AE sensor that outperforms conventional AE sensors. It also identified areas for improvement, in particular, the need for better modeling of wave propagation.

Proctor (1986) [87] improved the original design, suggesting several options for backing masses, one of which had several cutoffs, forming a multi-sided polygon, in order to eliminate the symmetry of the original cylindrical mass. The PZT element was also placed in an asymmetrical location. These modifications drastically reduced interference reflections, improving the flatness of the frequency spectrum compared to the original design.

Glaser et al. (1998) [88] proposed an innovative embedded AE sensor design to measure particle velocity in solid materials based on Proctor's improved design. The goal was to create a reliable sensor to quantitatively study wave propagation and acoustic emission with sensitivity comparable to that of the commercial resonant sensor while keeping the high-fidelity flat-frequency response. These characteristics make this sensor ideal for material science investigations. The conical PZT element is identical in dimensions to the original Proctor design. However, the backing mass is made of a lead-base alloy, with the back end showing a cutoff angle of 30° to prevent direct reflections. A small field-effect transistor (FET) preamplifier is used to improve impedance matching. The PZT element, the backing mass, and the FET preamplifier are embedded in rubber, with a small portion of the PZT exposed. Finally, there is a brass casing to ruggedize the sensor. The final dimensions of the sensor are considerably smaller than those of the original Proctor design.

Lee and Kuo (2001) [89] proposed a novel device to measure surface waves [89]. This device is composed of two laser-micro-machined PZT cone elements with an aperture diameter of around 200 μm to 400 μm and a height of 250 μm. The backing mass and the casing are made of copper. This compact design allows accurate generation and detection of surface waves (Rayleigh and Lamb waves) in metallic materials. Tests on different substrates reveal consistent waveforms in close agreement with theoretical predictions. It was concluded from experimental results that the optimal frequency occurs when the aperture size is one-half or one-quarter of the wavelength. Lee and Lin [90] refined the laser-micro-machined process, allowing for more precise dimensions of the conical tip. The sensor design was also refined to include a grounding electrode on the outside surface of the sensor so that both electriccally conductive and non-conductive specimens can be measured. After achieving fairly good agreement between experimental measurements and theoretical predictions, the potential of the sensor to be a cost-effective and high-fidelity AE sensor for engineering applications was confirmed.

Although it was already noticed right after the conical sensor was proposed that it is not just an excellent high-fidelity sensor, but also an excellent transmitter [83], it was only used as a calibrated AE source for sensor calibration at the beginning of 2000s [41, 91]. An innovative self-calibrating AE source based on the original conical design proposed by Proctor was proposed with a few modifications [51, 20, 21].

The first modification was the dimension of the PZT element with a tip diameter of 1 mm, a wide-end diameter of 10 mm, and a height of 3 mm. The first innovation was a thin brass shim installed on the tip of the PZT element, performing the role of wear plate, allowing usage in non-conductive materials such as optically transparent glass block. It also used a brass backing mass; however, on the back end of the backing it was permanently coupled a wide-band differential (WD) sensor supplied by Mistras Group Inc. The setup consisted of a PZT element, a brass backing, and the WD sensor that was spring-loaded, and everything was integrated inside an aluminum case.

The principle of operation of this transmitter is based on the fact that when the conical PZT is excited by an electrical signal, it generates an elastic wave that propagates into the propagation medium to which the transmitter is coupled, and also into the backing mass, which is sensed by the backing sensor. A high coupling efficiency between the transmitter and the propagation medium means that the elastic wave will propagate with more energy into the propagation medium and less energy will be detected by the backing sensor. In fact, there is an inverse linear relationship between the coupling efficiency and the backing energy. A later version of the transducer, without the backing sensor and with the backing mass replaced by one made of tungsten epoxy, was proposed [92].

Ono et al. (2008) [28] investigated the transfer functions of commonly used AE sensors to understand their response to various waveforms. Two AE sources were used; the first one was a conical transmitter and the other was a pulsed laser. It was concluded that the conical transmitter is capable of generating reliable and consistent AE signals, which makes it preferred for calibration. Although the pulsed laser is capable of exciting sensors at high frequencies, the conical transmitter is more appropriate for lower frequencies within

the range of operation of AE sensors (50 kHz to 1 MHz). In the same year, Cervena and Hora [50] investigated the original design of the conical sensor using FEM, calculating different responses for various backing mass sizes. It was concluded that a larger backing mass improves the frequency response, and it was also possible to obtain close agreement between the simulations and the theoretical predictions. The major contribution of this work was the establishment of a FEM model to predict the response of the conical sensor, paving the way for many other works related to FEM modeling of AE sensors [15, 93, 94, 95].

McLaskey and Glaser (2010) [34] studied the generation and propagation of stress waves resulting from the Hertzian ball impact using an array of conical sensors. The sensors were custom-made by the authors, with a PZT element tip of 1.75 mm and a thin wear plate made of brass [88]. They were calibrated via glass capillary fracture and ball impact, and were able to distinctly sense longitudinal, shear, and Rayleigh waves with displacement as small as 1 pm over the frequency range of 20 kHz to 1 MHz. The experimental measurements showed good agreement with theoretical predictions for different ball sizes and propagation media. The authors also acknowledged the importance of the conical sensor in advancing sensor calibration and elastic wave propagation studies.

Sause et al. (2017) [22] presented a test setup for AE sensor verification using a conical transducer inspired by Proctor's design. The conical transducer used in this setup has a conical PZT-5A tip with dimensions identical to the one proposed by Proctor, but the brass mass, however, has a different shape, in which the angle of the cone matches the conical part of the brass mass. It is permanently coupled to an aluminum block using a silver-based paint to improve the electrical contact between the block and the PZT element. The conical transducer plays both the transmitter and receiver roles. When it is required to check the overall condition of the verification setup, the transducer plays the role of a sensor to measure the PLBs performed on the surface of the block. When it is required to verify an AE sensor, the transducer acts as a transmitter that generates pulses that are measured by the SUT. This conical transducer has demonstrated remarkable endurance, exhibiting only minor measurement variation over almost a decade, confirming the robustness and long-term stability of the conical sensor, as previously observed by Frick and Proctor (2011) [96].

Aperture Effect

A comprehensive explanation of the aperture effect is given by Monier et al. (2012) [97]. Considering a wave propagating on the surface of a medium, the AE sensor measures the normal velocity, pressure, or displacement at its contact surface, which is not uniform. Therefore, the sensor measures the average velocity, pressure, or displacement, which depends on the contact surface of the sensor and the wavelength of the wave, and can cause destructive interference, reducing the amplitude of the signal at some frequencies. This phenomenon of averaging and reducing the signal amplitude at certain frequencies is more pronounced for sensors with a larger contact area, and it is called the aperture effect.

When an AE sensor is calibrated, its response is compared to the response of the medium. However, the sensor itself disturbs the wave with its presence due to the aperture effect. This effect is considered in calibration procedures, treated as an intrinsic property of the sensor, and is thus characterized during calibration [68]. Therefore, the most suitable standard sensors for AE calibration are non-contact types, such as capacitive sensors [98, 68, 13], or sensors with a small contact area, such as conical sensors [77, 88, 90]. Laser interferometers are also an option; however, their signal-to-noise ratio must be carefully considered [41, 99, 91, 100]. Figure 2.10 shows that a typical AE sensor exhibits multiple dips in its sensitivity curve, which become more pronounced at higher frequencies. In the same figure, the conical sensor, on the other hand, has a much flatter response, which can be greatly attributed to its considerably smaller fixture size.

There is no aperture effect for the longitudinal wave, or it is greatly minimized, because the wave hits the face of the sensor in-phase [33]. However, for this to happen, the source must be on the axis of the sensor and sufficiently distant, so that the curvature of the waves approximates a line compared to the diameter of the sensor [97, 94, 33, 100]. This situation is unlikely to occur in AE applications without a proper design of the measurement setup. Therefore, the aperture effect must be taken into account when considering the frequency range of interest. Proctor concluded experimentally that when the wavelength of interest is similar to the diameter of the sensor, interference will be present in the response of the transducer [77]. Esward et al. (2002) [41] observed that, for instance, the wavelength of a 1 MHz compressional wave in glass is 6 mm, and as the vast majority of sensors are much larger than 6 mm in diameter, consequently, the aperture effect will be present for this specific case of sensor calibration. Lee and Kuo (2001) [89] when developing a device to measure surface waves via a conical sensor, concluded experimentally that the best results are obtained when the wavelength is at most one-half of the aperture size. Wu and McLaskey (2018) [33] established the aperture frequency f_{aper}, Equation 2.6, based on earlier work [101, 102]. Above this frequency, the aperture effect starts to significantly affect the response of the sensor.

$$f_{\text{aper}} = \frac{C_R}{\phi} \tag{2.6}$$

Where:

- C_R is the Rayleigh wave speed in the medium (e.g., the material of the test specimen, such as aluminum).
- ϕ is the diameter of the sensor.

There are some approaches to remove the aperture effect; however, they require precise characterization of the sensor. One method to compensate for the aperture effect involves dividing the Rayleigh wave sensitivity by the aperture function in the frequency domain to derive the longitudinal wave sensitivity [97]. It is important to note that this approach was validated experimentally, with results showing good agreement in the low-frequency range

and deviations in the high-frequency range. Moreover, the authors claim that longitudinal and shear waves are linked in such a way that it is necessary only to characterize the sensor using the Rayleigh wave (reciprocity calibration), and the other two (longitudinal and shear) sensitivities can then be obtained. More recently, a similar method was proposed that also uses division in the frequency domain; however, this method used a different aperture function [33] with a relatively good alignment between the experimental results and theoretical predictions.

2.5 AE Features

The AE DAQ system is a multichannel analog-to-digital converter, with an aliasing filter, that is able to record transient signals at a high sampling rate of several MHz. Transient signals in waveform format retain all information, making them the best way to perform advanced analysis. As can be expected, recording signals in their transient form, such as depicted in Figure 2.7, can require a large amount of computer memory. This can be the case when a substantial number of signals are generated and many channels are required to properly monitor the entire surface of the test specimen.

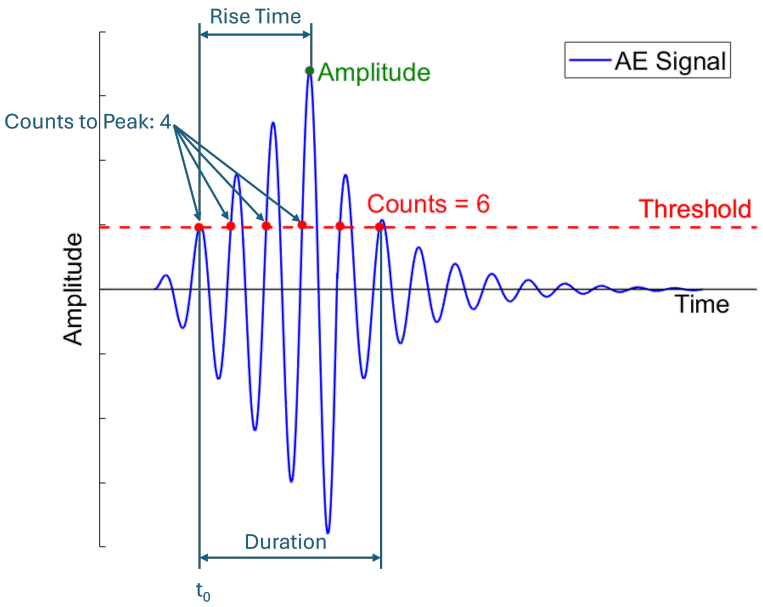

Figure 2.7: Illustration of an AE transient signal with its features.

One way around this is to record the AE signal in its parametric form, or AE features. Not only does it have the advantage of drastically reducing the required memory, but it also makes it easier to interpret the nature of the physical phenomena in question [56, p. 41] [48, pp. 132–133]. For example, a rapid increase in amplitude can be an indicator that

the specimen is collapsing [103]. Similarly, an increase in the root mean square (RMS) value can be an indicator of leakage in pressure equipment [104].

There is a wide variety of AE features, and Figure 2.7 illustrates only a few features. One very important feature is the amplitude of the signal, which is defined as the maximum amplitude of the transient signal. Another feature is the count, which is the number of times a signal crosses a certain threshold in the ascending direction. Similarly, the counts to peak feature is defined as the number of times a signal crosses a certain threshold in the ascending direction up to reaching the peak value. The Duration is defined as the time between the first and last time the signal crosses the threshold. The rise time is defined as the time between the signal first crossing the threshold and when the maximum peak occurs. Energy is defined as the area under the curve and above the threshold of the rectified signal, delimited by the duration.

2.6 Uncertainty Analysis

The JCGM 100:2008 guide [105] is used to assess the uncertainty of the measurements. There are two types of uncertainty: Type A uncertainty includes all uncertainties evaluated using statistical methods. For example, when a measurement is repeated under identical conditions, the mean and standard deviation can be determined. Type B uncertainty is assessed by methods other than statistical analysis. It relies on previous knowledge and may be based on scientific judgment, assumptions, and expertise. A typical example of this type is the uncertainty specified on the calibration certificate.

The ASME PTC 19.1:2018 [106] also specifies two types of uncertainty, known as random and systematic uncertainties. Unlike JCGM 100:2008, both can be obtained by statistical methods. Random uncertainty represents variations in measurements that are unpredictable, such as electronic noise or operator influence. This type of uncertainty can be reduced by averaging and assumed to be symmetrically distributed around zero. Systematic uncertainty accounts for predictable variations, such as temperature and instrument bias. It cannot be reduced by averaging and can cause an offset from the true value.

Although ASME PTC 19.1:2018 defines the types of uncertainty more clearly, JCGM 100:2008 was chosen to express uncertainty in this research because it is more widely accepted. The formulation to calculate the expanded uncertainty is given in Appendix A.

2.7 AE Sensor Calibration

In this section, the two types (impulse and reciprocity) of AE sensor calibration with international impact will be discussed, along with the newly proposed calibration methods.

Although calibration is not the main objective of this thesis, calibration procedures are the foundation and have a strong influence on the conception of the mobile verification device; therefore, a section is dedicated to them.

A proper calibration of an AE sensor consists first of correlating the electrical signal of the sensor with the physical quantity that is most appropriate for the phenomenon involved [99, 107, 33], which can be displacement, velocity, or pressure. Proper calibration allows for reliability, comparability, and reproducibility of experiments performed by different laboratories with consistent results, allowing further understanding of the AE phenomenon [40, 13, 30, 99]. It allows linking the acoustic signals to their sources (crack growth, delamination, corrosion, etc.) [98]. Calibration also enables the discrimination of system distortions from wave propagation effects and the source mechanism [33].

2.7.1 Impulse Calibration

Primary Calibration

The first internationally recognized standard for AE sensor calibration is ASTM E 1106 [6], first published in June 1986. This standard is based mainly on the work done by Franklin Breckenridge [68, 67, 13] and Nelson Hsu [13] and is intended for the primary calibration of the AE sensor. References [68, 67, 13] were also used in ISO 12713:1998 [10], which is similar to ASTM E 1106 in terms of purpose. This procedure calibrates reference sensors, which are then used as standards to calibrate AE sensors for field and laboratory applications. The main component of this calibration procedure is a large steel block with a specular finish (ASTM A 508 class 2 [108]). The block measures 0.9 m in diameter and 0.43 m in length and weighs approximately 2 tonnes. It serves as the propagation medium.

The calibration procedure involves placing the AE sensor to be calibrated, also called the sensor under test (SUT), and the standard sensor, namely a high-fidelity capacitive sensor [68], on top of the steel block. Both sensors are positioned symmetrically in opposite directions at 100 mm from the AE artificial source. The AE artificial source is a glass capillary fracture, which, when broken, generates a pulse that is measured by both sensors. Briefly explained, the sensitivity chart is obtained by the division of the Fast Fourier Transform (FFT) of the SUT by the FFT of the standard sensor.

Secondary Calibration

A secondary calibration procedure is the ASTM E 1781 [7] standard, which is very similar to ASTM E 1106, and intended to calibrate sensors that will be used in field and laboratory tests. The major difference from the previous procedure is that it does not use the high-fidelity capacitive sensor, but rather the sensor that was calibrated by the capacitive sensor. The second difference is a consequence of the first, where the sensitivity of the

capacitive sensor must be considered to compute the sensitivity chart of the SUT. The counterpart of the secondary calibration of AE sensors is the ISO 12714:1999 [9] standard.

Limitations and Considerations of the Impulse Calibration

The steel block used in ASTM E 1106 and ASTM E 1781 was specifically designed, in terms of material and dimensions, to represent a typical propagation medium for a pressure vessel. At the time when the standard was published, the AE technique was most commonly used to inspect this type of equipment and to detect classical sources of AE [41]. The dimensions of the block also play a role in making it appropriate for generating Rayleigh and longitudinal waves, which are also present in pressure vessels with thick walls.

However, today the AE technique is applied to many additional areas, including cavitation detection [109, 110], assessment of machine tool wear [111, 112], and monitoring the intensity of chemical reactions [113, 114], just to name a few. Furthermore, a wide variety of materials are now used, including new alloys, composite materials, and hybrid materials. With the emergence of these new materials and the increased computational power available today, Lamb waves in thin plates and shells have become more relevant. Consequently, this type of calibration is, to some extent, obsolete and no longer representative of most AE applications.

Several issues are associated with the glass capillary fracture used in the aforementioned procedures. The first issue is the variation of the capillary dimensions caused by the manufacturing process [115, 116], and the second is the low rate of the breakage [115, 31, 116]. Another issue with using the glass capillary for primary calibration is that the free surface displacement caused by the capillary break, at the same position as the RS sensor, is sometimes used as a substitute for the standard sensor signal. Elasticity theory used to calculate the free surface displacement assumes that the capillary fracture acts as a point load. However, Burks (2011) [117] demonstrated using FEM that the loading area is approximately elliptical rather than a point. This results in changes to the peak amplitude of the Rayleigh wave as demonstrated by Hamstad (2011) [118].

Another negative aspect of ASTM E 1106 and ASTM E 1781 is that both surfaces (top and bottom) of the steel block must be polished to a specular finish with very tight flatness tolerances. This requirement, combined with the massive size of the steel block, requires a substantial initial investment to implement these procedures and is not practical [53].

Other drawbacks of ASTM E 1106 include the requirement for a high-fidelity capacitive sensor, which is difficult to fabricate [77]. Furthermore, because this sensor serves as a primary standard, damage or malfunction can compromise the traceability of both primary and secondary calibrated sensors. One possible solution is to measure free surface displacement using a laser interferometer. Several studies have already implemented this approach [99, 91, 100, 119, 44].

Another limitation of impulse calibration is that its frequency range is restricted from

100 kHz to 1 MHz. This is a major limitation because this procedure cannot properly calibrate AE sensors for highly attenuated materials, as shown in Figure 2.6 in Section 2.4.3 [79].

2.7.2 Reciprocity Calibration

The reciprocity calibration method, first proposed by Maclean (1940) [120] for electroacoustic transducers, such as hydrophones, is based on the reciprocity theorem for electrical circuits. It applies to electromechanical transducers that are either purely electrostatic or purely electromechanical in nature and exhibit a reversible property [40]. The calibration of the AE sensor using the reciprocity method was first proposed by Hatano and Mori (1976) [121]. The procedure uses three transducers calibrated by Rayleigh waves. Each transducer alternately functions as a transmitter and receiver, and input and output voltages are measured such that no reference sensor is required.

Hsu and Breckenridge (1981) [13] critically reviewed the reciprocity method. Hatano later further developed the method [122, 123]. In 1998, a code with international impact, ISO/TR 13115 [8], was released based on these works. It addresses the primary calibration of AE sensors using the reciprocity method. Like ASTM E 1106, this standard requires a large transfer block, resulting in a significant initial investment. Furthermore, both experimental studies [100] and FEM simulations [94] have shown that the same sensor can exhibit varying sensitivity responses depending on the propagation medium. Figure 2.8 presents a sensitivity in decibel scale, as given in Equation 2.7. This figure illustrates the sensor behavior when different materials are used as a propagation medium [94]. The implication is that the absolute calibration of a sensor is considered for one specific material, and is not valid if the sensor is used in another material.

Although there are studies that present good agreement between reciprocity and impulse methods [123, 40, 124], and between reciprocity and laser interferometer measurements [100, 107], the reciprocity method for the AE sensor is questioned in the scientific community because the assumption of reciprocity, the capacity of the AE transducer to operate as a transmitter and receiver, does not hold for all AE sensors [107, 125, 126]. Because of that, there is an effort in the scientific community to challenge this method [127].

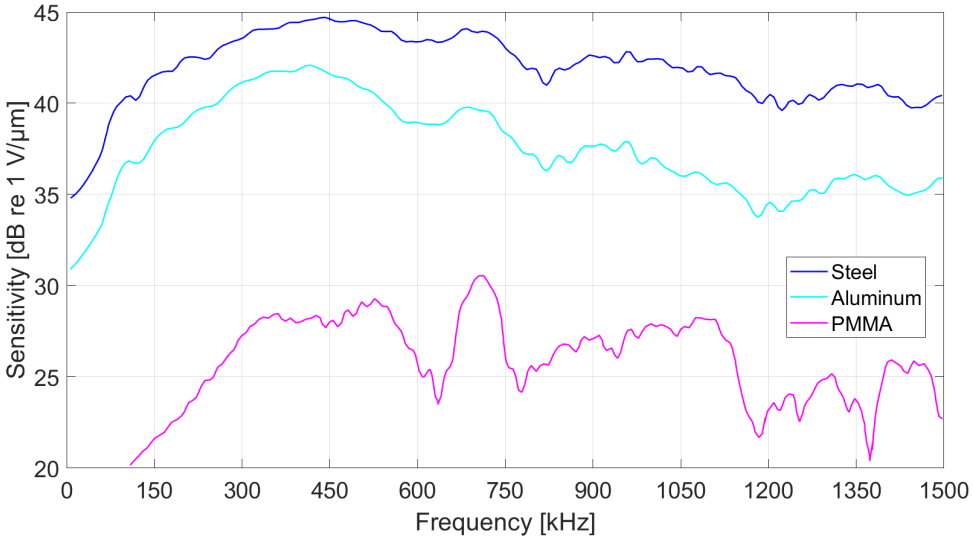

Figure 2.8: Sensitivity curves of an AE sensor numerically obtained for different propagation media materials (steel, aluminum, and PMMA). Adapted from [94].

$$\mathrm{dB} = 20 \cdot \log_{10}\left(\frac{A}{A_{\mathrm{ref}}}\right) \tag{2.7}$$

Where:

- dB is the value in decibels.
- A is the measured amplitude (e.g., voltage).
- A_{ref} is the reference amplitude.

2.7.3 New Methods of AE sensor Calibration

As discussed in Sections 2.7.1 and 2.7.2, the calibration standards with international impact have several negative aspects that make their implementation prohibitive. Therefore, many researchers have proposed new calibration methods that address the weaknesses of these standards. Several methods will be summarized in this section without the ambition of being a comprehensive review.

A major negative aspect of those standards is the need for a large transfer block, weighing more than 2 t, which is required to characterize sensors in the range of interest from 100 kHz to 1 MHz [6, 7, 8]. A large block is advantageous for proper characterization

at the lower limit because it allows the low-frequency components to be characterized without the reflections of the high-frequency components. This lower limit of interest is also a limitation of these standards, since low-resonance sensors have become increasingly relevant nowadays.

Esward et al. (2002) [41, 91] made a significant effort to establish a practical method for calibration of AE sensors. They used an innovative propagation medium made of transparent glass with relatively small dimensions (300 mm × 300 mm × 50 mm), suitable for measurements in the range from 100 kHz to 1 MHz. The authors noted that glass is easier to machine to achieve flatness tolerances and has wave propagation velocities comparable to aluminum. An innovative self-calibrated AE conical transducer was also implemented as an AE source [20, 21], and the reference measurements were performed by a laser interferometer. They identified surface preparation, choice of coupling agent, and applied force as the main sources of uncertainty, which significantly affect the repeatability of sensor coupling. The variability due to surface issues was estimated to cause deviations in the sensitivity of approximately 5 % to 30 %. In some cases, depending on the methodology, this variation could range from 0.18 V/pm to 0.37 V/pm. An additional advantage of the transparent glass medium is that the laser interferometer and SUT measurements can be performed simultaneously, as the laser beam passes through the glass and can be focused on the SUT wear plate. This eliminates the need for sequential measurements, which in other methods can increase uncertainty because the SUT and reference sensors do not experience identical excitation.

Theobald (2009) [44] proposed a method using two hemispherical aluminum blocks as the propagation medium to measure the out-of-plane and in-plane displacement AE sensor sensitivity, with laser interferometer reference measurements, covering a frequency range from 100 kHz to 3 MHz.

Ono et al. (2010) [30] used a rectangular aluminum plate (150 mm × 150 mm mm × 50 mm) as the propagation medium and performed reference measurements using a laser interferometer, measuring a range from 20 kHz to 1 MHz. They employed a broadband ultrasonic transducer and PLBs as simulated AE sources. They recommended revising the ASTM E 976 [12] to incorporate power spectral density (PSD).

Ono et al. (2017) [53] extended the method using a flat aluminum bar, measuring 25.4 mm x 6.4 mm x 3660 mm, and a laser interferometer to measure the normal displacement of guided waves from 22 kHz to 1.5 MHz, using an ultrasonic transducer as the AE source. Optimal measurement conditions were a 1 N contact force, Vaseline as the coupling agent, and a 15-minute wait before measurement to minimize re-coupling uncertainty.

Augutis et al. (2016) [115] proposed guided wave calibration of bars and plates, using a laser interferometer and a piezoelectric transducer as the AE source, covering frequencies from tens of kHz to several hundred kHz.

Ono has been the sole author of other relevant publications on AE sensor calibration, including one in which various methods are employed using solid blocks as the propagation

medium and a frequency range of 30 kHz to 2 MHz. Reference measurements were carried out using a laser interferometer, and the simulated AE source used was an ultrasonic transducer. The sensitivity values of typical AE sensors were found to range from 1 V/nm to 4.5 V/nm. The variation between methods was also found to generally be within ± 2 dB, but depending on the frequency range, this variation could exceed 5 dB. In other studies, Ono also carried out a comprehensive review of calibration methods, in which various types of propagation media were used with similar frequency ranges that extended as low as 10 Hz [55, 127, 119, 54].

McLaskey and Glaser (2010) [34] used plates of different materials, steel, aluminum, glass, and PMMA (polymethyl methacrylate), measuring 610 mm x 610 mm x 50 mm. The frequency range was 20 kHz to 1.5 MHz. Two types of simulated AE sources were used: spheres of various materials to generate Hertzian impacts with lower-frequency components, and breaking glass capillary tubes to provide high-frequency components. A PZT conical sensor performed the reference measurements. The study aimed not to establish a calibration procedure, but to demonstrate that the measurements agree with Hertz's theory, providing a basis for absolute sensor calibration. A variation in sensitivity of ± 3 dB was also observed due to coupling problems such as contact force and waiting time before measuring. The deviation between the theoretical and experimental spectral analysis was as low as 1 % to 2 %.

Another relevant initiative is the face-to-face (F2F) method, in which the sensor is directly coupled to the transmitting transducer without a propagation medium. Reference measurements can be taken at the coupling surface of the transmitting transducer using a laser interferomete [52, 128] or by measuring a calibrated receiving transducer, RS or standard sensor [116, 128]. Although there is a proposal to make this method an absolute calibration standard for AE sensors [129], there are other authors who do not consider it an absolute calibration procedure because no propagation medium is used [94].

Xiao et al. (2015) [128] reported excellent agreement of the F2F method, with only a 0.8 dB deviation between the frequency spectrum measured by a laser vibrometer and that obtained via the NIST calibration procedure. For the SUT, model R15 supplied by Mistras Group Inc., the deviation of the resonance frequency was less than 2 % compared to the laser vibrometer method. The expanded uncertainty (95 % confidence level) was 0.82 dB. In another study, it was possible to obtain a difference in sensitivity of less than 5 % compared to the factory calibration of the R15 sensor [116].

A major limitation of the absolute calibration of AE sensors is the fact that there is no single sensitivity curve. The sensor sensitivity changes as the material and shape of the propagation medium change. A further step towards resolving this limitation is to deal with the problem by means of a numerical approach. A relevant contribution in this direction was made by Cervena and Hora (2008) [50], when they investigated the performance of a high-fidelity piezoelectric cone transducer with a backing mass, designed by NIST [77, 84, 87, 86], by means of FEM. The COMSOL Multiphysics software was used to simulate the AE source and the transducer response due to different backing mass sizes.

Sause et al. (2012) [15] also investigated the piezoelectric cone transducer with FEM and COMSOL Multiphysics software. The simulated AE source was the PLB, and the propagation medium was a rectangular aluminum plate measuring 1000 mm x 750 mm x 3 mm. The frequency range was from 1 kHz to 2 MHz. The aim was to investigate the effects of varying the cone tip of the piezoelectric element on the transducer's signal response. The authors concluded that the best tip diameter was 1.5 mm, which achieved the best balance between amplitude sensitivity and spectral flatness. Good agreement was also obtained between the experimental and simulated results. Figure 2.9 shows the simulated and experimentally measured signal from the conical sensor.

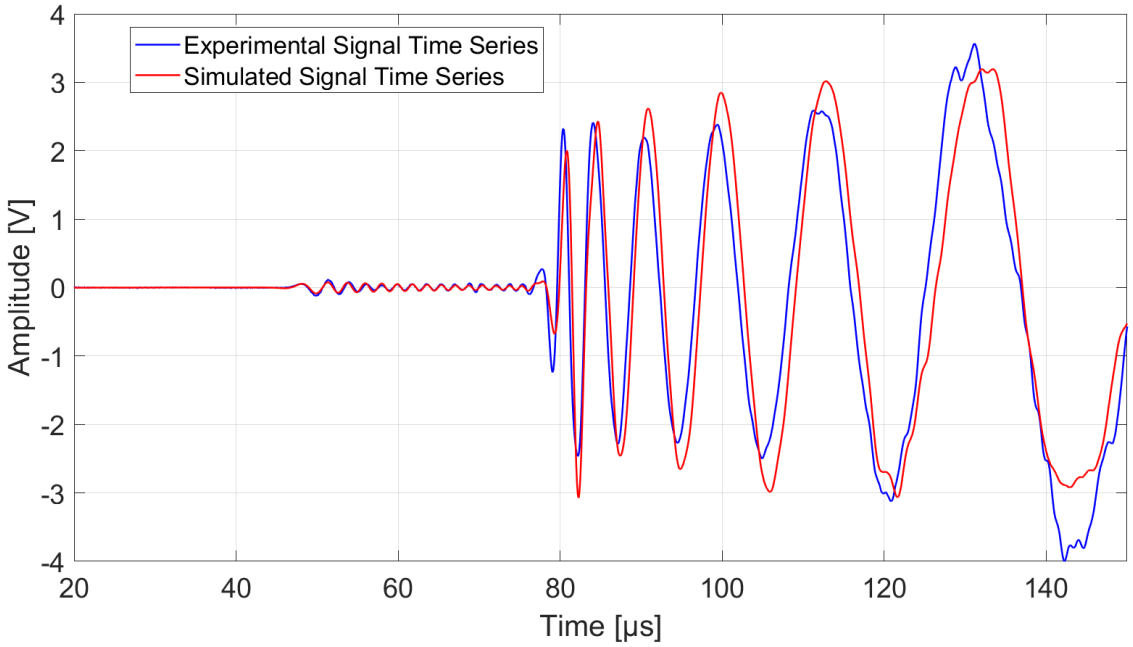

Figure 2.9: Simulated and experimental signal waveform of the conical sensor. Adapted from [15].

Zhang et al. (2017) [130] also contributed a relevant paper on the numerical approach to absolute AE sensor calibration. The authors investigated the responses of three types of AE sensors, including commercial sensors and a custom sensor designed to detect shear waves [29], experimentally and numerically (using COMSOL Multiphysics). The simulated AE sources were the PLB and a laser pulse. The propagation medium was a rectangular steel plate with dimensions of 254 mm x 254 mm x 12.7 mm, and the frequency range was from 10 kHz to 1 MHz. Good agreement was shown between the numerical and experimental results, with correlation coefficient values ranging from 0.80 to 0.89, depending on the AE simulated source and the specific sensor.

Wul and McLaskey (2018) [33] also used experimental measurements to validate theoretical and numerical models for broadband calibration of AE sensors in the frequency range of 1 kHz to 1 MHz. In the experiment, a thick aluminum plate with dimensions of 614 mm x 614 mm x 100 mm was used. Ball impacts of different sizes and materials

were used as the AE source to control the frequency content measured by the sensor. It was demonstrated that FEM can simulate low-frequency excitations, while generalized ray theory can model high-frequency excitations, enabling broadband calibration. For high-frequency components up to 1 MHz, the agreement between the FEM and generalized ray theory was within 2 dB. For low-frequency components from 1 kHz to 10 kHz, the agreement between the accelerometer data and the FEM was within a few dB, except between 6 kHz and 8 kHz, where the deviation reached up to 10 dB. The authors reported coupling effects (hot glue) that introduced frequency-dependent attenuation, and small incompatibilities between the material and dimensions of the plates and their digital model as sources of uncertainty.

Another relevant investigation of absolute calibration simulation was performed by Sause and Hamstad (2018) [94], who studied the response of two types of AE sensors: a typical AE sensor design and the conical sensor [15]. The frequency range of interest was from 0 Hz to 1.5 MHz. The relevance of this work is to demonstrate the viability of Lamb waves generated in thin plates for use in the absolute calibration of AE sensors. Figure 2.10 presents the simulated sensitivity curves for the conical and typical AE sensors, where the propagation medium is a steel plate and the excitation is the PLB. The conical sensor exhibits a flatter response than the typical AE sensor. This is attributed to the aperture effect, which is more pronounced in the typical sensor. Additionally, the backing mass of the conical sensor contributes to spectral flatness, as it delays high-frequency reflections.

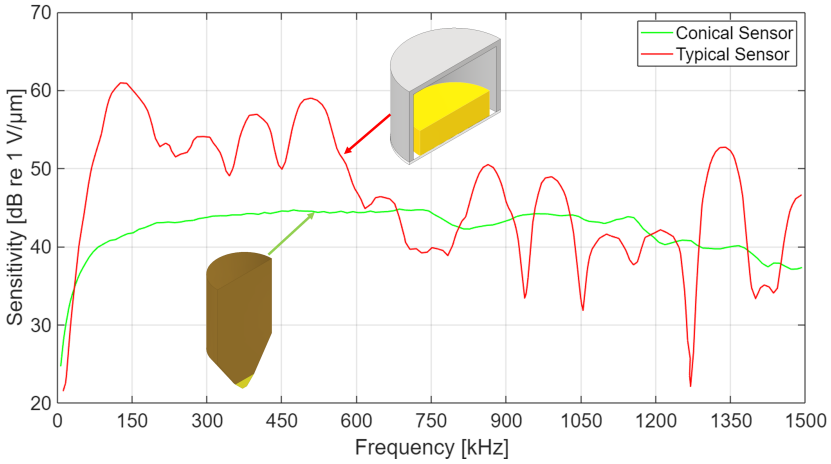

Figure 2.10: Simulated sensitivity curves for conical and typical design AE sensors for Lamb waves in a steel plate. Adapted from [94].

A final observation about the calibration procedure is that its main purpose is to establish the AE sensor's sensitivity curve, e.g., amplitude (mV/μm) vs. frequency (kHz), across the entire frequency spectrum. In other words, the purpose of the calibration standards is to establish the sensitivity graph of the sensor to allow the AE operator to choose which sensor is most appropriate for the specific application required or to compare

the results. Their purpose is not to establish criteria for passing or failing a sensor; that is the purpose of verification standards, Section 2.8.

2.8 AE Sensor Verification

As discussed in Sections 2.7.1 and 2.7.2, setting up an AE sensor calibration laboratory that strictly follows ASTM and ISO standards presents several challenges. AE operators often address the limited availability of absolute calibration services by using simpler verification procedures. A few such standards exist, and the most relevant are summarized below.

The first standard to be mentioned is ASTM E 976 [12], which specifies procedures for testing and comparing the performance of acoustic emission sensors in a simple and cost-effective way. In summary, these procedures consist of measuring the response of the AE sensor to repeatable acoustic waves that propagate in a block or rod. The acoustic wave sources can be an ultrasonic transducer, gas jet, or PLB. Regardless of the type of propagation medium or acoustic wave source, this standard emphasizes the necessity of making a verification setup as reproducible as possible with respect to SUT coupling, acoustic wave source, cables, and amplifier. A major advantage of ASTM E 976 is that it provides criteria for estimating sensor degradation.

The second standard is ASTM E 2075 [131], which specifies a procedure to routinely check the sensitivity of AE sensors. This standard can be considered easier to implement and execute compared to ASTM E 976. The main limitation of this procedure is the acrylic rod used as the propagation medium. As a polymer, its mechanical properties are highly sensitive to temperature variations. Therefore, the procedure must always be performed at a consistent temperature, which is a significant disadvantage, especially since the standard is also intended for field verification.

Another relevant standard is the DGZfP SE02 [11], whose goal is to present guidelines for sensor verification and sensor coupling in laboratories. It allows a variety of materials and shapes for the propagation medium, and consequently permits different types of waves, including Rayleigh waves and Lamb waves. It also recommends three types of AE sources: PLB, piezoelectric transducer, and hard ball impact. It establishes the criteria for acceptance of the AE sensor and the periodicity of verification. Its current version is intended to be implemented in both laboratory and field environments.

2.8.1 Field Verification of AE Sensors

A widely used field verification test for AE sensors is described in ASTM E 2374 [132]. This standard is intended to verify the performance of the AE system, referring not only to the sensors, but also to the amplifiers and AE channels. A key advantage of this method

is that verification is performed with the sensors installed on the test specimen. If a particular sensor is much less sensitive than the others, or vice versa, the sensor can be replaced. The standard provides a general assessment of sensor performance relative to others and suggests criteria for replacing sensors that deviate significantly. However, this code does not establish criteria for when a sensor is no longer usable for work.

Chen et al. (2024) [133] proposed a method for verifying AE sensors in rotating machinery, performing both quantitative analyses in the time and frequency domains to identify faulty sensors. The experimental results indicated that RMS and spectral entropy were the best features to detect a faulty sensor. Although this study provides valuable insights into sensor verification, it is specific to rotating machinery.

Priebe et al. (2024) [134] proposed an innovative approach to the self-diagnosis of AE sensors. They explored the potential of using electromechanical impedance (EMI) spectra for AE sensor self-diagnosis. Reinhardt et al. (2024) [47, 135] later refined this method by examining factors affecting the EMI spectra through combined numerical and experimental approaches. Using an aluminum plate as the propagation medium, the impact of temperature (from -50 °C to +10 °C), structural parameters (material and thickness), and coupling properties was investigated. The frequency range studied was from 100 kHz to 450 kHz.

Chapter 3

Design and Development of the Mobile AE Verification Device

3.1 Conceptual Design

The mobile verification device was designed and developed to meet the following criteria of the calibrAEte project:

1 - The device must use a wave-based approach, allowing multiple materials to be used as the propagation medium (rods or plates).

2 - It must be simple to use and inexpensive, increasing the likelihood of adoption by AE operators.

3 - It must operate with minimal human intervention.

4 - It must be reproducible and reliable.

5 - It must support the verification of sensors from different manufacturers.

6 - It must allow for in-field sensor verification.

The first criterion for the mobile verification device is that it employs a wave-based approach. Two shapes of the propagation medium could be used: a rod or a plate, which excludes the use of the F2F method.

Although rods typically have smaller cross-sectional areas than plates, they pose certain challenges as propagation media in verification devices. The main challenge stems from their cylindrical shape. When using a rod to verify AE sensors, one end couples to the SUT, while the other introduces the AE simulated source. Two piezoelectric transducers were chosen for the verification device: one acts as a transmitter to produce AE

simulated signals, while the other measures the signals to assess the device's condition. Machining the cylindrical surface of the rod flat would be necessary to properly couple the transmitter at its center.

Plates, in contrast, usually have a much larger surface area, allowing all transducers to be mounted vertically on one side without machining. They require less complex tooling to reach their final dimensions, provided that they are obtained with the required thickness. Plates are easy to obtain not only in metallic, but also in non-metallic materials such as Carbon Fiber Reinforced Polymer (CFRP), Glass Fiber Reinforced Polymer (GFRP), glass, etc. This is an advantage in cases where verifying sensors across different materials is needed.

A plate made of aluminum alloy 5754 measuring 500 mm × 400 mm × 3 mm (length, width, and thickness) was chosen as the propagation medium. Although steel more closely matches the acoustic impedance of the AE sensor wear plate, aluminum is less dense, reducing the weight of the mobile device. Figure 3.1 illustrates the main component of the mobile verification device. The 3 mm thickness balances stiffness and weight, while the other dimensions ensure at least 30 μs of usable signal without significant reflections when testing the WD sensor. The usable signal excludes pre-trigger time. This minimum signal length is based on the requirements of the benchmark verification device [22].

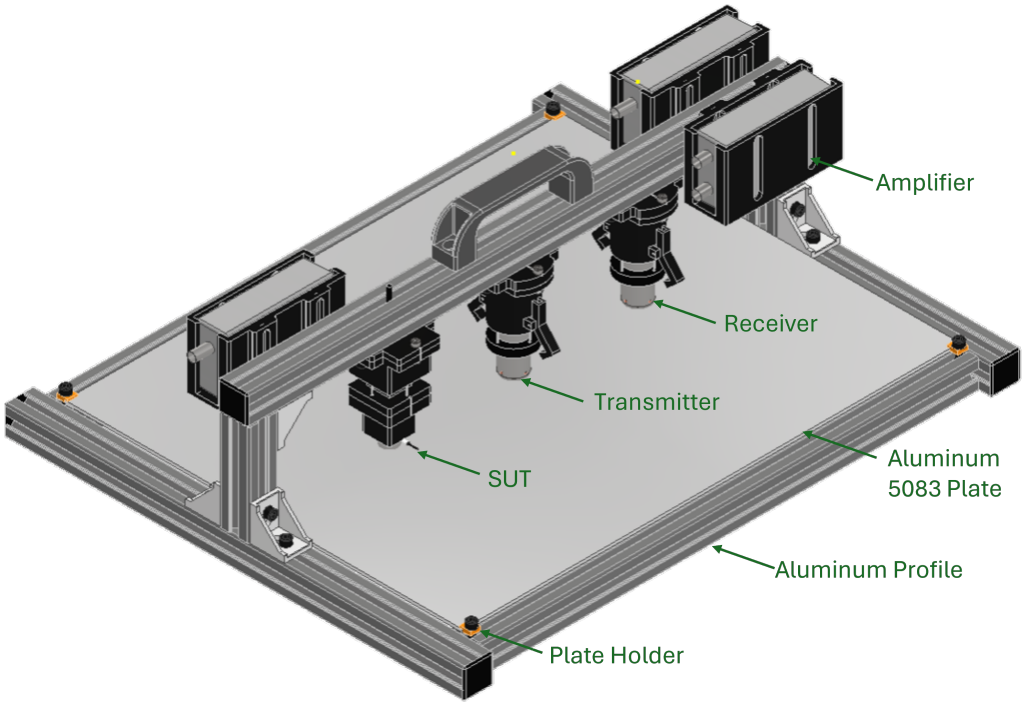

Figure 3.1: Illustration of the mobile verification device. Adapted from [23].

A transmitter transducer was chosen to produce the AE simulated signals in order

to make the process of sensor and device verification more automated and reproducible. The principle of verification of both the SUT and the verification device is to check their condition by comparing to a previous reference signal. If there is some level of agreement between the current measurement and a previous reference, the SUT or the device is approved.

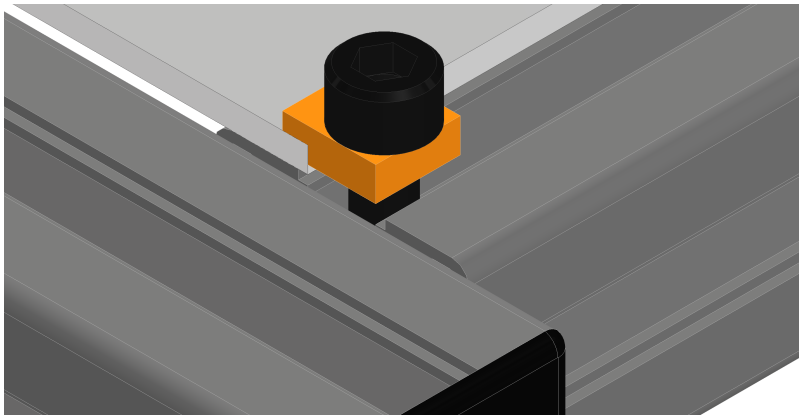

Figure 3.2: Zoom view of the plate holder. Adapted from [23].

As can be observed in Figure 3.1, the transmitter transducer is positioned in the middle of the receiver transducer and the SUT, 125 mm from each of them. The function of the transmitter transducer is to generate elastic waves that are measured by both the receiver transducer and the SUT. Because of this, it is convenient to position it in the middle of the two. As the conical sensor has a high-fidelity performance, the transmitter and receiver transducers are identical and are modified versions of the conical sensor. Another reason to use Lamb waves from aluminum plates is that their feasibility in characterizing AE sensors was already confirmed, as presented in Sections 2.7.3 and 2.4.3.

3.2 Structural Design

The mobile device consists of two structural frames constructed from 30 mm x 30 mm extruded profiles. The first frame supports the plate, while the second has bridge shape, housing the amplifier hodlers, the coupling mechanisms for the transmitter and receiver transgenders, and the SUT, as shown in Figure 3.1. The mobile device has overall dimensions of 560 mm x 460 mm x 170 mm (length, width, and height). Detailed drawings of the main components are provided in Appendix B.

The transmitter and receiver transducers, constructed by the author, are a modified version of the conical transducer described in previous experiments [22] and numerical studies [94, 15, 93]. The main components of the conical transducer, consistent with previous references and this thesis, are the PZT-5A conical tip and the brass mass, whose

conical angles matches that of the PZT tip. The brass mass includes a cylindrical section that further contributes to delaying reflections of elastic waves. Figure 3.3 presents a cross-section illustration of the transmitter and receiver transducers.

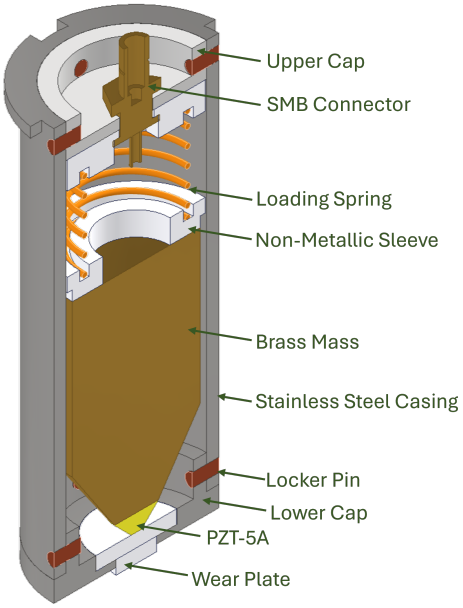

Figure 3.3: Cross-section illustration of the transmitter and receiver transducers. Adapted from [136].

The first major modification in the design is the addition of a wear plate. Since these transducers must be decoupled from the propagation medium for transportation, the PZT-5A elements cannot be cemented directly to the medium's surface, as done in [22]. An alternative is an exposed PZT tip. However, as noted in [84], repeated coupling and decoupling of the exposed PZT tip can cause its deterioration, compromising the device operation over time. This design was chosen because a similar version with the PZT-5A permanently coupled to the propagation medium operated for nearly a decade with minimal signal degradation [22]. There is also another work that reinforces the endurance of this design, showing that it was able to keep almost the same response for more than two decades [96]. Although the lifetime of such transducers is closely related to how often they are used, it is still an exceptional characteristic that the transducers have not shown a strong deterioration due to the aging process.

The wear plate is made of Alumina Al_2O_3 disks, one measuring 12 mm in diameter and 2 mm thick. The second measures 6 mm in diameter and 2 mm thick. Both disks were bonded using a high-performance ceramic adhesive supplied by Ted Pella Inc, with the lower cap serving as a template. Figure 3.4 illustrates the wear plate bonding procedure. After cleaning all components, the 12 mm disk was glued to the lower cap. Both bonding

surfaces were then moistened, and the high-performance ceramic adhesive was applied immediately afterward. A clamping force was applied to ensure intimate contact, and the assembly was cured in an oven at 90 °C for two hours.

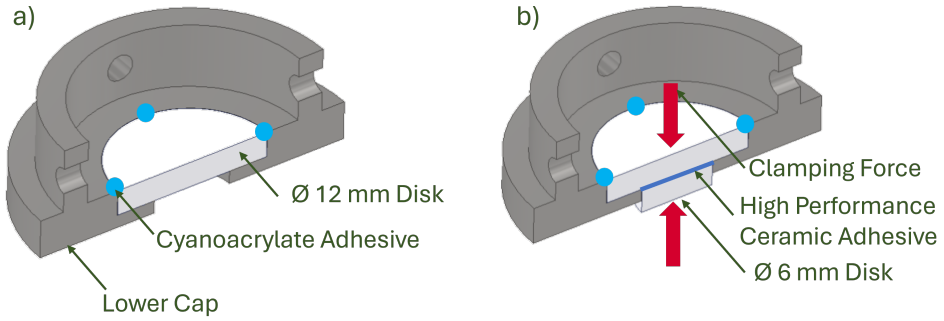

Figure 3.4: Illustration of the bonding procedure for the wear plate.

Since the smaller diameter PZT tip serves as the ground terminal and alumina is non-conductive, conductive silver paint was applied to the inner upper region of the wear plate to ensure electrical contact between the wear plate, lower cap, and PZT tip. The same conductive paint was applied at the interface between the PZT element and the brass mass. Before assembly, the smaller diameter region of the brass mass was carefully sanded with progressively finer abrasive paper up to a grit size of 2000 [84]. This procedure is necessary to promote optimal electrical and mechanical contact during bonding. After both surfaces were cleaned with isopropyl alcohol, a fine film of adhesive was applied to both surfaces and then pressed together.

Non-metallic sleeves were glued to the back end of the brass mass and the bottom of the upper cap using cyanoacrylate adhesive. Both sleeves are ring-shaped with an inner groove to accommodate the loading spring. These components use non-conductive material to prevent electrical contact between the brass mass (positive terminal) and the stainless steel casing (negative terminal). A cable connects the back end of the brass mass to the positive terminal of the SMB connector, not represented in Figure 3.3. Finishing the design of the transducers, there are locking pins to hold all the components together. The non-metallic sleeves were 3D-printed from carbon fiber-reinforced nylon (Markforged 800 Onyx), while the stainless steel casing and upper and lower caps were printed using a Metalx printer.

To allow both the transmitter and the receiver transducers to be coupled and decoupled from the propagation medium, a coupling mechanism illustrated in Figure 3.5 is used. The mechanism ensures consistent positioning and orientation of the transducers on the propagation medium. Locking mechanisms secure the transducers in the retracted position during transport to prevent damage. A cover, bolted to the aluminum profile (bolts not shown), is mounted on top of the coupling mechanism. There is also a hole in the cover lid and consequently in the extruded aluminum profile to allow cable passage.

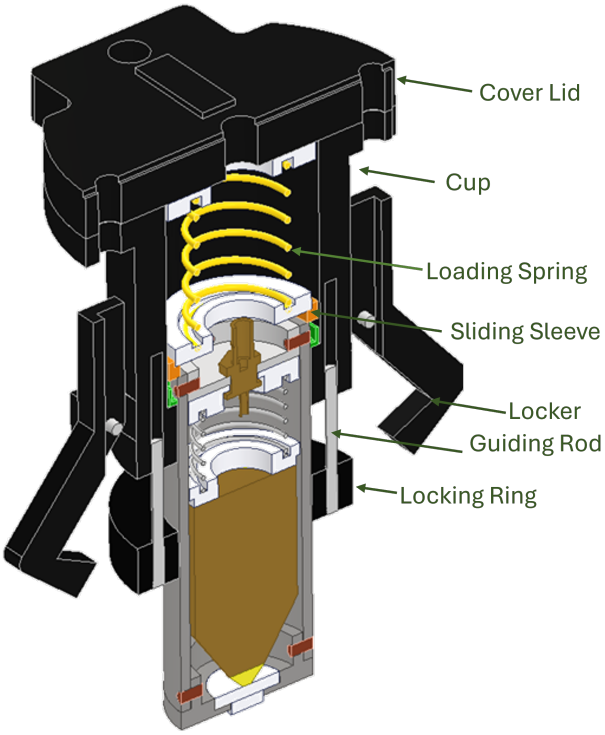

Figure 3.5: Illustration of the coupling mechanism of the transmitter and receiver transducers. Adapted from [23].

Similarly to the coupling mechanism of the transmitter and receiver transducers, there is a coupling mechanism for the SUT, as shown in Figure 3.6. The sensor adapter at the bottom is designed to have the external dimensions of the sensor. Special care was taken with the tolerances so that the sensor can be inserted and removed from the adapter with ease, however, without being excessively loose. There is also a cutout in the adapter, not shown in the picture, to allow the cable and connector to fit into the adapter and determine the orientation of the sensor. The adapter can be easily removed, allowing other adapters for different sensors. The SUT coupling mechanism is attached to the aluminum extruded profile in the same way as the coupling mechanism for the transmitter and receiver transducers. Despite the spring and the guiding rods, all other components were 3D-printed in carbon fiber-reinforced nylon, model 800 Onyx, supplied by Markforged.

As will be demonstrated in Section 4.3, the 3D-printed SUT coupling mechanism has shown lower repeatability compared to the coupling mechanism for the transmitter and receiver transducers and the coupling mechanism of the benchmark device. Therefore, it was rebuilt using metallic components with tighter tolerances. Figure 3.7 presents this improved SUT coupling mechanism. The principle of operation is the same as that of the previous one, using a spring load mechanism. The sensor adapter was also 3D-printed in carbon fiber-reinforced nylon. Despite the bolts and springs, all other components were built from aluminum. Both the first and the improved versions were designed to impose

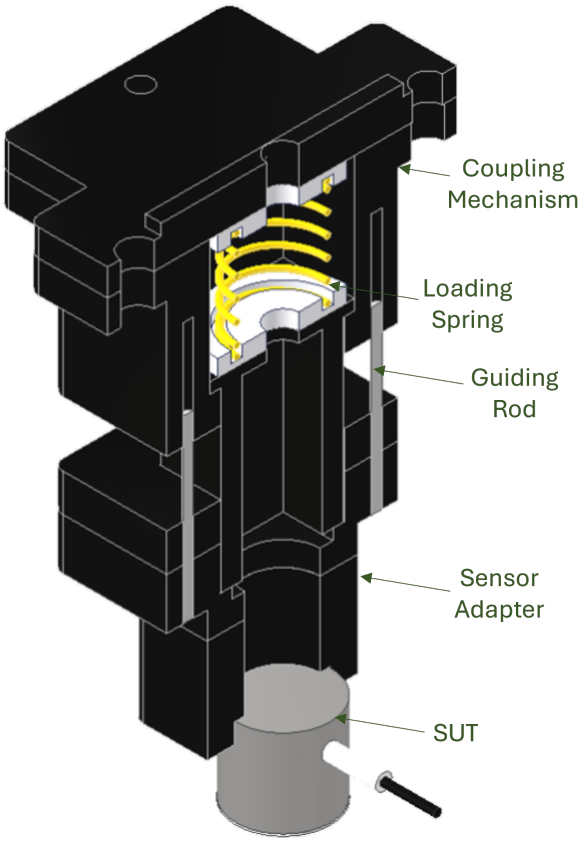

Figure 3.6: Illustration of the 3D-printed SUT coupling mechanism. Adapted from [23].

a coupling force of approximately 10 N.

The mobile verification device incorporates three amplifiers (model 2/4/6, supplied by Mistras Group Inc.). One amplifier is used for the receiver transducer, and another is used for the SUT if the sensor does not have a built-in amplifier. The third amplifier is dedicated to the transmitter transducer but is used only when the transmitter needs to be tested as a sensor. For example, during the device auto-check procedure described in Section 3.3.1, if the sensor fails its verification, a PLB can be performed to determine whether the transmitter, the receiver, or both are malfunctioning.

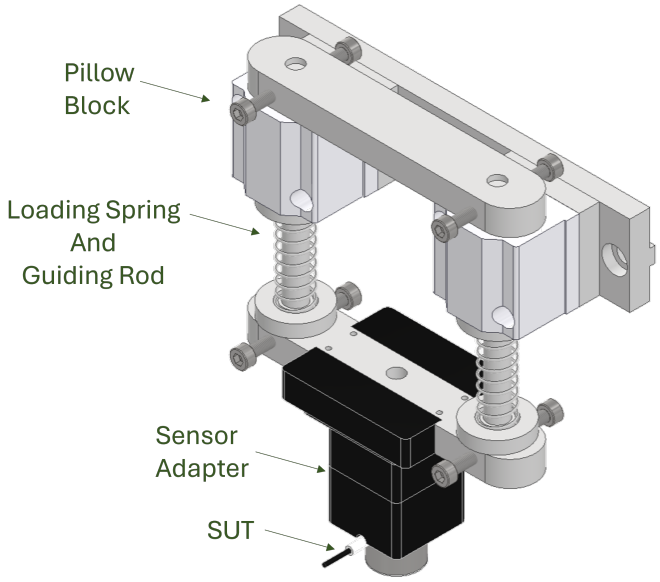

Figure 3.7: Illustration of the improved SUT coupling mechanism.

An arbitrary waveform generator, model 33210A, supplied by Agilent, is used to generate square pulses. Its output is connected to an amplifier, model WA301, supplied by Aim TTi, to increase the signal amplitude. The output of the amplifier is connected to the transmitter transducer. The amplified output drives the transmitter transducer. The optimal excitation signal is a rectangular pulse with a repetition frequency of 15 Hz, amplitude 10 Vpp, zero offset, window width of 10 μs, and an edge rise time of 20 ns, as illustrated in Figure 3.8. The gain of the amplifiers is set to 10x, exciting the transducer with a 100 V amplitude.

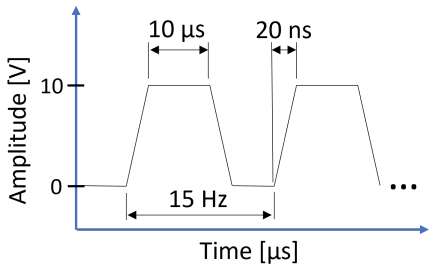

Figure 3.8: Diagram of the pulse used in the mobile verification device.

The DAQ system used is a 4-channel AMSY-MB2-V1, supplied by Vallen Systeme GmbH. The final component of the mobile verification device is a laptop, which connects via USB to the AMSY-MB2-V1, the waveform generator, and a borescope camera when it

is required to read the sensor ID. Figure 3.9 (top) presents an illustration, and Figure 3.9 (bottom) presents a picture of the entire mobile verification device.

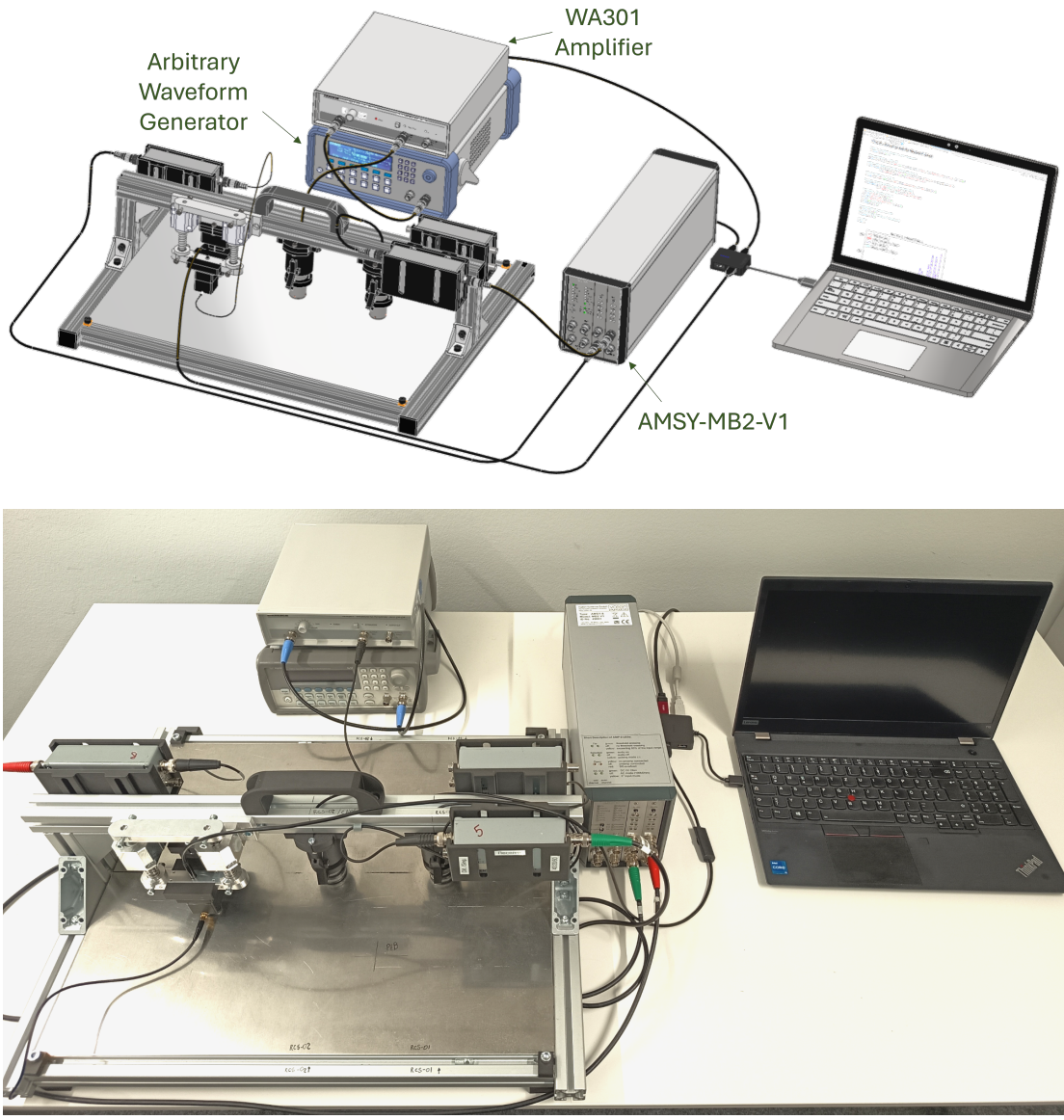

Figure 3.9: Top: Illustration of the verification setup with the arbitrary waveform generator, amplifier, AMSY-MB2-V1, and laptop [137, 138]. Bottom: Actual photograph of the mobile verification device. Adapted from [23].

3.3 Operational Procedure

The protocol to operate the mobile device is divided into two steps, the first step is the device auto-check and the second step is the sensor verification itself. The purpose of the device auto-check is to verify its overall performance. There are two possible ways in which the device can undergo inconvenient modifications in its performance. The first is possible damage during transport, and the second is the fact that the device must be partially disassembled before transportation and reassembled before use. Therefore, it must be re-qualified to mitigate the possibility that the device is at fault rather than that the SUT is damaged.

3.3.1 Device Auto-Check

To accurately assess the condition of the mobile device, a minimum of 600 measurements is required. Each measurement consists of one waveform generated by the pulse of the transmitter transducer and measured by the receiver transducer. Figure 3.10a presents a typical waveform of the device auto-check, where 600 measurements are averaged. In Figure 3.10b, the dark blue line indicates the average value, while the light blue shaded area shows the maximum and minimum values. The waveform in Figure 3.10a displays a typical Lamb wave signal with two distinct modes: the S_0 mode begins at approximately 40 μs and the A_0 mode at approximately 55 μs. To avoid reflections, the signal was truncated at 116.4 μs.

After computing the experimental standard error of the mean (ESEM), as given in Equation 3.1, for the maximum amplitudes of the auto-check measurements, as shown in Figure 3.12, it was observed that the ESEM stabilizes after approximately 300 measurements. However, to ensure robustness in the uncertainty analysis, a sample size of twice this amount was chosen.

$$\mathrm{ESEM}_k = \frac{\sqrt{\frac{1}{k-1}\sum_{i=1}^{k}(x_i - \bar{x}_k)^2}}{\sqrt{k}} \tag{3.1}$$

Where:

- ESEM_k is the experimental standard error of the mean at step k.
- k is the number of observations up to step k.
- x_i is the observed value at index i.
- $\bar{x}_k$ is the cumulative mean of the first k observations.

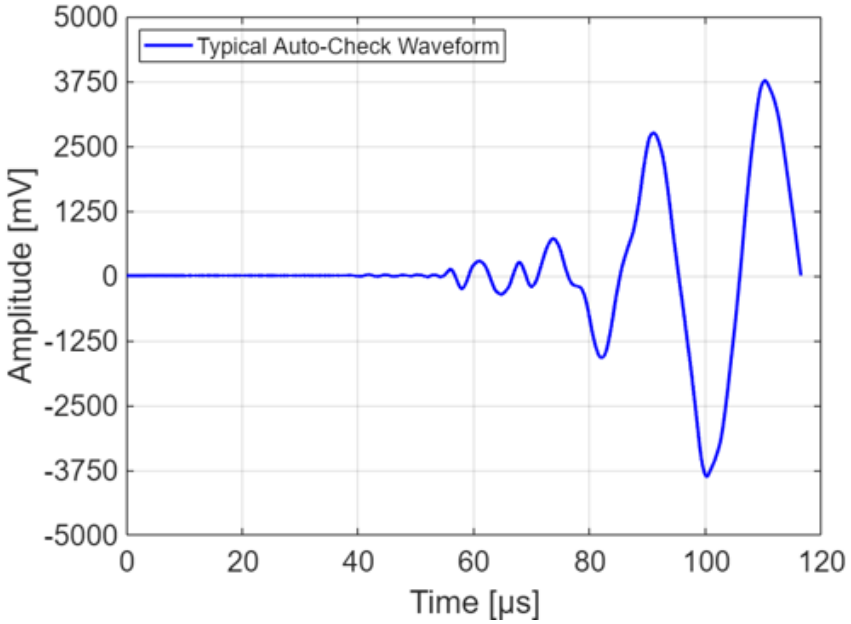

Figure 3.10: Typical waveform of the device auto-check with average as well as maximum and minimum values.

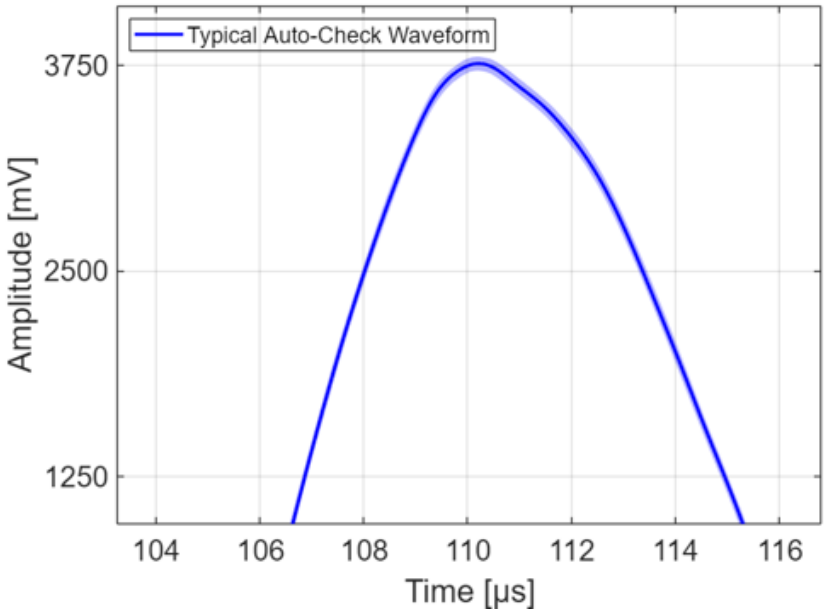

Figure 3.11: A magnified view of the waveform from approximately 107 μs to 115 μs.

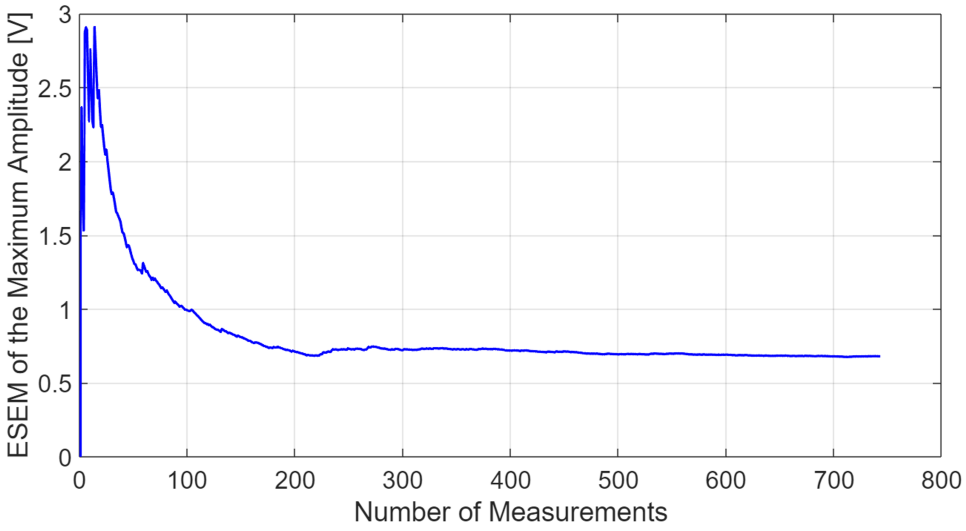

Figure 3.12: Experimental standard error of the mean of the maximum amplitude of typical auto-check measurement.

The reference data consist of 600 measurements and represent the mobile device in an undamaged state. During verification, the current measurements are compared with the reference. If the AE features fall within the allowed uncertainty, the mobile device is approved, enabling AE sensor verification. Appendix C presents the full procedure to perform the device auto-check.

3.3.2 Sensor Verification

After approving the mobile device, the SUT is coupled to the propagation medium using silicone grease, model KORASILON-Paste (medium viscosity), supplied by Kurt Obermeier GmbH & Co. KG. This coupling agent was chosen because it is the same one used in almost all the tests performed in the Department of Mechanical Engineering at the University of Augsburg. Although there are other coupling agents that perform better, as presented in Section 2.3, using the same coupling agent to verify the sensor is more practical. This coupling agent was used in all tests.

Similarly to the device auto-check, 600 measurements of the SUT are performed, and if the AE features of the current measurements are within the allowed uncertainty, the SUT is approved. Figure 3.4 presents the ESEM of the maximum amplitude of a WD sensor. The ESEM begins to stabilize after approximately 400 measurements. Therefore, a total of 600 measurements was also chosen to perform sensor verification to ensure statistical robustness in the analysis and to have the same number of measurements as the device auto-check.

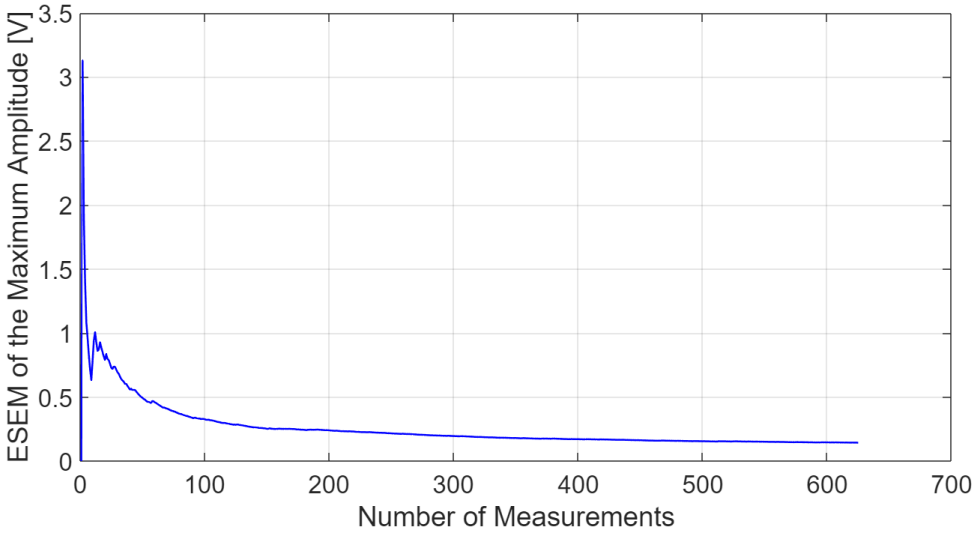

Figure 3.13: Experimental standard error of the mean of the maximum amplitude of a typical measurement of a WD sensor as the SUT.

3.4 Signal Acquisition and Processing

In terms of data acquisition, both measurements, the device auto-check and sensor verification, are performed using a 10 MHz sampling frequency. Measurements are acquired with a 60 dB gain, except for sensors with a built-in amplifier. The amplifier model 2/4/6 has an analog band-pass filter with a pass-band ranging from 20 kHz to 1.2 MHz.

Signal post-processing begins by converting the data from the transient data format (TRADB) to comma-separated values (CSV) using a Python script in Jupyter Notebook. Appendix D presents the Python code that automates sensor verification measurements, including file conversion. Subsequently, data cleaning is performed to remove potentially faulty measurements. Most faulty measurements are those made at the beginning and the end due to mis-synchronization between the pulse of the arbitrary waveform generator and the DAQ system.

Additional faulty measurements can arise from AE signals not generated by the transmitter transducer, such as mechanical shocks or electromagnetic interference. A cross-correlation filter is used to eliminate these faulty measurements. The filter computes the average waveform and then evaluates the cross-correlation between this average and each individual waveform using Equation 3.2. Waveforms with a maximum cross-correlation below 0.9 are discarded.

$$R_{xy}[k] = \frac{\sum_j x[j] \cdot y[j+k]}{\sqrt{\sum_j x[j]^2 \cdot \sum_j y[j+k]^2}} \tag{3.2}$$

Where:

- $R_{xy}[k]$ is the normalized cross-correlation at lag k.
- $x[j]$ is the first discrete signal.
- $y[j]$ is the second discrete signal.
- j is the current sample index of the signal.

Cross-correlation is a feature that measures the similarity between two signals as a function of the time lag between them [139]. It is used to identify delays or time shifts, as well as the signal itself, such as the radar signal reflecting back to the receiver. The reflected signal is expected to have some similarity with the transmitted signal. In other words, a signal can be recognized if the cross-correlation with a reference signal exceeds a certain threshold. Equation 3.2 computes the normalized cross-correlation between two discrete signals, that can assume values between -1 and 1. -1 indicates a perfect negative correlation, which means that one signal is an inverted version of the other. 1 indicates a perfect positive correlation, which means that both signals perfectly overlap with each other. 0 indicates no correlation, which means that they are orthogonal or unrelated in terms of alignment.

Figures from 3.14a to 3.14d present a real AE signal, the original signal, which was gradually distorted artificially. It is evident that as the distortion increases, the normalized cross-correlation values decrease. In real-world applications, there are many factors that can distort an AE signal, such as reflections, temperature variation, mechanical noise, and degradation of the coupling agent, or the sensor, just to name a few.

The next step is to truncate each waveform to eliminate the main reflection. The truncation time is case-specific and depends mostly on the geometric dimensions of the sensor and its piezoelectric element. The final step is to compute the features.

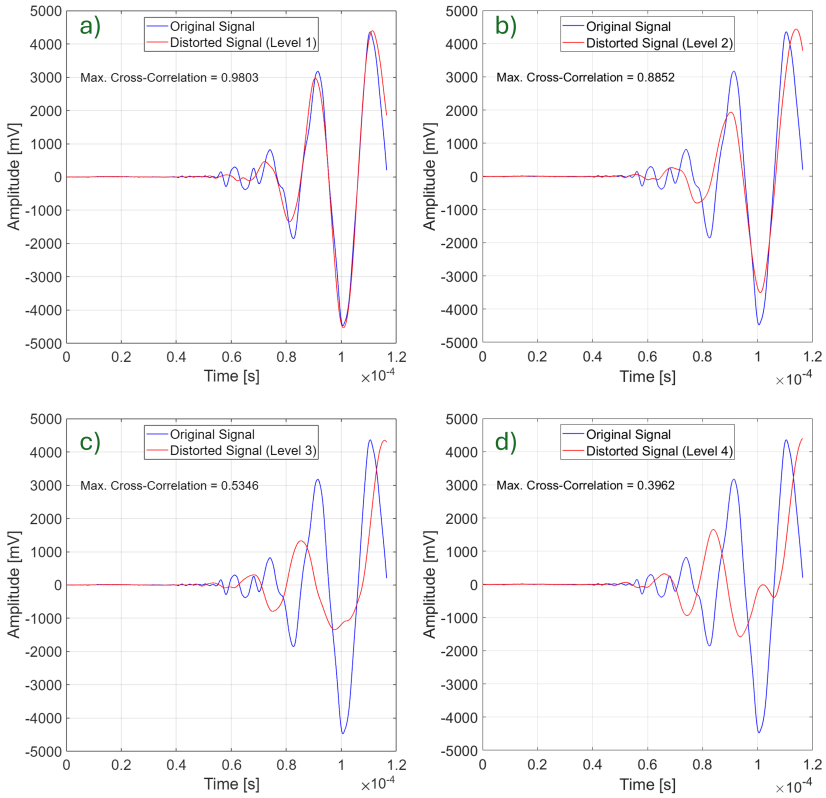

Figure 3.14: Normalized cross-correlation values between a real AE signal and gradually distorted signals.

Chapter 4

Experimental Qualification of the Mobile Verification Device

To ensure the robustness and reliability of the mobile verification device, a series of qualification tests were conducted to assess its performance. Critical analysis of the qualification test results enabled the refinement of the test protocols and the identification and quantification of error sources and weak points in the design.

Each qualification test focuses on a specific aspect of the performance of the mobile verification device. The angle sensitivity test determines the optimal transducer positions and orientations and identifies the best choices for transmitter and receiver transducers. The assembling test assesses whether measurements remain repeatable after partially disassembling and reassembling the device. The settlement test establishes the required settling time before measurements. Environmental tests verify the stability and sensitivity of the device under varying temperature and humidity conditions. The human-reproducibility test quantifies the variability introduced by different operators.

4.1 Angle Sensitivity Test

The purpose of the angle sensitivity test is to evaluate the response of the manufactured transducers at different angular orientations. This allows the determination of the optimal orientation for both transducers and the identification of which prototype is best suited as the transmitter or receiver.

Figure 4.1a presents the test setup for the angle sensitivity test. The plate and lower frame are the same as those of the mobile verification device. The extruded aluminum profile, to which the transducer holder is bolted, does not touch the plate. The test consists of performing 10 PLBs for each angle orientation, 125 mm from the transducer. Although the reversibility of an AE transducer is questionable [107, 125, 126], measuring both trans-

ducers as sensors provides a reliable estimate of their performance as transmitters.

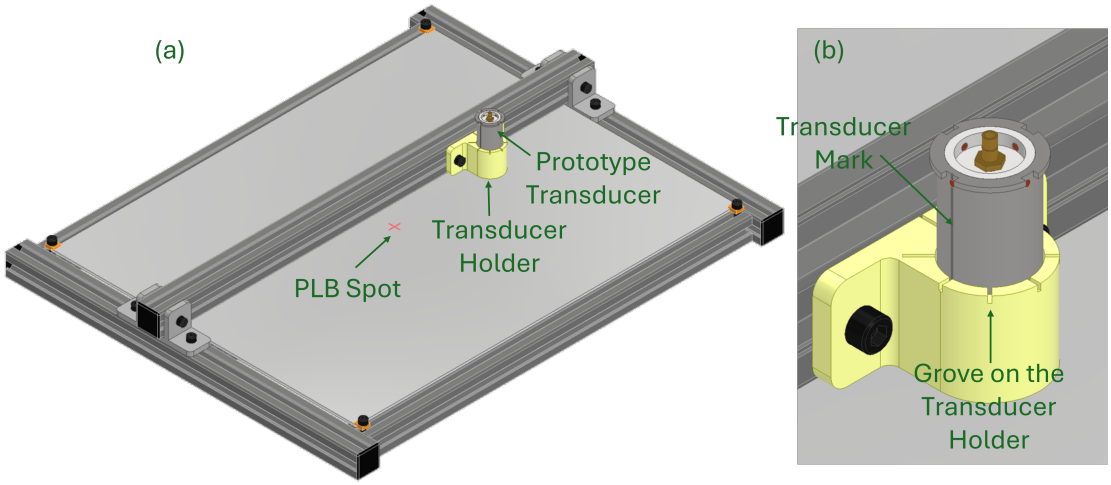

Figure 4.1: (a) Illustration of the angle sensitivity test. (b) Detail of the transducer and its holder.

Figure 4.1b presents the details of the transducer and its holder. Each groove in the transducer holder corresponds to an angle ranging from 0° to 315°, with 45° increments. There is a mark on the transducer that allows alignment with the grooves, as shown in Figure 4.1b. The environmental conditions were maintained at 23 °C ±2 °C, 53 % ±4 % RH.

Figure 4.2a and Figure 4.2d present the average signal waveform of the chosen receiver and transmitter due to the PLBs at different angles of orientation, respectively. No digital filtering was applied; the only filter was the amplifier's analog band-pass filter from 20 kHz to 1.2 MHz. The amplifier gain was set to 60 dB, and each waveform was truncated at 65 μs to avoid primary reflections.

Two distinct Lamb modes are visible in Figure 4.2a and Figure 4.2d, starting at approximately the same times for both transducers. The S_0 mode starts at approximately 25 μs and the A_0 mode starts at approximately 40 μs. Both transducers exhibit similar responses in shape and magnitude across all orientations; however, the transducer in Figure 4.2d shows less variation.

Figures 4.2b and 4.2e present the histogram of the measurements of Figures 4.2a and 4.2b, respectively. Most measurements cluster around zero, indicating no offset.

As the response of the transducers is difficult to visualize from Figures 4.2a, 4.2b, 4.2d, and 4.2e, Figures 4.2c and 4.2f present the RMS values of each angle orientation for the receiver and transmitter transducers, respectively. The transmitter exhibited more evenly distributed RMS values than the receiver; therefore, it was selected as the transmitter. This is a relevant feature for a transmitter transducer, since it can generate elastic waves

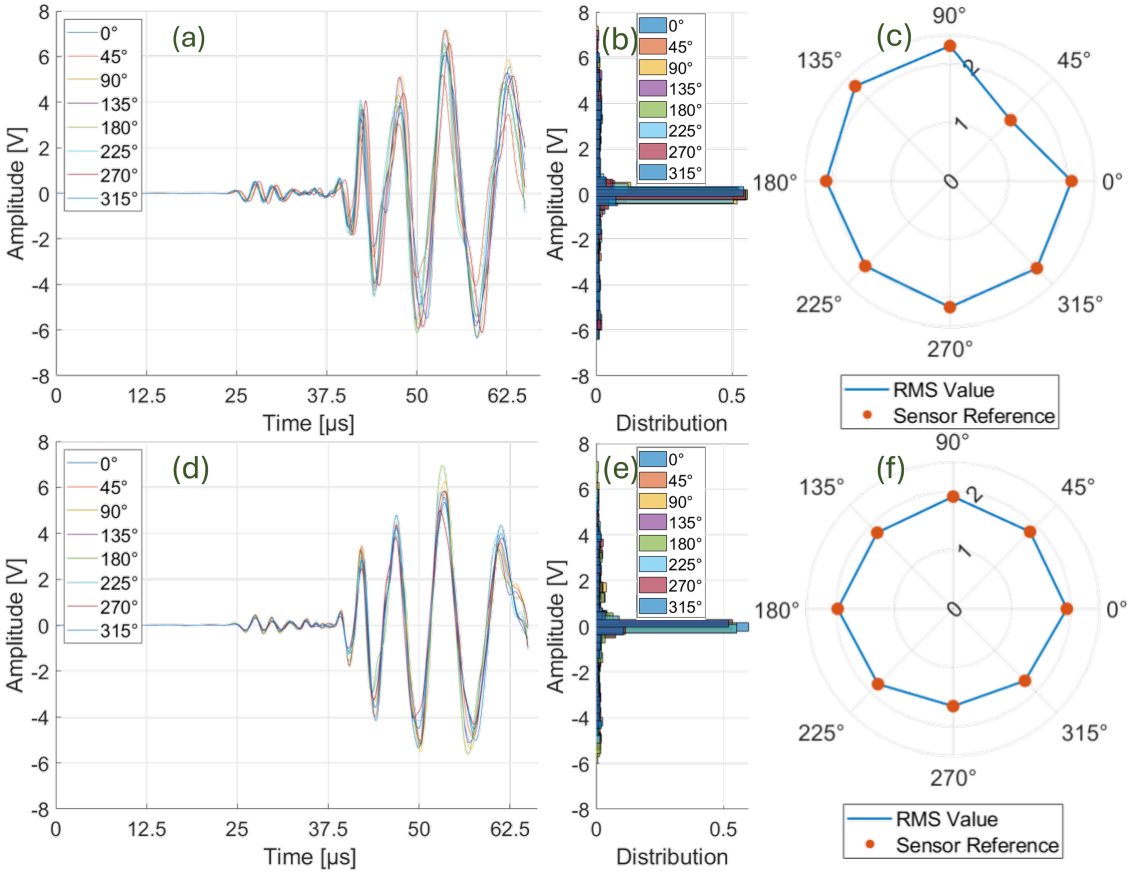

Figure 4.2: (a) Signal time series of the receiver in different angle orientations. (b) Distribution of the signal time series of the receiver. (c) RMS values of the receiver in polar coordinates. (d) Signal time series of the transmitter in different angle orientations. (e) Distribution of the signal time series of the transmitter. (f) RMS values of the transmitter in polar coordinates. Adapted from [23].

more symmetrically in all directions. The 45°/225° orientation was the one that produced almost equal values; therefore, this orientation was chosen for the transmitter transducer in the mobile verification device, with 45° towards the SUT and 225° towards the receiver.

The receiver transducer plot shows a drastic drop in response at 45°. This is attributed to a slight inclination of the transducer's wear plate after curing of the high-performance ceramic adhesive, as discussed in Section 3.2. Since 90° yields the highest response, it was chosen to face the transmitter transducer in the mobile verification device.

4.2 Assembly Validation

To ensure the flatness of the aluminum frame that the aluminum plate rests on, it was fixed to a T-slot mounting plate, as shown in Figure 4.3. The clamp bolts were lightly torqued merely to maintain contact between the aluminum frame and the T-slot mounting plate. Afterward, the joining bolts of the aluminum profiles were tightened, and the frame was removed from the T-slot mounting plate. The bridge-format aluminum frame, which houses the transmitter and receiver transducers and the SUT coupling mechanism, was mounted atop the other frame and carefully aligned.

Figure 4.3: Picture of the frame being aligned on the fixing table.

The aluminum plate was mounted on the main frame and secured using plate holders (Figure 3.2). After the device was fully assembled, a reference measurement was recorded for later comparison. The aluminum plate was then disassembled from the mobile verification device and reassembled. Immediately thereafter, a long-term measurement exceeding 14 hours was performed in auto-check mode. Since the device is intended to work with different plate materials, it is essential to assess the impact of reassembling the plate. During this test, the aluminum frames were kept assembled. Environmental conditions were maintained at $23\,^{\circ}\mathrm{C} \pm 2\,^{\circ}\mathrm{C}$ and $53\,\% \pm 4\,\%$ RH. The pulse settings were identical to those specified at the end of Section 3.2, except that the repetition frequency for this test was 33 mHz. It took 220 minutes for Assembly 01 to stabilize and 110 minutes for Assembly 02. Figure 4.5 presents the signal time series of the reference measurement before and after the assembly test. The two waveforms almost perfectly overlap, indicating that

reassembling the propagation medium caused no relevant change.

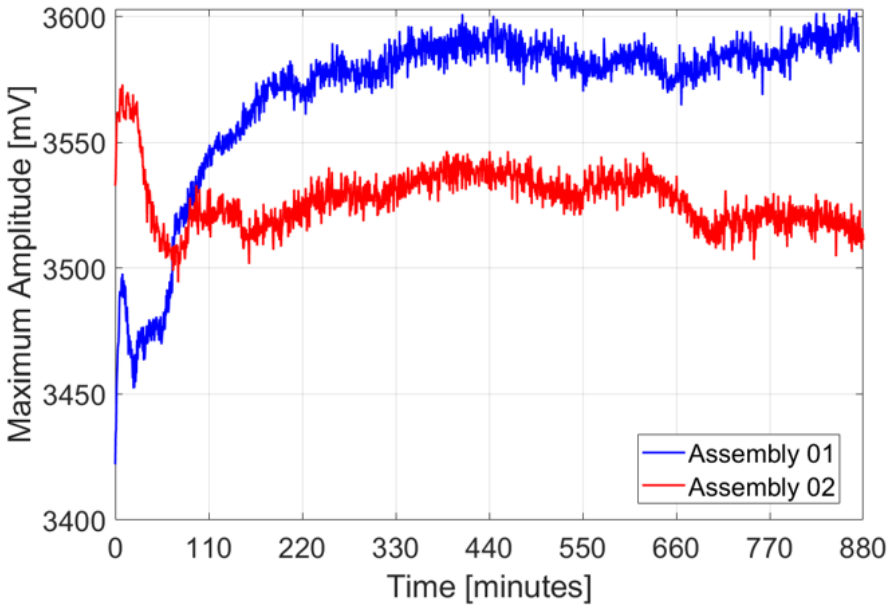

Figure 4.4: Maximum amplitude plot after reassembling the propagation medium.

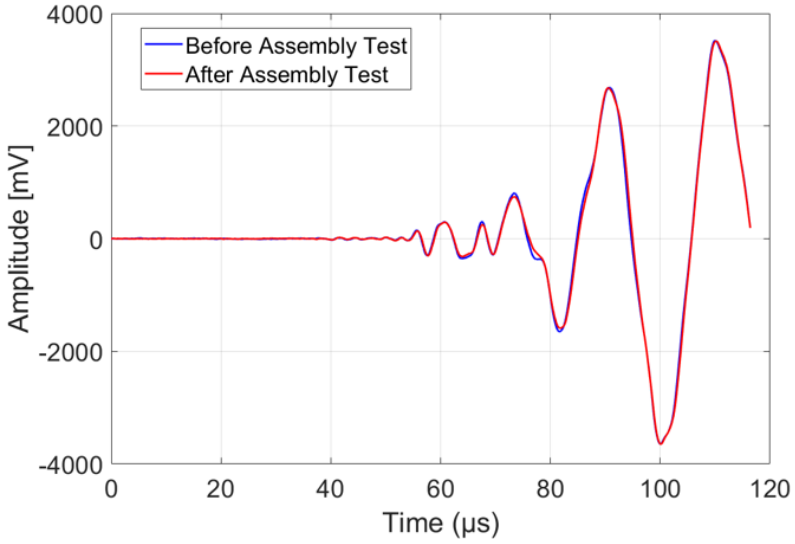

Figure 4.5: Signal time series before and after the assembly test.

4.3 Human-Reproducibility Test

A crucial capability of the mobile verification device is its reproducibility across multiple operators. Therefore, a human-reproducibility test was performed to check this capability. The test consists of performing the measurements required for operating the device, the device auto-check, and sensor verification, by six operators, and comparing the results of the same operators with the measurements they performed in the benchmark verification device. Figures from 4.6a to 4.6c present illustrations of the benchmark verification device [22]. It consists of an aluminum block as the propagation medium, a sensor coupling mechanism on top, as shown in Figure 4.6b, and a PZT transducer on the bottom, as shown in Figure 4.6c, which operates as a receiver when device verification is performed and as a transmitter when sensor verification is performed. Benchmark device verification involves performing PLB on the top surface of the aluminum block while measuring with the PZT conical transducer on the bottom. This procedure is not included for the mobile verification device, as PLBs are not used as the standard excitation method. For sensor verification, the PZT conical transducer is excited using rectangular pulses with the following parameters: 50 Hz repetition frequency, 10 Vpp amplitude, zero offset, 4 ms duration, and 20 ns edge length. The function generator used is the same as that of the mobile verification device, and the AE DAQ system consists of a PCI-2 system supplied by Mistras Group Inc. The benchmark procedure follows the guidelines provided by DGZfP SE-02 [11].

Each operator performed each test three times: 1) device auto-check, 2) sensor verification using the mobile verification device, and 3) sensor verification using the benchmark device. The WD sensor was reassembled between measurements. The mobile verification device transducers were also reassembled between the sensor and the auto-check measurements. The environmental conditions were maintained at 23 °C ±2 °C, 53 % ±4 % RH.

Figure 4.7a presents the signal time series of the WD sensor measured by the operators using the benchmark device. Each color represents the average of the 600 waveforms measured three times for each operator (dark lines), and the maximum and minimum values (light-shaded colors). Similarly, Figure 4.8a presents the measurements performed by the mobile verification device. Figure 4.9a presents the signal time series of the auto-check of the mobile verification device.

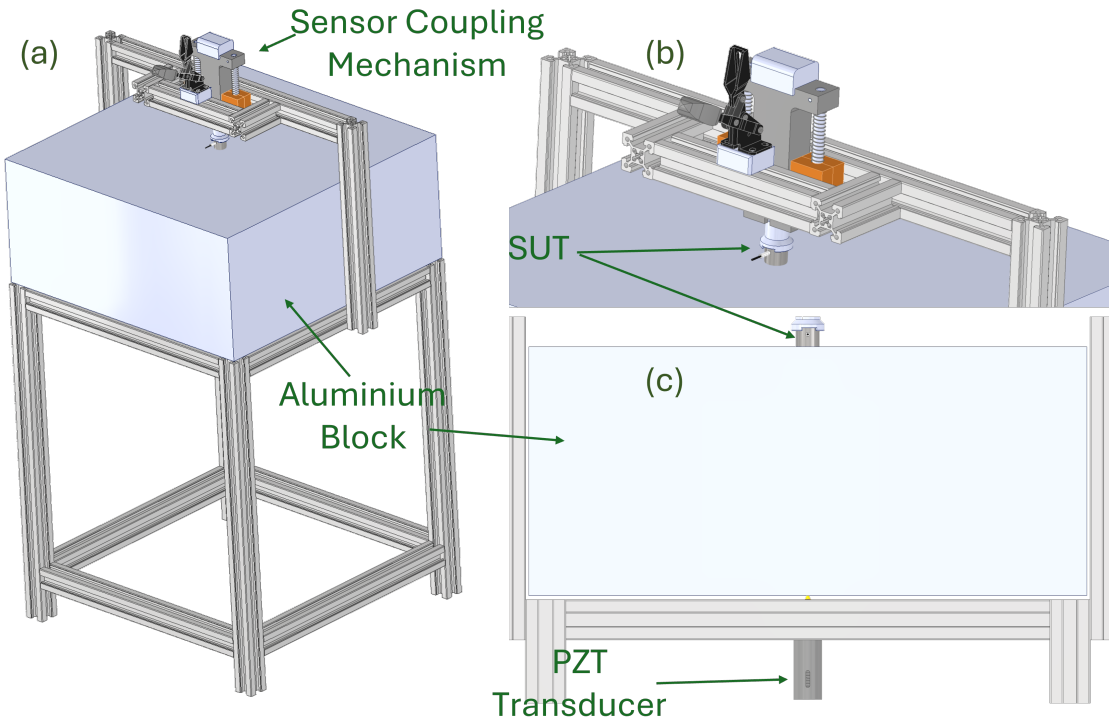

Figure 4.6: (a) Benchmark verification device [22]. (b) Detail of the SUT's coupling mechanism. (c) Details of the PZT transducer.

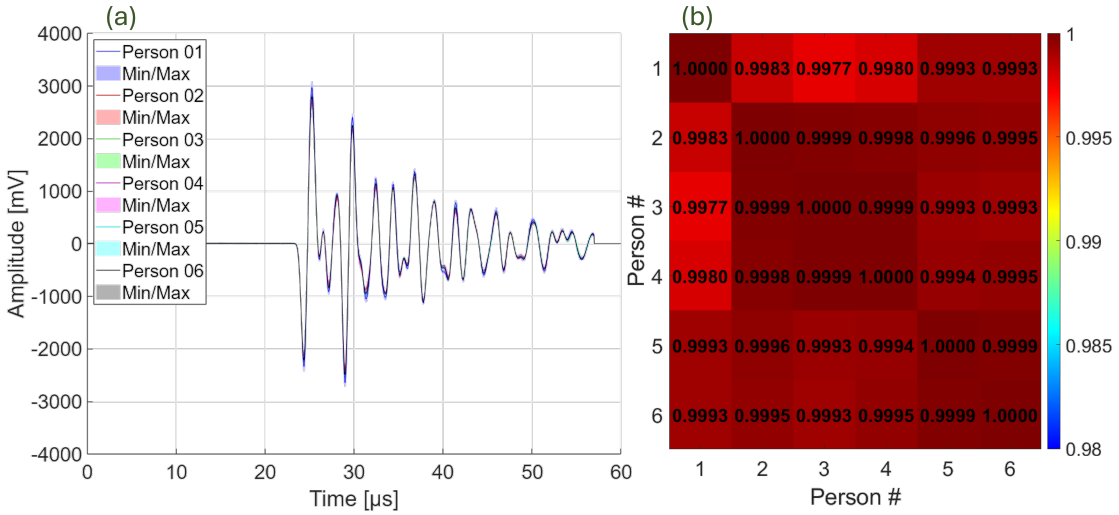

Figure 4.7: (a) Signal time series of the WD sensor measured by six persons using the benchmark verification device. (b) Colormap of normalized cross-correlation among all measurements of the benchmark verification device. Adapted from [23].

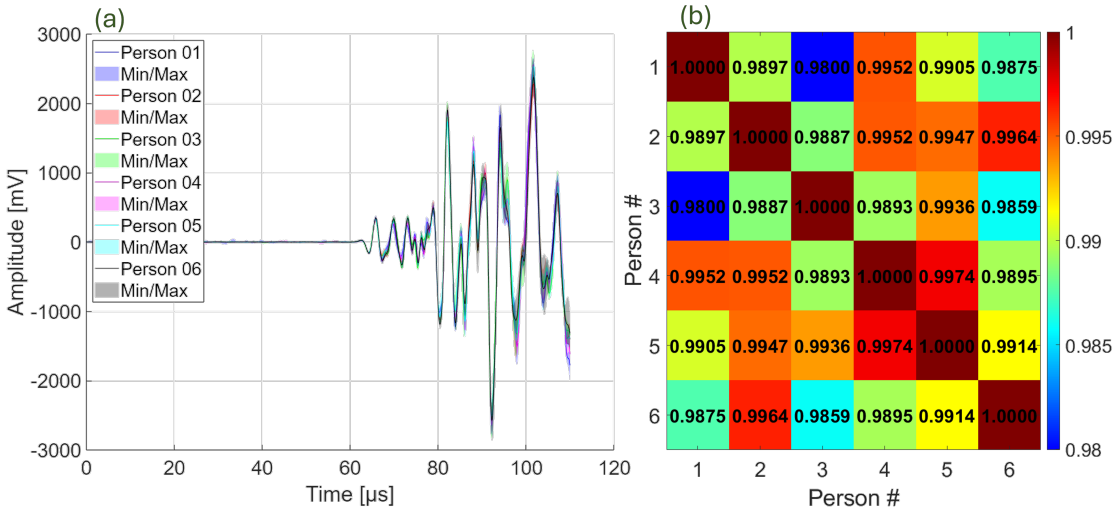

Figure 4.8: (a) Signal time series of the WD sensor measured by six persons using the mobile verification device. (b) Colormap of normalized cross-correlation among all measurements of the mobile verification device. Adapted from [23].

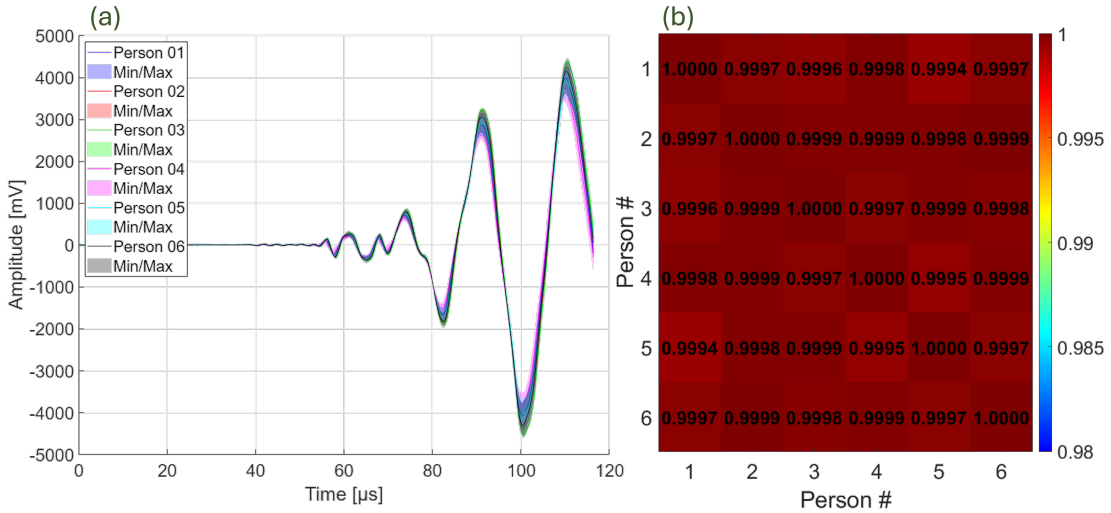

Figure 4.9: (a) Signal time series of the auto-check measured by six persons using the mobile verification device. (b) Colormap of normalized cross-correlation among all auto-check measurements. Adapted from [23].

As can be observed, both devices measure signals with clearly different characteristics, and this is directly related to the shape of the propagation medium. The benchmark verification device operates using bulk longitudinal waves, which results in a transient signal that decays over time. The mobile verification device operates using Lamb waves, which

exhibit a transient signal that increases over time. In the case of the mobile device autocheck, both S_0 and A_0 modes can be clearly observed, with S_0 starting at approximately 40 μs and A_0 at approximately 55 μs.

The measurements of the receiver transducer of the mobile verification device have shown the best results with a minimum cross-correlation of 0.9994. This is because the transmitter and receiver transducers couple to the surface at the same position and orientation due to their coupling mechanisms. The measurements of the SUT of the benchmark verification device have shown a slightly smaller minimum normalized cross-correlation, of 0.9977. The slightly worse performance of the benchmark SUT measurements can also be explained by the coupling mechanism of the SUT. Although it allows the sensor to couple at the same position, it cannot ensure the same sensor orientation as the coupling mechanisms of the transmitter and receiver transducers of the mobile verification device. The SUT measurements performed by the mobile verification device have shown the worst performance, with a minimum cross-correlation value of 0.9800. The reason for this is also related to its coupling mechanism, more specifically to the dimensional tolerances. Although the coupling mechanism of the mobile verification device also allows the same sensor orientation due to a cut-out in the adapter for the sensor cable, this variation in tolerances creates variation in the distance between the transmitter transducer and the SUT. This does not happen with the benchmark verification device because the distance between the transmitter transducer and the SUT is dictated by the thickness of the aluminum block, which is constant and stable. Another aspect that also increases the uncertainty in the distance between the transmitter transducer and the SUT is the fact that the sensor must have to play a little looser inside the adapter to make it easier to insert and remove the sensor from the adapter.

Although all cross-correlation values are remarkably high, indicating that the mobile verification device and the benchmark verification device have comparable performances in terms of reproducibility, there is room for improvement in the SUT coupling mechanism of the mobile verification device. Therefore, Section 4.4 presents the performance of the improved coupling mechanism compared with the 3D-printed coupling mechanism.

4.4 Improvement of the SUT Coupling Mechanism

As the SUT 3D-printed coupling mechanism performed worse compared to the coupling mechanism of the transmitter and receiver transducers and the coupling mechanism of the benchmark device, a new SUT coupling mechanism was created. Many components of the improved coupling mechanism were machined from aluminum, which is more stable and allows tighter tolerances, as shown in Figure 3.7. Only the sliding bushings of the pillow linear guide and the sensor adapter were not manufactured in aluminum.

Three scenarios were tested: the 3D-printed coupling mechanism, as shown in Fig-

ure 4.10a, the improved coupling mechanism with original sliding bushings, as shown in Figure 4.10b, and the improved coupling mechanism with tighter-tolerance sliding bushings made of Polytetrafluoroethylene (PTFE), as shown in Figure 4.10b. As the major goal was to compare the performances of the 3D-printed and improved coupling mechanisms, they were tested under the same conditions, including the same operator and SUT, to keep the variables as consistent as possible.

Five measurements were performed, with the SUT reassembled between them, for each of the three scenarios using a VS900-M sensor. The settling time, i.e., the waiting time after assembling the SUT and starting the measuring, was 400 seconds, and each measurement had 600 waveforms. The pulse configuration was the same as described at the end of Section 3.2, and the environmental conditions were the same as those used in Section 4.2.

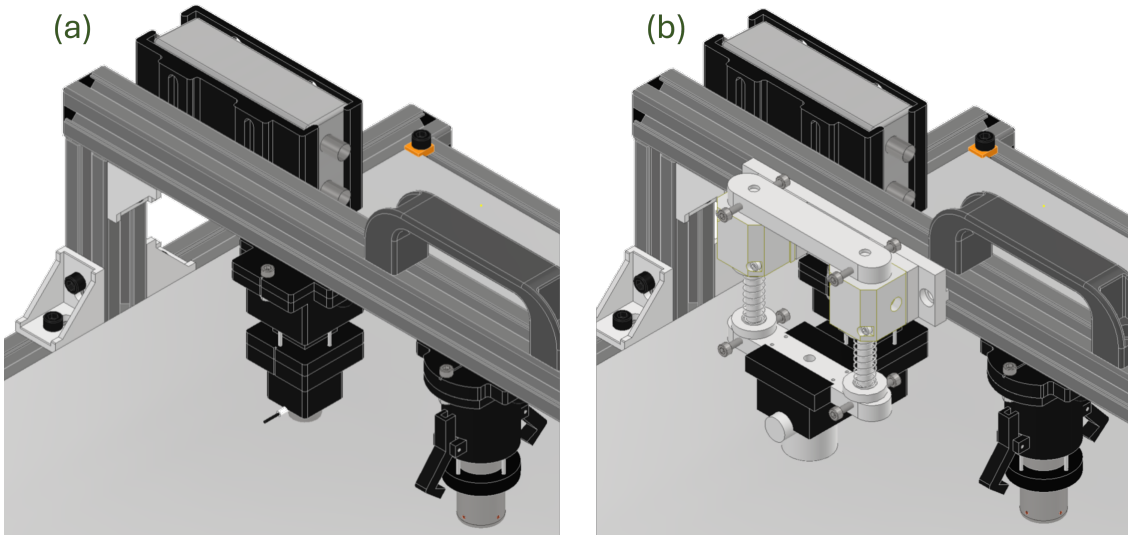

Figure 4.10: (a) The SUT 3D-printed coupling mechanism. (b) SUT improved coupling mechanism with original sliding bushings and tighter tolerance sliding bushings. Adapted from [23].

Figure 4.11a presents the average signal time series of the 3D-printed coupling mechanism obtained from the five measurements. Similarly, Figure 4.11b presents the average signal time series of the improved coupling mechanism equipped with the original sliding bushings and with the tighter-tolerance PTFE sliding bushings. All tests were performed with 60 dB amplification, and signals were truncated at 125 μs for comparison. The two scenarios using the improved coupling mechanism showed similar waveforms. In contrast, the waveforms produced by the 3D-printed mechanism differ noticeably, which can be attributed to the different positioning of the improved mechanism relative to the transmitter and receiver transducers. Because it is no longer aligned with the transmitter and receiver transducers, the sensor couples to the aluminum plate with a different orientation. This change in the waveform shape also alters the frequency spectrum, as shown in Figure 4.12.

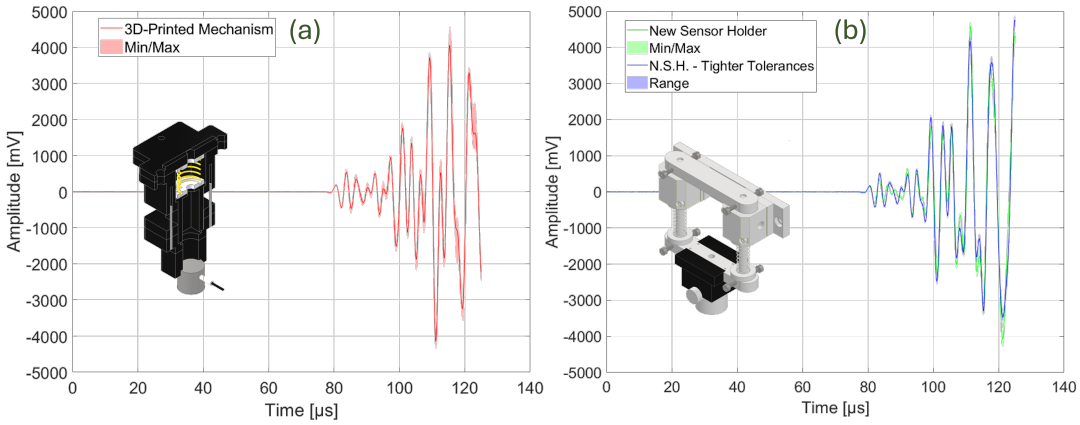

Figure 4.11: (a) Signal time series of the 3D-printed coupling mechanism. (b) Signal time series of the improved coupling mechanism with original sliding bushings and tighter tolerance sliding bushings.

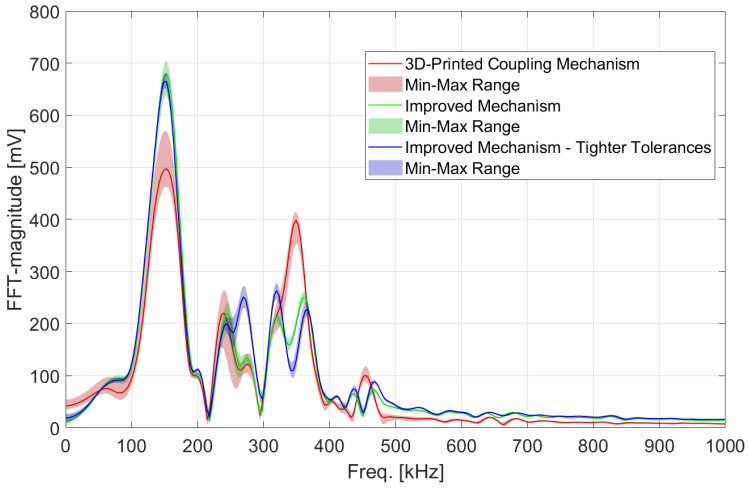

Figure 4.12: Frequency spectrum of the three coupling mechanism scenarios.

Overall, the main difference between the two coupling mechanisms is that the 3D-printed one exhibited greater variation, which is expected since it has looser tolerances. Another clear difference appears at 150 kHz, where the improved mechanism shows a higher FFT magnitude. The configuration using the PTFE sliding bushings shows higher amplitude for the second coupled peak in the range from 200 kHz to 300 kHz. In the range between 300 kHz and 400 kHz, the improved mechanism exhibits a single peak at around 350 kHz, whereas the 3D-printed mechanism shows two coupled peaks, one at approximately 320 kHz and another at approximately 360 kHz. The improved coupling

mechanism has shown more resonance frequencies in the range between 400 kHz and 500 kHz.

Figure 4.13 presents the maximum cross-correlation values among the tests of the three scenarios.

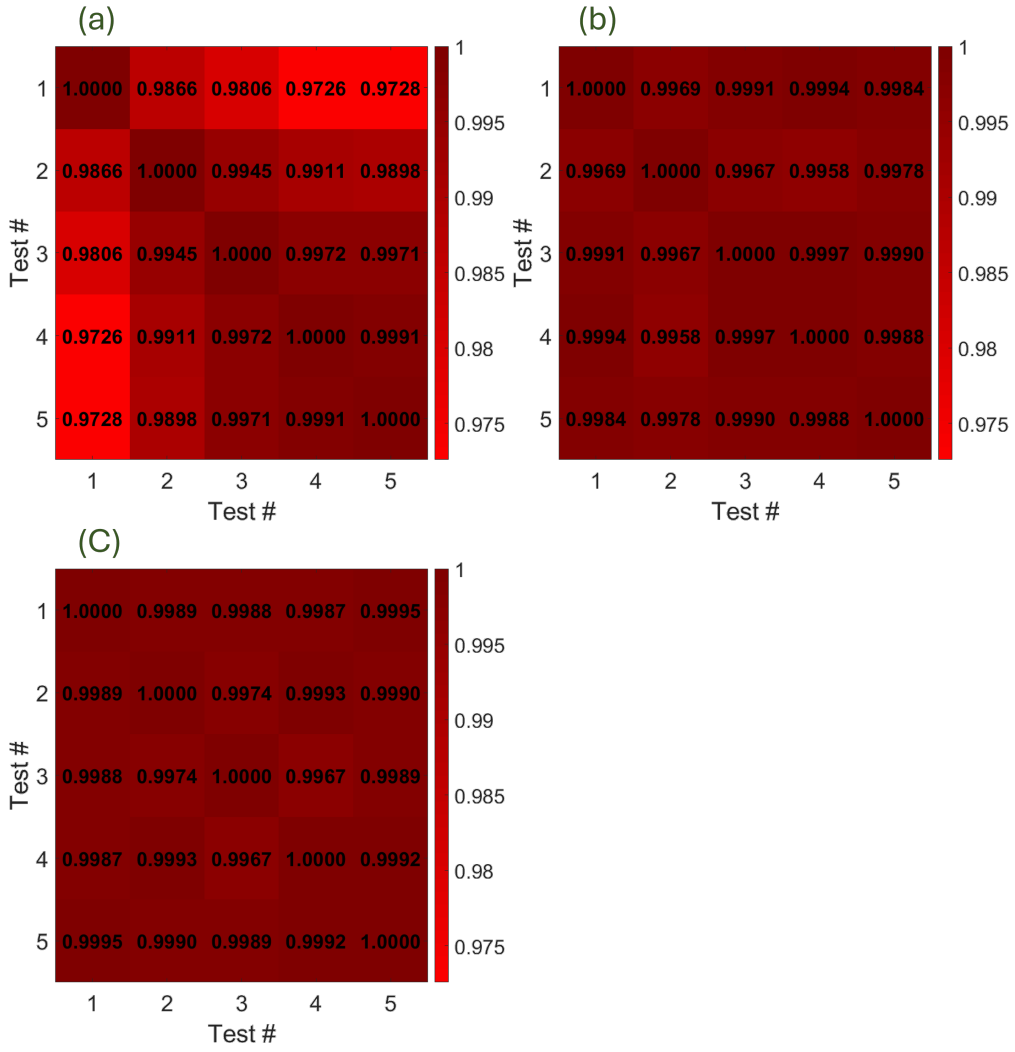

Figure 4.13: Maximum cross-correlation among the tests of: (a) 3D-printed coupling mechanism, (b) Improved mechanism with original sliding bushings, (c) improved mechanism with tighter tolerance sliding bushings.

The minimum normalized cross-correlation value for the improved mechanism with tighter tolerance sliding bushings was 0.9967, compared to 0.9958 for the mechanism with original sliding bushings, and 0.9726 for the 3D-printed mechanism. Therefore, the improved mechanism with sliding bushings with tighter tolerances has shown superior per-

formance in terms of repeatability among the tests. This is also confirmed in Figure 4.14, where uncertainties in the mean maximum amplitudes are shown with a 2σ confidence level for each scenario in the form of error bars.

The improved mechanism with tighter tolerances has shown not only more similar mean values, but also less uncertainty for all measurements. The mean and its associated uncertainty for the new sensor coupling mechanism with tighter tolerances were 4760 mV ± 65 mV. The 3D-printed mechanism has shown the worst repeatability among them: 4076 mV ± 220 mV.

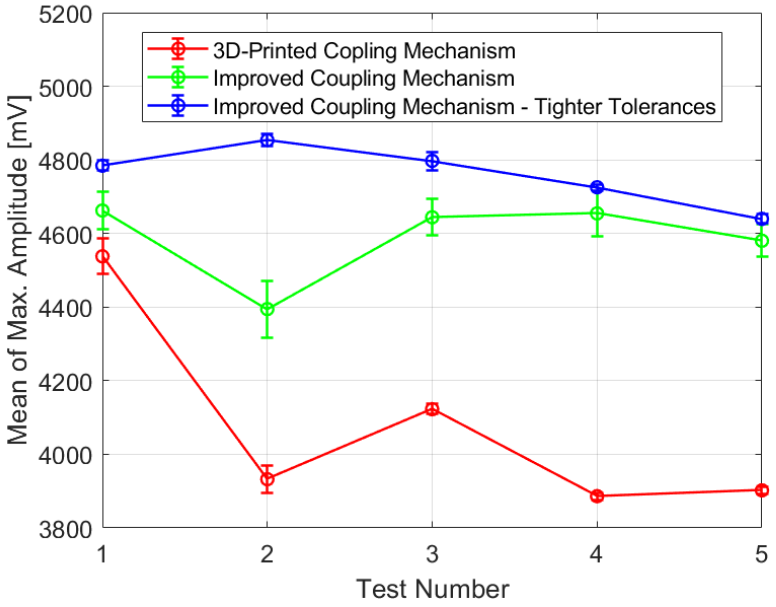

Figure 4.14: Maximum amplitude uncertainties for different tests and scenarios.

4.5 Settlement Test

During the first measurements of the mobile verification setup, a high variation in the results was observed. To investigate this variability, a settlement test was performed. This test consists of spreading a fixed amount of coupling agent, approximately 50 mg, onto the sensor wear plate using a spatula to avoid bubble formation, and then beginning the measurements immediately after assembling the sensor on the mobile verification device in order to study the settling behavior of the coupling agent.

The pulse configuration for this test is the same as described in Section 3.2, except for the repetition frequency, which was set to 1 Hz. For each sensor investigated, the settlement test had a duration of at least 900 s (or 15 minutes). The sensors tested were:

WD [140], VS30-V [141], VS150-M [142], VS900-M [143], and VS150-RSC [144]. The WD sensor is supplied by Mistras Group Inc., and the others are supplied by Vallen Systeme GmbH, as shown in Figure 4.15.

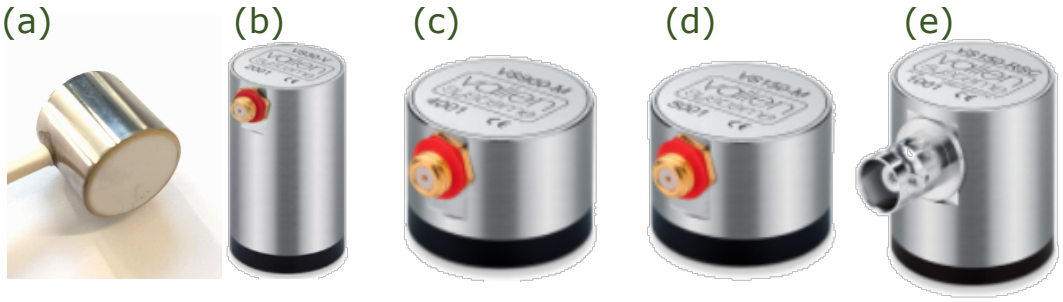

Figure 4.15: AE sensors: (a) WD, (b) VS30-V, (c) VS150-M, (d) VS900-M, and (e) VS150-RSC.

Table 4.1 presents specification values for the tested sensors.

Table 4.1: Specifications of selected AE sensors.

Model	Diameter [mm]	Height [mm]	Weight [g]	Freq. Range [kHz]
WD	17.8	16.5	20	125 – 1000
VS30-V	20.3	37.0	69	25 – 80
VS150-M	20.3	14.3	24	100 – 450
VS900-M	20.3	14.3	22	100 – 900
VS150-RSC	28.6	31.5	81	100 – 450

As an illustration of the settlement behavior of an AE sensor, Figure 4.16 presents the 900 waveforms of the WD sensor, in which considerable variation can be observed. Since it is difficult to identify any clear trends directly from these waveforms, the maximum amplitude of each waveform was calculated for every test and every sensor, and the results were plotted in Figure 4.17a. Each curve represents three tests for each sensor, normalized by the maximum amplitude measured. Each waveform has at least 94 μs in total length, ensuring a representative signal duration.

It is worth noting that although the VS150-M and VS900-M sensors have the same external dimensions, they have exhibited opposite settlement behavior. The VS150-M sensor begins with high amplitudes, then decreases to a minimum before showing a monotonic increase. In contrast, the VS900-M sensor starts with a minimum amplitude, increases to a maximum, and then exhibits a monotonic decrease.

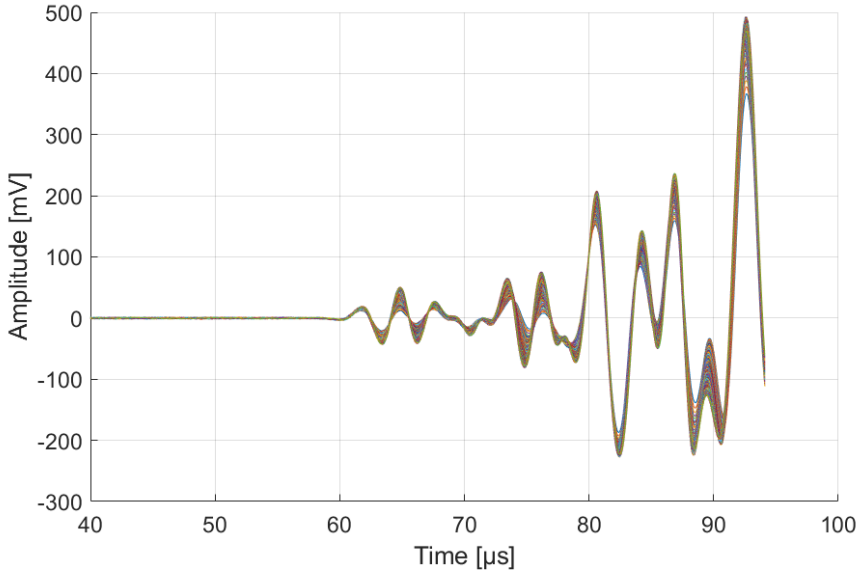

Figure 4.16: 900 waveforms of the settlement test for the WD sensor.

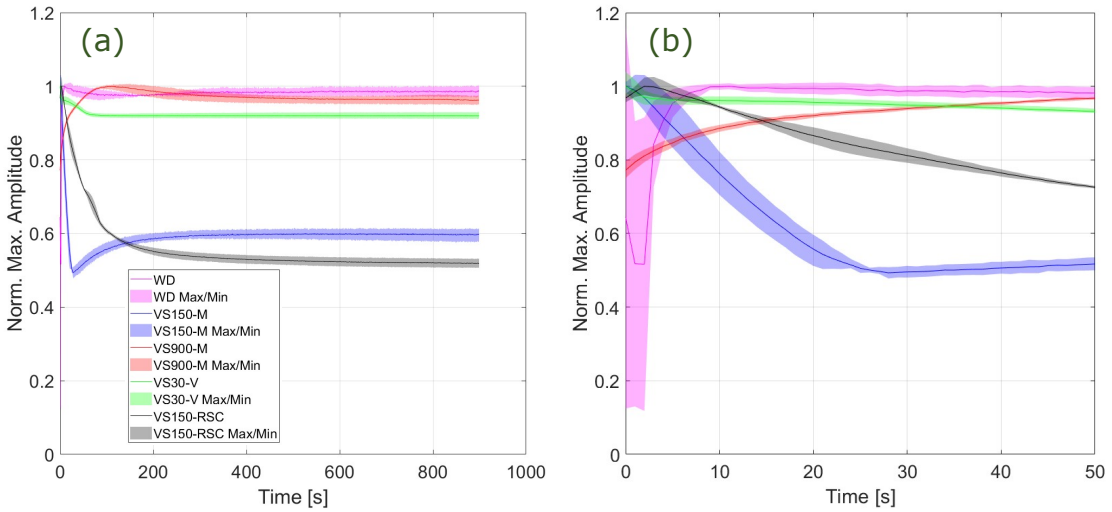

Figure 4.17: (a) Normalized maximum amplitude of the sensors: WD, VS30-V, VS150-M, VS150-RSC, and VS900-M. (b) Zoomed-in view of the initial 50 s of the data shown in (a). Adapted from [23].

Finally, as shown in Figure 4.17a, there are sensors that settle quickly, such as the VS30-V, and sensors that need more time, such as the VS150-RSC. Therefore, it is important to observe the settlement time for each sensor before performing the measurement.

4.6 Environmental Testing

This section is divided into two main topics, the environmental tests of the mobile verification device and the SUTs. The objectives are to investigate their performance over a broad range of temperatures and humidity levels, and to check whether the setup remains stable afterward.

4.6.1 Environmental Tests of the Mobile Verification Device

The environmental test of the mobile verification device was performed with the device operating in auto-check mode, with only one modification: the pulse repetition frequency was set to 0.1 Hz to avoid generating large data files. To investigate the behavior of the mobile verification device under varying environmental conditions, the device, together with the transducers, cables, and amplifiers, was placed inside a WK3-340/70 climate chamber supplied by Weiss Technik. The only components not placed inside the chamber were the WA301 amplifier, the AE DAQ system, and the arbitrary function generator. Figure 4.18 shows a photograph of the experimental setup.

Figure 4.18: Picture of the climate chamber and the instrumentation for the mobile verification device.

The first investigation aimed to determine the temperature accommodation time. The temperature was varied from 25 °C to -10 °C, while the relative humidity was maintained at 75 %. Measurements were performed using the receiver transducer with 40 dB amplification and lasted for 400 minutes (6 hours and 40 minutes). Figure 4.19 presents the maximum amplitude for each waveform over time. It can be observed that it took approximately 85 minutes to stabilize the measurements from 25 °C to -10 °C, or 2 minutes and 24 seconds for each °C variation in a rough estimation.

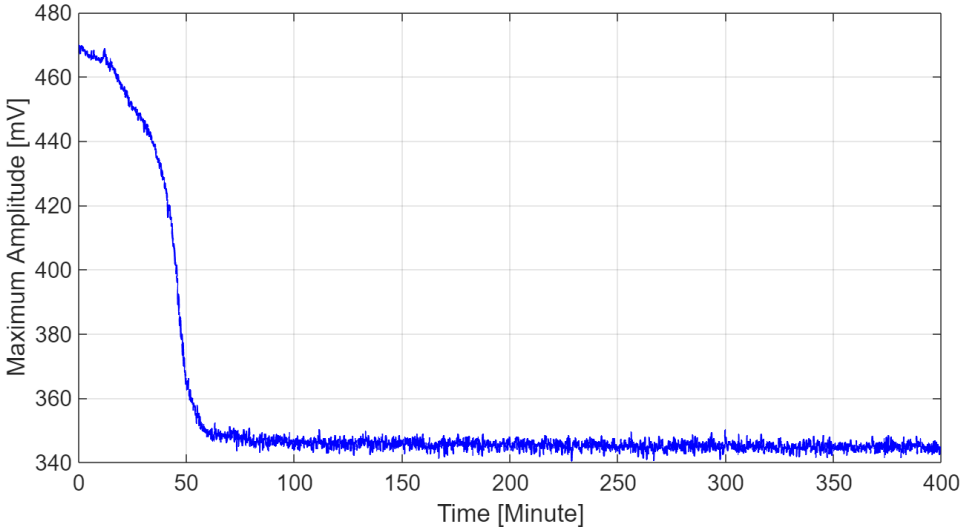

Figure 4.19: Temperature accommodation of the mobile verification device.

The second investigation aimed to characterize the behavior of the mobile verification device at different temperatures and to evaluate its stability afterward. Measurements were performed with 60 dB amplification, while the temperature was varied from -10 °C to 45 °C in 5 °C steps. This temperature range was chosen because it represents the maximum operating range of the instrumentation equipment. Although less time is required, a two-hour temperature accommodation period was used, as suggested by the previous temperature accommodation test. The device was operated in auto-check mode, performing one auto-check at each temperature. Relative humidity was maintained at 75 %.

Figure 4.20a presents the waveforms at each temperature, truncated at 116.4 μs to eliminate reflections. Each waveform represents the average of 600 measurements, with shaded areas indicating maximum and minimum values. An increase in maximum amplitude with temperature can be observed, which is more clearly depicted in Figure 4.20b. This trend is explained by the decrease in stiffness of the propagation medium as temperature increases; for the same input force, greater displacement occurs.

Figure 4.20a also shows that as the maximum amplitude increases, the time at which it occurs is delayed, suggesting a decrease in frequency with increasing temperature. This effect is more clearly observed in Figure 4.21, where the frequency spectrum is plotted for all temperatures. Around 50 kHz, both the frequency and amplitude decrease as temperature increases, consistent with observations reported by Lopes et al. (2018) [145].

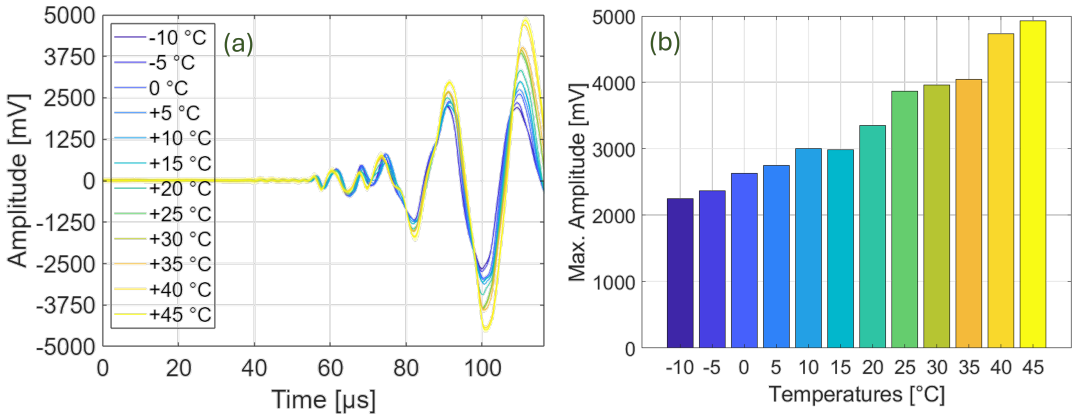

Figure 4.20: (a) Signal time series of the receiver at different temperatures. (b) Maximum amplitude trend of the signal time series at different temperatures. Adapted from [23].

The maximum frequency amplitude follows a pattern very similar to the maximum waveform amplitude, as can be observed in Figure 4.22. The trend of the peak frequency is better observed in Figure 4.22b. It is important to mention that zeros were added to the truncated signal, increasing its final length by 100 μs, this procedure was adopted to increase the resolution of the peaks in Figure 4.21.

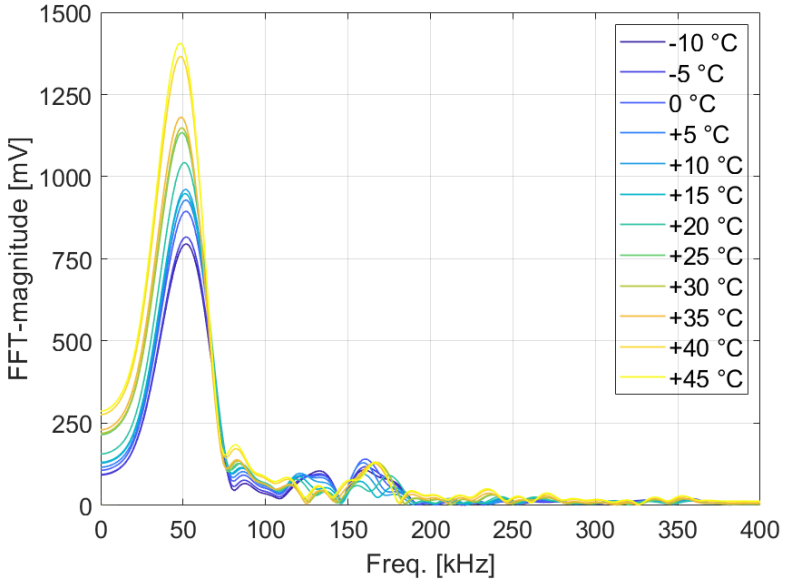

Figure 4.21: Frequency spectrum of the signal time series curves obtained at different temperatures. Adapted from [23].

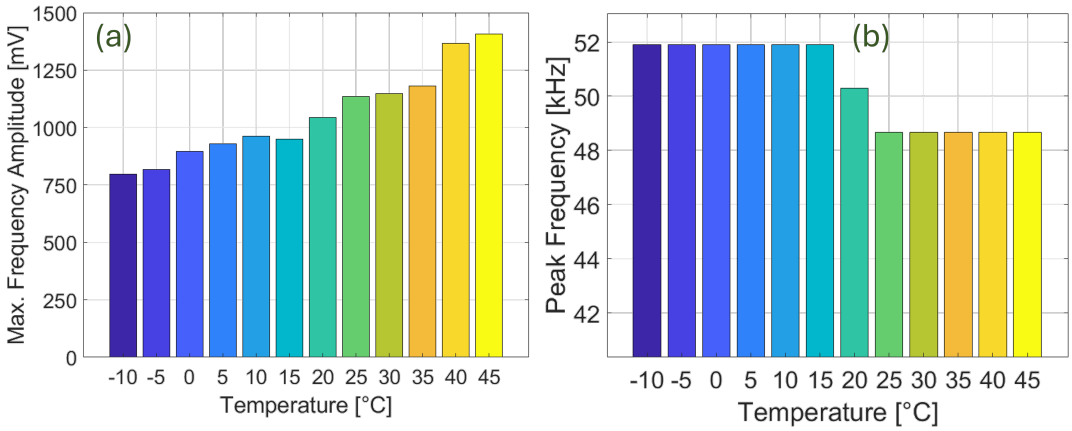

Figure 4.22: (a) Maximum frequency amplitude trend at constant RH (75 %). (b) Maximum peak frequency trend of the frequency spectrum at constant RH (75 %). Adapted from [23].

The response of the mobile verification device was also investigated under a broad variation in humidity. The test protocol consisted of of keeping the temperature constant, at 25 °C, and varying the RH from 0 % to 100 % in 10 % steps. Figure 4.23a presents the receiver transducer signal time series at different humidity levels, and Figure 4.23b presents the maximum amplitude for each level of RH. It can be observed that RH causes a slight variation in the maximum amplitude. From 40 % RH to 100 % RH, the variation in the maximum amplitude was 1.5 %.

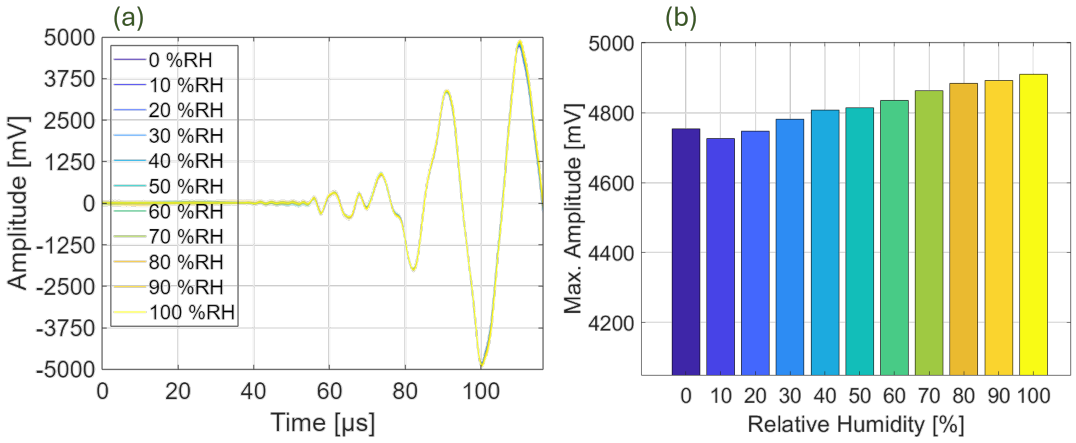

Figure 4.23: (a) Signal time series of the receiver at different RH levels at constant temperature (25 °C). (b) Maximum amplitude for each RH level at constant temperature (25 °C).

Figure 4.24 presents the receiver waveforms before and after the climate chamber tests, where a strong similarity between the two signals is observed, suggesting that the device remains stable after significant temperature and RH variations.

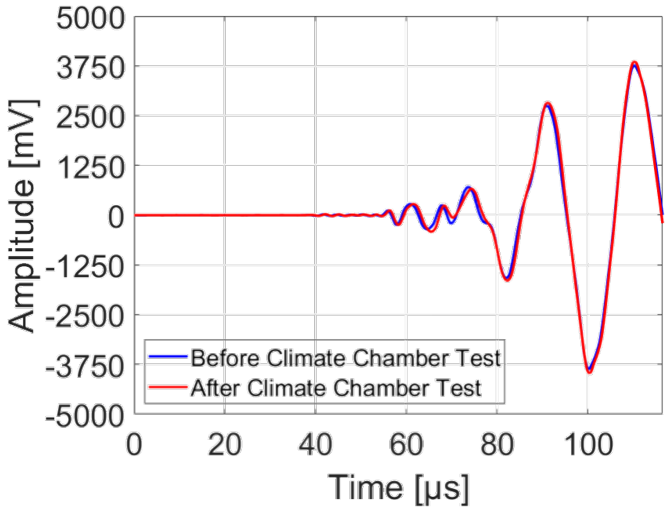

Figure 4.24: Signal time series of the receiver before and after the climate chamber test. Adapted from [23].

4.6.2 Environmental Tests of the SUTs

Similarly to the tests in Section 4.6.1, in which the influence of temperature on the mobile device was investigated, each sensor in Figure 4.15 was also exposed to a wide range of temperatures. The tests were automated by a Python script written in Jupyter Notebook, where the measurements of the mobile device and the variation of the temperature of the climate chamber were synchronized. The code can be found in Appendix E. A study of the impact of the RH on the measurements was not performed because it produced only small variations in the measurements, as presented in Section 4.6.1.

WD Sensor

Figure 4.25a presents the signal time series of the WD sensor over the temperature range from -10 °C to 45 °C in 5 °C steps. Measurements were performed with 60 dB amplification, and each signal was post-processed following the procedure described in Section 3.4. Waveforms were truncated at 94.1 μs to avoid reflections. The maximum amplitude was calculated to evaluate the influence of temperature on the measurements, as shown in Figure 4.25b. An increasing trend in maximum amplitude with temperature is observed, with a minimum of 1743 mV at -10 °C and a maximum of 2154 mV at 45 °C. This corresponds

to a total maximum amplitude variation of 23.5 % over a temperature range of 55 °C.

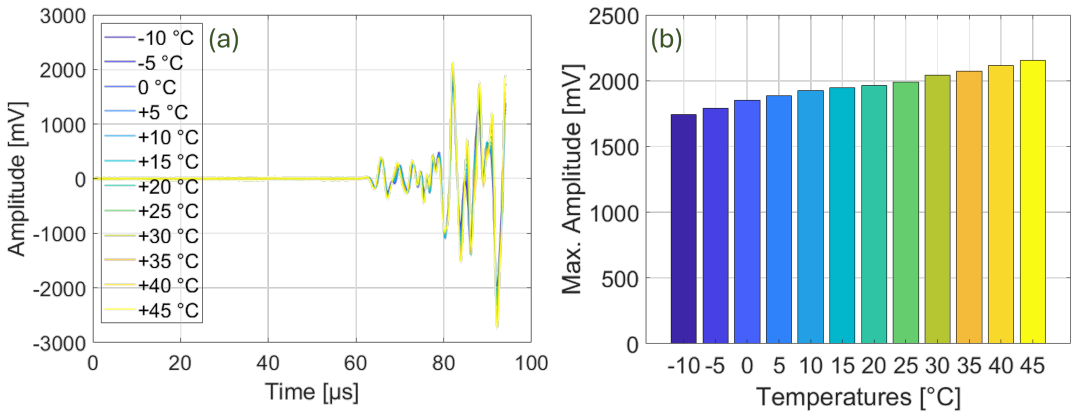

Figure 4.25: (a) Signal time series of the WD sensor at different temperatures. (b) Maximum absolute amplitude trend of the signal time series.

Figure 4.26 presents the frequency spectrum of the signal time series of Figure 4.25a, where multiple dominant frequencies can be observed. Zeros were added to the truncated signal, increasing its final length by 100 μs, to improve frequency resolution.

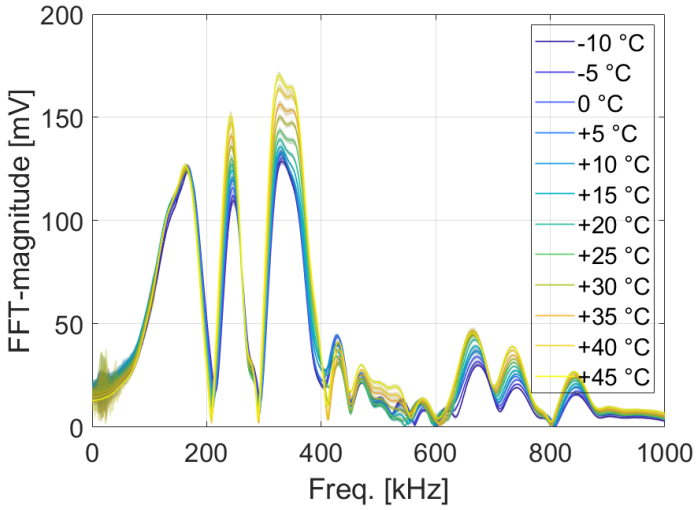

Figure 4.26: Frequency spectrum of the signal time series at different temperatures of the WD sensor.

The three most prominent frequencies are approximately 165 kHz, 240 kHz, and 325 kHz. These resonance frequencies and the anti-resonances around 200 kHz, 270 kHz and

400 kHz are also present in the sensitivity chart provided by the sensor manufacturer, as shown in Figure 4.27. The maximum frequency amplitude follows the trend of the maximum amplitude of the signal time series, as can be observed in Figure 4.28a. Similarly to the receiver transducer measurements, the peak frequency decreases with increasing temperature, as can be observed in Figure 4.28b.

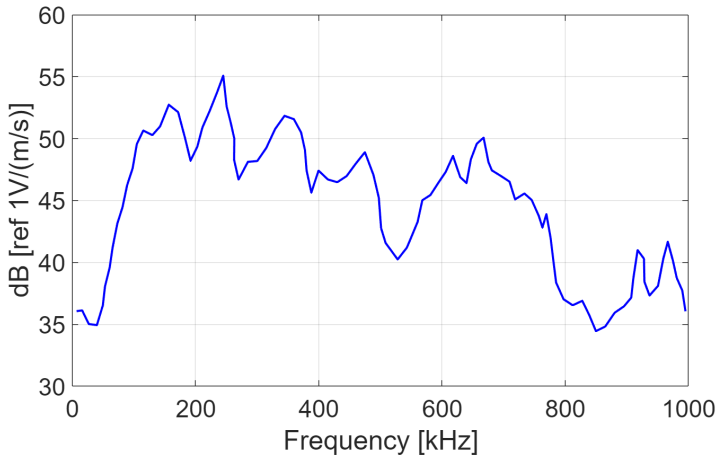

Figure 4.27: Sensitivity chart of the WD sensor. Adapted from [140].

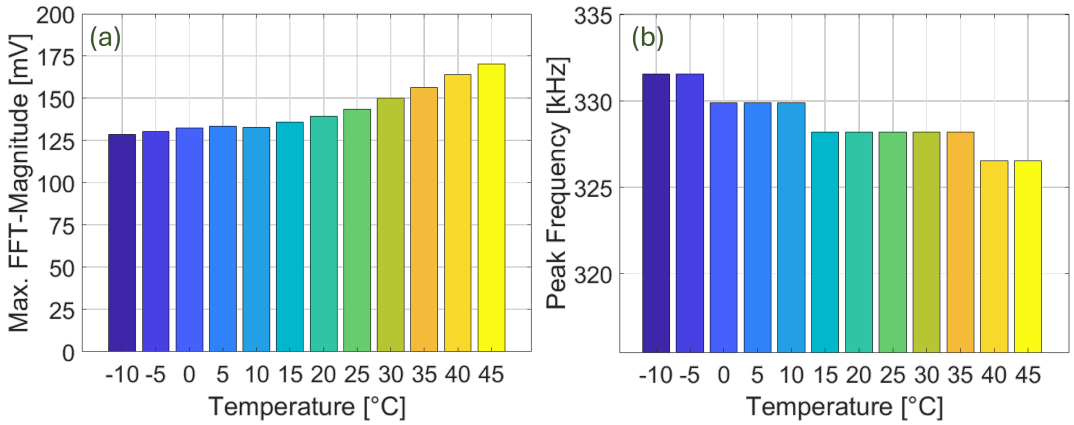

Figure 4.28: (a) Maximum FFT-magnitude trend of the frequency spectrum of the WD sensor. (b) Peak frequency trend of the frequency spectrum of the WD sensor.

VS30-V Sensor

Figure 4.29a presents the signal time series of the VS30-V sensor over the temperature range from -5 °C to 45 °C in 5 °C steps. The lower limit at -5 °C is determined by

the sensor minimum operating temperature. Measurements were performed with 60 dB amplification, and each signal was post-processed following the procedure described in Section 3.4. Waveforms were truncated at 105 μs to avoid reflections. The maximum absolute amplitude was calculated to evaluate the influence of temperature on the measurements. Figure 4.29b shows the maximum absolute amplitude versus temperature, revealing an increasing trend with increasing temperatures. The maximum amplitude increases from 1200 mV at -5 °C to 1670 mV at 45 °, which represents a variation of 39.1 % over a 50 °C temperature range.

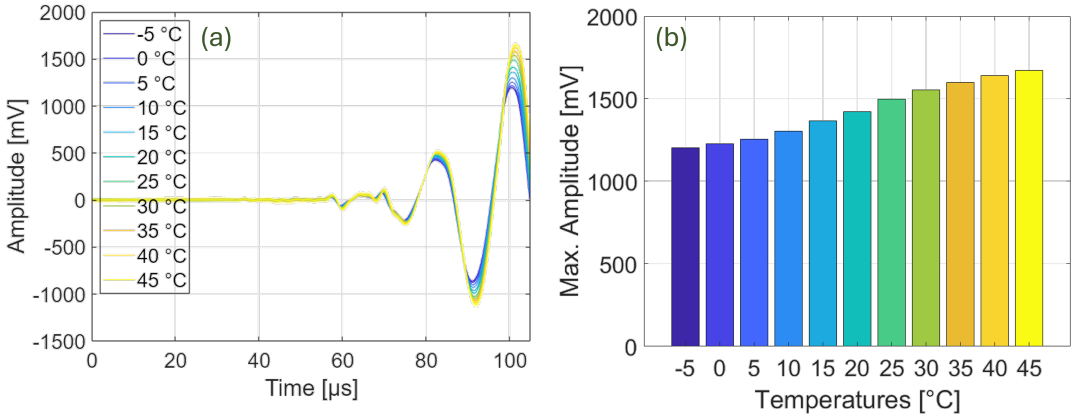

Figure 4.29: (a) Signal time series of the VS30-V sensor at different temperatures. (b) Maximum amplitude trend of the signal time series at different temperatures.

Figure 4.30a presents the frequency spectrum of the signal time series of Figure 4.29a. Zeros were added to the truncated signal, increasing its final length by 100 μs, and its frequency resolution.

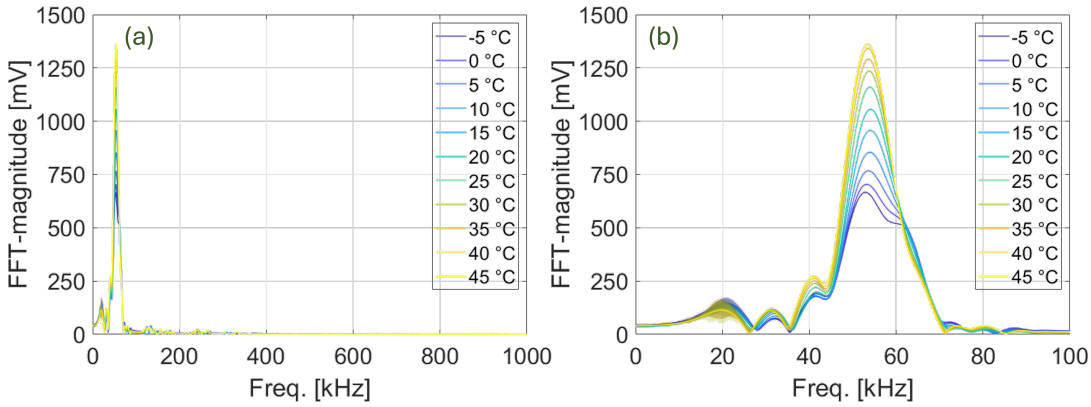

Figure 4.30: (a) Frequency spectrum of the signal time series at different temperatures of the VS30-V sensor. (b) Magnification of the frequency spectrum from 0 Hz to 100 kHz.

A narrow frequency range can be observed that aligns with the sensor datasheet, showing a frequency range from 25 kHz to 80 kHz [141]. Figure 4.30b presents a magnification of the frequency spectrum from 0 Hz to 100 kHz with one dominant frequency at around 55 kHz. The frequencies around this value are the most sensitive according to the sensitivity chart of the sensor manufacturer, as shown in Figure 4.31. Other relevant resonance frequencies can be observed at around 25 kHz and 30 kHz, and these resonances are also present in the sensitivity chart [141] provided by the sensor manufacturer.

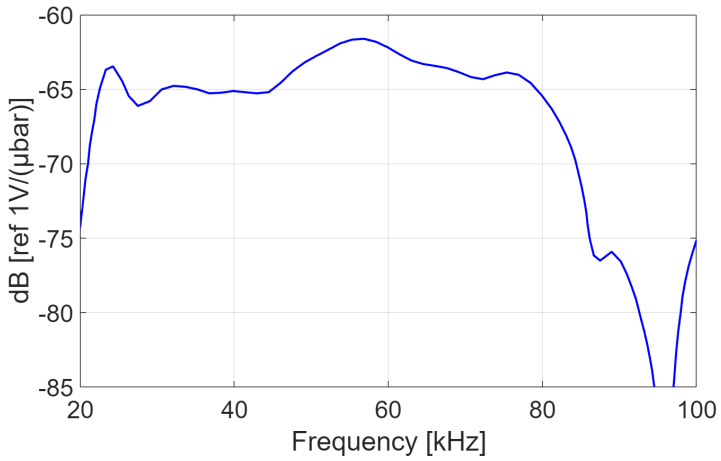

Figure 4.31: Sensitivity chart of VS30-V sensor. Adapted from [141].

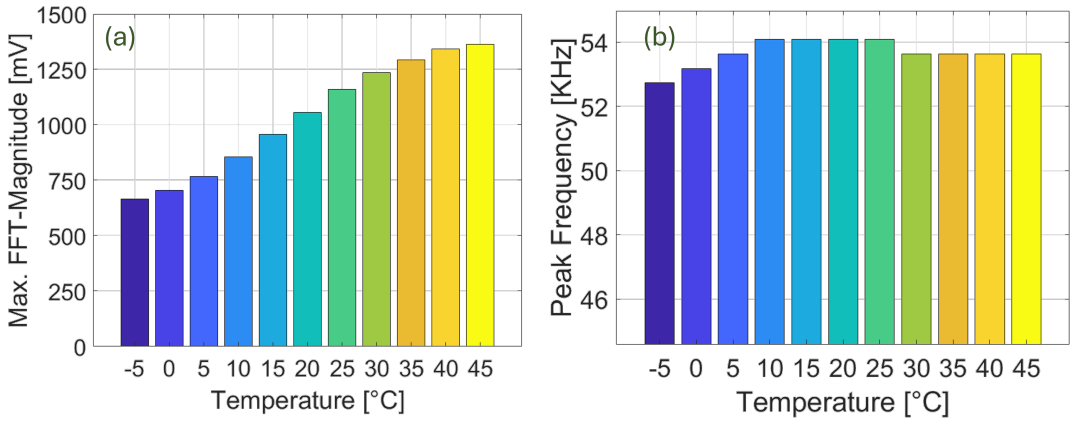

Figure 4.32: (a) Maximum FFT-magnitude trend of the frequency spectrum of the VS30-V sensor. (b) Peak frequency trend of the frequency spectrum of the VS30-V sensor.

Figure 4.32a presents a bar graph showing the maximum FFT magnitude at each temperature, where the same trend of the maximum amplitude of the signal time series

can be observed. The peak frequency, on the other hand, shows a different trend, in which it increases from -5 °C to 10 °C, then stays stable up to 25 °C, decreases at 30 °C, and remains stable up to 45 °C.

VS150-M Sensor

Figure 4.33a presents the signal time series of the VS150-M sensor from -10 °C to 45 °C in 5 °C steps. A 60 dB amplification was used, and each signal was post-processed following the procedure described in Section 3.4. Each waveform was truncated at 115 μs to avoid reflections. The maximum absolute amplitude was calculated to show the influence of temperature on the measurement, as shown in Figure 4.33b. The maximum amplitude varied from from 2130 mV at -10 °C to 2580 mV at 10 °C, which represents a variation of 21.1 %.

Figure 4.34 presents the frequency spectrum of the signal time series shown in Figure 4.33a. Zeros were appended to the truncated signal, extending its final length by 100 μs to improve frequency resolution. Multiple frequencies can be observed, with the dominant frequency around 150 kHz, which corresponds to the sensor's resonance. Other notable frequencies appear around 50 kHz, 225 kHz, 265 kHz, and 325 kHz, while anti-resonances occur at 200 kHz and near 300 kHz. These features are consistent with the sensitivity chart provided by the sensor manufacturer, as shown in Figure 4.35.

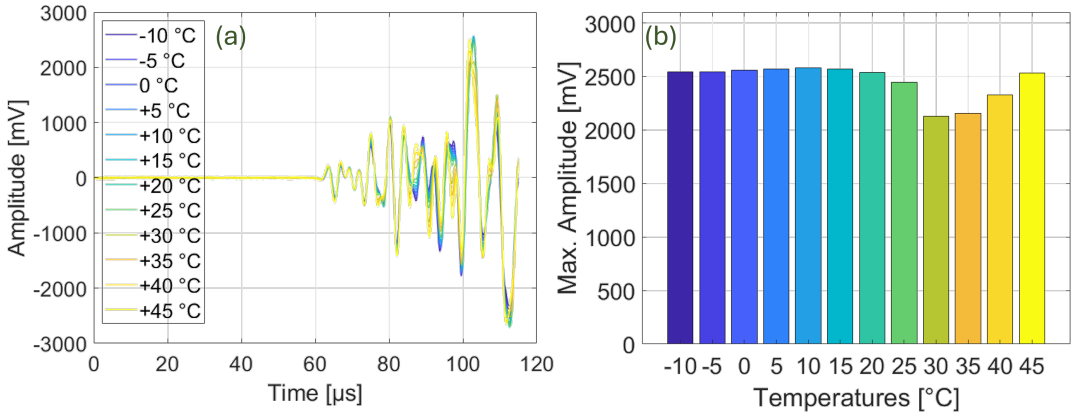

Figure 4.33: (a) Signal time series of the VS150-M sensor at different temperatures. (b) Maximum amplitude trend of the signal time series.

Figure 4.36a presents the maximum FFT magnitude from Figure 4.34. The measurements exhibit stable behavior, with the largest variation ranging from 318 mV at 20 °C to 339 mV at 10 °C, corresponding to 6.5 %. The peak frequency increases from -10 °C to 25 °C, followed by a sharp drop at 30 °C, after which it decreases gradually. This sudden drop is explained by the coupled peaks around 160 kHz, as shown in Figure 4.36b. As

temperature increases, the peak around 170 kHz loses predominance to the peak near 150 kHz.

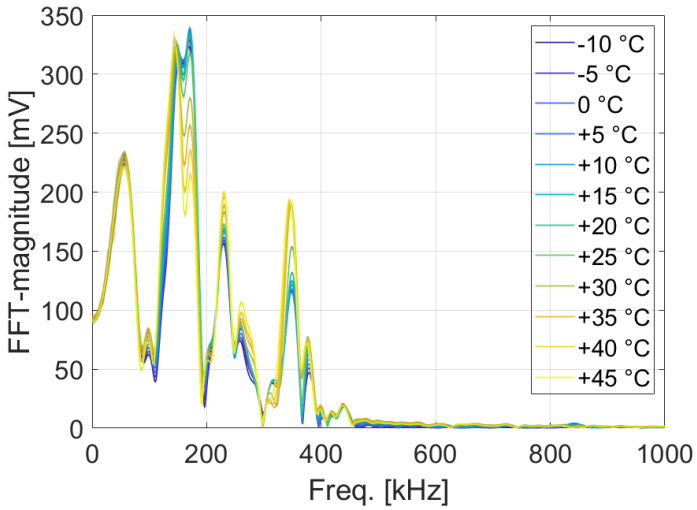

Figure 4.34: Frequency spectrum of the signal time series at different temperatures of the VS150-M sensor.

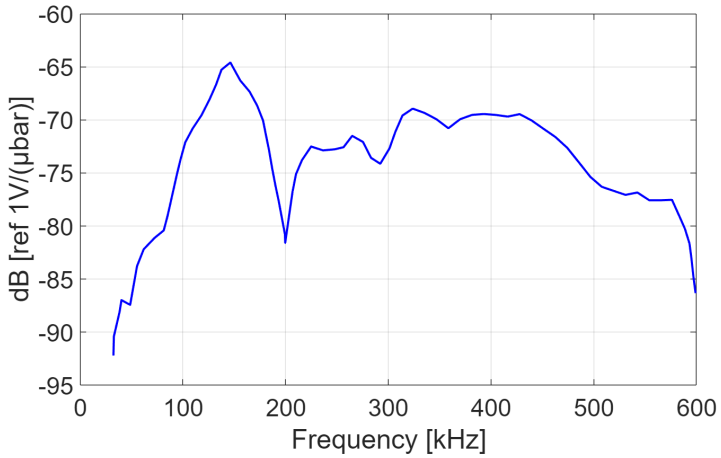

Figure 4.35: Sensitivity chart of VS150-M sensor. Adapted from [142].

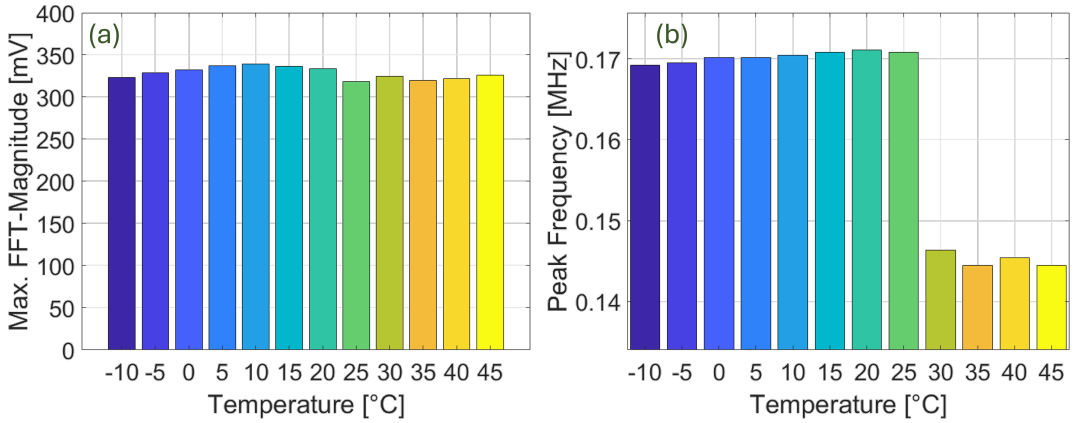

Figure 4.36: (a) Maximum FFT-magnitude trend of the frequency spectrum of the VS150-M sensor. (b) Peak frequency trend of the frequency spectrum of the VS150-M sensor.

VS900-M Sensor

Figure 4.37a presents the signal time series of the VS900-M sensor from -10 °C to 45 °C in 5 °C steps. An amplification of 60 dB was used, and each signal was post-processed following the procedure described in Section 3.4. Each waveform was truncated at 94.1 μs to avoid reflections. The maximum absolute amplitude was calculated to evaluate the influence of temperature on the measurements, as shown in Figure 4.37b. The VS900-M sensor exhibits an increasing trend in maximum absolute amplitude with rising temperatures, followed by a slight decrease at higher temperatures. The maximum amplitude varied from 470 mV at -10 °C to 503 mV at 35 °C, corresponding to a 7 % variation.

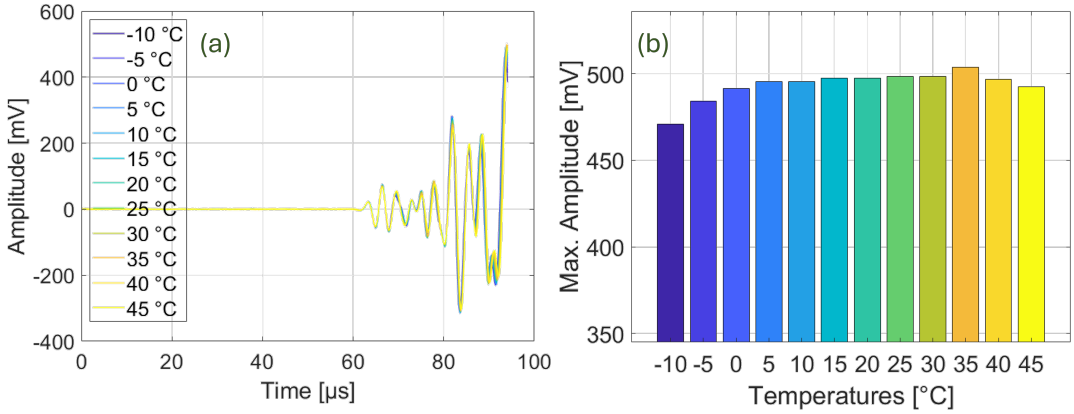

Figure 4.37: (a) Signal time series of the VS900-M sensor at different temperatures. (b) Maximum amplitude trend of the signal time series.

Figure 4.38 presents the frequency spectrum of the signal time series from Figure 4.37a. Zeros were appended to the truncated signal, increasing its total length by 100 μs and improving the frequency resolution. Multiple frequencies are observed, with dominant peaks at approximately 160 kHz, 260 kHz, 325 kHz, 370 kHz, and 440 kHz. Among these, the frequencies at 160 kHz, 325 kHz, and 440 kHz, as well as anti-resonances near 200 kHz and 400 kHz, are also reported in the sensitivity chart provided by the sensor manufacturer, as shown in Figure 4.39. The maximum FFT magnitude (Figure 4.40a) and the peak frequency (Figure 4.40b) exhibit an overall decreasing trend with increasing temperature.

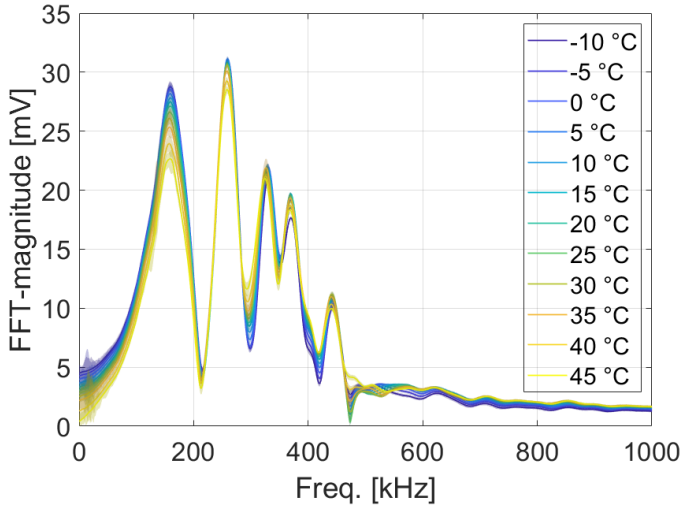

Figure 4.38: Frequency spectrum of the signal time series at different temperatures of the VS900-M sensor.

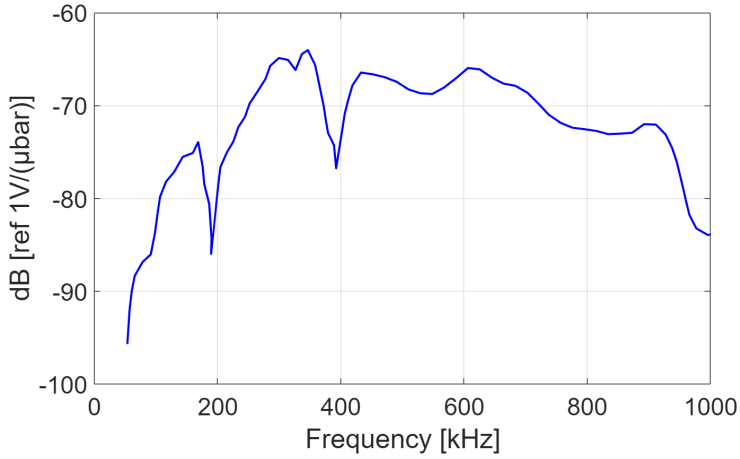

Figure 4.39: Sensitivity chart of VS900-M sensor. Adapted from [143].

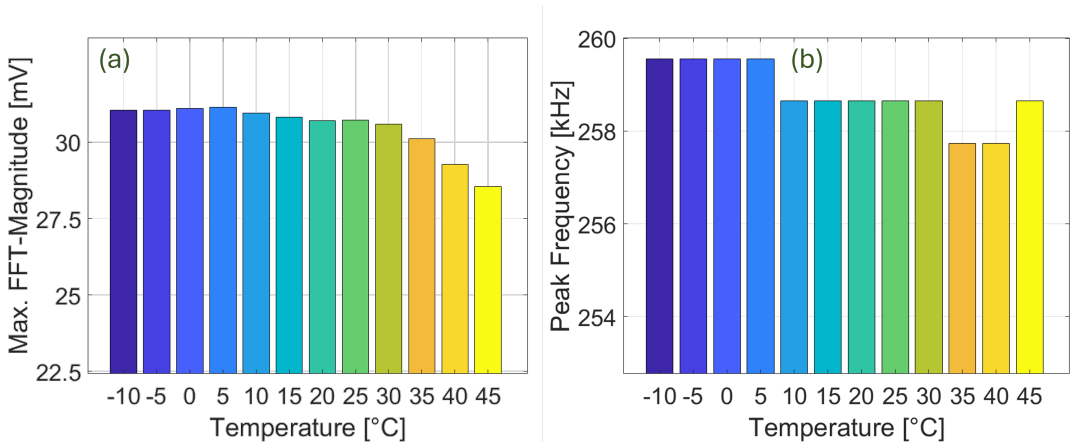

Figure 4.40: (a) Maximum FFT-magnitude trend of the frequency spectrum of the VS900-M sensor. (b) Maximum peak frequency trend of the frequency spectrum of the VS900-M sensor.

VS150-RSC Sensor

Figure 4.41a presents the signal time series of the VS150-RSC sensor from -10 °C to 45 °C in 5 °C steps. An amplification of 34 dB was used, and each signal was post-processed following the procedure described in Section 3.4. Each waveform was truncated at 85 μs to avoid reflections. The maximum amplitude was calculated to evaluate the influence of temperature on the measurement, as shown in Figure 4.41b. The VS150-RSC sensor exhibits a decreasing trend in maximum amplitude with increasing temperature. The maximum amplitude varied from 222 mV at -10 °C to 162 mV at 45 °C, corresponding to a total variation of 37 %.

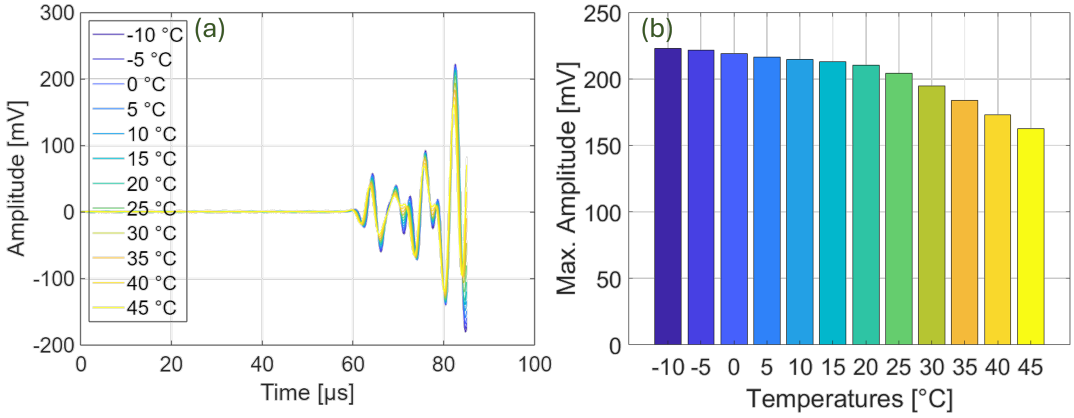

Figure 4.41: (a) Signal time series of the VS150-RSC sensor at different temperatures. (b) Maximum amplitude trend of the signal time series.

Zeros were added to the truncated signal, extending its final length by 100 μs, and improving the frequency resolution. Multiple frequencies can be observed in Figure 4.42, with the dominant frequencies around 160 kHz, 215 kHz, and 275 kHz.

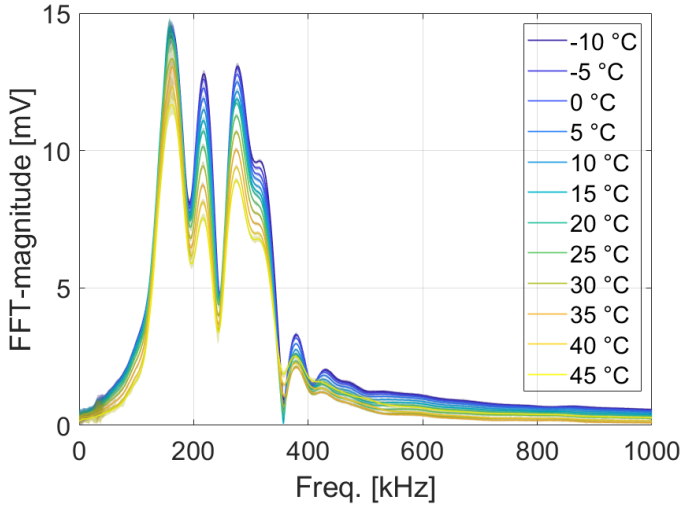

Figure 4.42: Frequency spectrum of the signal time series at different temperatures of the VS150-RSC sensor.

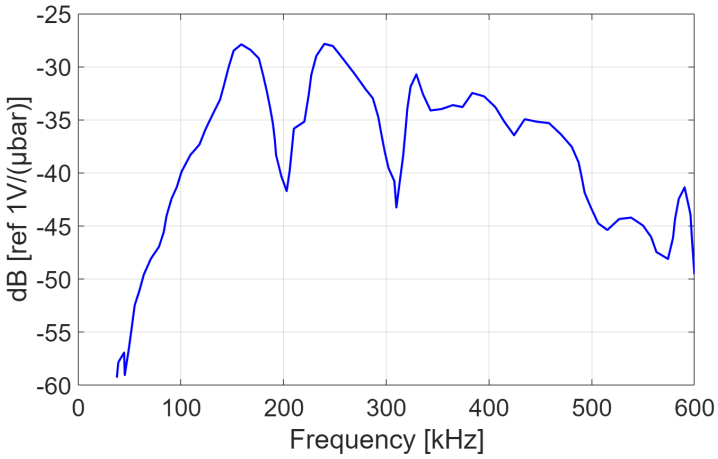

Figure 4.43: Sensitivity chart of VS150-RSC sensor. Adapted from [144].

A resonance frequency around 150 kHz is expected, as the sensor is designed for resonance at this frequency. This resonance, along with the anti-resonance at 200 kHz, is also shown in the sensitivity chart provided by the sensor manufacturer (Figure 4.43). The maximum FFT magnitude (Figure 4.44a) exhibits a decreasing trend with increasing

temperature, while the peak frequency (Figure 4.44b) remains largely stable, showing only slight oscillations around 160 kHz.

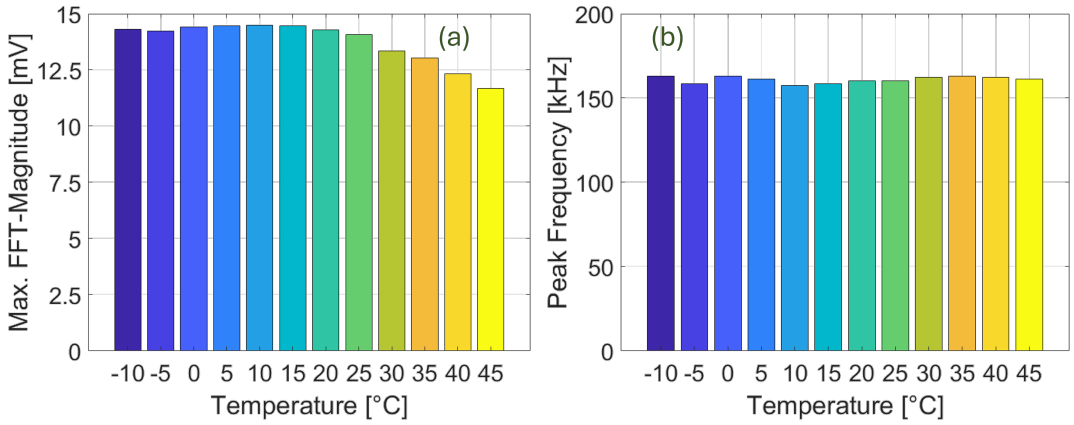

Figure 4.44: (a) Maximum FFT-magnitude trend of the frequency spectrum of the VS150-RSC sensor. (b) Peak frequency trend of the frequency spectrum of the VS150-RSC sensor.

Chapter 5

Experimental Validation of the Mobile Verification Device

5.1 Impact Test

The objective of this chapter is to evaluate the performance of the mobile verification device in detecting degraded sensors. To achieve this, sensors were gradually degraded through controlled impacts. Figure 5.1 illustrates the free-fall drop device, which consists of aluminum profiles with tube holders. The tubes guide a 24 g steel ball to strike the lateral surface of the sensors. The drop height of the steel ball can be adjusted by adding or removing tubes. The sensor holder is tilted by 15° relative to the horizontal to avoid double impacts and reduce the energy of each hit.

Three sensors: WD, VS30-V, and VS900-M were degraded by impact. After each impact, the sensors were measured using both the mobile and benchmark verification devices. Pulse settings for the mobile device measurements were the same as described in Section 3.2, and each measurement consisted of 600 waveforms. A settling time of at least 400 s was allowed before measurements. Environmental conditions were 23 °C ± 2 °C and 53 % ± 4 % RH, except for the VS30-V sensor, for which the data logger malfunctioned; in this case, historical maximum and minimum temperatures were used. Each measurement was processed according to the procedure described in Section 3.4.

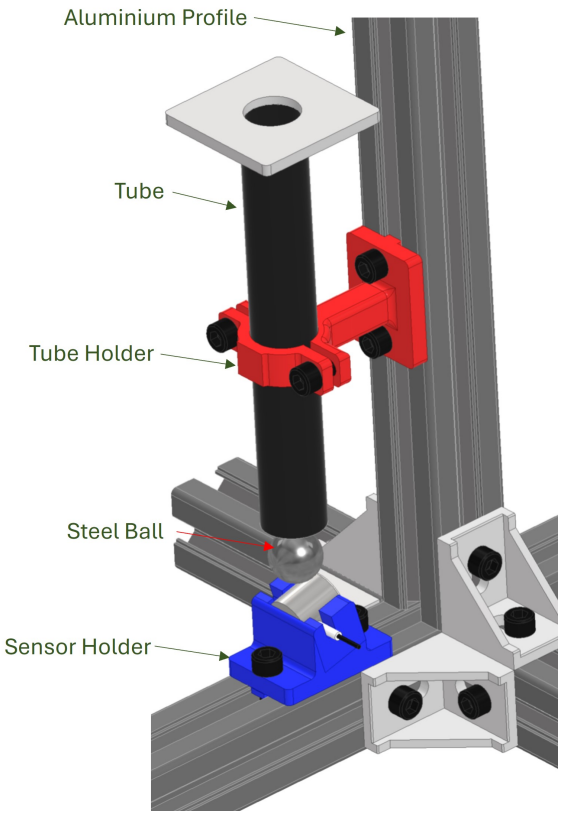

Figure 5.1: Illustration of the steel ball drop device. Adapted from [23].

5.2 WD Sensor

The WD sensor was impacted starting from a height of 70 mm, with increments of 50 mm. Each height was tested at least three times, except for 1820 mm, where only a single impact was performed due to the sensor advanced stage of degradation. Measurements after each impact were performed with 60 dB amplification for both the mobile and benchmark verification devices.

Figure 5.2a presents the signal time series of the WD sensor in its baseline (undamaged state) and after the impact test (damaged), measured with the mobile verification device. A significant change in the waveform is observed, particularly a decrease in amplitude. These changes are also evident in Figure 5.2b, which shows the frequency spectrum of the signal time series. As expected, the magnitude of the frequency spectrum decreases significantly, with noticeable changes in the resonance peaks. Although three regions of dominant resonance frequencies remain, their sensitivity is drastically reduced. Additionally, frequencies above 400 kHz show a flatter, less responsive behavior, indicating a marked degradation in the sensor performance.

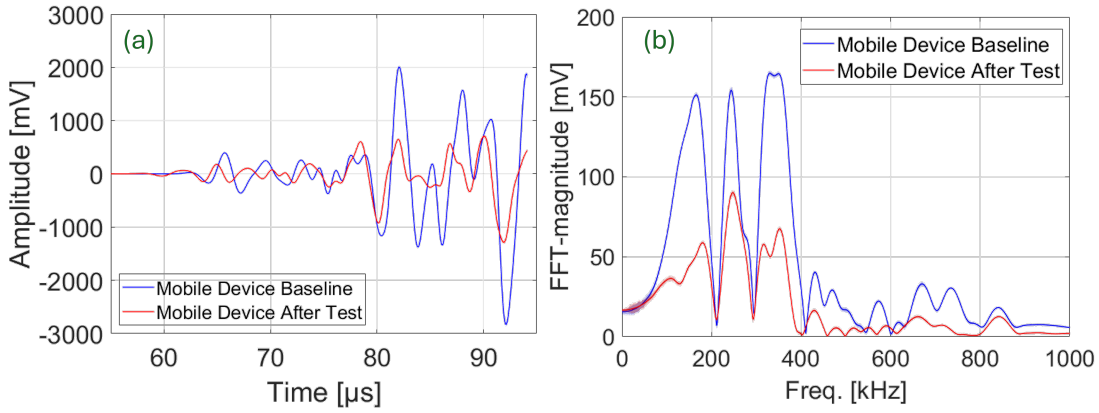

Figure 5.2: WD sensor measured by the mobile verification device before and after the impact test. (a) Signal time series. (b) Frequency spectrum. Adapted from [23].

Figure 5.3a presents the signal time series from the baseline of the WD sensor (undamaged state) and after the impact test (damaged) measured by the benchmark verification device. Similar to the mobile verification device, a significant change in the waveform can be observed, especially a decrease in amplitude. In addition, the usable signal length of the damaged state decreased by approximately 10 μs. Consequently, these changes impacted the frequency spectrum, as shown in Figure 5.3b, where a significant decrease in frequency magnitudes can be observed. In this case, the most pronounced changes occurred in the lower frequencies, up to approximately 300 kHz. Above that frequency, the frequency spectrum of the damaged state resembles that of the undamaged state, however, it has lower magnitudes.

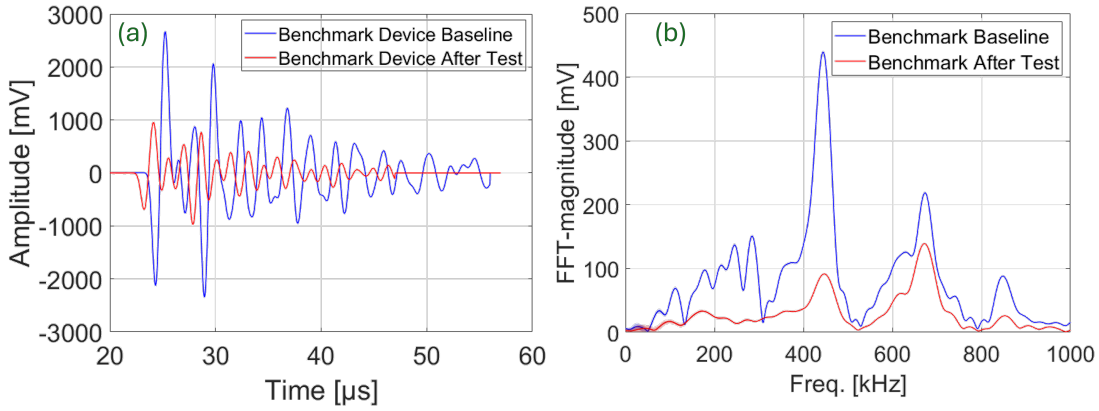

Figure 5.3: WD sensor measured by the benchmark verification device before and after the impact test. (a) Signal time series. (b) Frequency spectrum. Adapted from [23].

To provide a proper comparison of the performance of both devices, Figure 5.4 presents

the RMS values of the WD sensor test for the mobile and benchmark verification devices. The RMS values were calculated using the equation in Table 6.1. The x-axis represents the cumulative drop energy of the steel ball, calculated as the cumulative sum of its gravitational potential energy for each impact height.

A noticeable trend change in the mobile verification device occurs around 3.75 J, while the benchmark device detects a similar change at 5 J, showing a more sensitive response up to 6 J. Beyond this energy level, both devices display comparable sensitivity. A distinct measurement is observed for the mobile verification device at approximately 5.5 J, showing an exceptional increase in RMS value, most likely caused by a temporary increase in the sensor sensitivity due to the impact.

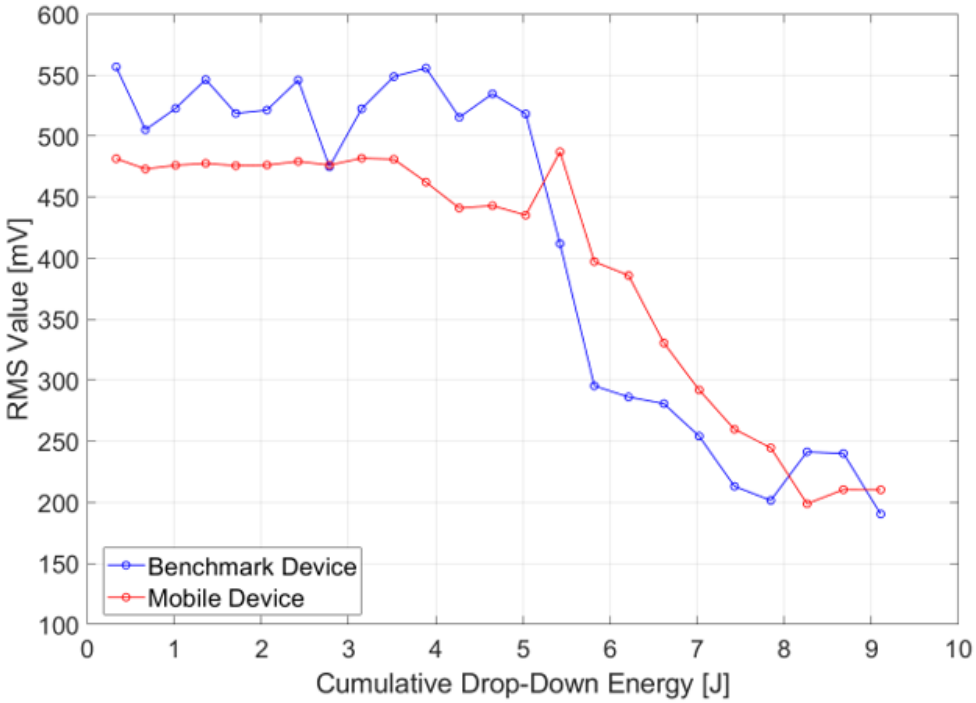

Figure 5.4: RMS values of the WD sensor impact test. Adapted from [23].

Figure 5.5a illustrates the internal components of the WD sensor, showing its two piezoelectric elements. Figure 5.5b presents a scanning acoustic microscopy (SAM) image of the undamaged state of the WD sensor, obtained by a microscope model V8 supplied by KSI with a 15 MHz ultrasound transducer. Both the inner disk and outer ring piezoelectric elements are clearly visible. Figure 5.5c shows the SAM image of the damaged sensor, where the inner disk has completely detached from the wear plate, and the outer ring is partially detached.

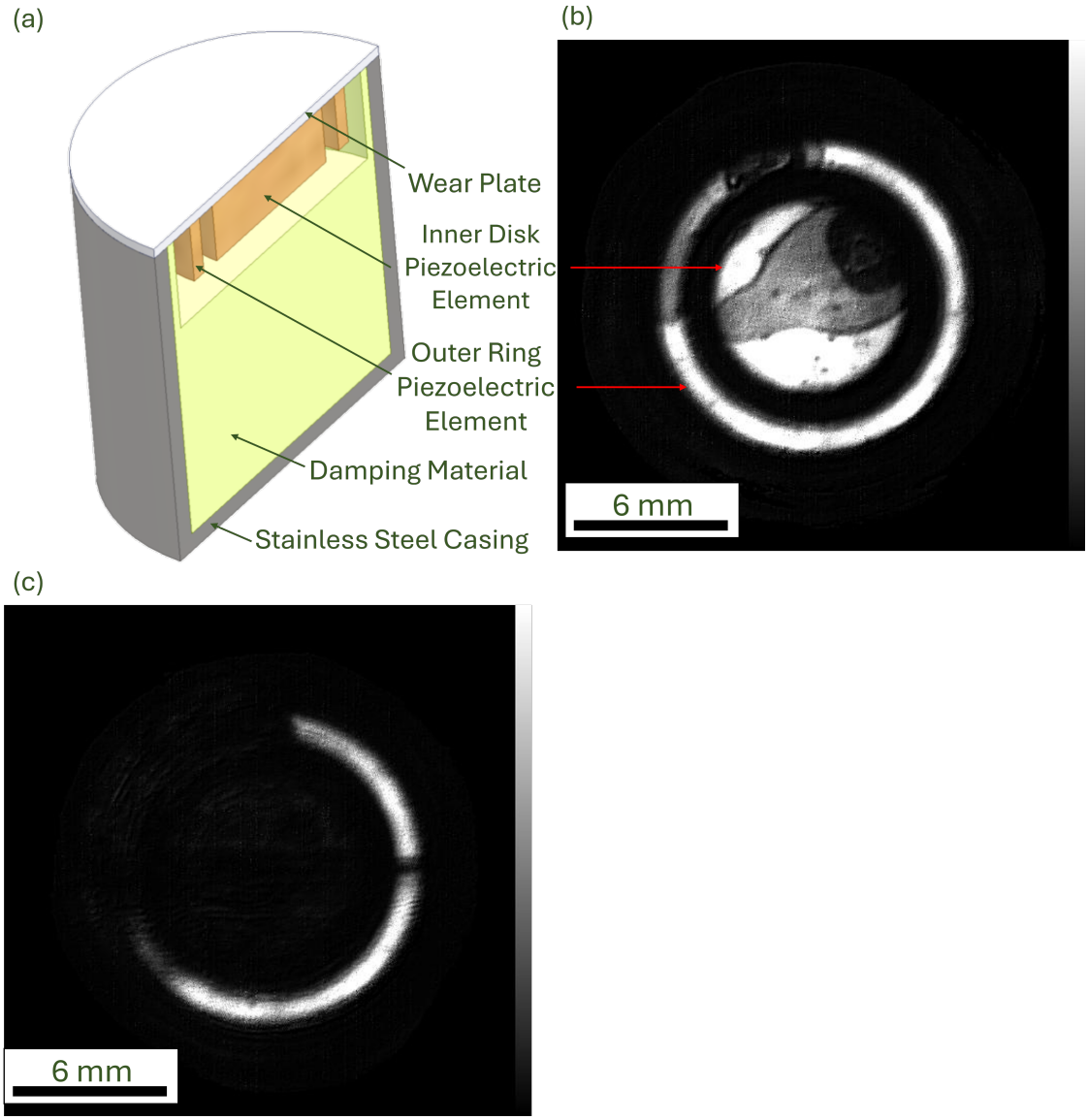

Figure 5.5: (a) Illustration of the inner part of the WD sensor. Scanning acoustic microscopy (SAM) backwall echo inspection at approximately 3.5 mm from the wear plate: (b) Before the impact test. (c) After the impact test. Adapted from [23].

5.3 VS900-M Sensor

The impact test of the VS900-M sensor started at a height of 2000 mm, with a 100 mm increment up to 2500 mm. Then, the next height tested was 2700 mm, followed by 3000 mm, and afterward, the increment was 500 mm up to 4000 mm. Each height was

tested three times, except for the last step, which was tested four times. The signals were truncated at 94.1 μs for the mobile verification device and at 57 μs for the benchmark verification device.

Figure 5.6a presents the signal time series from the baseline of the VS900-M sensor (undamaged state) and after the impact test (damaged) measured by the mobile verification device. It can be observed that there is a complete change in the shape of the waveform, with the damaged state showing a slight decrease in amplitude. Figure 5.6b presents the frequency spectrum of the signal time series of Figure 5.6a, where the undamaged state shows lower magnitudes up to 400 kHz.

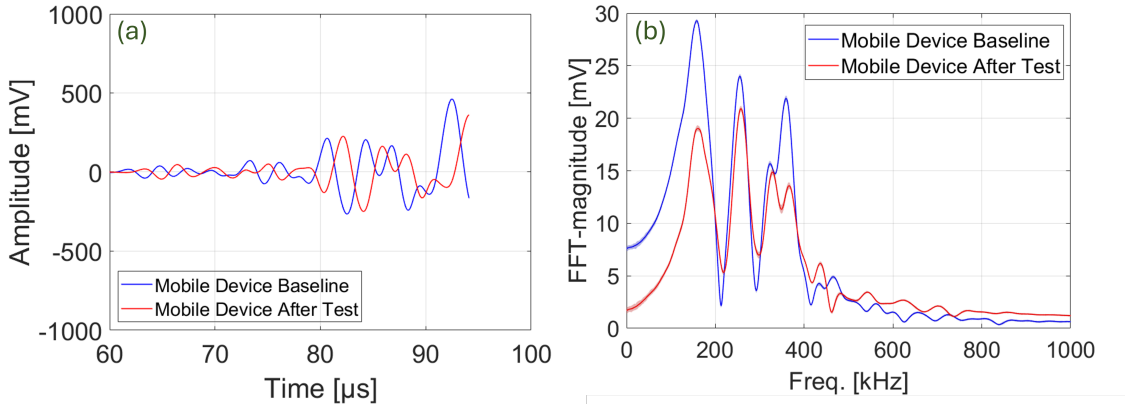

Figure 5.6: VS900-M sensor measured by the mobile verification device before and after the impact test. (a) Signal time series. (b) Frequency spectrum.

Unlike the mobile verification device, the benchmark verification device detected a significant decrease in the signal time series and frequency spectrum amplitudes, as shown in Figures 5.7a and 5.7b, respectively.

Similar to the WD sensor, the usable signal length of the damaged VS900-M sensor decreased by approximately 10 μs. A significant reduction in magnitude is also evident in the frequency spectrum.

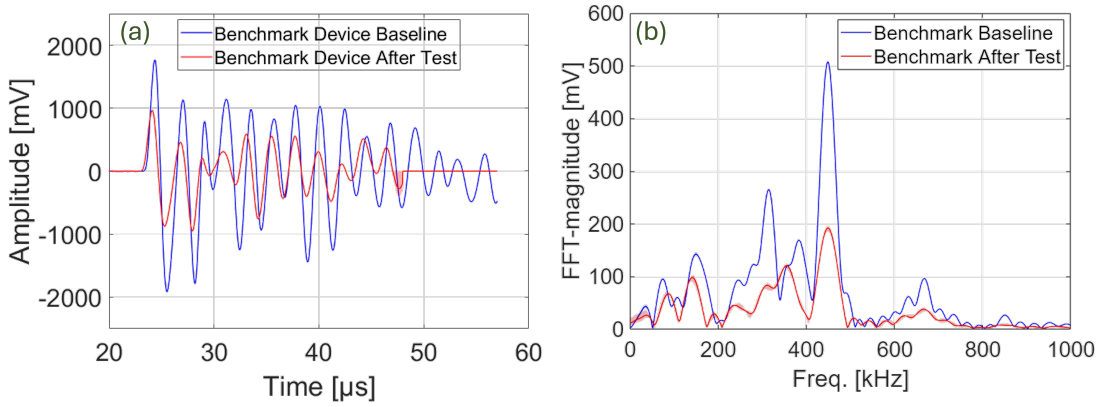

Figure 5.7: VS900-M sensor measured by the benchmark verification device before and after the impact test. (a) Signal time series. (b) Frequency spectrum.

Figure 5.8 compares the performance of the mobile and benchmark verification devices using RMS values for the VS900-M sensor.

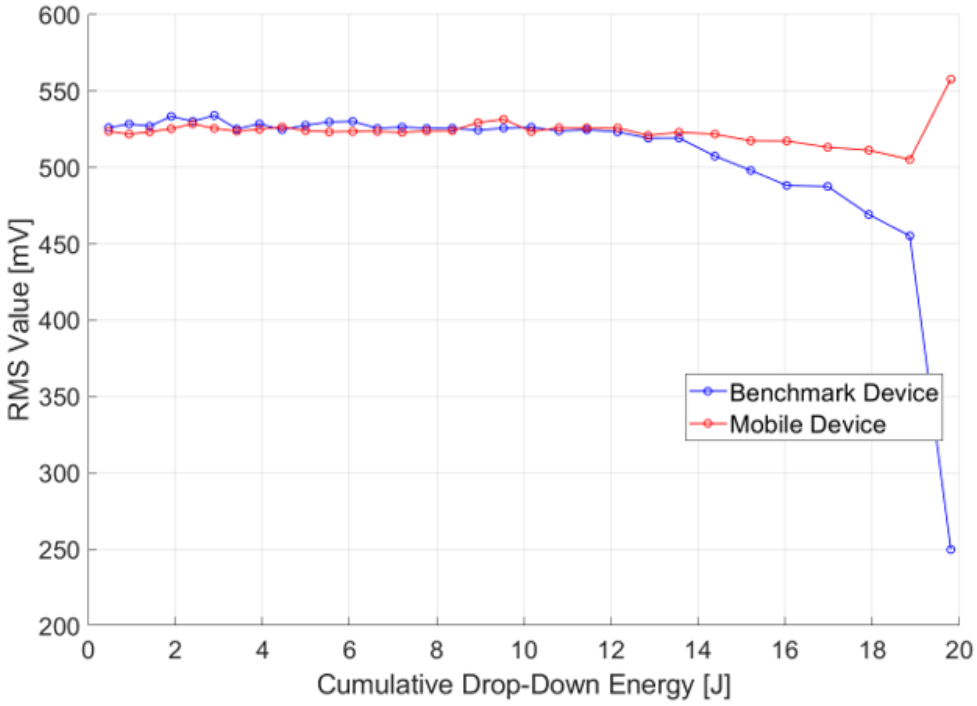

Figure 5.8: RMS values of the VS900-M sensor during the impact test.

For clarity, the RMS values of the mobile verification device were offset by +450 mV.

Both devices exhibit similar trends up to 12 J. Beyond this energy, a noticeable trend change occurs, with RMS values decreasing for both devices, although the benchmark verification device shows a more pronounced variation.

For the final measurements, an opposite trend is observed: the mobile verification device shows a significant increase, while the benchmark device shows a sharp decrease. This discrepancy could be attributed to the different wave types used by the devices; the mobile verification device uses Lamb waves, while the benchmark device uses longitudinal waves. In the final stage of damage, Lamb waves may be more sensitive to the sensor condition. Alternatively, changes in the electrical contact within the sensor could affect its response, contributing to the observed differences.

Figure 5.9a presents an X-ray inspection of the VS900-M sensor in the undamaged state, and Figure 5.9b shows it after the impact test. It can be observed that the piezoelectric element broke into multiple pieces, and a small portion of it remained attached to the metallic membrane.

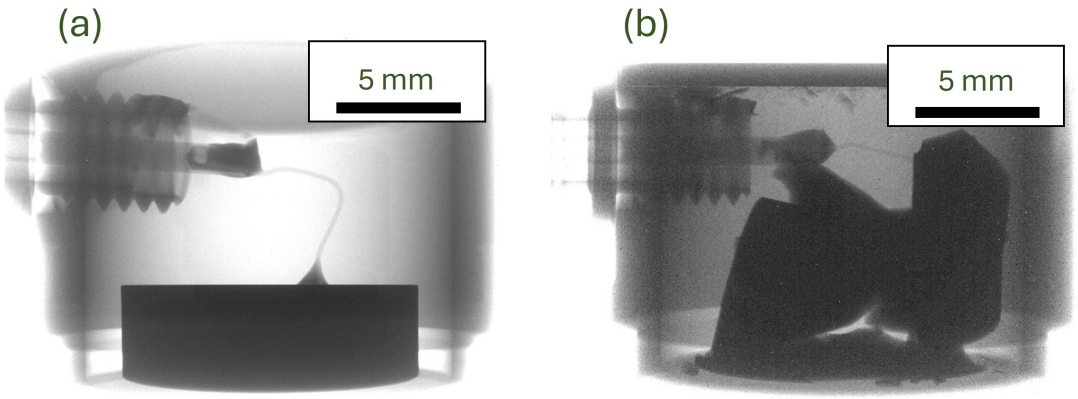

Figure 5.9: X-ray inspection of the VS900-M. (a) Before impact test. (b) After the impact test.

5.4 VS30-V Sensor

The impact of the VS30-V sensor started at a height of 150 mm, with a 100 mm increment. Each height was tested at least three times until 950 mm, where it was impacted only twice. The signals were truncated at 104 μs for the mobile verification device and at 57 μs for the benchmark verification device.

Figure 5.10a presents the signal time series from the baseline of the VS30-V sensor (undamaged state) and after the impact test (damaged) measured by the mobile verification device. Similar to the WD sensor, the amplitudes decreased significantly. A change in the

shape of the waveform can also be observed. Figure 5.10b presents the frequency spectrum of the signal time series of Figure 5.10a, where a significant decrease in magnitude can be observed. The major peak around 50 kHz is still present in the damaged state, and the frequency spectrum above this frequency shows a flatter and less sensitive response.

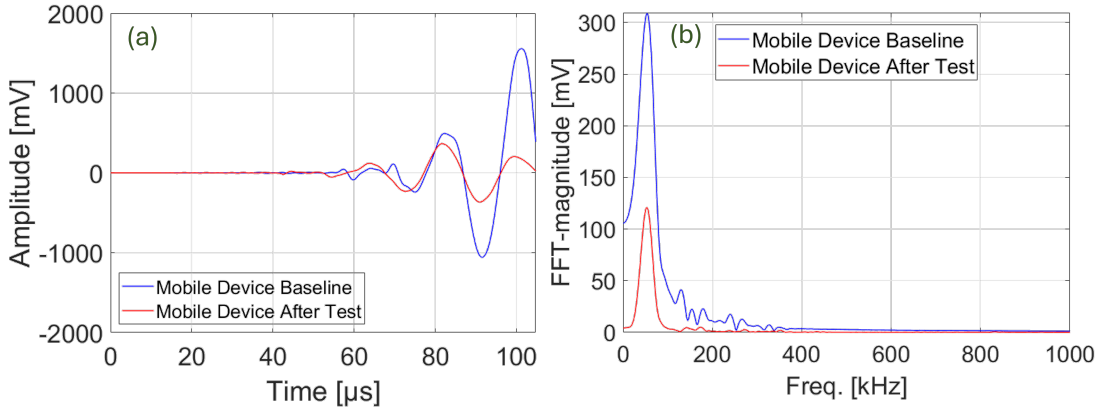

Figure 5.10: VS30-V sensor measured by the mobile verification device before and after the impact test. (a) Signal time series. (b) Frequency spectrum.

Similar to the mobile verification device, the benchmark verification device also showed a significant decrease in sensitivity in the signal time series and the frequency spectrum, as shown in Figures 5.11a and 5.11b, respectively.

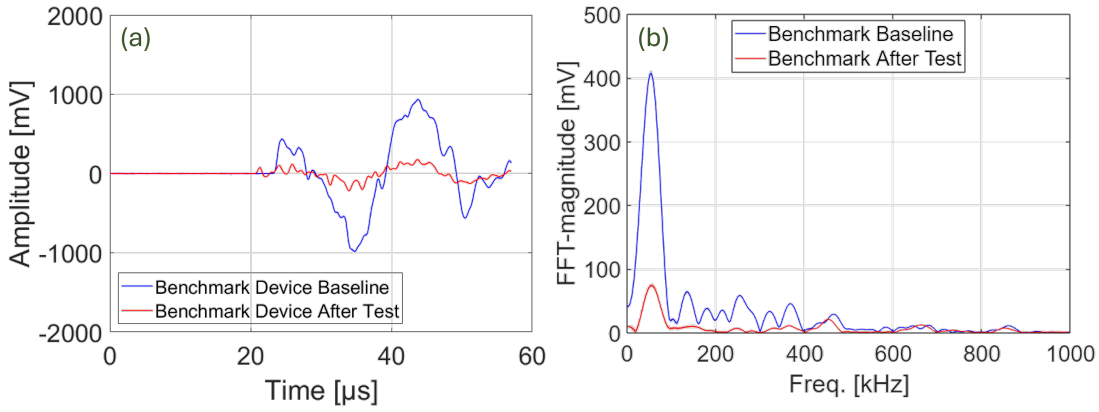

Figure 5.11: VS30-V sensor measured by the benchmark verification device before and after the impact test. (a) Signal time series. (b) Frequency spectrum.

Figure 5.12 presents a comparison of the performance of the mobile and benchmark verification devices in the form of RMS values. There are several points that must be

addressed in this plot. The first is that, in order to slow down the degradation process, after impacting the sensor at 950 mm, the steel ball drop height was decreased to 550 mm and then increased again to 850 mm. The second is that the benchmark verification device showed remarkably consistent measurements up to 850 mm. A third issue is that at approximately 3 J, there is a drastic drop in the RMS value for both devices, and just before 4 J, the RMS value increases for both devices. Afterward, there is a decreasing trend, and at 5 J, there is another drastic decrease in the RMS values. After 5 J, the RMS values remain at a slightly higher level than the first drastic drop.

There are two possible explanations for these drastic variations in the measurements. The first is a potential bad connection within the sensor, where impacts could either degrade or improve the electrical contact. The second possibility is that the impacts alter the residual polarization of the PZT element, thereby affecting its electrical response. This behavior of piezoelectric elements has been observed in previous studies [146, 147]. These facts could also explain the outlier measurement of the WD sensor in Figure 5.4 at approximately 5.5 J.

Unfortunately, neither the SAM nor the X-ray images were able to detect the type of damage present in the VS30-V sensor.

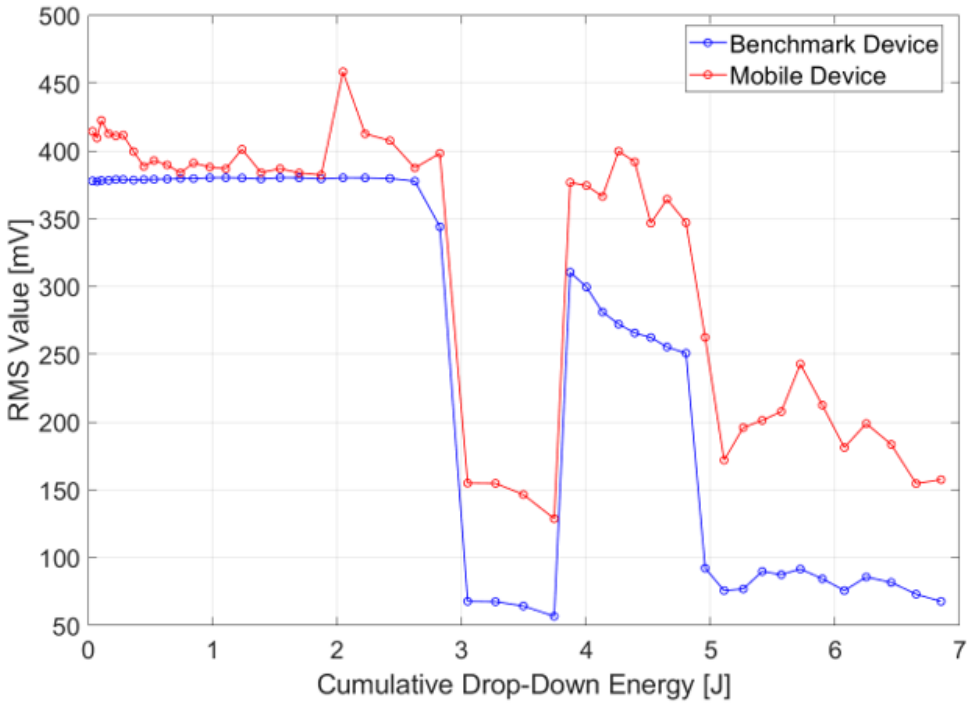

Figure 5.12: RMS values of the VS30-V sensor during the impact test.

Chapter 6

Verification Criteria

As explained in Section 3.3, the sensor verification and setup auto-check are based on the comparison of their measurements with the previously determined baselines. Therefore, it is reasonable to consider a deviation in the measurement that is greater than the uncertainty as an evaluation criterion. If the current measurement of a certain sensor shows values outside the uncertainty range, this sensor can be considered not approved. Consequently, an uncertainty analysis is necessary to calculate the expanded measurement uncertainty and establish a verification criterion.

This analysis considers both the baseline measurements of the AE sensors and the measurements taken during sensor degradation in the impact test, as presented in Section 5.1. In this analysis, two main sources of uncertainty were considered: variation in sensor coupling and in temperature.

The coupling uncertainty was calculated by mounting each AE sensor five times on the aluminum plate of the mobile verification device and measuring 600 waveforms per mounting, with a settling time of at least 400 s. The uncertainty due to temperature was calculated from measurements of each sensor during the environmental tests presented in Section 4.6. Influences from different operators were not considered, as only one operator performed the measurements after each impact. The uncertainty of the AE DAQ system was also not included, since the coupling uncertainty was found to be two orders of magnitude greater than the DAQ system resolution.

The procedure for calculating coupling uncertainty involved computing the 48 features listed in Table 6.1 for each of the five measurements, re-mounting the sensor between measurements. After computing the features, the mean of each feature was calculated using Equation (A.1), followed by the sample standard deviation using Equation (A.2).The experimental standard deviation of the mean was then obtained using Equation (A.3). The same procedure was applied to calculate the temperature-related uncertainty at 20 °C and 25 °C, which were chosen because the baseline and impact-test measurements were conducted within this temperature range. Finally, the coupling uncertainty and the temperature uncertainty at 20 °C and 25 °C were fed into Equation (A.5) to calculate the

Type B uncertainty.

Table 6.1 presents a list of AE and statistical features along with their definitions.

Table 6.1: Definitions of the features. Adapted from [48].

Feature	Definition	Unit
Counts (N_{AE})	Number of threshold crossings between t_0 (time of the first threshold crossing) and t_{term} (time of the last threshold crossing)	[#]
Duration (t_{AE})	Time between the first and last threshold crossing ($t_{term} - t_0$)	[μs]
Peak time (t_{peak})	Time of the maximum amplitude	[μs]
Peak frequency (f_{peak})	Maximum peak frequency	[Hz]
Amplitude at Peak Frequency (A_{freq})	The magnitude of the signal spectrum at the peak frequency, representing the maximum spectral amplitude obtained from the FFT	[mV]
Counts to peak (N_{peak})	Number of threshold crossings between t_0 and t_{peak}	[#]
Amplitude (v_{max})	Maximum amplitude	[V]
Rise Time (t_{rise})	$t_{\text{peak}} - t_0$	[μs]
Number of samples (n)	Number of discrete samples (voltage measurements)	[#]
Root Mean Square (RMS)	$RMS = \sqrt{\frac{1}{n}\sum_{i=1}^{n} v_i^2}$, with v_i representing the voltage measurement at time t_i, and n as the total number of values in the signal	[V]
Average Signal Level (ASL)	$ASL = \frac{1}{n}\sum_{i=1}^{n} \lvert v_i \rvert$	[V]
Average Frequency (f_{avg})	$f_{\text{avg}} = \frac{N_{AE}}{t_{AE}}$	[Hz]
Reverberation Frequency (f_{rev})	$f_{\text{rev}} = \frac{N_{AE} - N_{\text{peak}}}{t_{AE} - t_{\text{peak}}}$	[Hz]
Initiation Frequency (f_{init})	$f_{\text{init}} = \frac{N_{\text{peak}}}{t_{\text{peak}}}$	[Hz]
Amplitude Rate to Peak (φ_{rise})	$\varphi_{\text{rise}} = \frac{v_{\text{max}}}{t_{\text{peak}}}$	[V/s]
Absolute Energy (W_{AE})	$W_{AE} = \sum_{i=1}^{n} \frac{v_i^2}{10\text{k}\Omega}\Delta t$ with 10kΩ input impedance of the AE DAQ system	[aJ]
Frequency Centroid (f_{centroid})	$f_{\text{centroid}} = \frac{\sum_{i=1}^{n} f_i \cdot A_i}{\sum_{i=1}^{n} A_i}$ with f_i representing the individual frequency values and A_i its amplitude	[Hz]
Weighted Peak Frequency (W_{peak})	$W_{\text{peak}} = \sqrt{f_{\text{peak}} \cdot f_{\text{centroid}}}$	[Hz]

Feature	Definition	Unit
Partial Power (P_{partial})	$P_{\text{partial}} = \frac{\sum_{i=f_a}^{f_b} A_i^2}{\sum_{i=f_{\text{start}}}^{f_{\text{end}}} A_i^2} \times 100$ Frequency range of investigation from f_{start} (0 kHz) to f_{end} (1200 kHz) and frequency range of • Partial Power 1 from 0 kHz to 150 kHz. • Partial Power 2 from 150 kHz to 300 kHz. • Partial Power 3 from 300 kHz to 450 kHz. • Partial Power 4 from 450 kHz to 600 kHz. • Partial Power 5 from 600 kHz to 900 kHz. • Partial Power 6 from 900 kHz to 1200 kHz.	[%]
Fall time (t_{fall})	$t_{\text{fall}} = t_{\text{term}} - t_{\text{peak}}$	[μs]
Counts from peak (N_{fall})	Number of threshold crossings after the peak till signal duration	[#]
Termination Frequency (f_{term})	$f_{\text{term}} = \frac{N_{\text{fall}}}{t_{\text{fall}}}$	[Hz]
Mean value ($\bar{v}$)	$\bar{v} = \frac{1}{n} \sum_{i=1}^{n} v_i$	[V]
Minimum value (v_{min})	Minimum amplitude value	[V]
Range (R_{rang})	$R_{\text{rang}} = v_{\text{max}} - v_{\text{min}}$	[V]
Median values (M)	$M = \begin{cases} v_{\frac{n+1}{2}} & \text{if } n \text{ is odd} \\ \frac{1}{2}\left(v_{\frac{n}{2}} + v_{\frac{n}{2}+1}\right) & \text{if } n \text{ is even} \end{cases}$ with $v_{\frac{n+1}{2}}$ the middle value in the sorted list of signal values	[V]
Skewness value (γ)	$\gamma = \frac{n}{(n-1)(n-2)} \sum_{i=1}^{n} \left(\frac{v_i - \bar{v}}{\sigma}\right)^3$	[dimensionless]
Kurtosis value (γ_2)	$\gamma_2 = \frac{n(n+1)}{(n-1)(n-2)(n-3)} \sum_{i=1}^{n} \left(\frac{v_i - \bar{v}}{\sigma}\right)^4 - \frac{3(n-1)^2}{(n-2)(n-3)}$	[dimensionless]
Entropy value (H)	$H = -\sum_{i=1}^{n} p(v_i) \log_2 (p(v_i))$ with $p(v_i) = \frac{\text{count}(v_i)}{n}$	[dimensionless]
Mean Absolute Deviation (MAD)	$MAD = \frac{1}{n} \sum_{i=1}^{n} \lvert v_i - \bar{v} \rvert$	[V]
Interquartile Range (IQR)	$IQR = Q_3 - Q_1$ • Q_3: The third quartile (75th percentile) of the signal. • Q_1: The first quartile (25th percentile) of the signal.	[V]

Feature	Definition	Unit
Pearson correlation value (P_e)	$P_e = \frac{\sum_{i=1}^{n}\left(Vst_i - \bar{Vst}\right)\left(Vsc_i - \bar{Vsc}\right)}{\sqrt{\sum_{i=1}^{n}\left(Vst_i - \bar{Vst}\right)^2}\sqrt{\sum_{i=1}^{n}\left(Vsc_i - \bar{Vsc}\right)^2}}$ • Vst_i: The i-th value in the first dataset (in this case, the first half of the signal). • $\bar{Vst}$: The mean value of the first dataset (Vst). • Vsc_i: The i-th value in the second dataset (in this case, the second half of the signal). • $\bar{Vsc}$: The mean value of the second dataset (Vsc). • $P_e = 1$: Perfect positive correlation. • $P_e = -1$: Perfect negative correlation. • $P_e = 0$: No linear correlation.	[dimensionless]
Autocorrelation at Lag 1 (r_1)	$r_1 = \frac{\sum_{i=1}^{n-1}(v_i - \bar{v})(v_{i+1} - \bar{v})}{\sum_{i=1}^{n}(v_i - \bar{v})^2}$	[dimensionless]
Variance (σ^2)	$\sigma^2 = \frac{1}{n}\sum_{i=1}^{n}\left(v_i - \bar{v}\right)^2$	[V^2]
Standard Deviation of Differences ($\sigma_{\Delta v}$)	$\sigma_{\Delta v} = \sqrt{\frac{1}{n-1}\sum_{i=1}^{n-1}\left(\Delta v_i - \overline{\Delta v}\right)^2}$ • Δv_i: The difference between consecutive values in the signal ($v_{i+1} - v_i$). • $\overline{\Delta v}$: The mean of the differences Δv_i.	[V]
Occupied Bandwidth (OBW)	$OBW = f_2 - f_1$ • f_1 and f_1: Lower and upper cutoff frequencies such that $\sum_{k=f_1}^{f_2}\lvert S[k]\rvert^2\Delta f = \alpha\sum_{k=0}^{n-1}\lvert S[k]\rvert^2\Delta f$, where α is the percentage of total signal power (default $\alpha = 0.99$ for 99%). • $S[k]$: The discrete Fourier transform of the signal. • $\Delta f = \frac{F_s}{n}$: The frequency bin width, where F_s is the sampling frequency.	[Hz]

Feature	Definition	Unit
Spectral Flatness (SF)	$SF = \frac{\text{geomean}(\lvert X[k]\rvert)}{\text{mean}(\lvert X[k]\rvert)}$ • $X[k]$: The discrete Fourier transform of the signal. • $\lvert X[k]\rvert$: The magnitude of the DFT coefficients. • geomean($\lvert X[k]\rvert$): The geometric mean of the magnitudes. • mean($\lvert X[k]\rvert$): The arithmetic mean of the magnitudes.	[dimensionless]
Spectral Roll-off (SR)	the frequency below which a fixed percentage (85 %) of the total power of the AE signal spectrum is contained. It is defined as the frequency f_r satisfying $\sum_{k=0}^{k_r} \lvert X[k]\rvert^2 \geq 0.85 \sum_{k=0}^{N-1} \lvert X[k]\rvert^2$ • $\lvert X[k]\rvert^2$: The energy at frequency bin k. • f_r: The frequency corresponding to the roll-off point. • N: The total number of frequency bins.	[Hz]
Harmonic-to-Noise Ratio (HNR)	$HNR = 10 \log_{10} \left(\frac{P_h}{P_n} \right)$ • $P_h = \sum_{k \in \text{harmonic}} \lvert X[k]\rvert^2$: The total power of the harmonic components. • $P_n = \sum_{k \in \text{noise}} \lvert X[k]\rvert^2$: The total power of the noise components.	[dimensionless]
Spectral Entropy (SE)	$SE = -\sum_{k=0}^{N-1} p_k \log(p_k)$ where $p_k = \frac{\lvert X[k]\rvert^2}{\sum_{j=0}^{N-1} \lvert X[j]\rvert^2}$: normalized power spectrum	[dimensionless]

The uncertainty in the measurements during the impact test is considered Type A. Therefore, only the mean and the sample standard deviation were calculated. The next step is to calculate the combined uncertainty by combining Type A and Type B uncertainties using Equation (A.7). Finally, the expanded uncertainty can be obtained using Equation (A.7), assuming that each feature follows a normal distribution and a 2σ confidence level.

For each sensor, many features were unable to capture the degradation trend caused by successive impacts. Figure 6.1 presents the mean value of the feature duration and its uncertainty range for the baseline of the WD sensor. The blue error bars represent the mean and uncertainty range of the measurements after each impact. It can be concluded that duration is a feature that did not vary with sensor degradation, as all measurements remained within the baseline uncertainty range. Therefore, this feature was not considered for use as a verification criterion. Similarly, many other features were also excluded because they did not reflect the degradation process of the sensors.

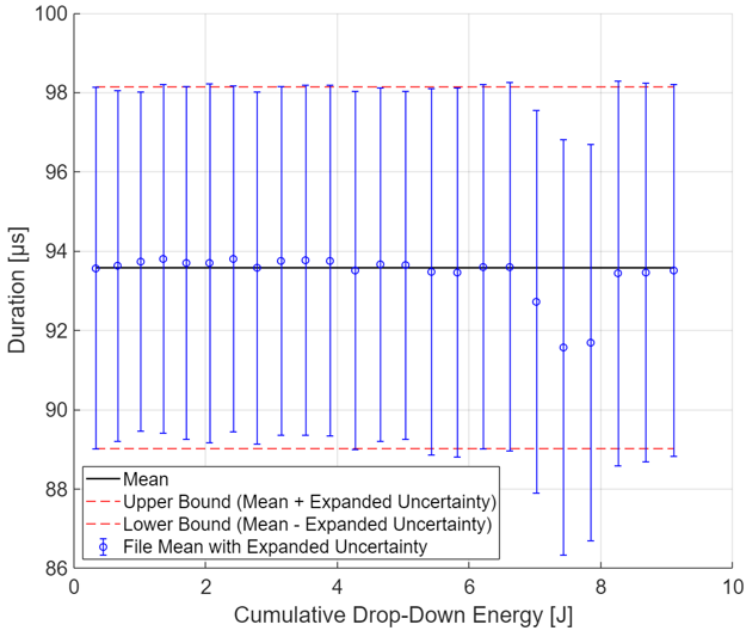

Figure 6.1: Mean and expanded uncertainty values of the baseline and of the measurements after each impact of the WD sensor.

6.1 WD Sensor

In total, 18 features were able to capture the degradation process for the WD sensor. Figure 6.2 presents a graph of the cumulative drop-down energy at the point when each feature first exceeds the uncertainty range. Considering all 18 features, the mean drop-down energy at which the measurements first exceeded the baseline uncertainty is 4.32 J. The first feature to exceed this limit was the skewness value, at 1.36 J.

Figure 6.3a shows the mean and expanded uncertainties of the baseline and the measurements after each impact for the skewness value. For illustration, the features amplitude, RMS values, and partial power 1 are plotted in Figures 6.3b, 6.3c, and 6.3d,

respectively. These plots define the criteria for verifying an AE sensor, establishing three levels of degradation:

- Deviation level 1: Minor deviation from the baseline, indicating light degradation. This corresponds to measurements exceeding the baseline uncertainty but remaining within ±2.5 times the expanded uncertainty of the baseline.

- Deviation level 2: Moderate deviation from the baseline, indicating moderate degradation. This corresponds to measurements exceeding ±2.5 times but remaining below ±7 times the expanded uncertainty of the baseline.

- Deviation level 3: High deviation from the baseline, indicating severe degradation. This corresponds to measurements exceeding ±7 times the expanded uncertainty of the baseline.

When a measurement falls outside the defined uncertainty range, the sensor is considered not approved.

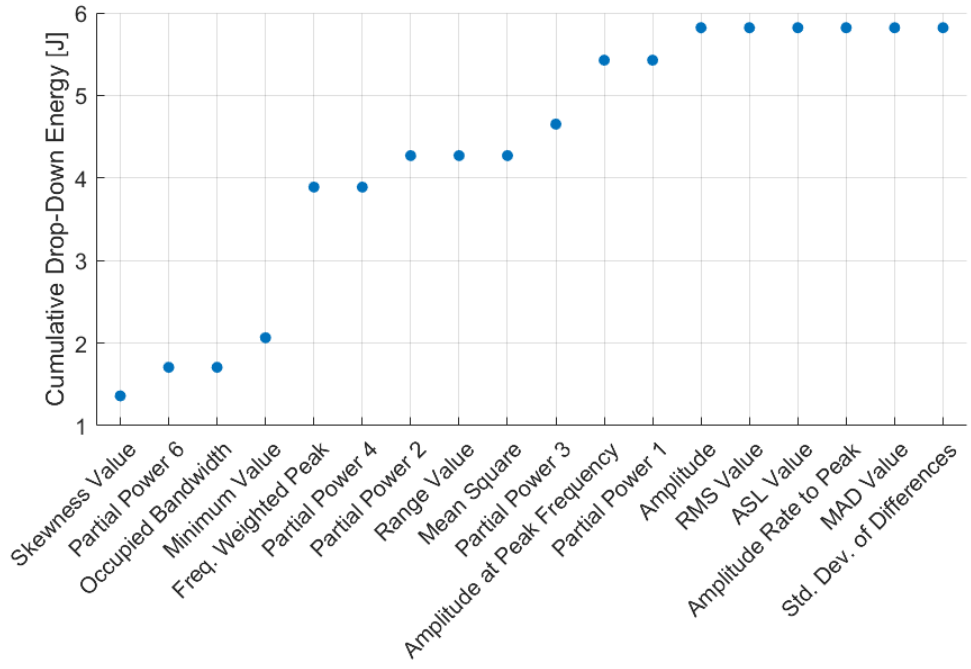

Figure 6.2: Cumulative drop-down energy at which each feature first exceeds the uncertainty range of the WD sensor baseline.

As can be noticed, although the skewness value was the first to exceed the limits of uncertainty, as the impact test continued, it started to show measurements withing the range of uncertainty slightly before 6 J. At that point, however, many other features were

showing values outside the range of uncertainty, such as the amplitude, RMS, and partial power 1. Figure 6.4 presents a graph of the number of features outside the uncertainty limits, showing a growing trend with increasing cumulative drop-down energy. After the first feature exceeded the uncertainty, there were a minimum of two features outside the range of uncertainty.

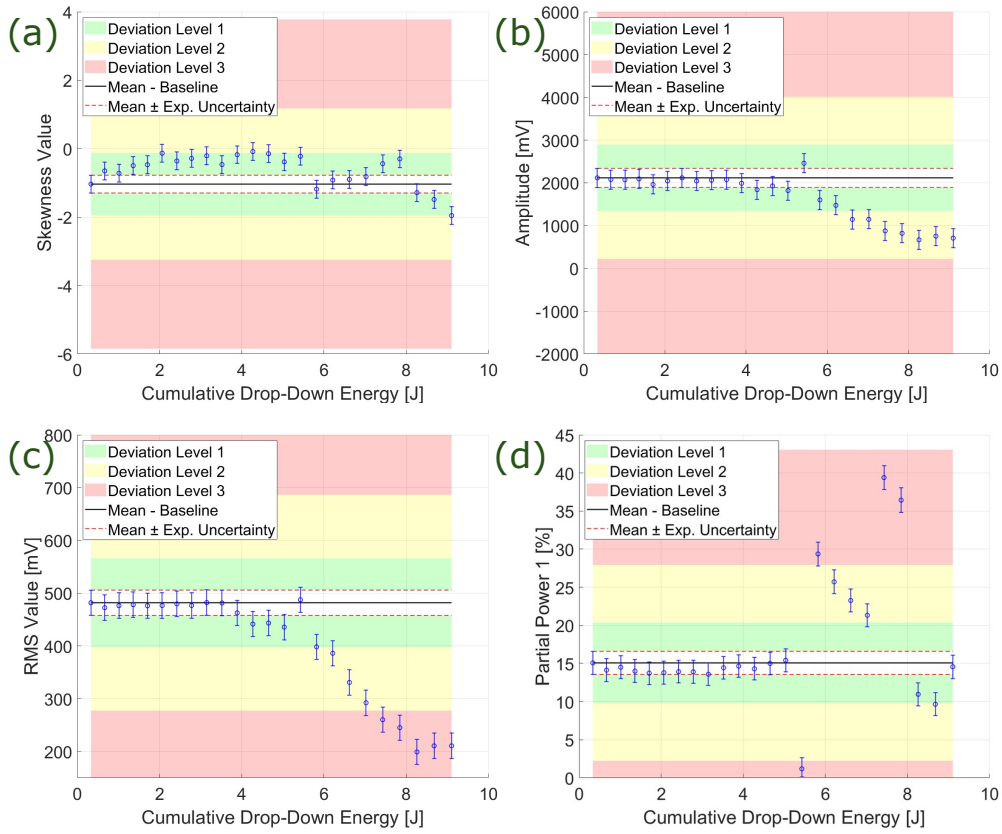

Figure 6.3: Mean and expanded uncertainty values of the baseline and of the measurements after each impact for the WD sensor. (a) Skewness value. (b) Amplitude. (c) RMS value. (d) Partial power 1.

Table 6.2 presents the absolute expanded uncertainty values for the 18 features in the second column, and the relative expanded uncertainty in the third column. The relative expanded uncertainty was calculated using Equation A.8 and can be used to compare the results with other verification devices, serving as a general guide for industry.

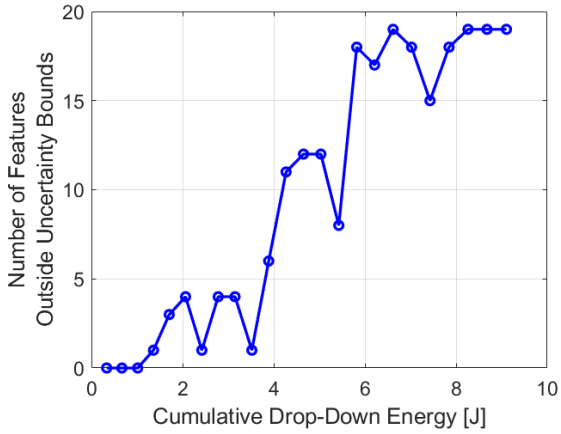

Figure 6.4: Number of features outside the uncertainty bounds of the baseline vs. cumulative drop-down energy for the WD sensor.

Table 6.2: Expanded and relative expanded uncertainties of the selected features for the WD sensor.

Feature	Expanded Uncertainty	Relative Expanded Uncertainty [%]
Amplitude [mV]	222.85	10.53
RMS Value [mV]	24.0	4.99
ASL Value [mV]	9.2	5.04
Amplitude Rate to Peak [V/s]	2751610.4	10.67
Amplitude at Peak Frequency [mV]	10.30	5.85
Freq. Weighted Peak [kHz]	45.8	6.65
Partial Power 1 [%]	1.5119	10.02
Partial Power 2 [%]	1.6954	4.98
Partial Power 3 [%]	2.6682	6.55
Partial Power 4 [%]	0.1935	18.94
Partial Power 6 [%]	0.0615	18.20
Minimum Value [mV]	138.7	4.74
Range Value [mV]	352.0	6.98
Skewness Value	0.26	25.11
MAD Value [mV]	10.12	5.42
Std. Dev. of Differences [mV]	3.0	7.12
Mean Square [mV^2]	16684.9	7.19
Occupied Bandwidth [kHz]	286.6	16.64

6.2 VS900-M Sensor

Figure 6.5 presents the graph of the cumulative drop-down energy at each feature first exceeds the uncertainty range for the VS900-M sensor. In this case, there were six features that showed early deviation: amplitude, RMS value, Amplitude Rate to Peak, Amplitude at Peak Frequency, range, and standard deviation of differences. The VS900-M sensor showed more features that were able to capture the degradation trend of the sensor. The average cumulative drop-down energy for early deviation, considering all features, is 7.21 J, and the cumulative drop-down energy for the features that showed early deviation is 0.94 J.

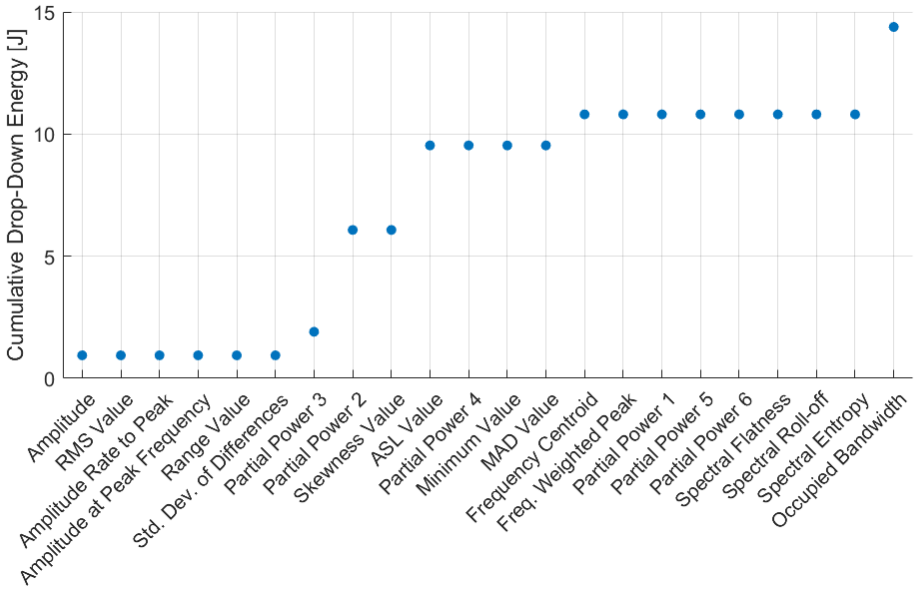

Figure 6.5: Cumulative drop-down energy at which each feature first exceeds the uncertainty range of the baseline: VS900-M sensor.

Figure 6.6 presents some features that showed early deviation with the same degradation trend, such as the amplitude, RMS value, range, and standard deviation of the differences. Although some features show the same degradation trend, each feature has its own magnitude values and sensitivity to impact, so that, for a more robust assessment of the condition of the sensor, all the features that are able to show the degradation process are kept. Figure 6.7 presents the number of features outside the uncertainty limits as a function of the cumulative drop-down energy, where it can be observed that at least one feature was outside the limits above 5 J.

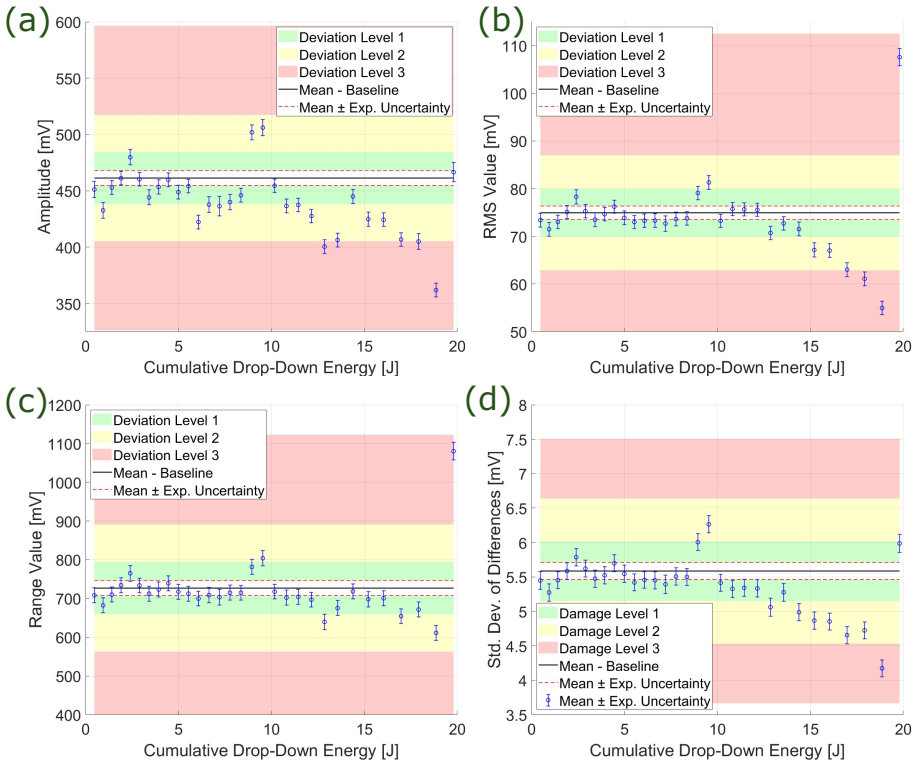

Figure 6.6: Mean and expanded uncertainty values of the baseline and of the measurements after each impact for the VS900-M sensor. (a) Amplitude. (b) RMS Value. (c) Range Value. (d) Standard deviation of the differences.

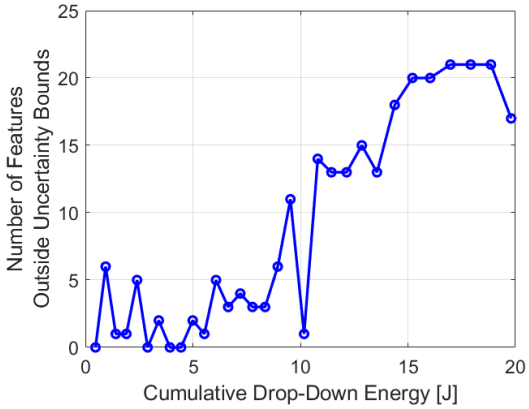

Figure 6.7: Number of features outside the uncertainty bounds of the baseline vs. cumulative drop-down energy for the VS900-M sensor.

Table 6.3 presents the absolute expanded uncertainty values for 22 features and the

relative expanded uncertainty. In general, it can be observed that the uncertainties of the VS900-M sensor are lower than those of the WD sensor. This is more evident when comparing the relative expanded uncertainties. The reason for this can be partially explained by the fact that the improved coupling mechanism was used for the VS900-M and the 3D-printed coupling mechanism was used for the WD sensor.

Table 6.3: Expanded and relative expanded uncertainties of the selected features for the VS900-M sensor.

Feature	Expanded Uncertainty	Relative Expanded Uncertainty [%]
Amplitude [mV]	6.5	1.43
RMS Value [mV]	1.4	1.89
ASL Value [mV]	0.9	3.23
Amplitude Rate to Peak [V/s]	68827.1	1.38
Amplitude at Peak Frequency [mV]	291.2	1.00
Frequency Centroid [kHz]	136.8	14.70
Freq. Weighted Peak [kHz]	33.1	8.59
Partial Power 1 [%]	1.1590	3.91
Partial Power 2 [%]	1.4801	3.87
Partial Power 3 [%]	0.2984	1.38
Partial Power 4 [%]	0.1197	11.66
Partial Power 5 [%]	0.0803	31.81
Partial Power 6 [%]	0.0338	35.95
Minimum Value [mV]	15.7	5.93
Range Value [mV]	19.3	2.66
Skewness Value	0.08	4.35
MAD Value [mV]	0.9	3.03
Std. Dev. of Differences [mV]	0.1	2.22
Occupied Bandwidth [kHz]	132.9	19.65
Spectral Flatness	0.04	18.53
Spectral Roll-off [kHz]	303.5	21.87
Spectral Entropy	0.17	3.66

6.3 VS30-V Sensor

Figure 6.8 presents the graph of the cumulative drop-down energy at which each feature first exceeds the uncertainty range for the VS30-V sensor. In this case, the majority of the features were able to show early deviation. The average cumulative drop-down energy for early deviation, considering all features, is 0.38 J, and the cumulative drop-down energy for the features that showed early deviation is 0.36 J.

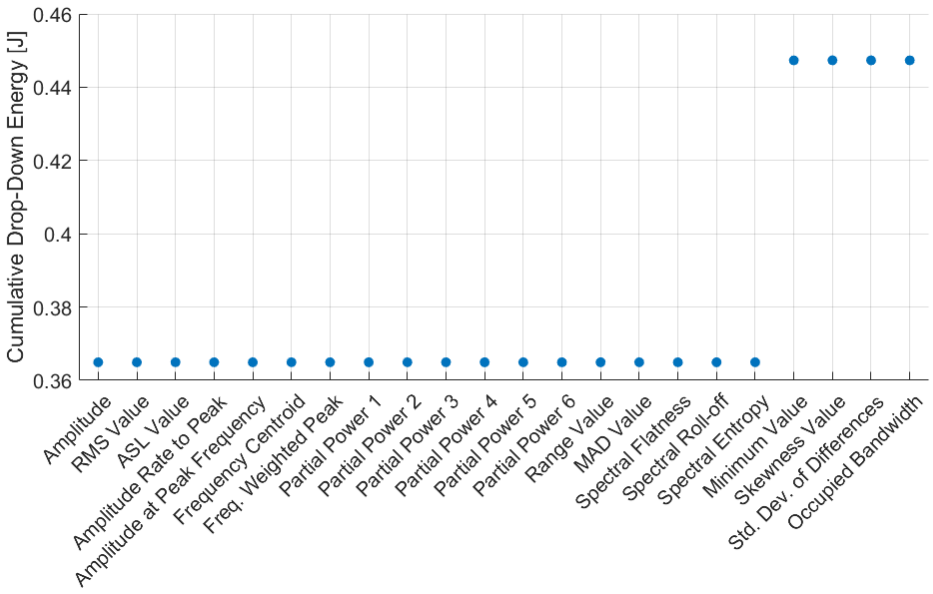

Figure 6.8: Cumulative drop-down energy at which each feature first lands outside the uncertainty range of the baseline: VS30-V sensor.

As an illustration, Figure 6.9 presents several features that showed early deviation from the baseline. It is important to note that the amplitude and ASL values exhibited very similar degradation trends. Similarly, the RMS, range, and standard deviation of the differences showed comparable trends for the VS900-M sensor, while amplitude and RMS showed similar trends for the WD sensor. Although not all are shown, many features display comparable degradation patterns. However, each feature has its own sensitivity; therefore, for a more conservative approach, all features capable of capturing the degradation trend are retained.

Figure 6.10 shows the number of features outside the uncertainty bounds as a function of the cumulative drop-down energy. It can be observed that up to approximately 2.1 J, all features remain within the baseline uncertainty bounds. This initial instability is also reflected in the uncertainty plots of the WD and VS900-M sensors and has been previously reported in the literature [134].

Table 6.4 presents the absolute expanded uncertainty values for all 22 features, along with the relative expanded uncertainty. The VS30-V sensor exhibited the same number of features capable of capturing the degradation trend as the VS900-M sensor.

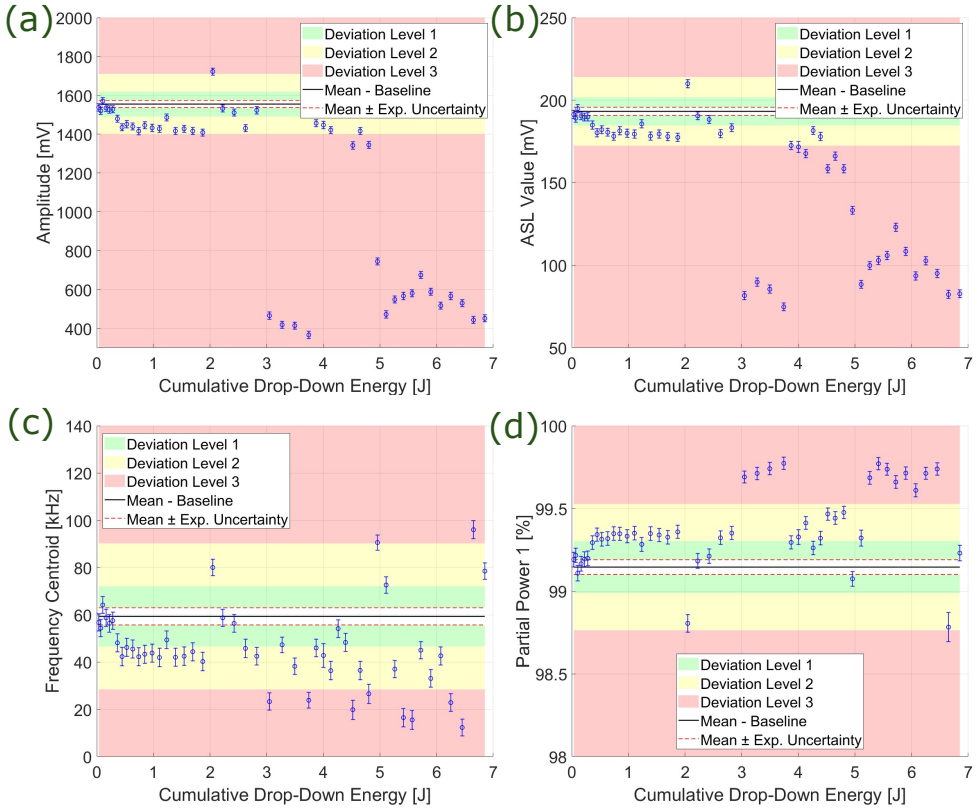

Figure 6.9: Mean and expanded uncertainty values of the baseline and of the measurements after each impact for the VS30-V sensor. (a) Amplitude. (b) ASL value. (c) Frequency Centroid. (d) Partial Power 1.

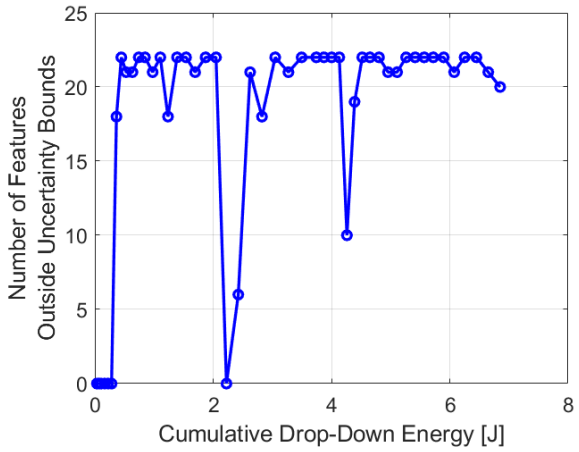

Figure 6.10: Number of features outside the uncertainty bounds of the baseline vs. cumulative drop-down energy for the VS30-V sensor.

The uncertainties in the measurements are smaller than those of the WD sensor, and this can be explained, to some extent, by the fact that this sensor was also tested using the improved coupling mechanism.

Table 6.4: Expanded and relative expanded uncertainties of the selected features for the VS30-V sensor.

Feature	Expanded Uncertainty	Relative Expanded Uncertainty [%]
Amplitude [mV]	18.4	4.00
RMS Value [mV]	4.7	6.29
ASL Value [mV]	2.4	8.36
Inverse Rise Slope [V/s]	178318.1	3.57
Amplitude at Peak Frequency [mV]	3.4	11.70
Frequency Centroid [kHz]	42.1	4.53
Freq. Weighted Peak [kHz]	8.2	2.14
Partial Power 1 [%]	0.4073	1.37
Partial Power 2 [%]	0.4597	1.20
Partial Power 3 [%]	0.2505	1.16
Partial Power 4 [%]	0.0362	3.53
Partial Power 5 [%]	0.0171	6.81
Partial Power 6 [%]	0.0089	9.50
Minimum Value [mV]	19.7	7.42
Range Value [mV]	36.9	5.08
Skewness Value	0.03	1.52
MAD Value [mV]	2.3	7.50
Std. Dev. of Differences [mV]	0.09	1.78
Bandwidth [kHz]	41.2	6.09
Spectral Flatness	0.01	5.34
Spectral Roll-off [kHz]	137.1	9.89
Spectral Entropy	0.06	1.36

6.4 Self Verification Criteria of the Mobile Verification Setup

Table 6.5 presents the absolute expanded uncertainty values for 28 features in the second column, and the relative expanded uncertainty in the third column for the measurement of the baseline of the receiver transducer.

Table 6.5: Expanded and relative expanded uncertainties of the selected features for the receiver transducer of the mobile verification device.

Feature	Expanded Uncertainty	Relative Expanded Uncertainty [%]
Amplitude [mV]	207.1	4.78
RMS Value [mV]	67.0	4.57
ASL Value [mV]	34.5	4.50
Amplitude Rate to Peak [V/s]	1855309.7	4.73
Frequency Peak Value [Hz]	61300.1	4.60
Frequency Centroid [Hz]	32904.8	12.79
Freq. Weighted Peak [Hz]	8365.713571	7.27
Partial Power 1 [%]	0.0435	0.04
Partial Power 2 [%]	0.0387	5.89
Partial Power 3 [%]	0.0030	8.78
Partial Power 4 [%]	0.0005	21.94
Partial Power 5 [%]	0.0007	23.77
Partial Power 6 [%]	0.0002	29.78
Minimum Value [mV]	203.6	4.52
Range Value [mV]	410.1	4.64
Skewness Value	0.01	54.45
MAD Value [mV]	36.4	4.50
Std. Dev. of Differences [mV]	1.0	4.60
Bandwidth [Hz]	1695.1	1.06
Spectral Flatness	0.01	17.22
Spectral Roll-off [Hz]	12000.2	7.76
Spectral Entropy	0.06	2.13

As the mobile verification device is intended to be used to verify AE sensors after its validation, and it is possible that it will be used for more investigations, degradation of any kind was not imposed on it to assess the behavior of the features. However, Table 6.5 presents reference uncertainty values that can be used as criteria. If one of the features is outside the uncertainty range, the mobile verification device auto-check must be considered not approved. The same applies to sensors, where the corresponding table of uncertainties must be used.

Chapter 7

Discussion, Conclusion and Future Work

7.1 Design of the Mobile Verification Device

In Chapter 3, the mobile verification device was introduced, where its components were presented in detail, including details of the design and assembly. The operation of the device is divided into two steps, the setup auto-check and the sensor verification. The setup auto-check is a preliminary step intended to avoid a faulty assessment of the SUT. Two options of coupling mechanisms were proposed, a 3D-printed one and another made of metallic components. Both coupling mechanisms have features that allow the sensor to couple at the same position and with the same orientation. This proved to be relevant for decreasing the variation among the measurements as discussed in Section 4.3, and, as can be noticed in Figures 4.2a and 4.2d, different sensor orientations produce different signal time series.

Approximately 300 waveform measurements were found to be sufficient to stabilize the experimental standard error of the mean, considering the amplitude and the mobile verification device auto-check. However, 600 measurements were chosen for a more robust statistical analysis for both the setup auto-check and the sensor verification. The data of each measurement were processed before any assessment of the setup and sensor conditions. The data processing is described in Section 3.4, where the measuring data were converted to CSV file format and then the first and last waveforms were deleted, and the cross-correlation filter was applied. Then, the features are computed for each individual waveform. Afterward, statistics such as mean and standard deviation are computed for each feature. Table 6.1 contains all the features studied in this work. The majority of these features were found not to be suitable for sensor verification. The appropriate features for sensor verification can be found in Tables 6.2, 6.3, and 6.4.

7.2 Qualification of the Mobile Verification Device

In Chapter 4 several tests were performed to validate the device. With the angle sensitivity test it was possible to establish which manufactured transducer would play the role of transmitter and receiver, as well as their orientation on the plate. One of the transducers showed a drastic decrease in sensitivity in one of the angle orientations as a result of a manufacturing problem with the wear plate. This was not a problem, since this transducer was chosen as the receiver, and it was placed on the plate with its most sensitive angle facing the transmitter transducer.

From the assembly test, where an assembly procedure for the aluminum frames was proposed. From the assembly test, it can be concluded that the propagation medium can be assembled multiple times, which is a relevant feature if sensor verification must be performed on different materials. However, more tests with different plate materials must be performed to fully confirm this hypothesis. A possible future work is to check whether plates made of the same material with very close mechanical properties can produce similar results. This could be of interest in case that a plate in use is accidentally damaged, and a backup plate can be used as a replacement.

The effect of operators was examined in the human-reproducibility test, in which six individuals performed measurements using both the mobile verification device and the benchmark verification device. The measurements obtained by the receiver of the mobile verification device proved to be the most reproducible, showing a minimum normalized cross-correlation of 0.9994, followed by the SUT measurements of the benchmark device, which showed a minimum normalized cross-correlation of 0.9977. The lowest reproducibility was observed for the SUT measurements performed with the mobile verification device, which resulted in a minimum normalized cross-correlation of 0.9800.

The high reproducibility of the receiver transducer is attributed to its coupling mechanism, which allows the transducer to couple to the propagation medium at the same position and with the same orientation each time. The SUT coupling mechanism of the benchmark verification device also ensures consistent positioning, but it does not ensure the same sensor orientation. The 3D-printed SUT coupling mechanism of the mobile verification device produced the least reproducible results, despite also constraining the sensor position and orientation. This reduced reproducibility is primarily due to its construction: the mechanism is made almost entirely from 3D-printed carbon-reinforced polymer components, a manufacturing process that cannot guarantee the tight tolerances for sliding parts. As a result, the distance between the SUT and the transmitter transducer varies between measurements. Moreover, the sensor must fit loosely inside the adapter to allow easy insertion and removal, which introduces additional variability in the measurements.

As the SUT 3D-printed coupling mechanism showed lower performance than the others, it was improved and a new version made of metallic components was built and investigated. This new version with sliding bushings showed better performance than the original bush-

ings and 3D-printed versions, having less variation for each individual test and among the tests, as shown in Figure 4.14. Although the 3D-printed coupling mechanism performed the worst, its minimum normalized cross-correlation values were not much inferior to the other mechanisms, making this device an attractive solution in terms of costs.

Settlement tests were performed for several sensors, consisting of applying the coupling agent on the sensor and starting the measurement right after it was coupled to the propagation medium. In the worst-case scenario, which corresponds to the WD sensor, a variation of the maximum amplitude for each waveform of approximately 80 % was observed. After 400 seconds, all sensors started to show a monotonic behavior, indicating settling in the measurements. It is fundamental to consider the settling behavior of each sensor before making the measurements that will be used for verification.

Environmental tests were performed with respect to temperature and humidity to characterize the behavior of the mobile verification device. First, a preliminary climate test was performed to establish the thermal accommodation time. The behavior of the mobile verification device was characterized for temperatures ranging from -10 °C to 45 °C. The pulses were generated by the transmitter transducer and measured by the receiver transducer of the mobile verification device. It was observed that there was an increasing trend in amplitude with temperature. The frequency spectrum response due to the temperature variation was also studied, showing an increasing trend of maximum FFT magnitude with increasing temperatures. This can be explained by the fact that, with increasing temperatures, the propagation medium loses stiffness, causing oscillations with higher amplitudes. This is in agreement with a similar study already reported [145]. The peak frequency showed a decreasing trend with increasing temperatures, which is also related to the loss of stiffness.

The behavior of the mobile verification device was also studied under the variation in relative humidity from 0 % RH to 100 % RH, keeping the temperature constant at 25 °C. The measurements of the pulses were also performed. A small variation of 1.5 % in the maximum amplitude was observed for the range from 40 % RH to 100 % RH, indicating that RH has a small influence on the mobile verification device. After the climate chamber tests, the measurements of the mobile verification device were compared with the measurements before the climate chamber test, and the results indicate that it remains stable after a wide range of temperature and RH variations.

Climate chamber tests for several AE sensors were also performed. An advantage of the mobile verification device is its dimensions and weight, allowing it to fit in a climate chamber and characterize the response of the sensors at different temperatures. Similarly to the mobile verification device, the temperature was varied from -10 °C to 45 °C for the sensors: WD, VS150-M, VS900-M, and VS150-RSC, and from -5 °C to 45 °C for the VS30-V sensor.

The WD sensor showed a behavior similar to that of the receiver transducer of the mobile verification device, where the maximum wave amplitudes and the maximum FFT magnitude increased with increasing temperatures. The WD sensor also showed a de-

creasing trend in amplitude at peak frequency with increasing temperature. The frequency spectrum of the WD sensor was compared with the sensitivity chart provided by the sensor manufacturer, and it shows some similar features.

The VS30-V also showed similar behavior, where the maximum wave amplitudes and the maximum FFT magnitude showed an increasing trend with increasing temperatures. However, the peak frequency showed a distinct trend, increasing up to 10 °C, then remaining stable up to 25 °C, then decreasing at 30 °C and remaining stable. The resulting frequency spectrum showed a narrow response, which was aligned with the sensor datasheet. The highest sensitivity of the sensor was around 55 kHz, which is also in agreement with the sensor datasheet.

The VS150-M was one of the sensors that showed less variation in the measurements for both the amplitude and FFT magnitude. Another relevant observation is that the frequency spectrum obtained with the mobile verification device has several identical features to the sensitivity chart provided by the sensor manufacturer, such as the resonances and anti-resonances.

The VS900-M also showed good agreement between the frequency spectrum obtained by the mobile verification device and the sensitivity chart provided by the sensor manufacturer, matching resonances and anti-resonances.

The VS150-RSC sensor showed a very distinct maximum amplitude trend, showing decreasing maximum amplitudes with increasing temperatures. One possible explanation for this can be the fact that this sensor has a built-in amplifier, and its inner electronic circuit could counteract the response of the piezoelectric ceramic. The maximum FFT magnitude also showed a decreasing trend with temperature, and the peak frequency showed a very stable behavior. The frequency spectrum obtained by the mobile verification device had a few characteristics that were also present in the sensitivity chart provided by the sensor manufacturer.

7.3 Validation of the Mobile Verification Device

The validation of the mobile verification device consisted of the gradual degradation of the WD, VS30-V, and VS900-M sensors by impact. Therefore, the ball drop device was constructed in such a way that the height of impact could be adjusted by adding tubes on top of each other. The sensors were impacted by a steel ball with a mass of 24 g. This weight was chosen because it is approximately the weight of the WD sensor, simulating a sensor drop-down event. The ball drop device allows the sensor to be impacted at the same lateral point on the sensor, making the impacts reproducible.

The first objective of the impact test is to assess the performance of the mobile verification device compared to the benchmark verification device. The benchmark verification device was constructed by taking into account the requirements of the DGZfP SE-02 stan-

dard for AE sensor verification. It consists of an aluminum block with a PZT transducer at the bottom and a sensor holder on top. The second objective of the impact test is to establish verification criteria for AE sensors based on experimental tests.

The first sensor to be gradually degraded was the WD sensor. After each impact, the sensor response was measured by both the mobile and benchmark verification devices. The measured waveforms before and after the impact test for the mobile and benchmark verification devices, as well as their respective frequency spectra, underwent significant changes, both showing a drastic decrease in magnitude. From the RMS value versus the cumulative drop-down energy graph of Figure 5.4, it can be observed that the mobile verification device detected the change in trend of the RMS values first, after 3.5 J. Although the benchmark verification device detected the change in trend later, it showed a more aggressive drop in RMS values, indicating more sensitive behavior. The impact-induced damage to the WD sensor was characterized by scanning acoustic microscopy, as shown in Figures 5.5a and b, where the inner piezoelectric disk was detached from the wear plate and the outer piezoelectric ring was partially detached.

The second sensor damaged by the impact test was the VS900-M. The graph of the RMS value versus the cumulative drop-down energy showed a decreasing trend after 12 J. However, the benchmark device showed a more drastic decrease. The last measurement before the sensor was completely damaged showed a significant increase in value for the mobile verification device and a significant decrease in value for the benchmark verification device. The possible reasons could be that the mobile and benchmark verification devices operate with different types of waves. The mobile verification device operates with Lamb waves, and the benchmark verification device operates with longitudinal waves. It is possible that in the final stage of damage, the Lamb wave was more sensitive than the longitudinal wave. Another explanation could be the loss or increase in electrical contact within the sensor, which would have a significant impact on the sensor response. The impact-induced damage was also characterized, in this case by X-ray inspection, as shown in Figures 5.9a and 5.9b, where the piezoelectric disk was broken into multiple pieces.

The final sensor to be degraded was the VS30-V. The measurements of both mobile and benchmark verification devices showed a drastic decrease in signal strength and frequency content after the impact test. The graph of the RMS value versus the cumulative drop-down energy showed a distinct behavior compared to the other sensors, where the RMS value decreased drastically and then recovered with increasing impact number, as can be observed in Figure 5.12. This behavior was also noticed in the measurements performed by the benchmark verification device. As mentioned, this sensor started to show degradation in its measurements after around 2.5 J of cumulative drop-down energy, making it the one that showed the earliest deviation. This can also be explained by its design, similar to that shown in Figure 2.5b. This sensor has a large backing mass/piezoelectric element that can magnify the stress at the interface between the metallic membrane and the piezoelectric element caused by impact. Unfortunately, it was not possible to characterize the damage in the sensor by imaging, either by X-ray or by SAM.

With the impact test, it was possible to assess the performance of the mobile verifi-

cation device in the detection of the degradation of the AE sensors and to compare its performance with the benchmark verification device. It can be concluded that the mobile verification device showed a performance similar to that of the benchmark verification device. Although the mobile verification device showed less sensitive behavior, it was able to detect the change in trend in the measurements first for the WD sensor and at approximately the same point for the other sensors.

7.4 Evaluation Criteria

Chapter 6 presented the evaluation criteria for three distinct AE sensors that were subjected to gradual degradation. It also presented the evaluation criteria for the mobile verification device. The criteria are based on the uncertainty limits, which represent the condition of the sensor in an undamaged state. If the current measurement of an AE sensor or the mobile verification device auto-check feature is outside the range of uncertainty compared with the reference value, the sensor or the device should be considered not approved. In this sense, three deviation levels were established for the degraded sensors. Deviation level 1 consists of measurements that lie outside the uncertainty up to two-and-a-half times the expanded uncertainty of the baseline. Deviation level 2 consists of measurements that lie outside deviation level 1 up to seven times the expanded uncertainty, indicating moderate damage. Deviation level 3 consists of measurements that lie outside deviation level 2, indicating severe damage.

It is important to mention that of the original 46 investigated features, only 18 features were able to capture the degradation progress of the WD sensor; therefore, the other features were not used in the verification criteria. For the VS900-M and VS30-V sensors, 22 features were able to capture the degradation progress of the sensors, and this difference in feature numbers can be explained, to some extent, by the fact that the WD sensor has a different design from the VS900-M and VS30-V sensors. Among the sensors, the VS900-M was the one that showed greater tolerance to impact, with the average cumulative drop-down energy of the features outside the uncertainty limits being the highest, 7.15 J, followed by the WD sensor at 4.19 J, and the VS30-V showing the lowest value of 0.41 J.

As observed in this study and as reported in previous work [134], the sensors can show unstable behavior such that it is possible that one sensor can pass the verification test and then fail later. Therefore, it is important to keep track of the sensor test results and not use sensors that have once failed the verification test in a high-responsibility AE test or in tests that require a long duration. For instance, a sensor that shows deviation level 1 could be still used to detect leakage in non-critical valves or to determine the wave velocity in a test specimen.

Tables from 6.2 to 6.5 present the reference values for the evaluation criteria of the WD, VS900-M, VS30-V, and the mobile verification device, respectively. Overall, the uncertainty values of the WD sensor are higher than those of the other sensors because the 3D-printed coupling mechanism was used to perform the measurements of this sensor,

which showed more variation in the measurements. The VS900-M and VS30-V measurements were performed with the improved coupling mechanism, which likely improved the variation in the measurements.

Possible future work for the mobile verification device could consider increasing the number of damaged sensors already investigated in this work, as well as including new sensor types. This could contribute to a more robust assessment of the mobile verification device and more robust verification criteria for AE sensors.

Another possible future work is to study the possibility that the mobile verification device can also perform sensor calibration, since it has a receiver transducer that could work as a reference sensor if the receiver is absolutely calibrated. Another aspect that reinforce this possibility is the fact that the measurements of the mobile verification device showed very similar features compared to the sensitivity chart of the sensors' manufacturer.

As the mobile verification device measurements are strongly influenced by temperature, another future work could be to find a methodology to compensate for the influence of temperature.

A possible point for improvement in the design of the mobile verification device is to find a means to increase the automation level. In this sense, a robotic automation approach could be advantageous in improving efficiency and reliability.

List of Figures

List of Tables

Glossary

A Measured amplitude of the signal, such as voltage or sound pressure level. 28

A_0 Fundamental antisymmetric Lamb wave mode. 51

$A_{\mathbf{ref}}$ Reference amplitude used as the baseline for calculating decibels. 28

$A_{\mathbf{freq}}$ Amplitude at Peak Frequency of the acoustic emission signal [V]. 92

C_L Longitudinal wave velocity in a homogeneous isotropic solid [m/s]. 7

C_R Rayleigh wave velocity [m/s]. 8, 9, 22

C_T Transverse (shear) wave velocity in a homogeneous isotropic solid [m/s]. 8

E Young's modulus [Pa]. 8

F_s Sampling frequency of the data acquisition system [Hz]. 94

G Shear modulus [Pa]. 8

H Entropy value of the acoustic emission signal [dimensionless]. 93

M Median value of the acoustic emission signal [V]. 93

N Total number of frequency bins in the discrete Fourier transform (DFT) of the acoustic emission signal. 95

N_{AE} Number of threshold crossings in an acoustic emission signal between the first crossing time t_0 and the last crossing time t_{term} [#]. 92

$N_{\mathbf{fall}}$ Number of threshold crossings after the peak till signal duration [#]. 93

$N_{\mathbf{peak}}$ Number of threshold crossings between t_0 and t_{peak} [#]. 92

P_e Pearson correlation coefficient [dimensionless]. 94

P_h Total power of the harmonic components of the acoustic emission signal spectrum. 95

P_n Total power of the noise components of the acoustic emission signal spectrum. 95

$P_{\mathbf{partial}}$ Partial power of the acoustic emission signal [%]. 93

Q_1 First quartile (25th percentile) of the signal amplitude distribution [V]. 93

Q_3 Third quartile (75th percentile) of the signal amplitude distribution [V]. 93

$R_{\mathbf{rang}}$ Range of the acoustic emission signal [V]. 93

$R_{xy}[k]$ Normalized cross-correlation function between two discrete signals $x[j]$ and $y[j]$ at lag k. 48

$S[k]$ Discrete Fourier Transform (DFT) of the acoustic emission signal at frequency index k. 94

S_0 Fundamental symmetric Lamb wave mode. 51

Vsc_i i-th value in the second dataset[V]. 94

Vst_i i-th value in the first dataset [V]. 94

W_{AE} Absolute energy of the acoustic emission signal [aJ]. 92

$W_{\mathbf{peak}}$ Weighted peak frequency of the acoustic emission signal. 92

$X[k]$ Discrete Fourier Transform (DFT) of the acoustic emission signal at frequency index k. 95

Δf Frequency bin width used in discrete spectral analysis [Hz]. 94

Δv_i Difference between consecutive signal amplitudes [V]. 94

α Fraction of the total spectral power used to define the occupied bandwidth [dimensionless]. 94

$\bar{Vsc}$ Mean value of the second dataset (Vsc) [V]. 94

$\bar{Vst}$ Mean value of the first dataset (Vst) [V]. 94

$\bar{v}$ Mean value of the acoustic emission signal [V]. 93

γ Skewness value of the acoustic emission signal [dimensionless]. 93

γ_2 Kurtosis value of the acoustic emission signal [dimensionless]. 93

$|X[k]|$ Magnitude of the DFT coefficient at index k. 95

$|X[k]|^2$ Energy content of the AE signal at frequency bin k, calculated as the squared magnitude of the DFT coefficient $|X[k]|^2$. 95

ν Poisson's ratio. 8

$\overline{\Delta v}$ Mean of the differences between consecutive signal samples [V]. 94

ϕ Diameter (aperture) of the acoustic emission sensor [m]. 9, 22

ρ Density of the material [kg/m^3]. 8

σ^2 Variance of the acoustic emission signal amplitude [V^2]. 94

$\sigma_{\Delta v}$ Standard deviation of the differences between consecutive samples of the acoustic emission signal [V]. 94

geomean($|X[k]|$) Geometric mean of the magnitudes of the DFT coefficients $|X[k]|$. 95

mean($|X[k]|$) Arithmetic mean of the magnitudes of the DFT coefficients $|X[k]|$. 95

$\varphi_{\mathbf{rise}}$ Amplitude rate to peak of the acoustic emission signal [V/s]. 92

f_1 Lower cutoff frequency of the AE signal spectrum used in the computation of the occupied bandwidth [Hz]. 94

f_r Roll-off frequency [Hz]. 95

$f_{\mathbf{aper}}$ Aperture frequency of an acoustic emission sensor. 22

$f_{\mathbf{avg}}$ Average frequency of the acoustic emission signal [Hz]. 92

$f_{\mathbf{centroid}}$ Frequency centroid of the acoustic emission signal [Hz]. 92

$f_{\mathbf{init}}$ Initiation frequency of the acoustic emission signal [Hz]. 92

$f_{\mathbf{peak}}$ Maximum peak frequency of the acoustic emission signal[Hz]. 92

$f_{\mathbf{rev}}$ Reverberation frequency of the acoustic emission signal [Hz]. 92

$f_{\mathbf{term}}$ Termination frequency of the acoustic emission signal [Hz] . 93

j Sample index representing the discrete time step of the signal. 48

n Number of discrete samples [#]. 92

p_k Normalized power spectrum of the acoustic emission signal [dimensionless]. 95

r_1 Autocorrelation coefficient at lag 1 [dimensionless]. 94

t_0 Time of the first threshold crossing in the acoustic emission signal [μs]. 92

t_{AE} Duration of the acoustic emission event [μs]. 92

$t_{\mathbf{fall}}$ Fall time of the acoustic emission signal [μs]. 93

$t_{\mathbf{peak}}$ Time at which the acoustic emission signal reaches its maximum amplitude within the event duration [μs]. 92

$t_{\mathbf{rise}}$ Rise time of the acoustic emission signal [μs]. 92

t_{term} Time of the last threshold crossing in the acoustic emission signal [μs]. 92

$v_{\max}$ Maximum amplitude of the acoustic emission signal [V]. 92

$v_{\min}$ Minimum amplitude value of the acoustic emission signal [V]. 93

$x[j]$ First discrete-time signal used in the cross-correlation computation. 48

$y[j]$ Second discrete-time signal used in the cross-correlation computation. 48

dB Value in decibels. 28

List of Acronyms

AE Acoustic Emission. 1

ASL Average Signal Level. 92

ASME American Society of Mechanical Engineers. 24

AST Auto Sensor Test. 6

ASTM American Society for Testing and Materials. 10

BNC Bayonet Neill–Concelman. 14

CFRP Carbon Fiber Reinforced Polymer. 36

DAQ Data Acquisition. 5

DGZfP Deutsche Gesellschaft für Zerstörungsfreie Prüfung. 33

EMAT Electromagnetic Acoustic Transducer. 13

EMI Electromechanical Impedance. 34

ESEM Experimental Standard Error of the Mean. 44

FBG Fiber Bragg Grating. 12

FEM Finite Element Method. 5

FET Field-Effect Transistor. 19

FFT Fast Fourier Transform. 25

GFRP Glass Fiber Reinforced Polymer. 36

HNR Harmonic-to-Noise Ratio. 95

ID Identification. 43

IQR Interquartile Range. 93

ISO International Organization for Standardization. 25

JCGM Joint Committee for Guides in Metrology. 24

MEMS Micro-Electromechanical Systems. 13

NDT Non-Destructive Testing. 9

NIST National Institute of Standards and Technology. 18

OBW Occupied Bandwidth. 94

PLB Pencil Lead Break. 5

PSD Power Spectral Density. 29

PTC Performance Test Code. 24

PTFE Polytetrafluoroethylene. 59

PVDF Polyvinylidene Fluoride. 19

PZT Lead Zirconate Titanate. 14

RMS Root Mean Square. 24

RS Reference Sensor. 30

SAM Scanning Acoustic Microscopy. 84

SE Spectral Entropy. 33, 95

SF Spectral Flatness. 95

SHM Structural Health Monitoring. 12, 13

SR Spectral Roll-off. 95

SUT Sensor Under Test. 25

TR Technical Report. 27

TRADB Transient Data Format. 47

UV Ultraviolet. 12

WD Wide-Band Differential. 20

Bibliography

[1] F. Saleem, Z. Ahmad, M. F. Siddique, M. Umar, and J.-M. Kim. Acoustic emission-based pipeline leak detection and size identification using a customized one-dimensional densenet. *Sensors*, 25(4):1112, 2025. URL: https://www.mdpi.com/1424-8220/25/4/1112, doi:10.3390/s25041112.

[2] J. F. Chen, H. S. Bi, Q. Wang, A. Q. Wang, H. Sheng, and H. X. Rong. The application of acoustic emission technology in oil and gas storage and transportation equipment. In *Environmental Protection and Resources Exploitation*, volume 807 of *Advanced Materials Research*, pages 2652–2657. Trans Tech Publications Ltd, 2013. URL: https://www.scientific.net/AMR.807-809.2652, doi:10.4028/www.scientific.net/AMR.807-809.2652.

[3] Y. Zhang, S. Xue, C. Chen, T. Ma, and B. Zhou. Study on acoustic emission characteristics and damage mechanism of wind turbine blade main spar with different defects. *Polymers*, 16(23):3261, 2024. URL: https://www.mdpi.com/2073-4360/16/23/3261, doi:10.3390/polym16233261.

[4] M. Fiedler, R. Xu, A. Lange, S. Marx, J. Ostermann, and T. Betz. Wire break detection in hybrid towers of wind turbines: A novel application to monitor tendons using acoustic emission analysis. *Applied Sciences*, 15(4):2164, 2025. URL: https://www.mdpi.com/2076-3417/15/4/2164, doi:10.3390/app15042164.

[5] D. G. Aggelis et al. Acoustic emission. In M. G. R. Sause and E. Jasiūnienė, editors, *Structural Health Monitoring in Aerospace Applications*, pages 175–217. Springer, 2021. doi:10.1007/978-3-030-72192-3.

[6] ASTM E 1106 - 86. Standard Test Method for Primary Calibration of Acoustic Emission Sensors. Standard, American Society for Testing and Materials, West Conshohocken, USA, June 1998.

[7] ASTM E 1781 - 98. Standard Practice or Secondary Calibration of Acoustic Emission Sensors. Standard, American Society for Testing and Materials, West Conshohocken, USA, June 1998.

[8] ISO/TR 13115:2011 - Non-destructive testing - Methods for absolute calibration of acoustic emission transducers by the reciprocity technique. ISO Technical Report ISO/TR 13115:2011, International Organization for Standardization, Geneva, Switzerland, 2011. Available at: https://www.iso.org/standard/52268.html.

[9] ISO 12714:1999 Non-destructive testing - Acoustic emission inspection - Secondary calibration of acoustic emission sensors. ISO Technical Report ISO 12714:1999, International Organization for Standardization, Geneva, Switzerland, 2011. Available at: https://www.iso.org/standard/52268.html.

[10] ISO 12713:1998 Non-destructive testing - Acoustic emission inspection - Primary calibration of transducers. ISO Technical Report ISO 12713:1998, International Organization for Standardization, Geneva, Switzerland, 1998. Available at: https://www.iso.org/standard/52268.html.

[11] DGZfP SE 02. Verification of Sensors and Their Coupling in Laboratories. Standard, German Society for Non-Destructive Testing, Berlin, Germany, June 2014.

[12] ASTM E 976-05. Standard Guide for Determining the Reproducibility of Acoustic Emission Sensor Response. Standard, American Society for Testing and Materials, West Conshohocken, USA, June 2005.

[13] N. Hsu and F. Breckenridge. Characterization and calibration of acoustic emission sensors. *Materials Evaluation*, 39:60–68, 1981.

[14] M. Sause. Investigation of pencil-lead breaks as acoustic emission sources. *Journal of Acoustic Emission*, 29:184–196, 2011.

[15] M. Sause, M. A. Hamstad, and S. Horn. Finite element modeling of conical acoustic emission sensors and corresponding experiments. *Sensors and Actuators A: Physical*, 184:64–71, 2012. URL: `https://www.sciencedirect.com/science/article/pii/S0924424712004232`, `doi:10.1016/j.sna.2012.06.034`.

[16] S. Kalafat and M. Sause. Acoustic emission source localization by artificial neural networks. *Structural Health Monitoring*, 14(6):633–647, 2015. URL: `https://journals.sagepub.com/doi/10.1177/1475921715607408`, `doi:10.1177/1475921715607408`.

[17] S. Kalafat and M. Sause. Localization of acoustic emission sources in fiber composites using artificial neural networks. In *31st Conference of the European Working Group on Acoustic Emission (EWGAE)*, Augsburg, Germany, 2014. URL: `https://www.researchgate.net/publication/281295451`.

[18] Jackson Custodio, Gustavo Tiboni, Carlo Giuseppe Filippin, Glauco de Mello, and Nestor Carlos Moura. Alternativa à sapata de nielsen para a obtenção de fonte de sinal na determinação da reprodutibilidade da resposta de transdutor de emissão acústica. In *Anais do XXVIII Congresso Nacional de Ensaios Não Destrutivos e Inspeção (CONAEND & IEV)*, Brazil, 2009. Apresentado no 14° IEV – Conferência Internacional sobre Evaluación de Integridad y Extensión de Vida de Equipos Industriales.

[19] F. R. Breckenridge, T. M. Proctor, N. N. Hsu, S. E. Fick, and D. G. Eitzen. Progress in ultrasonic measurements research in 1990: Transient sources for acoustic emission work. In *International Acoustic Emission Symposium*, Japan, 1990. National Institute of Standards and Technology.

[20] T. Yan, P. Theobald, and B. E. Jones. A self-calibrating piezoelectric transducer with integral sensor for in situ energy calibration of acoustic emission. *NDT & E International*, 35(7):459–464, 2002. URL: https://www.sciencedirect.com/science/article/pii/S096386950200021X?via%3Dihub, doi:10.1016/S0963-8695(02)00021-X.

[21] T. Yan, P. Theobald, and B. E. Jones. A conical piezoelectric transducer with integral sensor as a self-calibrating acoustic emission energy source. *Ultrasonics*, 42(1–9):431–438, 2004. URL: https://www.sciencedirect.com/science/article/pii/S0041624X03002622?via%3Dihub, doi:10.1016/j.ultras.2003.12.039.

[22] M. Sause, S. Schmitt, and P. Potstada. Kontinuierliche und wiederkehrende prufung von schallemissionssensoren. In *21. Kolloquium Schallemission - Vortrag 24*, Fulda, Germany, 2017.

[23] A. Fernandes De Oliveira Junior, T. Schlech, and M. Sause. Studies on a mobile acoustic emission sensor verification device. In *Proceedings of the 36th Conference of the European Working Group on Acoustic Emission*, volume 29, Potsdam, Germany, 2024. URL: https://www.ndt.net/search/docs.php3?id=30240, doi:10.58286/30240.

[24] P. Finkel, J. R. Mitchell, and M. F. Carlos. Experimental study of "auto sensor test–self test mode" for acoustic emission system performance verification. *AIP Conference Proceedings*, 509(1):1995–2002, 2000. doi:10.1063/1.1291316.

[25] Vallen Systeme GmbH. *Acoustic Emission Sensors - Specification*. Schaeftlarner Weg 26a, D-82057 Icking, Germany, April 2017. Specifications are subject to change as product developments are made. URL: http://www.vallen.de/.

[26] MISTRAS Group Inc. *R15I-AST Acoustic Emission Sensor - Product Data Sheet*. 195 Clarksville Rd, Princeton Jct, NJ 08550, USA, 2013. Specifications are subject to change without notice. Includes NIST Calibration Certificate. URL: http://www.mistrasgroup.com.

[27] D. A. Hutchins, R. J. Dewhurst, S. B. Palmer, and C. B. Scruby. Laser generation as a standard acoustic source in metals. *Applied Physics Letters*, 38(9):677–679, May 1981. URL: https://pubs.aip.org/aip/apl/article-pdf/38/9/677/18443609/677_1_online.pdf, doi:10.1063/1.92476.

[28] K. Ono, H. Cho, and T. Matsuo. Transfer functions of acoustic emission sensors. *J. Acoust. Emiss.*, 26:72–90, 2008.

[29] H. Yalcinkaya and D. Ozevin. The design and calibration of particular geometry piezoelectric acoustic emission transducer for leak detection and localization. *Measurement Science and Technology*, 24(9):095103, 2013. URL: https://iopscience.iop.org/article/10.1088/0957-0233/24/9/095103, doi:10.1088/0957-0233/24/9/095103.

[30] K. Ono. New characterization methods of AE sensors. *Journal of Acoustic Emission*, 28:256–277, 2010.

[31] Y. Matsuda, H. Nakano, K. Muto, and S. Nagai. Calibration of acoustic emission sensors with laser-generated ultrasonic wave. *Journal of the Acoustical Society of Japan (E)*, 13(2):91–96, 1992. doi:10.1250/ast.13.91.

[32] S. J. Davies, C. Edwards, G. S. Taylor, and S. B. Palmer. Laser-generated ultrasound: Its properties, mechanisms and multifarious applications. *Journal of Physics D: Applied Physics*, 26(3):329, March 1993. URL: https://iopscience.iop.org/article/10.1088/0022-3727/26/3/001, doi:10.1088/0022-3727/26/3/001.

[33] B. S. Wu and G. C. McLaskey. Broadband calibration of acoustic emission and ultrasonic sensors from generalized ray theory and finite element models. *Journal of Nondestructive Evaluation*, 37:8, 2018. URL: https://link.springer.com/article/10.1007/s10921-018-0462-8, doi:10.1007/s10921-018-0462-8.

[34] G. C. McLaskey and S. D. Glaser. Hertzian impact: Experimental study of the force pulse and resulting stress waves. *The Journal of the Acoustical Society of America*, 128(3):1087–1096, September 2010. URL: https://pubs.aip.org/asa/jasa/article-pdf/128/3/1087/15291986/1087_1_online.pdf, doi:10.1121/1.3466847.

[35] The Japanese Society for Non-Destructive Inspection. *Practical Acoustic Emission Testing*. Springer, Tokyo, Japan, 1st edition, 2006.

[36] R. V. Goldstein, V. A. Gorodtsov, and D. S. Lisovenko. Rayleigh and love surface waves in isotropic media with negative poisson's ratio. *Mechanics of Solids*, 49(4):422–434, 2014.

[37] I. A. Viktorov. *Rayleigh and Lamb Waves: Physical Theory and Applications*. Springer, 2013. Reprint of the original 1st 1967 edition by Plenum Press, New York.

[38] P. V. Vinh and P. G. Malischewsky. On the Rayleigh wave speed in orthotropic elastic solids. *Meccanica*, 40(4–6):455–461, 2005. URL: https://link.springer.com/article/10.1007/s11012-005-1603-6, doi:10.1007/s11012-005-1603-6.

[39] A. Huber. The dispersion calculator: A free software for calculating dispersion curves of guided waves. In *Proceedings of the 20th World Conference on Non-Destructive Testing (WCNDT)*, volume 29, pages 1–17, Incheon, South Korea, May 2024. NDT.net. doi:10.58286/29894.

[40] J. Keprt and P. Benes. A comparison of ae sensor calibration methods. *Journal of Acoustic Emission*, 26:60–71, 2008. URL: https://www.ndt.net/?id=10882.

[41] T. J. Esward, P. D. Theobald, S. P. Dowson, and R. C. Preston. An investigation into the establishment and assessment of a test facility for the calibration of acoustic emission sensors. Technical Report CMAM 82, National Physical Laboratory, Teddington, Middlesex, UK, July 2002. URL: https://example.com.

[42] ASTM E 650 - 97. Standard Guide for Mounting Piezoelectric Acoustic Emission Sensors. Standard, American Society for Testing and Materials, West Conshohocken, USA, 2002.

[43] ASTM E 750 - 04. Standard Practice for Characterizing Acoustic Emission Instrumentation. Standard, American Society for Testing and Materials, West Conshohocken, USA, May 2002.

[44] P. D. Theobald. Optical calibration for both out-of-plane and in-plane displacement sensitivity of acoustic emission sensors. *Ultrasonics*, 49(8):623–627, 2009. URL: https://www.sciencedirect.com/science/article/pii/S0041624X09000304, doi:10.1016/j.ultras.2009.03.004.

[45] P. Theobald, B. Zeqiri, and J. Avison. Couplants and their influence on AE sensor sensitivity. *Journal of Acoustic Emission*, 2011. URL: https://www.ndt.net/?id=10884.

[46] R. Hill and S. M. A. El-Dardiry. A theory for optimization in the use of acoustic emission transducers. *The Journal of the Acoustical Society of America*, 67(2):673–682, February 1980. doi:10.1121/1.383893.

[47] C. Reinhardt, S. Priebe, and I. Mueller. The influence of coupling-specific parameters and structural parameters on the electromechanical impedance of acoustic emission sensors. *e-Journal of Nondestructive Testing*, 29, October 2024. doi:10.58286/30268.

[48] M. Sause. *In Situ Monitoring of Fiber-Reinforced Composites*, volume 242 of *Springer Series in Materials Science*. Springer, January 2016. doi:10.1007/978-3-319-30954-5.

[49] R. Xu, R. Beltran Gutierrez, M. Kading, A. Lange, S. Marx, and J. Ostermann. Frequency dependent amplitude response of different couplant materials for mounting piezoelectric sensors. *NDT & E International*, 141, November 2023. doi:10.1016/j.ndteint.2023.102993.

[50] O. Cervena and P. Hora. Analysis of the conical piezoelectric acoustic emission transducer. *Applied and Computational Mechanics*, 2:123–134, 2008. URL: https://www.researchgate.net/publication/242592735_Analysis_of_the_Conical_Piezoelectric_Acoustic_Emission_Transducer.

[51] M. J. Evans, J. R. Webster, and P. Cawley. Design of a self-calibrating simulated acoustic emission source. *Ultrasonics*, 37(8):589–594, 2000. URL: https://www.sciencedirect.com/science/article/pii/S0041624X99001109, doi:10.1016/S0041-624X(99)00110-9.

[52] H. Vallen. AE sensor sensitivity verification using a stimulated motion, verified by laservibrometry. In *Proceedings of the 33rd European Working Group on Acoustic Emission (EWGAE)*, Senlis, France, September 2018. URL: https://www.ndt.net/article/ewgae2018/papers/21.pdf.

[53] K. Ono, T. Hayashi, and H. Cho. Bar-wave calibration of acoustic emission sensors. *Applied Sciences*, 7(10):964, 2017. URL: https://www.mdpi.com/2076-3417/7/10/964, doi:10.3390/app7100964.

[54] K. Ono. Frequency dependence of receiving sensitivity of ultrasonic transducers and acoustic emission sensors. *Sensors*, 18(11):3861, 2018. URL: https://www.mdpi.com/1424-8220/18/11/3861, doi:10.3390/s18113861.

[55] K. Ono. Progress in sensitivity verification of ae sensors. *Journal of Acoustic Emission*, 36:S37+, 2019. URL: https://link.gale.com/apps/doc/A675525266/AONE?u=anon~ea4b6a5&sid=googleScholar&xid=90e9b26f.

[56] C. U. Grosse, M. Ohtsu, D. G. Aggelis, and T. Shiotani. *Acoustic Emission Testing: Basics for Research – Applications in Engineering*. Springer Tracts in Civil Engineering. Springer International Publishing, 2021. URL: https://books.google.de/books?id=EYk4EAAAQBAJ, doi:10.1007/978-3-030-67936-1.

[57] J. Xu, K. Wang, Q. Ma, H. Li, P. Wang, R. Chen, Y. Qian, and D. Zeng. Study on acoustic emission properties and crack growth rate identification of rail steels under different fatigue loading conditions. *International Journal of Fatigue*, 172:107638, 2023. URL: https://www.sciencedirect.com/science/article/pii/S0142112323001391, doi:10.1016/j.ijfatigue.2023.107638.

[58] P. Tscheliesnig, G. Lackner, and A. Jagenbrein. Corrosion detection by means of acoustic emission (AE) monitoring. In *Proc. 19th World Conf. on Non-Destructive Testing (WCNDT)*, Munich, Germany, 2016. NDT.net. URL: http://ndt.net/?id=19241.

[59] A. Mishra, J. Dhebar, B. Das, S. S. Patel, and A. Rai. Leak detection in pipelines based on acoustic emission and growing neural gas network utilizing unlabeled healthy condition data. *Flow Measurement and Instrumentation*, 102:102816, 2025. URL: https://www.sciencedirect.com/science/article/pii/S0955598625000081, doi:10.1016/j.flowmeasinst.2025.102816.

[60] M. Giordano, A. Calabro, C. Esposito, A. D'Amore, and L. Nicolais. An acoustic-emission characterization of the failure modes in polymer-composite materials. *Composites Science and Technology*, 58(12):1923–1928, 1998. URL: https://www.sciencedirect.com/science/article/pii/S026635389800013X, doi:10.1016/S0266-3538(98)00013-X.

[61] A. Sharma. Condition monitoring of gearbox using experimental investigation of acoustic emission technique. *Procedia Engineering*, 173:1575–1579, 2017. Plasticity and Impact Mechanics. URL: https://www.sciencedirect.com/science/article/pii/S1877705816346562, doi:10.1016/j.proeng.2016.12.250.

[62] D. Tonelli, M. Luchetta, F. Rossi, P. Migliorino, and D. Zonta. Structural health monitoring based on acoustic emissions: Validation on a prestressed concrete bridge tested to failure. In *Applications of Acoustic Emission in Structural Health Monitoring*, pages 7272–7272. MDPI, 2020. URL: https://www.mdpi.com/1424-8220/20/24/7272, doi:10.3390/s20247272.

[63] C. G. Filippin, J. Borba, J. A. dos Reis Neto, L. M. Pires, L. Sirino, L. G. T. Ribas, M. A. Luzio, N. C. de Moura, P. C. Moro, and V. Silverio. *Emissao Acustica:*

Conceitos e Aplicacoes. Institutos Lactec and Usina Termeletrica a Gas de Araucaria (UEGA), Curitiba, PR and Araucaria, PR, Brazil, 1st edition, 2017.

[64] K. T. V. Grattan and T. Sun. Fiber optic sensor technology: An overview. *Sensors and Actuators A: Physical*, 82(1):40–61, 2000. URL: https://www.sciencedirect.com/science/article/pii/S0924424799003684, doi:10.1016/S0924-4247(99)00368-4.

[65] I. Perez and E. Udd. Acoustic emission detection using fiber bragg gratings. *Proceedings of SPIE - The International Society for Optical Engineering*, 4328:209–215, August 2001. doi:10.1117/12.435542.

[66] M. Majumder, T. K. Gangopadhyay, A. K. Chakraborty, K. Dasgupta, and D. K. Bhattacharya. Fibre bragg gratings in structural health monitoring-present status and applications. *Sensors and Actuators A: Physical*, 147(1):150–164, 2008. URL: https://www.sciencedirect.com/science/article/pii/S0924424708002380, doi:10.1016/j.sna.2008.04.008.

[67] F. R. Breckenridge. Acoustic emission transducer calibration by means of the seismic surface pulse. *Journal of Acoustic Emission*, 1:87–94, January 1982.

[68] F. R. Breckenridge and M. Greenspan. Surface-wave displacement: Absolute measurements using a capacitive transducer. *The Journal of the Acoustical Society of America*, 69(4):1177–1185, April 1981. doi:10.1121/1.385698.

[69] R. B. Thompson. A model for the electromagnetic generation and detection of rayleigh and lamb waves. *IEEE Transactions on Ultrasonics, Ferroelectrics, and Frequency Control*, 37(5):485–490, 1990. URL: https://ieeexplore.ieee.org/document/1538775, doi:10.1121/1.385698.

[70] Y. Y. Kim and Y. E. Kwon. Review of magnetostrictive patch transducers and applications in ultrasonic nondestructive testing of waveguides. *Ultrasonics*, 62:3–19, 2015. URL: https://www.sciencedirect.com/science/article/pii/S0041624X15001341, doi:10.1016/j.ultras.2015.05.015.

[71] M. Kogia, T. H. Gan, W. Balachandran, M. Livadas, V. Kappatos, I. Szabo, A. Mohimi, and A. Round. High temperature shear horizontal electromagnetic acoustic transducer for guided wave inspection. *Sensors*, 16:582, April 2016. URL: https://www.mdpi.com/1424-8220/16/4/582, doi:10.3390/s16040582.

[72] I. Baillie, P. Griffith, X. Jian, and S. Dixon. Implementing an ultrasonic inspection system to find surface and internal defects in hot, moving steel using EMATs. *Insight*, 49:87–92, 02 2007. doi:10.1784/insi.2007.49.2.87.

[73] X. Jian, I. Baillie, and S. Dixon. Steel billet inspection using laser-EMAT system. *Journal of Physics D: Applied Physics*, 40(5):1501, February 2007. URL: https://dx.doi.org/10.1088/0022-3727/40/5/029, doi:10.1088/0022-3727/40/5/029.

[74] Didem Ozevin. Mems acoustic emission sensors. *Applied Sciences*, 10(24):8966, 2020. URL: https://www.mdpi.com/2076-3417/10/24/8966, doi:10.3390/app10248966.

[75] P. Curie and J. Curie. Developpement, par pression, de l'electricite polaire dans les cristaux hemiedres a faces inclinees. *Comptes Rendus*, 91:294–295, 1880.

[76] J. Oliver. Elastic wave dispersion in a cylindrical rod by a wide-band short-duration pulse technique. *The Journal of the Acoustical Society of America*, 29(2):189–194, February 1957. arXiv:https://pubs.aip.org/asa/jasa/article-pdf/29/2/189/18736587/189_1_online.pdf, doi:10.1121/1.1908824.

[77] T. M. Proctor Jr. An improved piezoelectric acoustic emission transducer. *Journal of the Acoustical Society of America*, 71(5):1163–1168, May 1982. arXiv:https://pubs.aip.org/asa/jasa/article-pdf/71/5/1163/11552832/1163_1_online.pdf, doi:10.1121/1.387763.

[78] W. Zhang, H. Jia, G. Gao, X. Cheng, P. Du, and D. Xu. Backing layers on electroacoustic properties of the acoustic emission sensors. *Applied Acoustics*, 156:387–393, 2019. URL: https://www.sciencedirect.com/science/article/pii/S0003682X19302919, doi:10.1016/j.apacoust.2019.07.038.

[79] Vallen Systeme GmbH. Data Sheet of the Sensor VS75-V. https://www.vallen.de/sensors/low-frequency-sensors-30-100-khz/vs75-v/, 2025. Accessed: September 25, 2024.

[80] Y. Song, Z. Tang, R. Shi, S. Wang, D. Lin, and C. Luo. Design of PMN-PT-based dual-resonance acoustic emission sensor for partial discharge detection. *Sensors and Actuators A: Physical*, 373:115432, 2024. URL: https://www.sciencedirect.com/science/article/pii/S0924424724004266, doi:10.1016/j.sna.2024.115432.

[81] Vallen Systeme GmbH. Data Sheet of the Sensor VS900-M. https://www.vallen.de/sensors/broad-band-sensors/vs900-m/, 2024. Accessed: September 25, 2024.

[82] Vallen Systeme GmbH. Data Sheet of the Sensor VS150-R. https://www.vallen.de/sensors/non-integrated-preamplifier-sensors/vs150-r-2/, 2024. Accessed: September 25, 2024.

[83] M. B. Moffett, T. J. Mapes, and A. T. Grodotzke. A broadband acoustic emission transducer. *The Journal of the Acoustical Society of America*, 74(5):1577–1585, 1983. URL: https://ieeexplore.ieee.org/document/9593640, doi:10.1121/1.390078.

[84] T. M. Proctor. Some details on the nbs conical transducer. *Journal of Acoustic Emission*, 1(2):119–124, 1982.

[85] C. Chang and C. T. Sun. A new sensor for quantitative acoustic emission measurement. *Journal of Acoustic Emission*, 7:21–28, 1988.

[86] M. Greenspan. The NBS conical transducer: Analysis. *The Journal of the Acoustical Society of America*, 81(1):173–183, 1987. doi:10.1121/1.395027.

[87] T. M. Proctor. More-recent improvements on the NBS conical transducer. *Journal of Acoustic Emission*, 5(4):134–142, 1986.

[88] S. D. Glaser, G. G. Weiss, and L. R. Johnson. Body waves recorded inside an elastic half-space by an embedded, wideband velocity sensor. *The Journal of the Acoustical Society of America*, 104(3):1404–1412, 1998. doi:10.1121/1.424350.

[89] Y.-C. Lee and S. H. Kuo. A new point-source/point-receiver acoustic transducer for surface wave measurement. *Sensors and Actuators A: Physical*, 94(3):129–135, 2001. URL: https://www.sciencedirect.com/science/article/pii/S0924424701006823, doi:10.1016/S0924-4247(01)00682-3.

[90] Y.-C. Lee and Z. Lin. Miniature piezoelectric conical transducer: Fabrication, evaluation and application. *Ultrasonics*, 44:e693–e697, 2006. URL: https://www.sciencedirect.com/science/article/pii/S0041624X06002356, doi:10.1016/j.ultras.2006.05.197.

[91] P. D. Theobald, T. J. Esward, S. P. Dowson, and R. C. Preston. Acoustic emission transducers: Development of a facility for traceable out-of-plane displacement calibration. *Ultrasonics*, 43(5):343–350, 2004. URL: https://api.semanticscholar.org/CorpusID:25761498.

[92] P. Theobald. Towards traceable calibration of acoustic emission measurement systems: Development of a reference source at the UK's national physical laboratory. In *Proceedings of a Conference (Details Not Provided)*, 2004.

[93] A. Zelenyak, M. Hamstad, and M. Sause. Finite element modeling of acoustic emission signal propagation with various shaped waveguides. In *Proceedings of the 31st Conference of the European Working Group on Acoustic Emission (EWGAE)*, Dresden, Germany, September 2014. URL: https://www.ndt.net/?id=17571.

[94] M. Sause and M. A. Hamstad. Numerical modeling of existing acoustic emission sensor absolute calibration approaches. *Sensors and Actuators A: Physical*, 269:294–307, 2018. URL: https://www.sciencedirect.com/science/article/pii/S0924424717313717, doi:10.1016/j.sna.2017.11.057.

[95] M. Sause, M. A. Hamstad, and S. Horn. Finite element modeling of lamb wave propagation in anisotropic hybrid materials. *Composites Part B: Engineering*, 53:249–257, 2013. URL: https://www.sciencedirect.com/science/article/pii/S1359836813002242, doi:10.1016/j.compositesb.2013.04.067.

[96] S. Fick and T. Proctor. Long-term stability of the nist conical reference transducer. *Journal of Research (NIST JRES)*, 2011. URL: https://tsapps.nist.gov/publication/get_pdf.cfm?pub_id=908333.

[97] T. Monnier, D. Seydou, N. Godin, and F. Zhang. Primary calibration of acoustic emission sensors by the method of reciprocity: Theoretical and experimental considerations. *Journal of Acoustic Emission*, 30:152–166, 2012. URL: https://hal.science/hal-00869238.

[98] C. B. Scruby and H. N. G. Wadley. A calibrated capacitance transducer for the detection of acoustic emission. *Journal of Physics D: Applied Physics*, 11(11):1487,

1978. URL: https://dx.doi.org/10.1088/0022-3727/11/11/007, doi:10.1088/0022-3727/11/11/007.

[99] G. McLaskey and S. Glaser. Acoustic emission sensor calibration for absolute source measurements. *Journal of Nondestructive Evaluation*, 31, 2012. URL: https://link.springer.com/article/10.1007/s10921-012-0131-2, doi:10.1007/s10921-012-0131-2.

[100] L. Goujon and J. C. Baboux. Behaviour of acoustic emission sensors using broadband calibration techniques. *Measurement Science and Technology*, 14(7):903–908, 2003. URL: https://iopscience.iop.org/article/10.1088/0957-0233/14/7/302, doi:10.1088/0957-0233/14/7/302.

[101] D. Eitzen and F. Breckenridge. Acoustic emission sensors and their calibration. In R. Miller and P. McIntire, editors, *Nondestructive Testing Handbook, Second Edition*, volume 5: Acoustic Emission Testing, pages 121–132. American Society for Nondestructive Testing, Columbus, 1987.

[102] W. Prosser, M. Hamstad, J. Gary, and A. O'Gallagher. Finite element and plate theory modeling of acoustic emission waveforms. *Journal of Nondestructive Evaluation*, 18(3):83–90, 1999.

[103] A. Carpinteri, G. Lacidogna, and N. Pugno. Structural damage diagnosis and lifetime assessment by acoustic emission monitoring. *Engineering Fracture Mechanics*, 74(1):273–289, 2007. URL: https://www.sciencedirect.com/science/article/pii/S0013794406000622, doi:10.1016/j.engfracmech.2006.01.036.

[104] M. Wu, X. Dong, J. Yang, and S. Xue. Experimental research on detection of internal leakage of valves in pressure air pipes based on acoustic emission technology. *Journal of Physics: Conference Series*, 1600(1):012031, 2020. URL: https://dx.doi.org/10.1088/1742-6596/1600/1/012031, doi:10.1088/1742-6596/1600/1/012031.

[105] Joint Committee for Guides in Metrology. *Evaluation of measurement data - Guide to the expression of uncertainty in measurement*. Joint Committee for Guides in Metrology (JCGM), first edition, corrected version 2010 edition, 2008. JCGM 100:2008 (GUM 1995 with minor corrections). URL: https://www.bipm.org/en/publications/guides/gum.html.

[106] *ASME PTC 19.1-2018 - Test Uncertainty*. ASME, New York, NY, 2018 edition, 2018. Performance Test Codes. URL: https://www.asme.org.

[107] K. Ono. Calibration methods of acoustic emission sensors. *Materials*, 9(7):508, 2016. URL: https://www.mdpi.com/1996-1944/9/7/508, doi:10.3390/ma9070508.

[108] ASTM A508/508M -04. Standard Specification for Quenched and Tempered Vacuum-Treated Carbon and Alloy Steel Forgings for Pressure Vessels. Standard, American Society for Testing and Materials, West Conshohocken, USA, August 2017.

[109] L. Gaisser, O. Kirschner, and S. Riedelbauch. Cavitation detection in hydraulic machinery by analyzing acoustic emissions under strong domain shifts using neural networks. *Physics of Fluids*, 35(2):027128, 2023. URL: https://pubs.aip.org/aip/pof/article-pdf/doi/10.1063/5.0137068/16684950/027128_1_online.pdf, doi:10.1063/5.0137068.

[110] I. Fernandez-Osete, D. Bermejo, X. Ayneto-Gubert, and X. Escaler. Review of the uses of acoustic emissions in monitoring cavitation erosion and crack propagation. *Foundations*, 4(1):114–133, 2024. URL: https://www.mdpi.com/2673-9321/4/1/9, doi:10.3390/foundations4010009.

[111] E. Kannatey-Asibu and D. A. Dornfeld. A study of tool wear using statistical analysis of metal-cutting acoustic emission. *Wear*, 76(2):247–261, 1982. URL: https://www.sciencedirect.com/science/article/pii/0043164882900096, doi:10.1016/0043-1648(82)90009-6.

[112] P. Twardowski, M. Tabaszewski, M. Wiciak-Pikuła, and A. Felusiak-Czyryca. Identification of tool wear using acoustic emission signal and machine learning methods. *Precision Engineering*, 72:738–744, 2021. URL: https://www.sciencedirect.com/science/article/pii/S0141635921001884, doi:10.1016/j.precisioneng.2021.07.019.

[113] L. Noll, J. Mrowetz, K. Kretschmer, and D. Schroder. Acoustic emissions testing as a complementary tool to understand chemical and electrochemical changes in battery electrodes. *Journal of Power Sources*, 629:235978, 2025. URL: https://www.sciencedirect.com/science/article/pii/S037877532401930X, doi:10.1016/j.jpowsour.2024.235978.

[114] J. W. R. Boyd and J. Varley. The uses of passive measurement of acoustic emissions from chemical engineering processes. *Chemical Engineering Science*, 56(5):1749–1767, 2001. URL: https://www.sciencedirect.com/science/article/pii/S0009250900005406, doi:10.1016/S0009-2509(00)00540-6.

[115] S. V. Augutis, B. Muravin, and E. Vastakas. Application of waveguides for the calibration of acoustic emission transducers. In *Proceedings of the 32nd European Conference on Acoustic Emission Testing*, Prague, Czech Republic, 2016. URL: https://www.ndt.net/?id=20359.

[116] H. Lan, L. Yan, D. Xiao, Z. Jiao, and I-M. Chen. Surface-to-surface calibration of acoustic emission sensors. *Sensors and Actuators A: Physical*, 174:16–23, 2012. URL: https://www.sciencedirect.com/science/article/pii/S0924424711006716, doi:10.1016/j.sna.2011.11.014.

[117] B. Burks. Re-examination of NIST acoustic emission sensor calibration: Part I - modeling the loading from glass capillary fracture. *J. Acoustic Emission*, 29:167–174, 01 2011.

[118] M. A. Hamstad. Re-examination of NIST acoustic emission sensor calibration: Part II - finite element modeling of acoustic emission signal from glass capillary fracture. *Journal of Acoustic Emission*, 29:175–183, 2011.

[119] K. Ono. Rayleigh wave calibration of acoustic emission sensors and ultrasonic transducers. *Sensors*, 19(14):3129, 2019. URL: https://www.mdpi.com/1424-8220/19/14/3129, doi:10.3390/s19143129.

[120] W. R. MacLean. Absolute measurement of sound without a primary standard. *The Journal of the Acoustical Society of America*, 12(1):140–146, 1940. URL: https://pubs.aip.org/asa/jasa/article-pdf/12/1/140/18724943/140_1_online.pdf, doi:10.1121/1.1916085.

[121] H. Hatano and E. Mori. Acoustic-emission transducer and its absolute calibration. *The Journal of the Acoustical Society of America*, 59(2):344–349, 1976. doi:10.1121/1.380869.

[122] H. Hatano and T. Watanabe. Reciprocity calibration of acoustic emission transducers in Rayleigh-wave and longitudinal-wave sound fields. *The Journal of the Acoustical Society of America*, 101(3):1450–1455, 1997. URL: https://pubs.aip.org/asa/jasa/article-pdf/101/3/1450/11933374/1450_1_online.pdf, doi:10.1121/1.418170.

[123] H. Hatano, T. Chaya, S. Watanabe, and K. Jinbo. Reciprocity calibration of impulse responses of acoustic emission transducers. *IEEE Transactions on Ultrasonics, Ferroelectrics, and Frequency Control*, 45(5):1221–1228, Sep. 1998. doi:10.1109/58.726447.

[124] J. Keprt. Reciprocity and step function calibration of acoustic emission sensor. In *Proceedings of the 13st Conference STUDENT EEICT 2007*, pages 72–75, Brno, Czech Republic, 2007.

[125] R. Hill and N. L. Adams. Reinterpretation of the reciprocity theorem for the calibration of acoustic emission transducers operating on a solid. *Acta Acustica united with Acustica*, 43(5):315–322, 1979.

[126] R. Hill. Reciprocity and other acoustic emission transducer calibration techniques. *Journal of Acoustic Emission*, 1:73–80, 1982.

[127] K. Ono. Critical examination of ultrasonic transducer characteristics and calibration methods. *Research in Nondestructive Evaluation*, 30(1):19–64, 2019. URL: https://www.tandfonline.com/doi/full/10.1080/09349847.2017.1375585, doi:10.1080/09349847.2017.1375585.

[128] D. Xiao, Z. Zhang, H. Ren, B. Yang, Q. Pan, and C. Xu. Calibration principle for acoustic emission sensor sensitivity. In G. Shen and W. Zhang, editors, *Advances in Acoustic Emission Technology: Proceedings of the World Conference on Acoustic Emission-2013*, volume 158 of *Springer Proceedings in Physics*, pages 33–44. Springer Science+Business Media New York, 2015. URL: https://link.springer.com/chapter/10.1007/978-1-4939-1239-1_4, doi:10.1007/978-1-4939-1239-1_4.

[129] H. Vallen. Proposal for an absolute ae sensor calibration setup. *Springer Proceedings in Physics*, 2017. URL: https://api.semanticscholar.org/CorpusID:195562897.

[130] L. Zhang, H. Yalcinkaya, and D. Ozevin. Numerical approach to absolute calibration of piezoelectric acoustic emission sensors using multiphysics simulations. *Sensors and Actuators A: Physical*, 256:12–23, 2017. URL: https://www.sciencedirect.com/science/article/pii/S0924424716306902, doi:10.1016/j.sna.2017.01.009.

[131] ASTM E 2075-05. Standard Practice for Verifying the Consistency of AE-Sensor Response Using an Acrylic Rod. Standard, American Society for Testing and Materials, West Conshohocken, USA, June 2005.

[132] ASTM E 2374 - 16. Standard Guide for Acoustic Emission System Performance Verification. Standard, American Society for Testing and Materials, West Conshohocken, USA, June 2016.

[133] H. Chen, J. Lin, N. Chen, and G. Xu. An integrated approach to evaluate the measurement capability and acceptability of acoustic emission sensors. *Measurement Science and Technology*, 35(2):025132, 2023. URL: https://iopscience.iop.org/article/10.1088/1361-6501/ad0c47, doi:10.1088/1361-6501/ad0c47.

[134] S. Priebe, C. Reinhardt, A. Fernandes, H. Trattnig, M. Sause, and I. Mueller. Electromechanical impedance of acoustic emission sensors used for self-diagnosis. In *Proceedings of the 10th European Workshop on Structural Health Monitoring (EWSHM 2024)*, Potsdam, Germany, 2024. Published in e-Journal of Nondestructive Testing. URL: https://www.ndt.net/search/docs.php3?id=29632, doi:10.58286/29632.

[135] C. Reinhardt, A. Fernandes, M. Merzkirch, M. Sause, and I. Mueller. Self-diagnosis of acoustic emission sensors: Electromechanical impedance-based damage detection. In *15th International Workshop on Structural Helalth Monitoring*, Palo Alto, United States of America, September 2025. doi:10.12783/shm2025/37335.

[136] A. F. de Oliveira Junior, T. Schlech, and M. Sause. Improving acoustic emission measurement reliability in remote sites by using a mobile verification setup. In *Proceedings of the 19th EAWE PhD Seminar on Wind Energy*, pages 192–195. EAWE, 2023.

[137] P. Thelu. Microsoft surface book 2 (3D model), April 2020. Available: https://grabcad.com/library/microsoft-surface-book-2-1.

[138] S. Ullrich. LogiLink USB 2.0 Hub 4-Port, Smile, Black, UA0139 (3D Model), August 2021. Available: https://grabcad.com/library/logilink-usb-2-0-hub-4-port-smile-black-ua0139-1.

[139] J.-C. Yoo and T. H. Han. Fast normalized cross-correlation. *Circuits, Systems, and Signal Processing*, 28:819–843, 2009. doi:10.1007/s00034-009-9130-7.

[140] Mistras Group. Data Sheet of the WD Sensor. https://www.physicalacoustics.com/by-product/sensors/WD-100-900-kHz-Wideband-Differential-AE-Sensor, 2025. Accessed: February 01, 2025.

[141] Vallen Systeme GmbH. Data Sheet of the Sensor VS30-V. https://www.vallen.de/sensors/low-frequency-sensors-30-100-khz/vs30-v/, 2025. Accessed: February 01, 2025.

[142] Vallen Systeme GmbH. Data Sheet of the Sensor VS150-M. https://www.vallen.de/sensors/non-integrated-preamplifier-sensors/vs150-m-2/, 2025. Accessed: February 01, 2025.

[143] Vallen Systeme GmbH. Data Sheet of the Sensor VS900-M. httpss://www.vallen.de/de/sensoren/breitbandsensoren/vs900-m-2/, 2025. Accessed: February 01, 2025.

[144] Vallen Systeme GmbH. Data Sheet of the Sensor VS150-RSC. https://www.vallen.de/sensors/integrated-preamplifier-sensors/vs150-rsc-2/, 2025. Accessed: February 01, 2025.

[145] B. G. Lopes, F. A. Alexandre, W. N. Lopes, P. R. d. Aguiar, E. C. Bianchi, and M. A. A. Viera. Study on the effect of the temperature in acoustic emission sensor by the pencil lead break test. In *2018 13th IEEE International Conference on Industry Applications (INDUSCON)*, pages 1226–1229, Sao Paulo, Brazil, 2018. IEEE. doi:10.1109/INDUSCON.2018.8627213.

[146] R. Wang, E. Tang, G. Yang, and Y. Han. Experimental research on dynamic response of PZT-5H under impact load. *Ceramics International*, 46(3):2868–2876, 2020. URL: https://www.sciencedirect.com/science/article/pii/S0272884219328160, doi:10.1016/j.ceramint.2019.09.280.

[147] S. Han and C.-S. Huh. Study of high-voltage impulse generation using piezoelectric materials under elastic wave. *IEEE Transactions on Plasma Science*, 44(8):1429–1434, 2016. doi:10.1109/TPS.2016.2582533.

Appendix A
Calculation of Expanded Uncertainty

Calculation of Type A Uncertainty

The first step in calculating the expanded uncertainty is to calculate the arithmetic mean or average of the measurand, as given in Equation (A.1). It is calculated under the assumption that it varies randomly (random variable $\bar{X}_i$).

$$\bar{X}_i = \frac{1}{n}\sum_{i=1}^{n} X_i \tag{A.1}$$

Where:

- $\bar{X}_i$ is the mean value of the measurand obtained from a set of observations.
- n is the number of observations.
- X_i is an observed value with the index i.

The next step is to calculate the sample standard deviation of each variable S_{X_i} Equation (A.2).

$$S_{X_i} = \sqrt{\sum_{i=1}^{n} \frac{\left(x_{i,m} - \bar{X}_i\right)^2}{(n-1)}} \tag{A.2}$$

Where:

- $x_{i,m}$ is the $m - th$ individual measurement in the set for the variable S_{X_i}.

The next step is to calculate the experimental standard deviation of the mean $S_{\bar{X}_i}$ in Equation (A.3). This equation is meant for measurements that were taken in sequence under the same conditions i.

$$S_{\bar{X}_i} = \frac{S_{X_i}}{\sqrt{M_i}} \tag{A.3}$$

- M_i is the total number of measurements for S_{X_i}.

The final step to calculate Type A uncertainty is to compute the uncertainty of all uncertainties in the different measurement conditions in Equation (A.4).

$$S_{\bar{X}_{i,A}} = \frac{1}{\sqrt{J}} \left[\sum_{j=1}^{J} \left(S_{\bar{X}_{i,A,j}} \right)^2 \right]^{1/2} \tag{A.4}$$

Where:

- $S_{\bar{X}_{i,A,j}}$ is the values from Equation (A.3).
- J is the number of different conditions under which the measurements were taken.

Calculation of Type B Uncertainty

The Type B uncertainty is calculated by other means rather than statistical methods; therefore, it is more straightforward to compute compared to the Type A uncertainty. It is calculated using the contributions of elemental Type B sources of errors in Equation (A.5).

$$b_{\bar{X}_{i,B}} = \frac{1}{\sqrt{J}} \left[\sum_{j=1}^{J} \left(S_{\bar{X}_{i,B,j}} \right)^2 \right]^{1/2} \tag{A.5}$$

Where:

- $S_{\bar{X}_{i,B,j}}$ is the individual elemental Types B errors sources.
- J is the number of different types B elemental sources of errors.

Combined Standard Uncertainty in the Measurement

The combined standard uncertainty in the measurement is $u_{\bar{X}_i}$, expressed by Equation (A.6), which requires the values of Equations (A.4) and (A.5).

$$u_{\bar{X}_i} = \sqrt{\left(S_{\bar{X}_{i,A}}\right)^2 + \left(b_{\bar{X}_{i,B}}\right)^2} \tag{A.6}$$

Expanded Uncertainty in the Measurement

To calculate the expanded uncertainty in the measurement, it is necessary to multiply the combined uncertainty $u_{\bar{X}_i}$ by the coverage factor K_{CL}. This factor comes from statistical tables based on the Student's t-distribution or the normal distribution, depending on the degrees of freedom associated with the measurement uncertainty, and it accounts for a confidence level of typically 95% or 99%, depending on the rigor of the measurement.

$$U_{\bar{X}_i,CL} = K_{CL} u_{\bar{X}_i} \tag{A.7}$$

Another way to express the expanded uncertainty is to use the relative uncertainty, Equation (A.8).

$$\widehat{U}_{\bar{X}_i,CL} = \frac{U_{\bar{X}_i,CL}}{\bar{X}_i} \times 100(\%) \tag{A.8}$$

Finally, the measurement of one specific measurand is expressed by

$$\bar{X}_i \pm U_{\bar{X}_i,CL} \tag{A.9}$$

at a confidence level of CL%.

Appendix B
Drawings of the Mobile Verification Device

The dimensions in the drawings are shown in millimeters (mm) and are not to scale. Tolerances are not given because they were manually adjusted. The building material and assembly details can be found in the text.

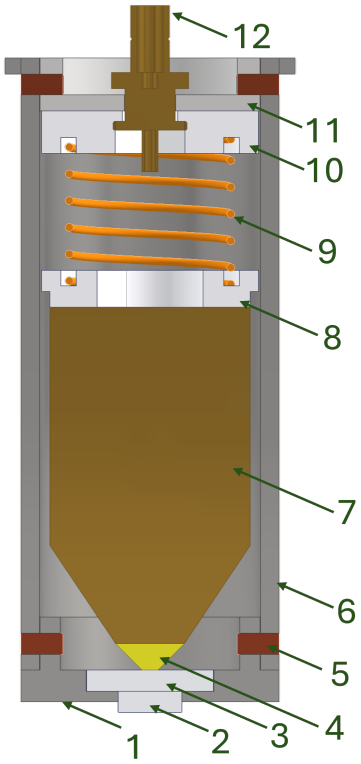

1 – Lower Cap.
2 – Lower Matching Layer.
3 – Upper Matching Layer.
4 – Conical PZT-5A Element.
5 – Locker Pin.
6 – Casing.
7 – Backing Mass.
8 – Lower Non-Metallic Sleeve.
9 – Spring Code LP 029M 01 S316.
10 – Upper Non-Metallic Sleeve.
11 – Upper Cap.
12 – SMB Connector.

Figure A.1: Transmitter and receiver transducers design.

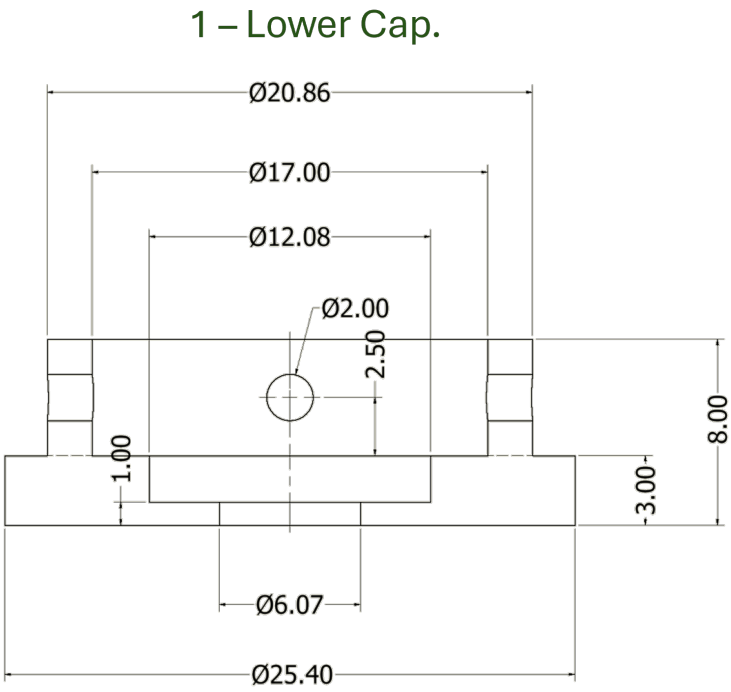

Figure A.2: Lower cap.

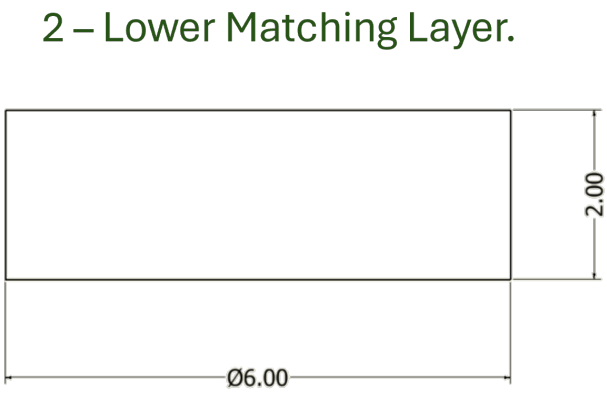

Figure A.3: Lower matching layer.

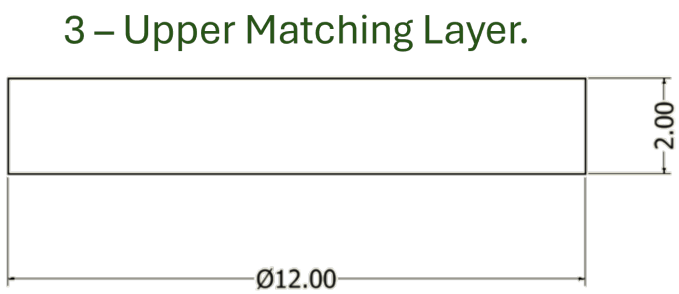

Figure A.4: Upper matching layer.

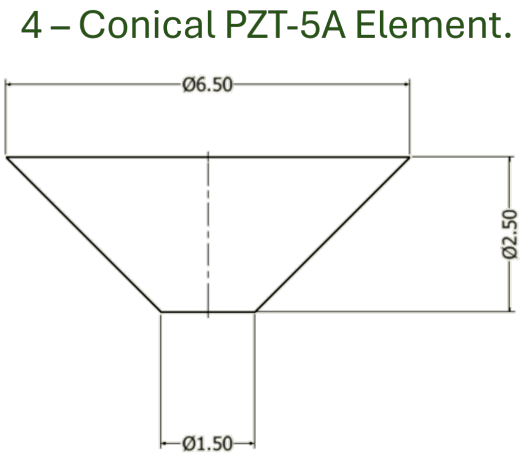

Figure A.5: Conical PZT-5A element.

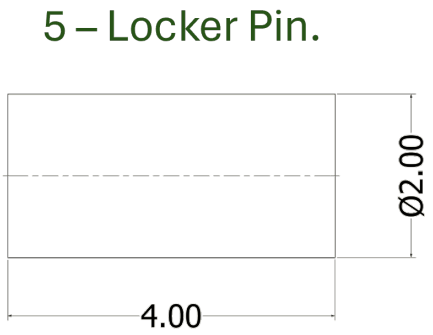

Figure A.6: Locker pin.

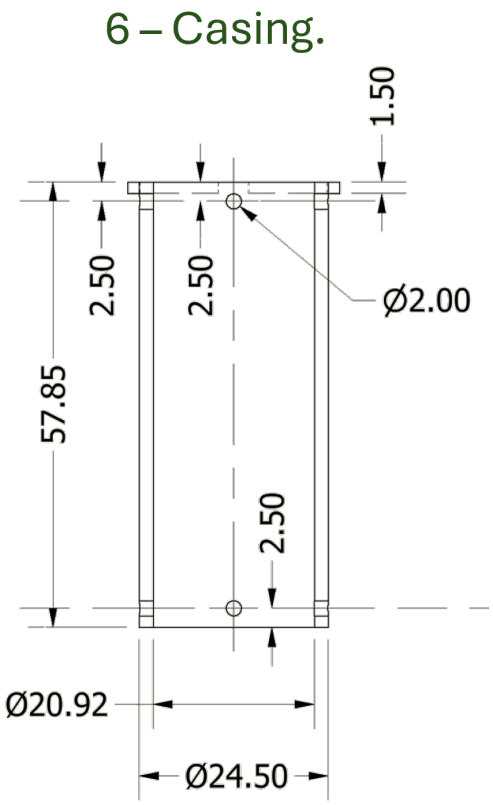

Figure A.7: Casing.

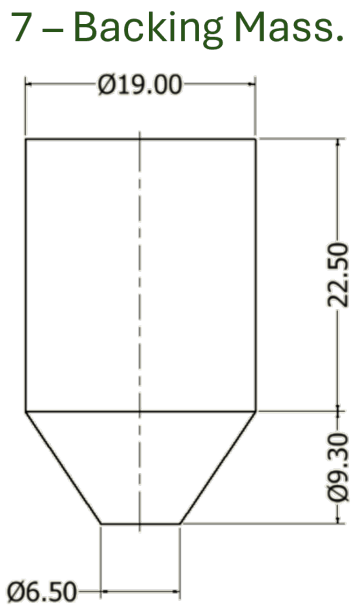

Figure A.8: Brass backing mass.

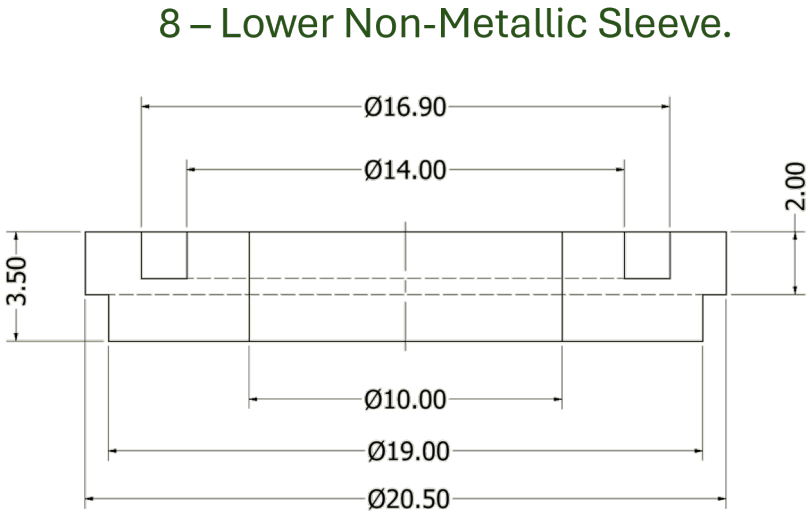

Figure A.9: Lower non-metallic sleeve.

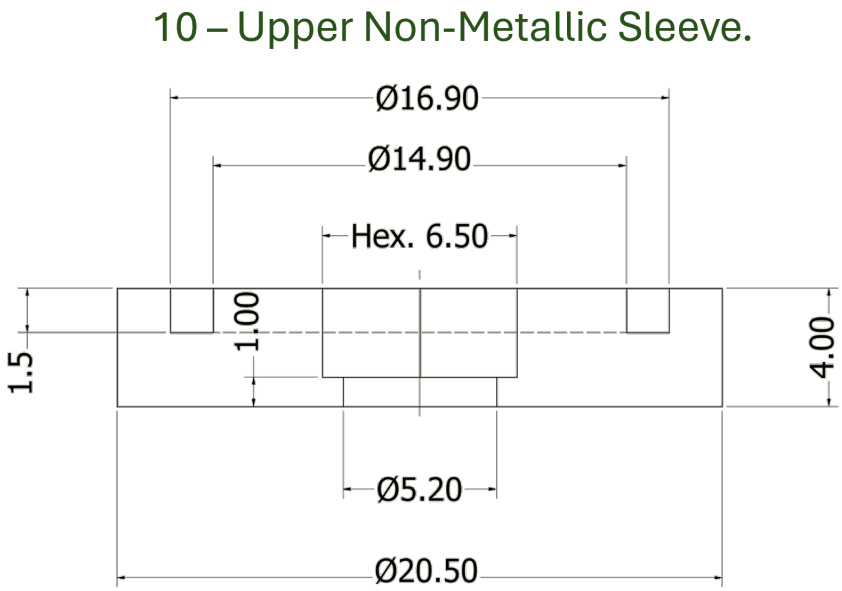

Figure A.10: Upper non-metallic sleeve.

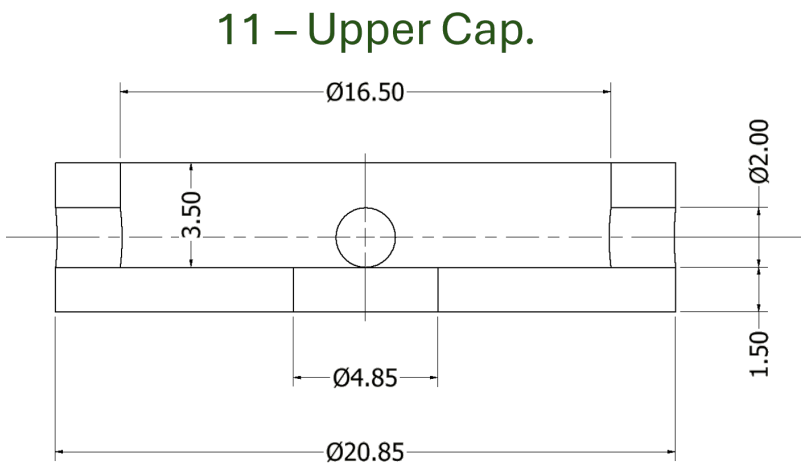

Figure A.11: Upper cap.

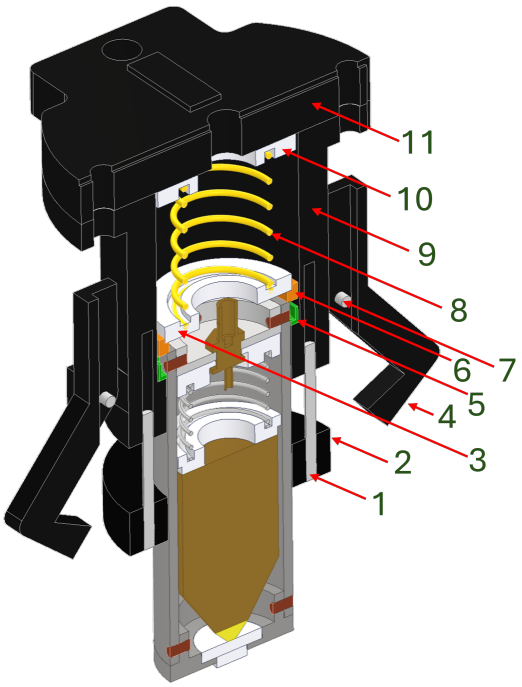

1 – Guiding Rod.
2 – Body Ring.
3 – Lower Spring Sleeve.
4 – Locker.
5 – Lower Sliding Sleeve.
6 – Upper Sliding Sleeve.
7 – Hinge Pin.
8 – Spring Code LP 072N 03 S316.
9 – Cup.
10 – Upper Spring Sleeve.
11 – Upper Cap.

Figure A.12: Transmitter and receiver coupling mechanism.

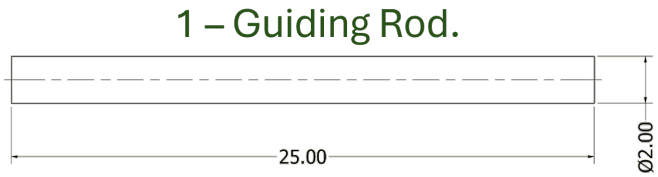

Figure A.13: Guiding rod.

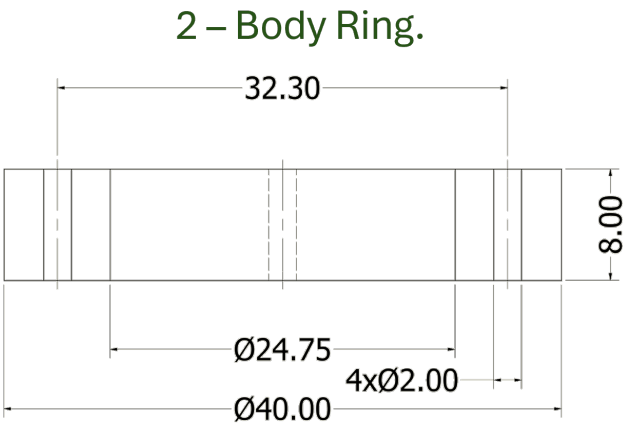

Figure A.14: Body ring.

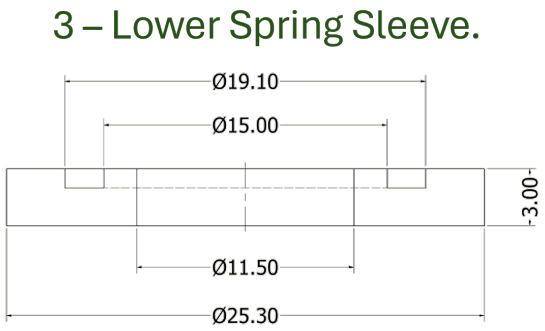

Figure A.15: Lower spring sleeve.

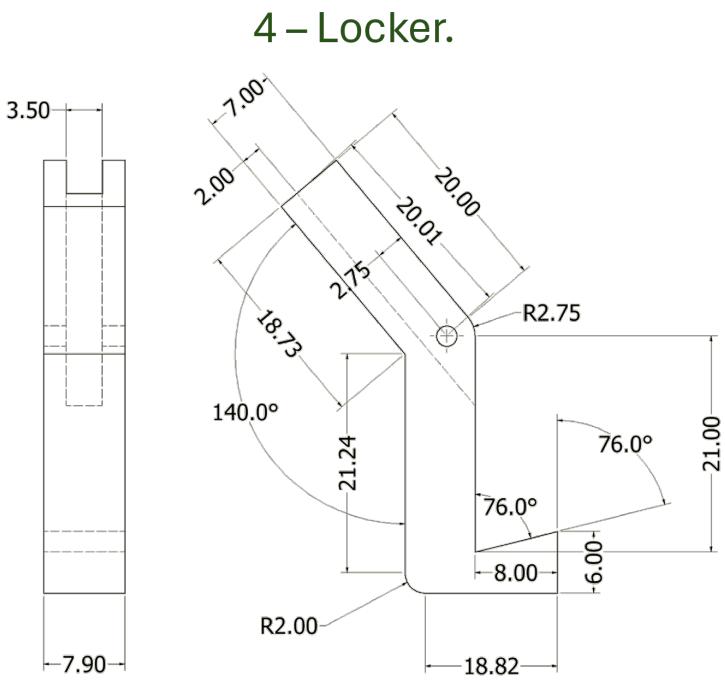

Figure A.16: Locker.

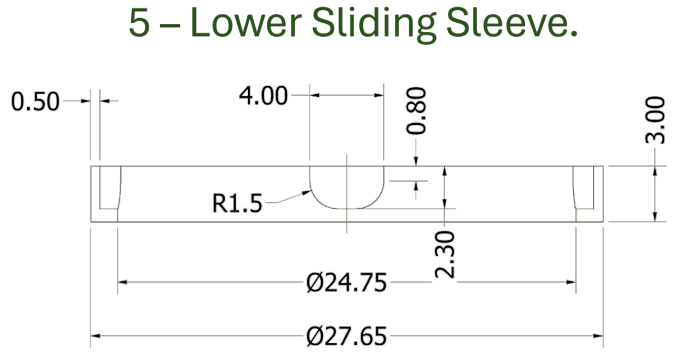

Figure A.17: Lower sliding sleeve.

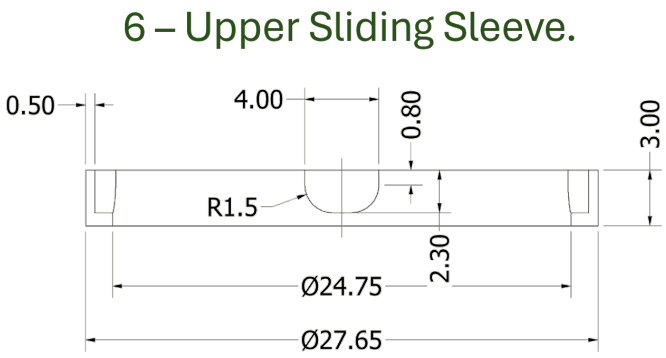

Figure A.18: Upper sliding sleeve.

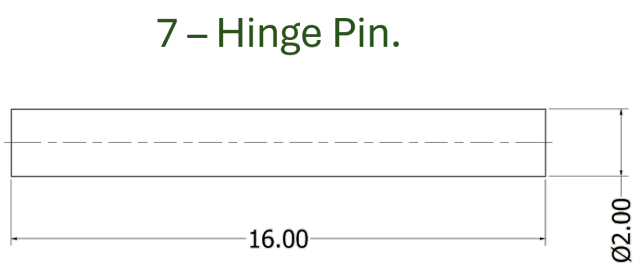

Figure A.19: Hinge pin.

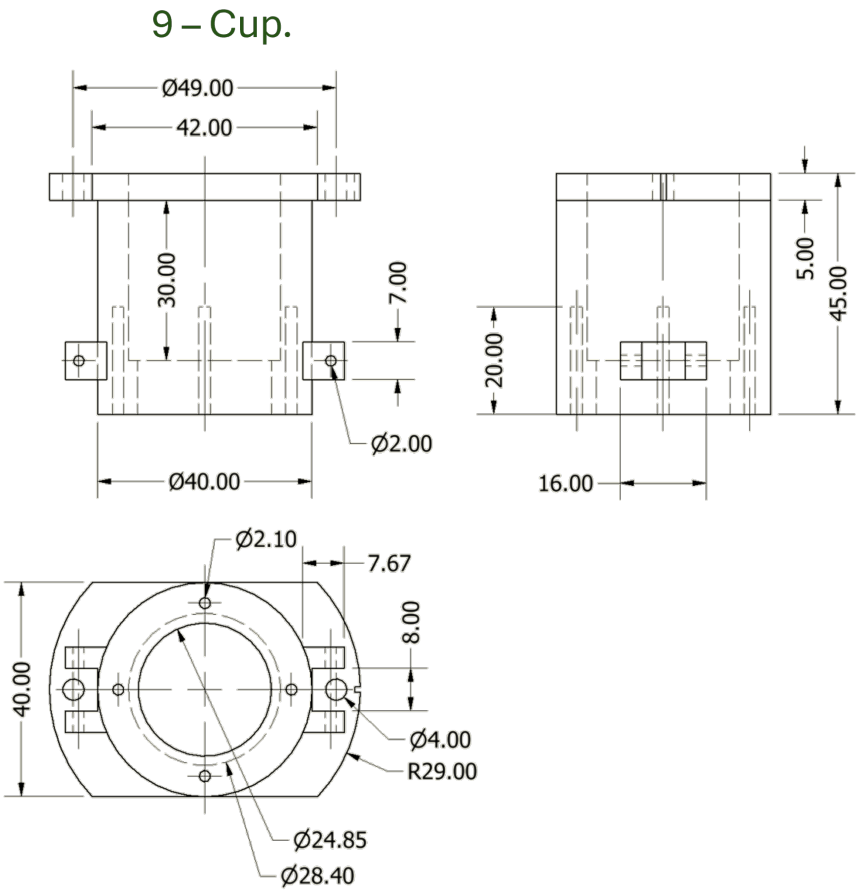

Figure A.20: Cup.

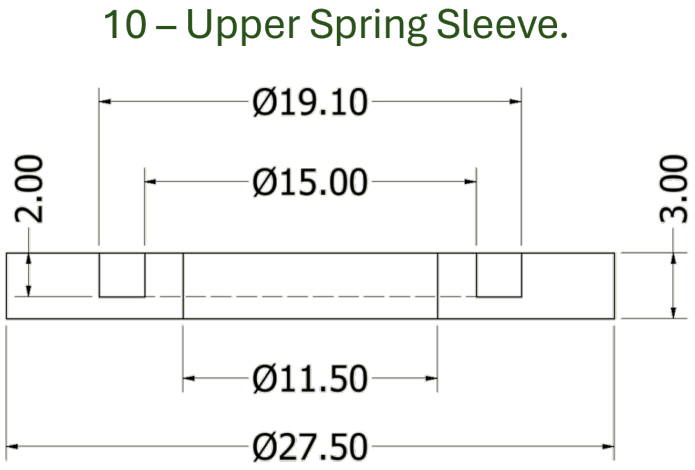

Figure A.21: Upper spring sleeve.

11 – Upper Cap.

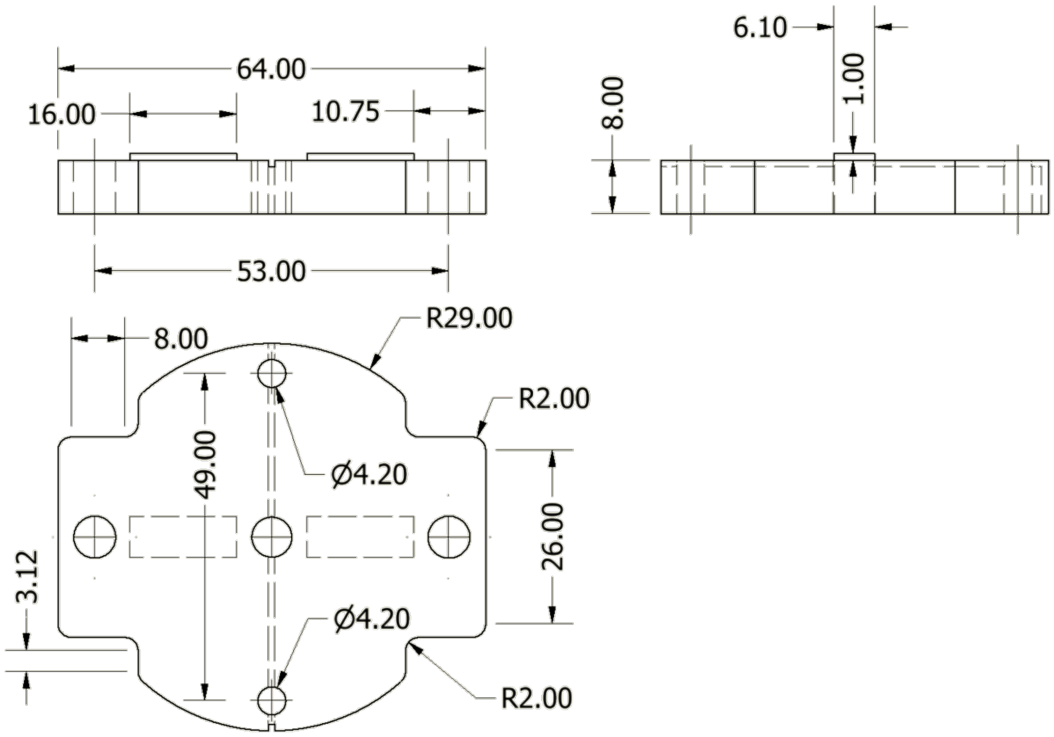

Figure A.22: Upper cap.

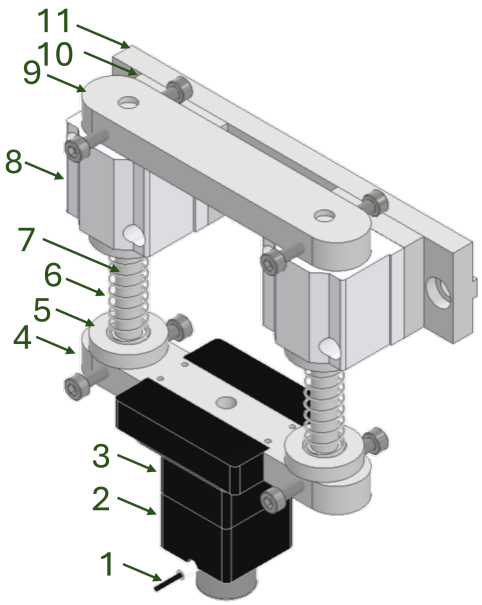

1 – SUT.
2 – WD Sensor Adapter.
3 – Upper Sensor Adapter
4 – Lower Stopper.
5 – Spring Sleeve.
6 – Spring Code LC 036G 08 S316.
7 – Guiding Rod.
8 – Pillow Block RGA-01-08.
9 – Upper Stopper.
10 – Spacer.
11 – Back Plate.

Figure A.23: Improved coupling mechanism.

2 – WD Sensor Adapter.

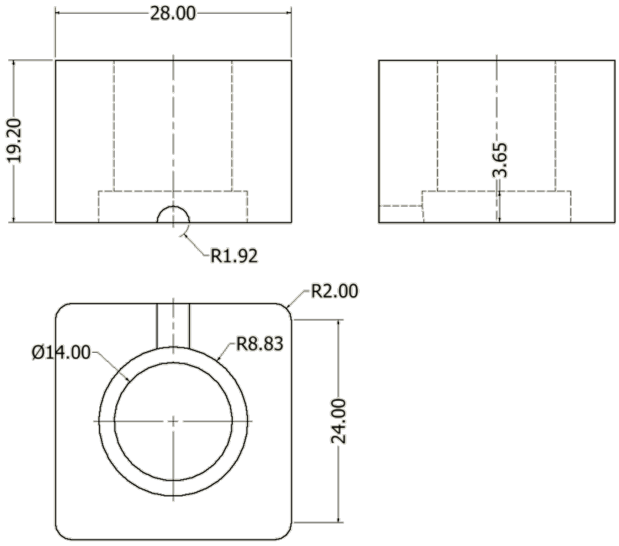

Figure A.24: WD sensor adapter.

3 – Upper Sensor Adapter.

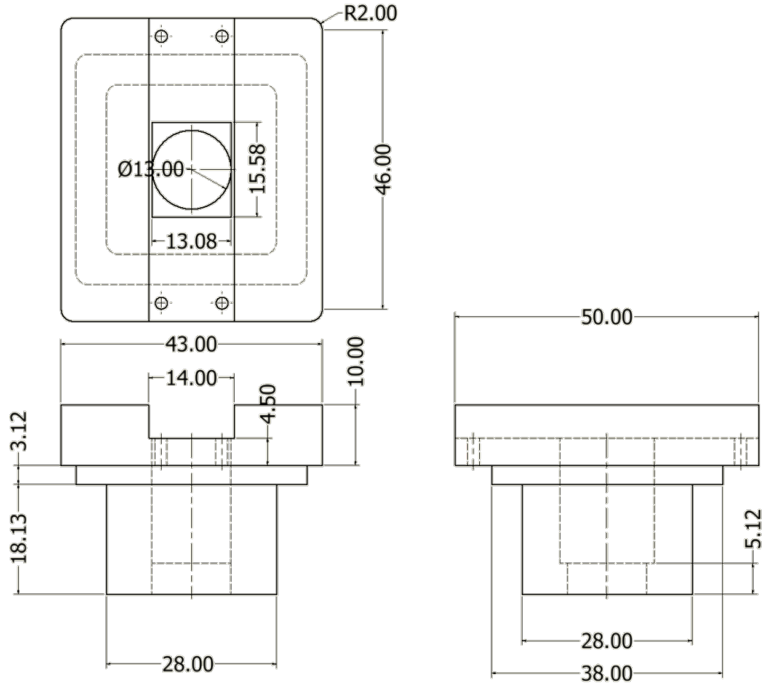

Figure A.25: Upper sensor adapter.

4 – Lower Stopper.

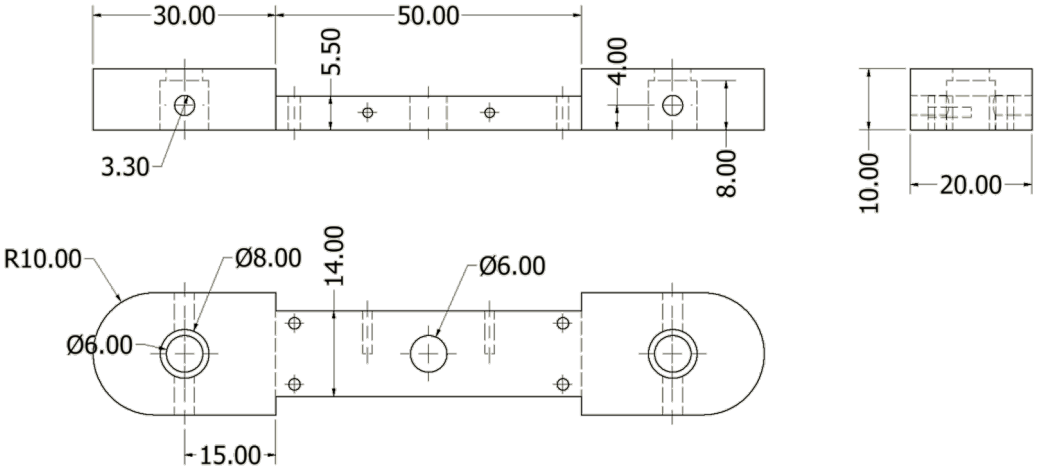

Figure A.26: Lower stopper.

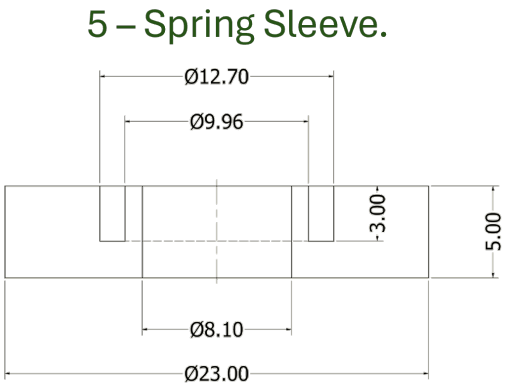

Figure A.27: Spring sleeve.

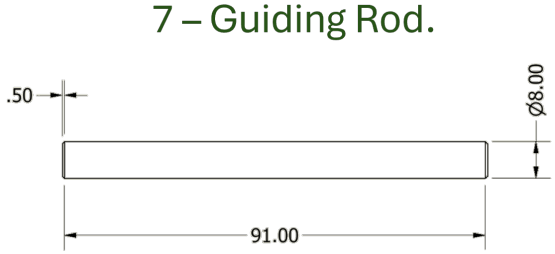

Figure A.28: Guiding rod.

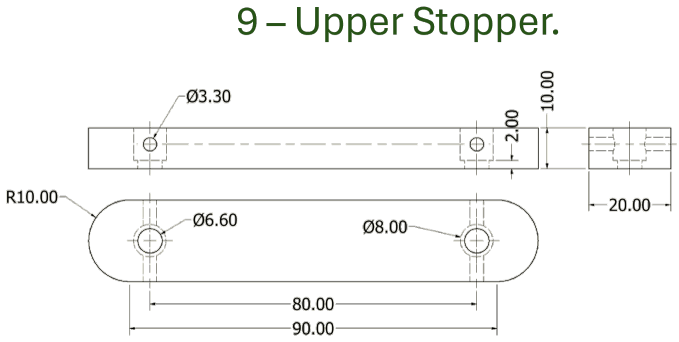

Figure A.29: Upper stopper.

10 – Spacer.

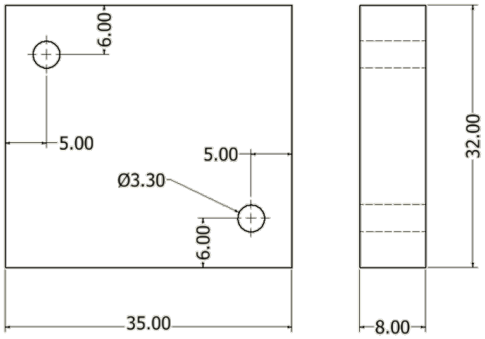

Figure A.30: Spacer.

11 – Back Plate.

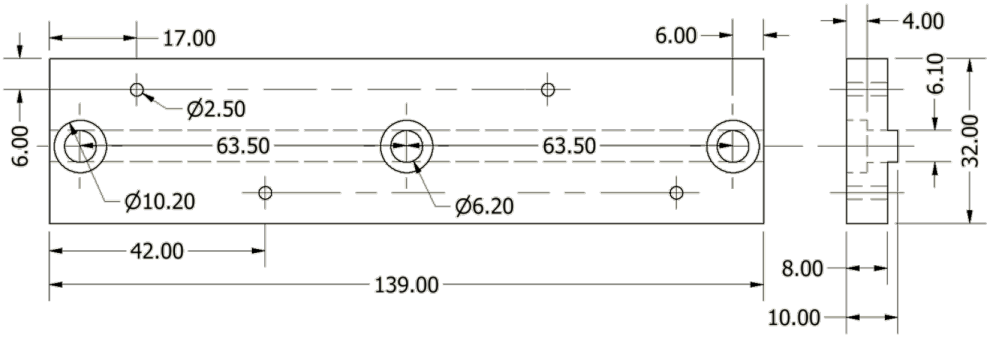

Figure A.31: Back plate.

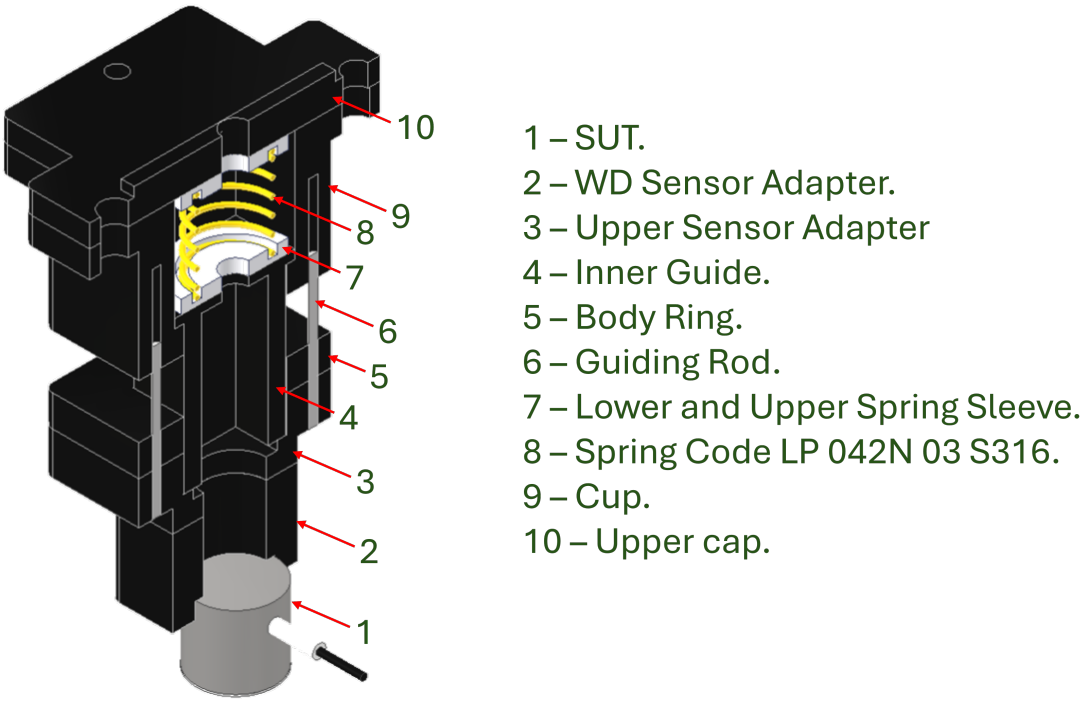

Figure A.32: 3D-printed coupling mechanism.

2 – WD Sensor Adapter.

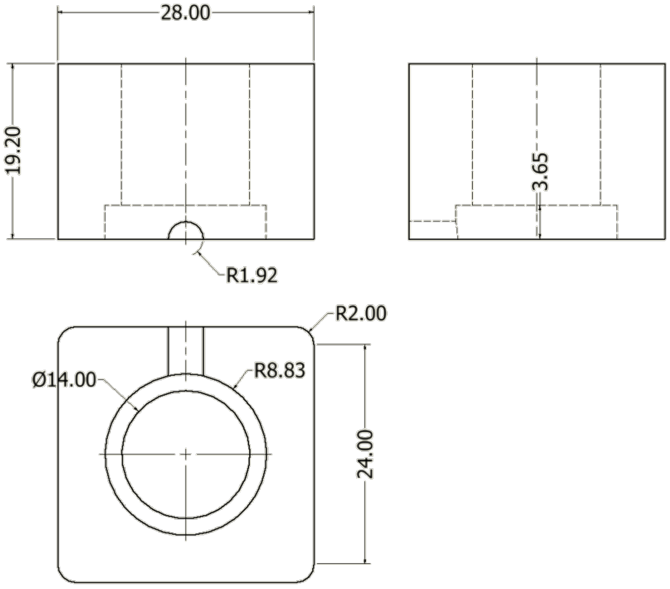

Figure A.33: WD sensor adapter.

3 – Upper Sensor Adapter.

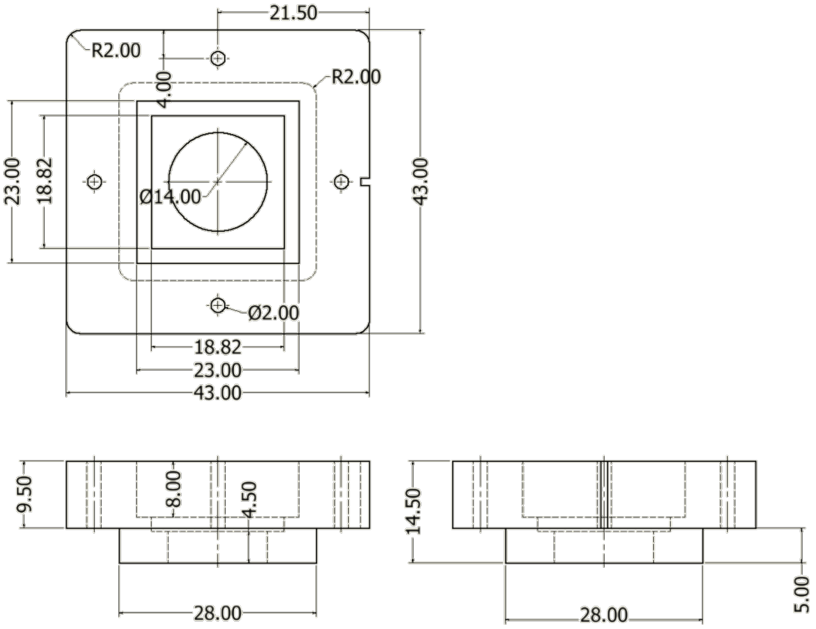

Figure A.34: Upper sensor adapter.

4 – Inner Guide.

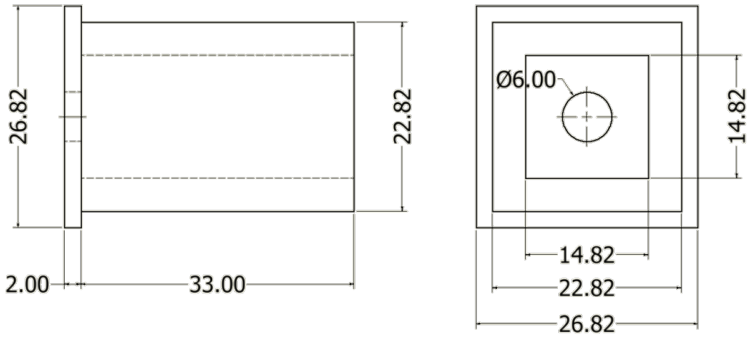

Figure A.35: Inner Guide.

5 – Body Ring.

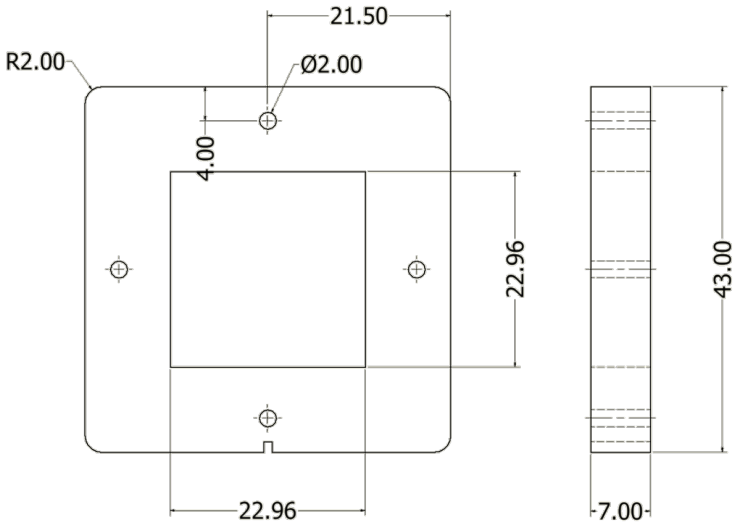

Figure A.36: Body ring.

6 – Guiding Rod.

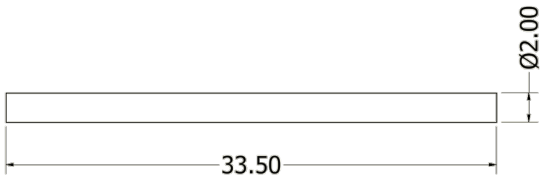

Figure A.37: Guiding rod.

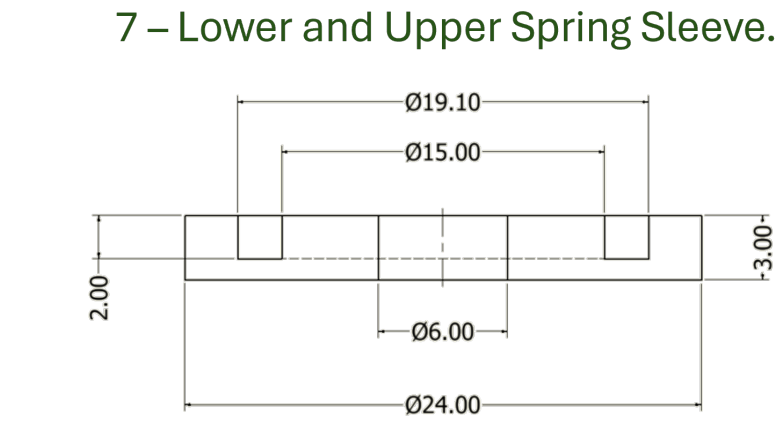

Figure A.38: Lower and upper spring sleeve.

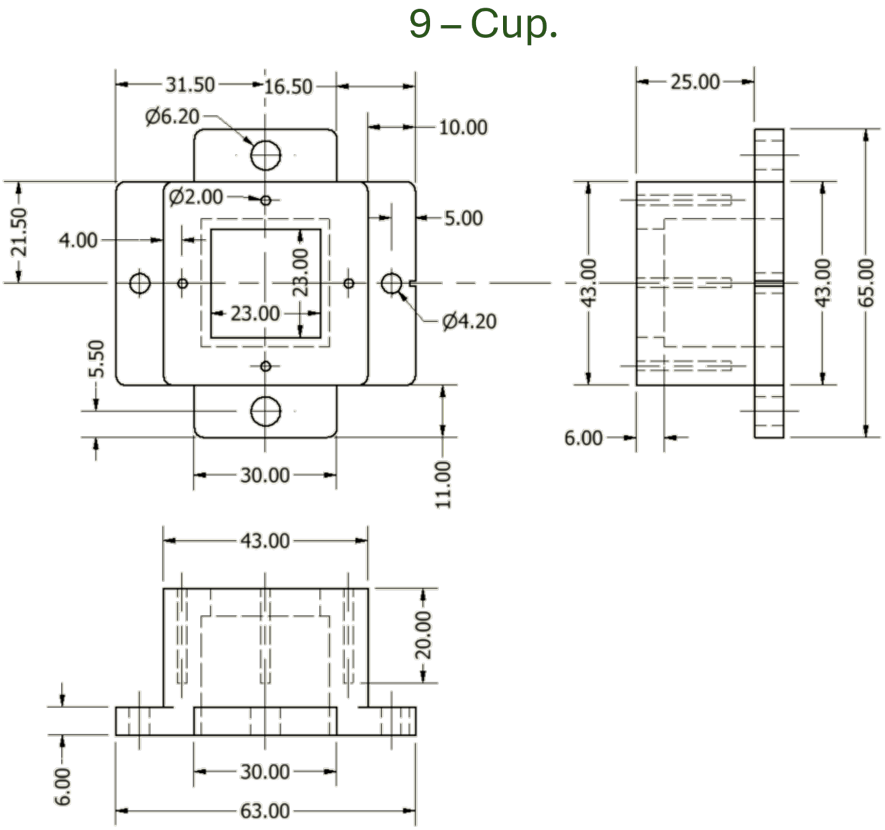

Figure A.39: Cup.

10 – Upper cap.

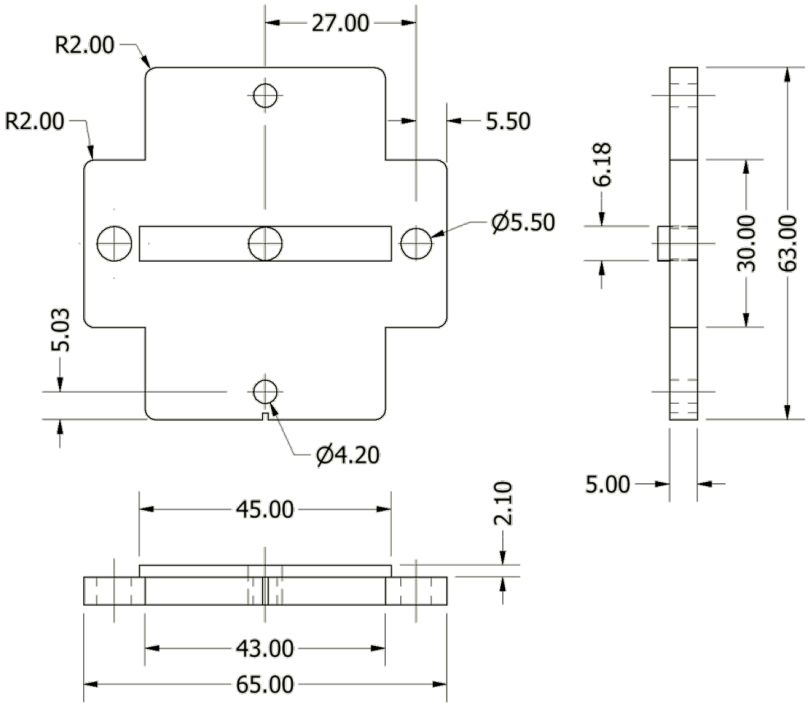

Figure A.40: Upper cap.

Appendix C
Operational Procedure of the Mobile Device

Introduction

Overview

This document is the operational manual of the mobile device for acoustic emission sensor verification. It contains information on how to operate the mobile device towards sensor verification. It also mentions a specific data acquisition setting for reference.

Acronyms

AE – Acoustic Emission

DAQ – Data Acquisition

PLB – Pencil Lead Break

PZT – Lead (plumbum) Zirconate Titanate

SMA – Sub-Miniature version A (connector)

STD – Standard

SUT – Sensor Under Test

TR – Transient Record

#	Document Title	Type of the Document
01	AMSY-6 System Specification	Instruction manual
02	AMSY-6 Chassis and AE Signal Processor Instruction Manual	Instruction manual
03	AMSY-6 Software Operation Manual	Instruction manual
04	2/4/6 Switch Selectable Gain Single Ended and Differential Preamplifier	Data sheet
05	Studies on a Mobile Acoustic Emission Sensor Verification Device, 36th EWGAE, Potsdam, 2024.	Conference Paper
06	Agilent 33210A 10 MHz Function/Arbitrary Waveform Generator	Instruction manual
07	WA301 Wideband Amplifier	Instruction manual

Table A.1: List of referenced documents

References

Setup

The mobile device, shown in Figure 1 is meant to verify acoustic emission sensors not just in the laboratory but also in the field. Its support structure consists of 30 mm x 30 mm extruded aluminum profiles. The frame supports the plate, made from the aluminum alloy $AlMg_3$ with dimensions 500 mm x 400 mm x 3 mm, serving as propagation medium for plate waves. The plate is point-mounted at the corners so that no undesirable reflections occur except via the edges of the plate, and it can vibrate freely. A supporting frame is an extension in the form of a bridge where the transmitter, receiver, the coupling mechanism of sensor under test (SUT), and amplifier holders are attached as can be observed in Figure A.41a.

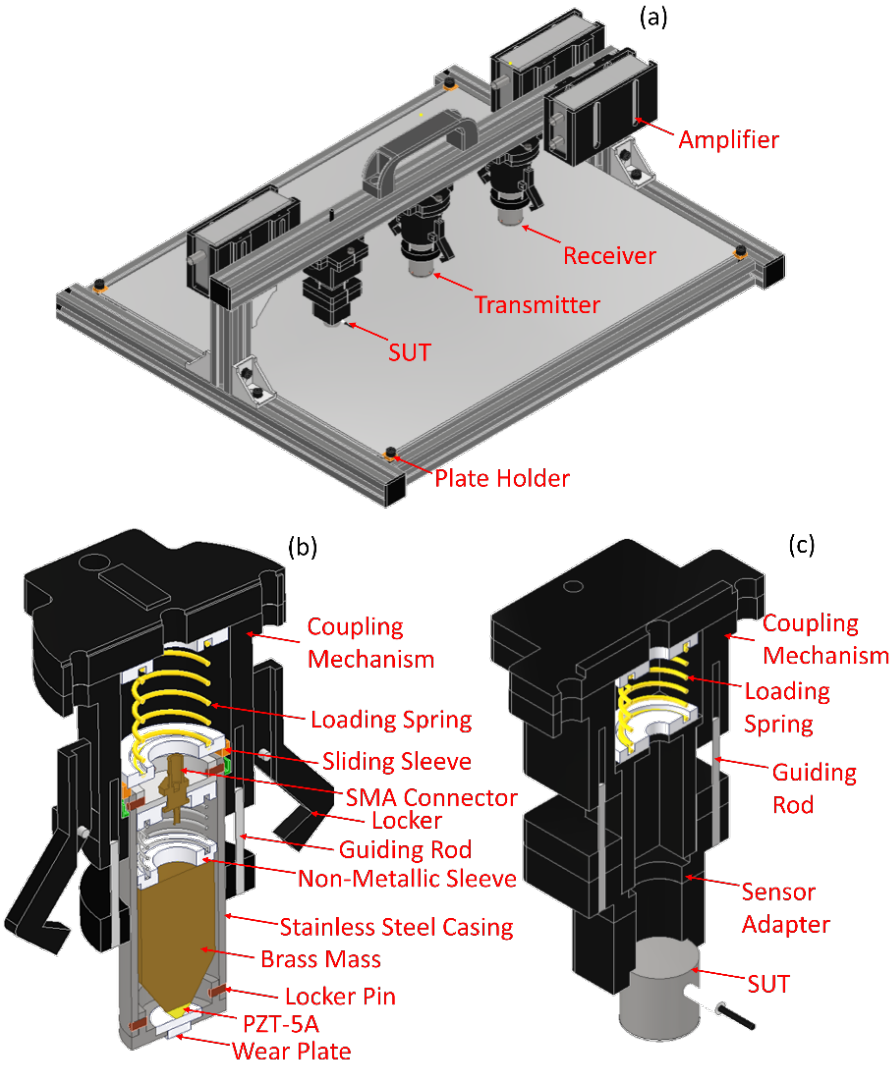

Figure A.41: (a) Illustration of the mobile device for acoustic emission sensor verification. (b) Illustration of the transmitter and receiver and their coupling mechanism. (c) Illustration of the SUT and its coupling mechanism.

The transmitter is a customized conical PZT capable to generate elastic waves that are measured by the SUT and the receiver. Therefore, it is positioned at the center of the plate, in between the SUT and the receiver, at a distance of 125 mm each.

The holder of the receiver was constructed by means of a spring-loaded mechanism and manufactured via 3D printing, and is identically to the holder of the transmitter and the details can be observed in Figure A.41b. Inside the receiver is a conical PZT element, which is damped by a brass cylinder and tensioned with a spring so that the pulse generator can compensate for thermal and mechanically induced expansion. There

is a spring-loaded mechanism for the receiver, transmitter and SUT (Figure A.41c), and guiding rod to allow them to couple and decouple with the aluminum plate at the same position and with the same orientation. The transmitter and receiver can be retrieved and be locked in position during transportation to avoid damage. Three amplifiers of model 2/4/6 supplied by Mistras Inc were used, with one for the SUT, when no built-in amplifier, one amplifier for the transmitter and one for the receiver.

Usually, an amplifier for the transmitter is not required, but has been integrated in case of testing the transmitter as a sensor by Pencil Lead Breaks (PLBs). Furthermore, there is one arbitrary waveform generator model 33210A supplied by Agilent and one amplifier model WA301 supplied by Aim TTi. The DAQ system used is AMSY- MB2-V1 model supplied by Vallen Systeme GmbH, with four channels. For other DAQ system manufactures, the settings must be adapted accordingly.

Operational Procedure

The operation of the mobile device for acoustic emission verification is divided in two steps, consisting of the device auto-check and the sensor verification.

Auto-Check

The device auto-check is a preliminary step before sensor verification, meant to verify the overall performance of the device. For transportation, the system is partly disassembled, so it needs to be re-qualified after re-assembly. Hence, this step is necessary to ensure that the setup is correct.

Start is transmitter and receiver in retrieved position, as shown in Figure A.42a. For the coupling between transmitter and the aluminum plate, use a spatula with approximately 50 mg to 60 mg of coupling agent KORASILON-Paste (medium viscosity) supplied by Kurt Obermeier GmbH & Co. KG. on the area where the transmitter will be positioned. The transmitter must be held with one hand, Figure A.42b, and with the other hand, the locking mechanism is released, Figure A.42c. Slowly release the transmitter towards the plate avoiding impact, as shown in Figure A.42d. Repeat the procedure for the receiver.

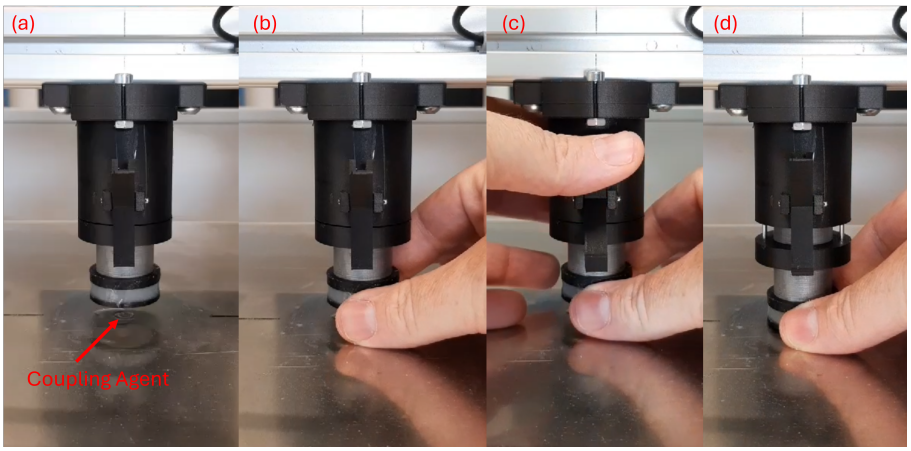

Figure A.42: (a) Transmitter in retrieved position. (b) Hold the receiver with one hand. (c) Release the locking mechanism. (d) Slowly release the transmitter towards the plate.

The cable of the receiver must be connected to the single input of its 2/4/6 amplifier and the switch must be in single position. The gain of the amplifier must be in 40 dB position and its output must be connected to the channel number 3 of the DAQ system.

The output of the arbitrary waveform generator must be connected to the input of the WA301 amplifier, and its 50 Ωoutput connected to the transmitter, Figure A.43.

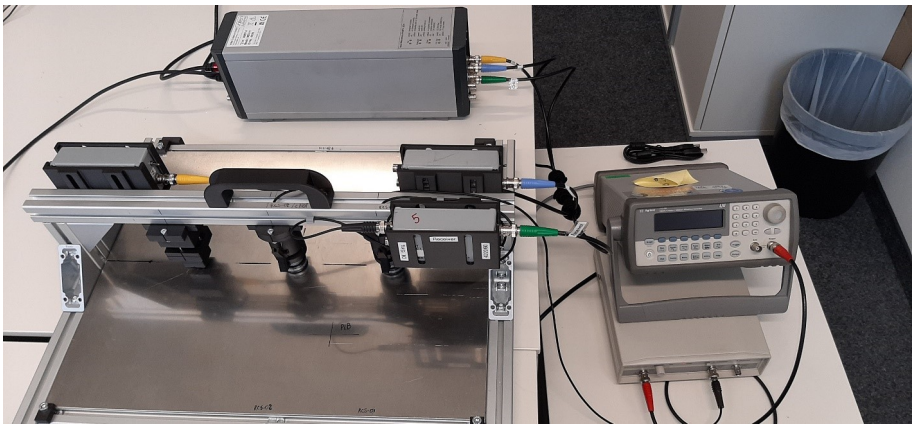

Figure A.43: Full verification setup.

Connect the power cords of the DAQ system, of the arbitrary function generator, and of the WA301 amplifier into the electric outlets and turn on all devices .

Select the function pulse on the arbitrary wave form and enter the following settings:

Frequency = 15 Hz

Amplitude = 10 Vpp (peak-to-peak)

DC-Offset = 0 V

Window width = 10 μs

Edge (rise time) = 20 ns

These settings were found to be optimal for the specific case of the transmitter and receiver measurements. Other pulse settings can be required to adapt to the response of specific SUTs.

On the front end of the DAQ system, select the position of the switches to enable AE and transient record (TR).

Connect the USB cable of the DAQ system to the laptop/pc and open the application "Vallen Control Panel". In the "Vallen Control Panel", open the application "Acquisition" under the tab "Normal Use", as shown in Figure A.44.

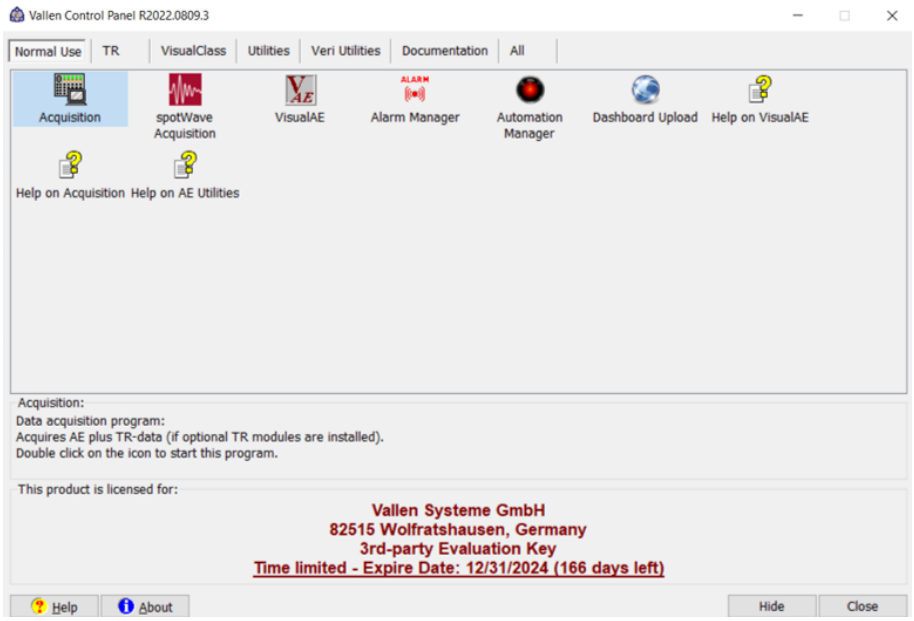

Figure A.44: Vallen Control Panel.

On "Vallen Acquisition", double-click on "Step 2", as shown in Figure A.45, and navigate to the folder where the pulse test template file should be saved and save with appropriate name.

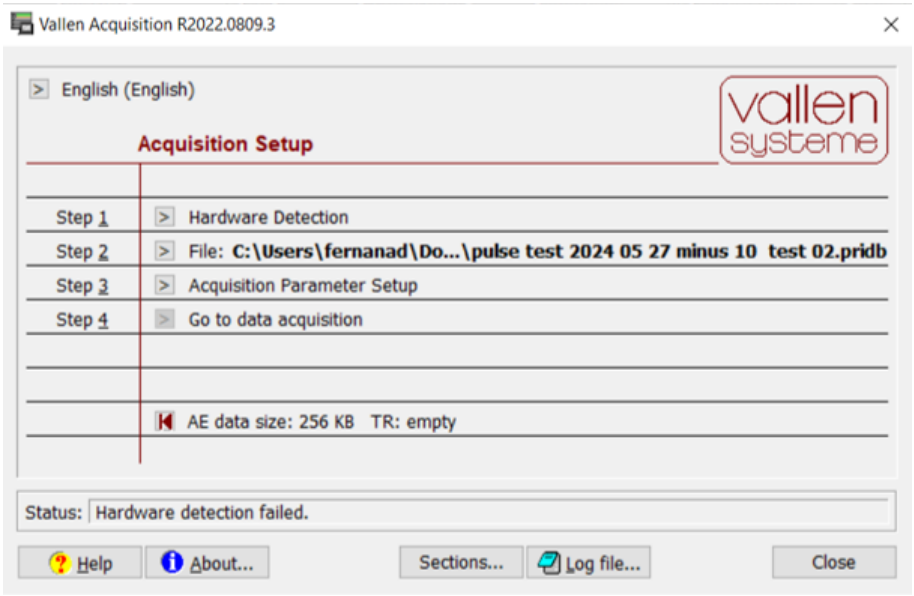

Figure A.45: Vallen Acquisition.

Afterward, the "Acquisition Parameter Setup" will automatically open. Click on "save" after setting the features according to Figure A.46.

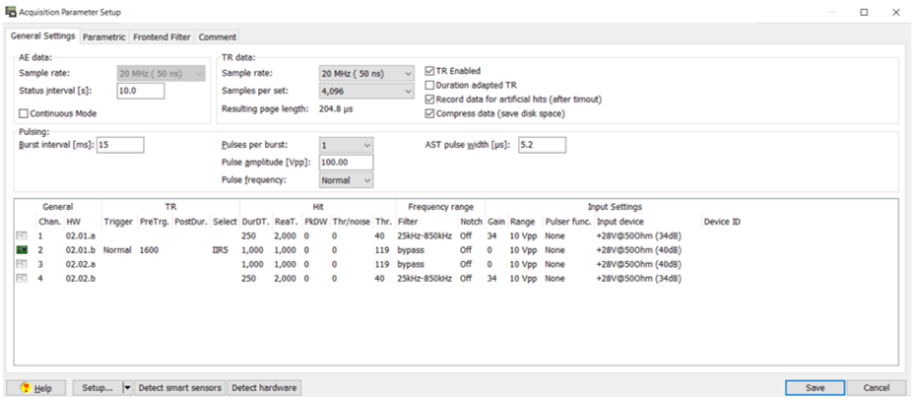

Figure A.46: Acquisition Parameter Setup.

Click on "Go to data Acquisition", then click "VisualAE", as shown in Figure A.47. Afterward, click on "Continue", select the option "Yes, browse for a setup file" and select the appropriate template.

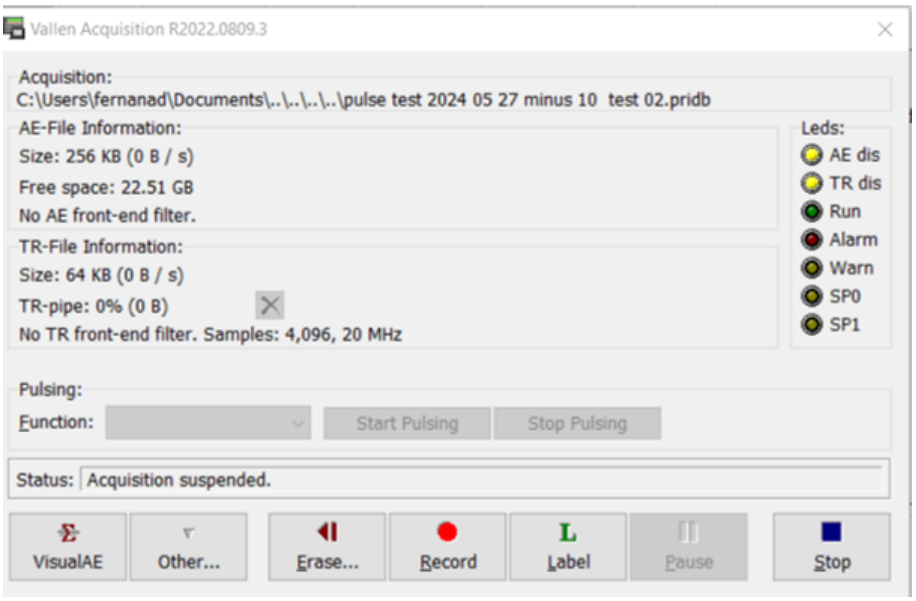

Figure A.47: Data acquisition menu.

Then, click on the green play button, as shown in Figure A.48, return to "Data Acquisition" and click on "Record". After that, press "Output" on the front end of the arbitrary function generator to collect at least 600 signals. Click on "Pause" to pause recording data, and then on "Stop".

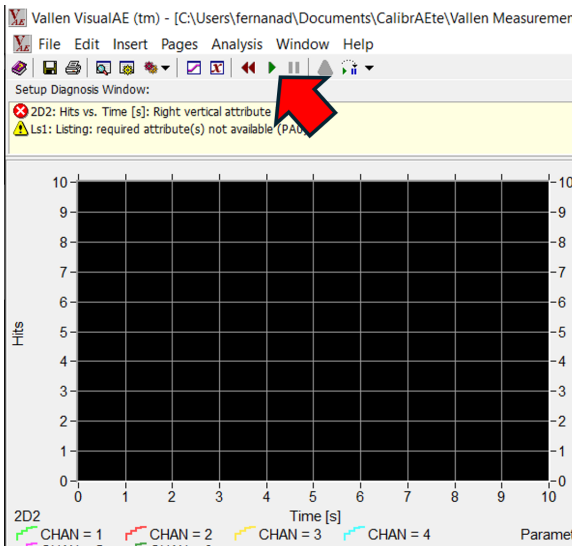

Figure A.48: Data Visualizer.

Sensor Verification

Once the setup is approved, the operator can move on to verify the AE SUT. For the coupling between SUT and the aluminum plate, use a spatula to spread approximately 50 mg to 60 mg of coupling agent KORASILON-Paste (medium viscosity) supplied by Kurt Obermeier GmbH & Co. KG on the wear plate of the sensor. Retrieve the coupling mechanism of the SUT by moving it upwards with one hand. Then, insert the sensor with the other hand in the hole of the sensor adapter, Figure A.49a-c. There exist different adapters depending on the model and geometry of the sensor. Afterward, slowly release the coupling mechanism for the SUT to move towards the plate avoiding impact.

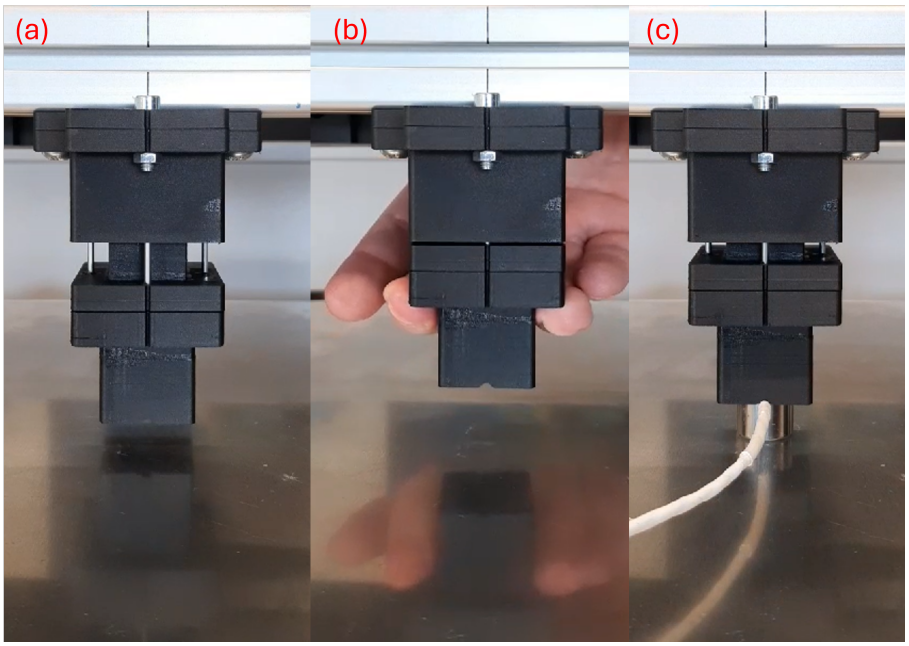

Figure A.49: (a) Coupling mechanism of the SUT in advanced position. (b) Coupling mechanism of the SUT in retrieved position. (c) Positioned SUT and coupled to the surface.

If the sensor has an integrated amplifier, connect the sensor to channel three of the AE DAQ system. If the sensor does not have an integrated amplifier, connect the SUT to the input of the 2/4/6 amplifier and select differential switch position for differential sensors, or single if the sensor has a single PZT element. In the case that the 2/4/6 amplifier is required, select the appropriate gain. Connect the output of the 2/4/6 amplifier to channel three of the AE DAQ system.

Similar to the auto-check procedure, select the appropriate pulse settings on the front end of the arbitrary function generator.

Before staring signal recording, it is important to observe a settlement time of the

coupling agent, which varies among the sensor types.

Similar to device auto-check, perform the data acquisition of 600 signals.

Storage and Transportation

The mobile device must be stored with the transmitter and receiver coupled to the plate with coupling agent, in order to avoid creep effect on the loading springs of the coupling mechanisms.

Transmitter and receiver must be moved into retrieved position before transportation, in order to avoid damage in case of mechanical shock.

After retrieving the transmitter for transportation, the leftover coupling agent must be removed. Therefore, move the transmitter into retrieved position and insert a wet tissue between the transmitter and the aluminum plate, Figure A.50. Move the transmitter downwards and rotate the wet tissue 360°, Figure A.50b. Move the transmitter back to retrieved position, Figure A.50c. Remove and discard the wet tissue, Figure A.50d. Repeat the same procedure for the receiver.

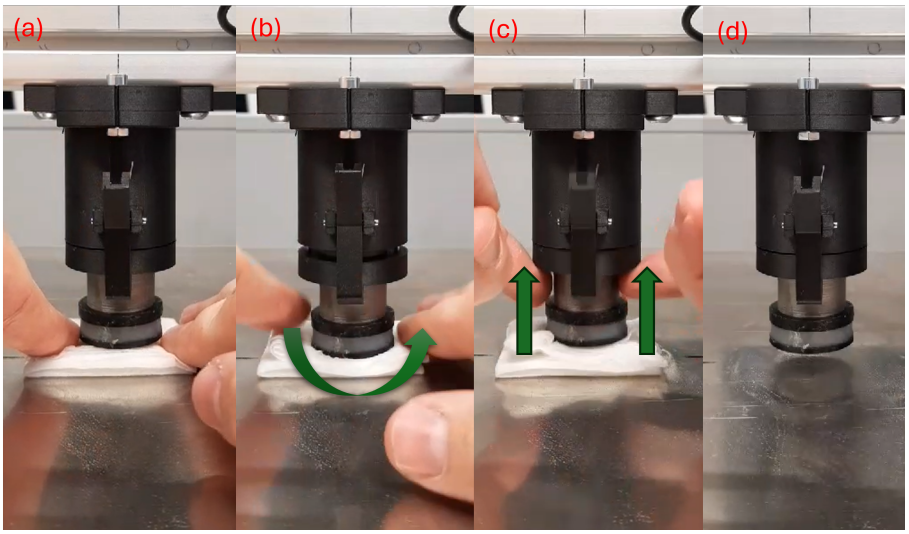

Figure A.50: (a) Insert the wet tissue between the transmitter and aluminum plate. (b) Move the transmitter downwards and rotate the wet tissue 360°. (c) Move the transmitter back to retrieved position. (d) Remove the wet tissue.

Appendix D
Example Code for Sensor Verification

The code to automate sensor verification can be found at:
`https://github.com/Adelmo-Ferandes/AE-sensor-verification-codes`

Appendix E
Example Code for Climate Chamber Test Automation

The code to automate climate chamber test can be found at:
`https://github.com/Adelmo-Ferandes/AE-sensor-verification-codes`